Modelling of the oxygen electrode for Solid Oxide Cells : study of the reaction mechanism and impact of the degradation

Elisa Effori

THÈSE

Pour obtenir le grade de

DOCTEUR DE L'UNIVERSITE GRENOBLE ALPES

Spécialité : **Matériaux, Mécanique, Génie civil, Electrochimie**

Arrêté ministériel : 25 mai 2016

Présentée par

Elisa EFFORI

Thèse dirigée par **M. Jérôme LAURENCIN, Docteur, CEA-LITEN**, et codirigée par **M. Laurent DESSEMOND, Professeur, LEPMI** préparée au sein du **CEA-LITEN** dans l'**École Doctorale I-MEP²**

Modélisation de l'électrode à oxygène pour cellules à oxyde solide : étude des mécanismes réactionnels et de l'impact de la dégradation

Thèse soutenue publiquement le **« 13/07/2021»**,
devant le jury composé de :

Mme. Elisabeth SIEBERT
Directrice de recherche, Laboratoire d'Electrochimie et de Physicochimie des Matériaux et des Interfaces (LEPMI) de Grenoble (Présidente de jury)
M. Nicolas BION
Chargé de Recherche, CNRS, Institut de Chimie des Milieux et Matériaux de Poitiers (IC2MP) (Rapporteur)
M. Pierre-Marie GEFFROY
Chargé de Recherche, CNRS, Institut de Recherche sur les CERamiques (IRCER) (Rapporteur)
M. Jean-Paul VIRICELLE
Professeur à l'Ecole des Mines de Saint Etienne, (Examinateur)
M. Jérôme LAURENCIN
Docteur, CEA-LITEN (Membre, directeur de thèse)
M. Laurent DESSEMOND
Professeur, LEPMI (Invité, co-directeur de thèse)
Mme. Marie PETITJEAN
Docteure, CEA-LITEN (Invitée, co-encadrante de thèse)

Index

Acknowledgements

The present thesis work was carried out at CEA-Liten of Grenoble (France) in the Laboratoire Essais et Systèmes (LES), which is part of the Service des Technologies Hydrogène (STH2) under the Département Thermique, Conversion et Hydrogène (DTCH). For this reason, I would like to thank Cyril Bourasseau and Julie Mougin, heads of the Laboratory and of the Service, respectively.

I would like also to thank the members of the jury: Nicolas Bion (IC2MP), Pierre-Marie Geffroy (IRCER) and Jean-Paul Viricelle (UMR CRNS) for the attention spent to revise my manuscript and for the interesting exchange that we had during the discussion of my PhD defense.

I want also to thank in particular Elisabeth Siebert for helping me many times during my PhD with her deep knowledge of the electrochemistry, and Claude Montella for introducing me to the cyclic voltammetry technique.

A special thank goes to my co-supervisor Marie Petitjean for being always present whenever I needed, and to my co-director Laurent Dessemond for following me with attention during the redaction of the manuscript.

I want to express my gratitude to my thesis director Jérôme Laurencin for giving me the possibility to work in his team during these last three years and a half. I consider him as an example of how a good researcher should be and I will do all my best to put in practice all the things I have learnt from him in my future work.

Je veux aussi remercier Pascal Giroud pour la professionnalité et la précision mises en place afin de réaliser les bancs d'essai pour les cellules symétriques. Travailler avec toi a été à la fois instructif et amusant. Merci aussi pour l'hospitalité que toi et Corinne m'avez toujours offerte. Merci à vous deux de m'avoir fait sentir comme si j'étais chez moi.

Thanks to Nathalie Giacometti for taking care of the SEM samples and also for her kindness. I want also to thank all the other colleagues of the "ancient" LTH: Jérôme A., Geraldine, Geraud, Pierre, Bruno, Philippe, Livia, Benjamin, Rémi, Amir, Antonietta, Bertrand, Karine, Thibault M., Stephane, Eric, Denis, Lionel, Sarah, Eglantine, Simon, Michel, and in particular Thibault D., Bastien, Jeremy and Maxime with whom I had the opportunity to work directly.

I would like to thank the other PhD students of the "Jérôme's team": Amira, Fede, Hamza, Lydia, Léa, Giuseppe and Tika and also the post-docs Giuse, Edu, Manon and Rakesh. I do not consider you only as colleagues, but as friends. Thanks for always being there for me, professionally and not only.

A heartfelt thanks to professor Paolo Piccardo (UNIGE) and Dario Montinaro (SolidPower) for allowing me discovering the amazing world of Solid Oxide Cells during my master thesis.

I thank all the friends who I had the chance to meet in Grenoble and my lifelong friends in Italy who have always made me feel close despite the distance. I spent amazing time with you during these years and I will never forget it.

Finally, I want to thank my family from the bottom of my heart for their constant love and support. Non ce l'avrei mai fatta senza di voi. Grazie mille per tutto.

Abstract

An elementary kinetic model was developed to predict the electrochemical response of porous LSCF and LSCF-CGO oxygen electrodes used in Solid Oxide Cells (SOC). For this purpose, an integrated approach coupling (i) electrochemical testing, (ii) advanced 3D characterizations and (iii) modeling was proposed. The microstructural properties extracted from the 3D electrodes volumes obtained by FIB-SEM tomography were implemented in the model as input parameters. The model was validated on a large set of experiments performed under different operating conditions by testing symmetrical cells in a three-electrode configuration. The reaction mechanism of both studied electrodes was thoroughly analyzed and the rate-determining steps for the electrodes have been identified. The LSCF model was also extended to simulate the cyclic voltammetry curves. The resulting simulations were compared with semi-analytical solutions to check the relevance of this simplified approach to assess the voltammetry response of porous LSCF electrodes. From the experimental point of view, long-term tests and post-test characterizations were performed at the electrode and complete cell levels as experimental evidences to support a proposed degradation mechanism for the LSCF demixing. In parallel, the experimental data for the validation of the micro model for the hydrogen electrode have been collected. Finally, a sensitivity analysis has been performed with the LSCF full elementary model to study the impact of LSCF decomposition on the electrode response.

Résumé

Un modèle cinétique élémentaire a été développé pour prédire la réponse électrochimique des électrodes à oxygène de type LSCF et LSCF-CGO utilisées dans les cellules à oxyde solide. Pour cela, une approche couplant i) des tests électrochimiques, ii) des caractérisations avancées et iii) de la modélisation a été proposée. Des reconstructions 3D des électrodes ont été obtenues par tomographie FIB-SEM. Ces dernières ont permis d'extraire les propriétés microstructurales qui ont été utilisées comme paramètres d'entrée du modèle. Ce modèle a été validé grâce à des expériences menées sur des cellules symétriques dans une configuration à trois électrodes, dans une large gamme de conditions opératoires. Des mécanismes réactionnels ont été proposés et les étapes cinétiques déterminantes des deux électrodes ont pu déterminées pour chaque électrode. Le modèle pour LSCF a été également étendu pour simuler les courbes de voltamétrie cyclique. Les simulations obtenues ont été comparées à des solutions semi-analytiques pour vérifier la pertinence de l'approche simplifiée. Des tests de longue durée ainsi que des caractérisations post-test ont été réalisés à l'échelle de l'électrode et de la cellule complète. Ceux-ci ont permis de confirmer expérimentalement un mécanisme de décomposition du LSCF. En parallèle, les données expérimentales pour la validation du micro-modèle pour l'électrode à hydrogène Ni-YSZ ont été collectées. Finalement, une analyse de sensitivité a été réalisée avec le modèle élémentaire pour LSCF afin d'étudier l'impact de la décomposition du LSCF sur la réponse de l'électrode.

List of Figures

List of Tables

List of Symbols

Roman Symbols:

A	Wave amplitude	(V)
$C_{dl}^{surface}$	Surface double layer capacitance	(F m^{-2})
$C_{dl}^{\mathrm{CGO/LSCF}}$	Double layer capacitance at the LSCF/CGO interface	(F m^{-2})
$C_{O_o^x}^{max}$	Maximum concentration of neutral oxygen atoms in LSCF	(mol m^{-3})
$C_{V_o^{\bullet\bullet}}$	Vacancies concentration in LSCF	(mol m^{-3})
$C_{V_o^{\bullet\bullet}}^{eq}$	Vacancies concentration in LSCF at equilibrium	(mol m^{-3})
D_{chem}	Bulk oxygen chemical diffusion coefficient in LSCF	(m^2 s^{-1})
D_i^{eff}	Effective diffusion for the i-th species	(m^2 s^{-1})
$D_{V_O^{\bullet\bullet}}$	Oxygen vancancies self-diffusion coefficient	(m^2 s^{-1})
D_{k,O_2}	Knudsen diffusion coefficient	(m^2 s^{-1})
D_{O_2,N_2}	Molecular diffusion coefficient	(m^2 s^{-1})
$D_{O^- - s_{LSCF}}$	Diffusion coefficient of the oxygen ad-ions	(m^2 s^{-1})
$D_{O - s_{LSCF}}$	Diffusion coefficient of the oxygen ad-atoms	(m^2 s^{-1})
$D_{O_2 - s_{LSCF}}$	Diffusion coefficient of the oxygen ad-molecules	(m^2 s^{-1})
E	Local electrode potential	(V)
$E_{act,i}$	Activation energy for the i-th species	(kJ mol^{-1})
F	Faraday's constant	(C mol^{-1})
F_{Tot}^{inlet}	Total inlet gas flow rate	(mol s^{-1})
$h^{\bullet}$	Hole defect in LSCF	(–)
$\vec{i}_{io/e'}$	Ionic current density in CGO/Electronic current density in LSCF	(A m^{-2})
j_{e^-}	Faradaic current density	(A m^{-2})
$J_{O_o^x}$	Flux of oxygen in the LSCF bulk	(mol·m^{-2}·s^{-1})
K_e^i	Thermodynamic equilibrium constant for the i-th species	(–)
k_{chem}	chemical kinetic constant	(m·s^{-1})
k_+	Forward reaction kinetic constants for R1 for the LSCF(*) or LSCF-CGO(**) electrode	(*) (mol m^{-1} s^{-1}) or (**) (mol m^{-2} s^{-1})
$k_{ox}^{LSCF/gas}$	Forward reaction kinetic constants for R2	(m^3 mol^{-1} s^{-1})
k_{ox}^{TPBls}	Forward reaction kinetic constants for R3 for the LSCF(*) or LSCF-CGO(**) electrode	(*) (m s^{-1}) or (**) (s^{-1})
k_{deion}	Forward reaction kinetic constants for R4	(s^{-1})

k_{ass}	Forward reaction kinetic constants for R5	($mol^2\ m^{-1}\ s^{-1}$)
k_{des}	Forward reaction kinetic constants for R6	(s^{-1})
$\mathcal{L}$	Laplace transform operator	(s^{-1})
ℓ	Electrode thickness	(µm)
ℓ_{CGO}	CGO electrolyte thickness	(µm)
ℓ_{YSZ}	YSZ electrolyte thickness	(µm)
$M(s)$	Mass transfer function	($s\ m^{-1}$)
M_i	Molar mass for the i-th species	($g\ mol^{-1}$)
m	Reaction order	(–)
$\vec{N}_i$	Molar flux of the i-th species	($mol \cdot m^{-2} \cdot s^{-1}$)
$O_o^x(LSCF)$	Oxygen atom in the LSCF lattice	(–)
$O_o^x(CGO)$	Oxygen atom in the CGO lattice	(–)
$O^- - s_{LSCF}$	Oxygen ad-ion on LSCF surface	(–)
$O - s_{LSCF}$	Oxygen ad-atom on LSCF surface	(–)
$O_2 - s_{LSCF}$	Oxygen ad-molecule on LSCF surface	(–)
O_2	Gaseous oxygen molecule	(–)
P_{O_2}	Oxygen partial pressure	(atm)
P_t	Total pressure	(atm)
$\bar{r}_{pores}$	Mean pore radius	(m)
R	Universal gas constant	($J\ mol^{-1}\ K^{-1}$)
R_s	Series resistance	$\Omega\ cm^2$
R_p	Polarization resistance	$\Omega\ cm^2$
R_c	Contact resistance	$\Omega\ cm^2$
s	Laplace variable	(–)
s_{LSCF}	Adsorption site on LSCF surface	(–)
$S_p^{CGO/LSCF}$	Specific surface area between CGO and LSCF for the LSCF(*) or LSCF-CGO (**) electrode	(*) (–) or (**) (m^{-1})
$S_p^{LSCF/gas}$	Specific surface area between LSCF and gas phase	(m^{-1})
$S_{el.}$	Electrode surface	(cm^2)
T	Absolute temperature or Wave period	(K) or (s)
V_i	Fuller's volume for the i-th species	(–)
$V_o^{\bullet\bullet}(LSCF)$	Oxygen vacancy in the LSCF lattice	(–)
$V_o^{\bullet\bullet}(CGO)$	Oxygen vacancy in the CGO lattice	(–)
$y_{(i)}$	Molar fraction of species i-th species	(–)

Greek Symbols:

$\alpha_{Ri}^{ox/red}$	Charge transfer coefficient for oxidation or reduction for the reaction Ri	(–)
Γ	Surface density of available sites on LSCF	(mol m^{-2})
ε_X	Phase volume fraction for the phase X	(–)
η	Overpotential	(V)
$\theta_{O^- - s_{LSCF}}$	Coverage of oxygen ions on LSCF	(–)
$\theta_{O - s_{LSCF}}$	Coverage of oxygen atoms on LSCF	(–)
$\theta_{O_2 - s_{LSCF}}$	Coverage of oxygen molecules on LSCF	(–)
$\theta_{s_{LSCF}}$	Free sites on the LSCF surface	(–)
$\theta_{O^- - s_{LSCF}}^{eq}$	Coverage rate of oxygen ions on LSCF at equilibrium	(–)
$\theta_{O - s_{LSCF}}^{eq}$	Coverage rate of oxygen atoms on LSCF at equilibrium	(–)
$\theta_{O_2 - s_{LSCF}}^{eq}$	Coverage rate of oxygen molecules on LSCF at equilibrium	(–)
$\theta_{s_{LSCF}}^{eq}$	Free site on LSCF at equilibrium	(–)
$\nu_{(i)}$	Kinetic rate of chemical/electrochemical reaction (i) in the electrode(*) or at the electrolyte interface(**)	(*) (mol m^{-3} s^{-1}) or (**) (mol m^{-2} s^{-1})
ν	Potential scan rate	(V s^{-1})
$\tilde{\mu}_i$	Electrochemical potential	(J mol^{-1})
ξ_{TPBls}	Density of triple phase boundary lengths for the LSCF(*) or LSCF-CGO(**) electrode	(*) (m^{-1}) or (**) (m^{-2})
ξ	Dimensionless electrode potential	(–)
π	Pi constant	(–)
$\sigma_{h^{\bullet}_{LSCF}}$	Electronic conductivity of LSCF	(S m^{-1})
$\sigma_{io,\ CGO}$	Ionic conductivity of CGO	(S m^{-1})
σ_i^{eff}	Effective conductivity for th i-th species	(S m^{-1})
φ_i	Potential	(V)
χ	Surface electrostatic potential	(V)
τ_X	Tortuosity factor for the phase X	(–)
ω	Angular frequency	(rad s^{-1})

List of Abbreviations

AFC	Alkaline Fuel Cell
CE	Counter Electrode
CGO	Ceria doped Gadolinium Oxide
CV	Cyclic Voltammetry
DFT	Density Functional Theory
EIS	Electrochemical Impedance Spectroscopy
FIB-SEM	Focused Ion Beam-Scanning Electron Microscopy
LSM	Lanthanum Strontium Manganite
LSCF	Lanthanum Strontium Cobalt Ferrite
LSV	Linear Sweep Voltammetry
MIEC	Mixed Ionic and Electronic Conductor
OER	Oxygen Electrode Reaction
OCP	Open Circuit Potential
PEM	Proton-Exchange Membrane
RE	Reference Electrode
SOC	Solid Oxide Cells
SOFC	Solid Oxide Fuel Cell
SOEC	Solid Oxide Electrolysis Cell
TPBls	Triple Phase Boundary lengths
WE	Working Electrode
XRD	X-ray Diffraction
YSZ	Yttria Stabilized Zirconia

Outline of the manuscript

In the first chapter, an overview of the main Solid Oxide Cells (SOCs) characteristics is presented. The operating modes, the most common components materials and the possible architectures of SOCs are be briefly described. A focus on SOCs performances and on the type of losses during operation is reported. A detailed review on the reaction and degradation mechanisms for the two electrodes (hydrogen and oxygen electrodes) allows highlighting the common knowledge along with the topics that still need a deeper investigation. In this frame, the main types of SOCs degradation phenomena are listed with a special focus on the Ni agglomeration and Ni migration for the Ni-YSZ hydrogen electrode and the LSCF demixing for the LSCF and LSCF-CGO oxygen electrodes. Finally, the framework of this work, its goals and the methodology are stated.

The second chapter is dedicated to the analysis of the experimental results recorded on single electrodes and complete cells. A comprehensive description of tested samples and of the experimental set-ups is given. The sets of electrochemical measurements and microstructural characterizations performed on LSCF and LSCF-CGO electrodes are reported in details. In parallel to the study on the oxygen electrodes, the results obtained on Ni-3YSZ electrodes have been presented. These data have been collected in the frame of a collaboration (Ph.D. thesis of Federico Monaco) for the validation of an elementary kinetic model of the hydrogen electrode. In addition, the durability behavior of LSCF in both fuel cell and electrolysis modes is discussed together with the corresponding post-test characterizations performed at the Paul Scherrer Institute Facility (PSI). Finally, the durability curves of two complete cells integrating LSCF as oxygen electrode and tested in dry and humid atmospheres in O_2 side are presented.

The modelling approach for the description of the electrochemical responses of LSCF and LSCF-CGO electrodes is described in the third chapter. The microstructural properties of both types of oxygen electrode have been used as input data for the modelling. The elementary kinetic including a detailed surface kinetic description is validated on a wide range of electrochemical characterizations. The validated model is used to analyze the respective roles of temperature, polarization and oxygen partial pressure on the electrode reaction mechanisms in SOFC and SOEC modes. Thus, the rate-determining steps in the oxygen electrodes are identified with a sensitivity analysis on the impedance diagrams by varying the reaction kinetic constants. Finally, the full

elementary model for the LSCF electrode is extended to compute CV curves as well. The relevance of this model to predict the CV curves of LSCF electrodes is thus checked as functions of temperature and imposed potential scan rates.

The last chapter is dedicated to an overview of all the results of the present thesis. The main conclusions are listed together with some outlooks related to the continuation of this work.

Introduction

The global temperature rise and the oceans acidification are two of the several consequences of the climate change [climate.nasa.gov] (Fig. 0-1). For this reason, many countries have decided to take urgent measures to contain this problematic before irremediable consequences. The *Paris agreement* is the most famous international treaty on the climate change. Its main goal is to reduce the peaks of greenhouse gas emissions in order to limit the global warming below 2 °C [UNFCCC Sites and platforms].

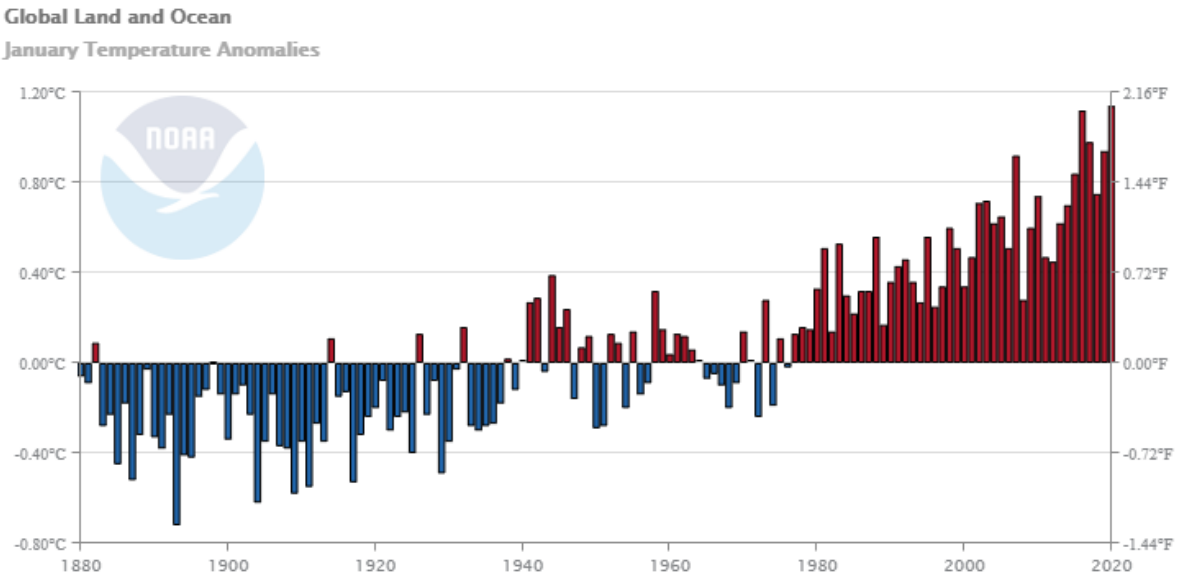

Fig. 0-1 Global land and ocean surface temperatures: January anomalies over the last 140 years. January 2020 was the hottest with 1.14 °C above the average [Source: NOAA (2020)].

In this frame, the use of Renewable Energies Sources (RES) could play a key role to lower the CO_2 emissions (Fig. 0-2). For instance, the *International Renewable Energy Agency* (IRENA) affirms that the investments in sustainable technologies could contribute to reduce about two thirds the emissions produced by crucial industrial and transport sectors [Reaching Zero with Renewables-IRENA]. However, the use of RES has still to face some important challenges. Indeed, their sources are neither continue or constant in time (for instance, a surplus of solar energy is expected in the warm seasons, while a deficit usually occurs during winter). For this reason, find a way to store or release energy on demand is of major importance to enable the definitive passage to green energies.

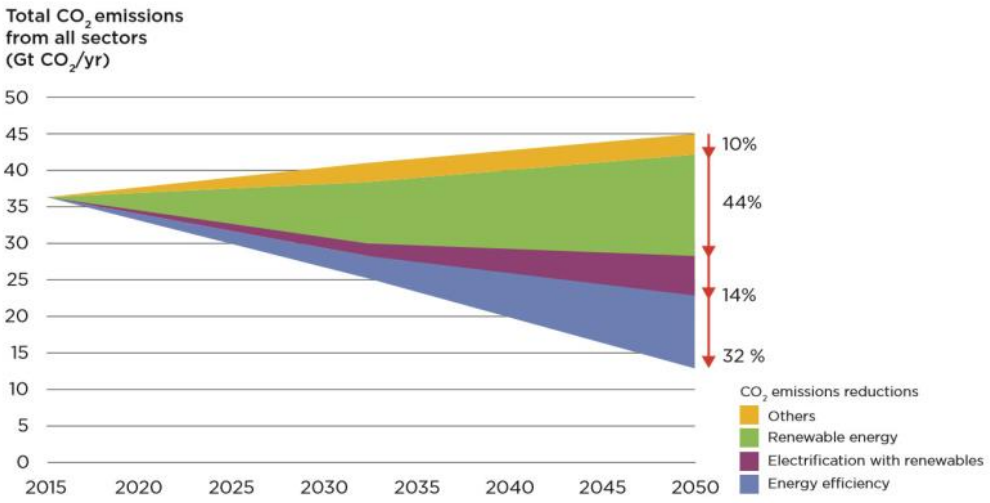

Fig. 0-2 Possible scenario of CO_2 percentage decrease from 2015 to 2050 if countries will invest in RES [Source: IRENA, IEA study concludes meeting 2˚C scenario possible with net positive economics, 2017].

Among all the possible technologies, hydrogen coupled fuel cells appears as one of the most promising energy systems. Indeed, on the one hand, hydrogen is one of the few energy carriers that can be produced with zero production of waste gases during the direct electrolysis of water. On the other hand, fuel cells present many advantages, such as the possibility to not generate polluting gases in operation with H_2 as fuel and the flexibility in the power generation that permits to this technology to range from power plant (megawatts) to portable electrical devices (less than 100 watts). Among the existing types of fuel cells, the Solid Oxide Fuel Cells (SOFCs) based on Solid Oxide Cells (SOCs) have recently attracted the attention thanks to their high efficiency, the fuel flexibility (H_2 but also alkanes, alcohols, ammonia etc. as fuels) and the co-production of heat easily recoverable. Moreover, SOCs can operate both in fuel cell mode (SOFC mode) and in electrolysis mode (SOEC mode). However, the widespread use of this technology is still hindered by the degradation of the individual components that reduces significantly the fuel cell or electrolyzer lifetime. SOCs are designed to operate at high temperatures and in harsh conditions (oxidative and reductive atmospheres, electrode polarization). The high operating temperature (600-900 °C) leads to many detrimental phenomena such as chemical reactivity between the compounds of cells and stacks, reactivity with gaseous contaminants or materials degradation. Experimental evidences have also shown that the degradation of SOCs depends on the operating

mode. The reason of this behavior is still not completely understood. Therefore, a better comprehension of the electrode reaction mechanisms is of prime importance to limit the performance losses over time. Indeed, only the achievement of a deeper knowledge of the fundamental electrochemical properties of SOCs based on state-of-the-art materials will enable to improve both the cell efficiency and durability making this technology full-fledged competitive on the market place.

Chapter I. Bibliography

1.1 General Aspects of SOCs

1.1.1 SOCs principle of functioning, components materials and architectures

Basis of functioning – SOCs are high temperature electrochemical devices usually composed of ceramic and metallic materials. The operating mode of SOCs relies on the electrochemical reactions occurring between oxidizing and reducing species. In the SOFC mode, the current is generated through the oxidation of the fuel (e.g. hydrogen, methane, carbon monoxide) and the reduction of oxygen, while in SOEC mode, the respective reactions are reversed to produce hydrogen and/or carbon monoxide from steam, carbon dioxide and oxygen under an electrical current. The gases produced in SOEC mode can be stored as tanks of chemical energy that can be subsequently used on demand to produce electricity. SOCs have recently attracted the green energy market attention thanks to their reversibility that makes these devices particularly compatible to be coupled with intermittent RES (e.g. wind turbines or solar panels) [Eriksonn2017, Staffell2019]. Moreover, high operating temperatures result in a very high efficiency, fuel flexibility and a co-production of high-quality heat in SOFC mode [Eguchi2002, Guaitolini2018]. This last feature makes SOFC as one of the most promising technology for clean residential energy supply through micro combined heat and power (micro-CHP) systems [Hawkes2007].

SOCs are usually composed by a dense ionic conductor electrolyte sandwiched between two porous electrodes exhibiting electronic or mixed conduction properties. The schematic operating principles of a SOC are shown in Fig. I-1. In SOFC mode, hydrogen is oxidized at the so-called hydrogen electrode (which behaves as an anode) to produce steam (forward reaction of Eq. (1)) and oxygen is reduced at the so-called oxygen electrode (which behaves as a cathode) to produce oxygen ions (forward reaction of Eq. (2)) (Fig. I-1a). The global chemical reaction yields the formation of steam (forward reaction of Eq. (3)). In SOEC mode, the backward reactions are activated and the hydrogen and oxygen electrodes behave as a cathode and an anode, respectively (Fig. I-1b). The reduction of steam produces oxygen ions which are oxidized. Regardless the operating mode, oxygen ions migrate through the dense electrolyte membrane.

$$H_2 + O^{2-} \leftrightarrow H_2O + 2e^- \quad (1)$$

$$\frac{1}{2}O_2 + 2e^- \leftrightarrow O^{2-} \quad (2)$$

$$H_2 + \frac{1}{2}O_2 \leftrightarrow H_2O \quad (3)$$

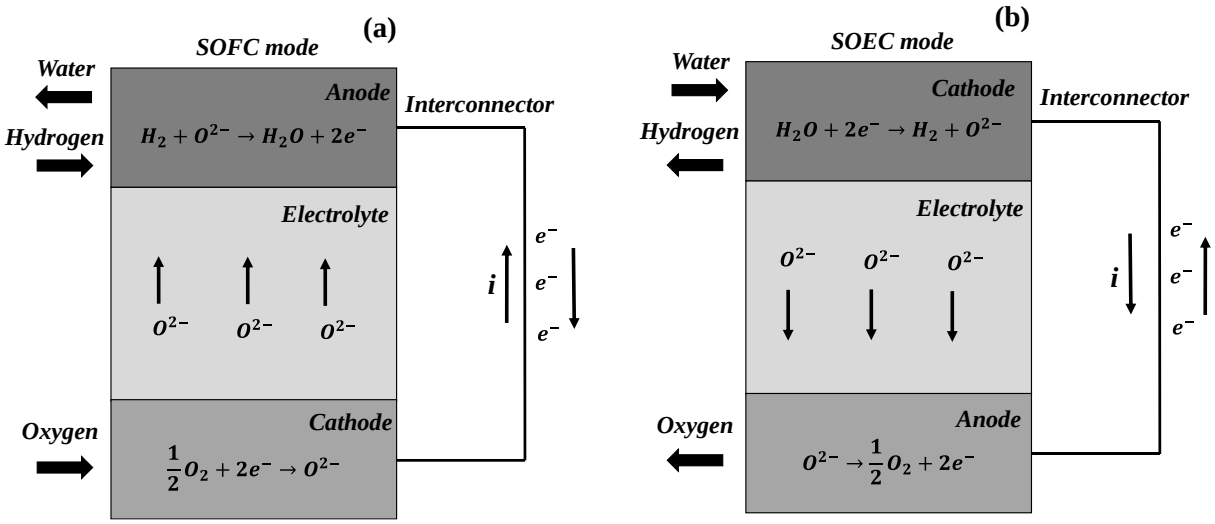

Fig. I-1 Scheme of the electrochemical half reactions that occur inside a SOC operating in fuel cell (a) and electrolysis (b) modes, respectively.

To allow the correct functioning of SOCs and to maximize their efficiency, each cell component must have precise characteristics.

Electrolyte - The electrolyte is the core of a SOC since it allows the passage of oxygen ions between the hydrogen and oxygen electrodes and ensures the gas tightness between the two electrode layers [Singhal2000]. Therefore, the choice of the electrolyte material is of fundamental importance. An electrolyte material must obey the following characteristics [Mahato2015]:

i) High ionic conductivity,

ii) Chemical stability over a large range of temperature and oxygen partial pressure,

iii) Chemical compatibility with respect to the other component materials (to avoid the formation of secondary phases),

iv) Reliable mechanical properties (high strength and toughness),

v) Coefficient of thermal expansion (CTE) compatible with those of the other cell components,

vi) Low cost and environmental friendly.

Many kinds of materials can be found in the literature as candidates for a SOC electrolyte, from the classical fluorite oxide based structure (e.g. ZrO_2 or CeO_2) to more recent compounds such as lanthanum-based perovskites [Fergus2006, Singhal2000]. However, despite the wide possibility, Yttria Stabilized Zirconia (YSZ) remains the most common used electrolyte material thanks to its excellent ionic conductivity, good chemical stability and its adapted CTE regarding the usual electrode materials [Hossain2017, Ivers-Tiffée2001]. Two types of YSZ electrolytes can be used depending on the level of doping: with 3 % mol of yttria (3YSZ) the zirconia presents a tetragonal phase with high mechanical properties, while, passing to 8 % mol of yttria (8YSZ), the zirconia change in a cubic phase with higher ionic conductivity (σ_{io}). Indeed, σ_{io} is an increasing function of the dopant content as described in Eq. 4 using the Kröger-Vink notation:

$$Y_2O_3 \xrightarrow{ZrO2} 2Y_{Zr}' + 3O_O^x + V_{\ddot{O}} \quad (4)$$

Accordingly, two moles of dopant create one mole of oxygen vacancies. These crystalline defects allow the migration of oxygen ions through the volume of the material [Singhal2000]. Despite its lower mechanical strength, 8YSZ is the most common electrolyte for SOCs since it presents a good compromise between ionic conductivity and mechanical resistance [Suciu2018]. As expected, the ionic conductivity of 8YSZ is thermally activated (Fig. I-2) [Zhang2007] and presents a value of 0.1 $S \cdot cm^{-1}$ at 1000 °C [Chen2002]. This characteristic explains the necessity of operating SOCs at high temperatures in order to maximize their performances.

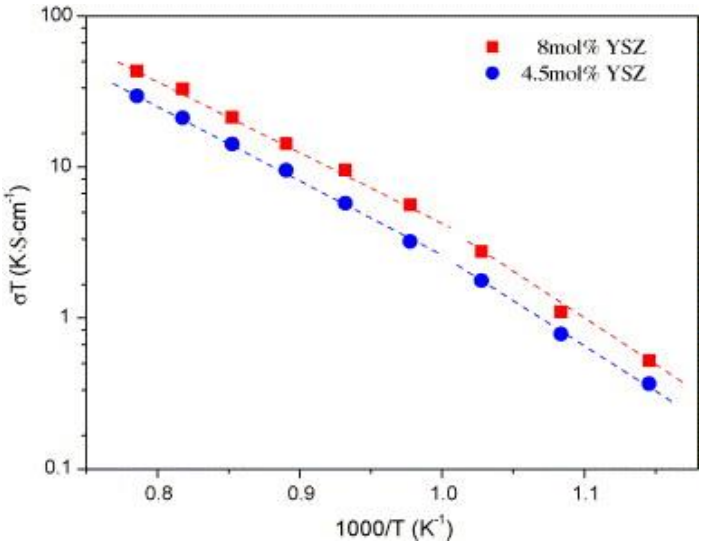

Fig. I-2 Evolution of the 8YSZ ionic conductivity as functions of the temperature and level of dopant. [Zhang2007].

As well as the electrolyte, the electrodes materials have to meet precise requirements [Singhal2000]:

i) High electronic conductivity,
ii) High catalytic activity for the electrochemical reactions,
iii) Chemical stability to avoid the reactivity with the other cell components,
iv) CTE matched with the electrolyte,
v) Sufficient porosity to allow the passage of the gas through the volume of the electrode,
vi) Low cost and environmental friendly.

Hydrogen electrode – The reaction in the hydrogen electrode occurs at the Triple Phase Boundary lengths (TPBls), where the oxygen ions, the hydrogen gas and the electrons meet [Zhu2003]. For this reason, the use of a material with a mixed ionic and electronic conductivity is favored, since it provides active sites in all the electrode volume. The common hydrogen electrode materials are composites made of an ionic conductor phase and a transition metal that provides the electronic conductivity [Shaikh2015]. In order to have a good CTE compatibility, the ionic phase is usually the same used for the electrolyte. Up to now, the most used transition metal is Nickel since it presents a good compromise between prize and catalytic activity [daSilva2017, Shaikh2015]. Thus, the most common composite material is the cermet (i.e. ceramic and metal composite) Ni-YSZ [Minh1993]. Since, a SOC is usually structurally supported by the H_2 electrode, the mechanical

properties of the cermet are extremely important [Pihlatie2009]. Moreover, a particular attention has to be paid during the hydrogen electrode manufacturing in terms of initial microstructural properties (such as the porosity level, the particle size diameter, the tortuosity etc.) to enhance the electrode performances and to limit the material degradation [Monaco2019].

Oxygen electrode - One of the most common material for the oxygen electrode is the composite composed of $La_{1-x}Sr_xMnO_{3-\delta}$ (LSM) and YSZ. Indeed, the mix of ionic and electronic conductor phases increases the number of the electroactive sites of an order of magnitude with respect to a simple electronic conductor (Fig. I-3a) [Sun2010]. Mixed Ionic and Electronic Conductors (MIECs) become of increasing interest for several decades. Indeed, their conduction properties combined in a single-phase compound results in higher performances, since the electrochemical reactions can take on all the surface of the electrode particles (Fig. I-3b) [Sun2010].

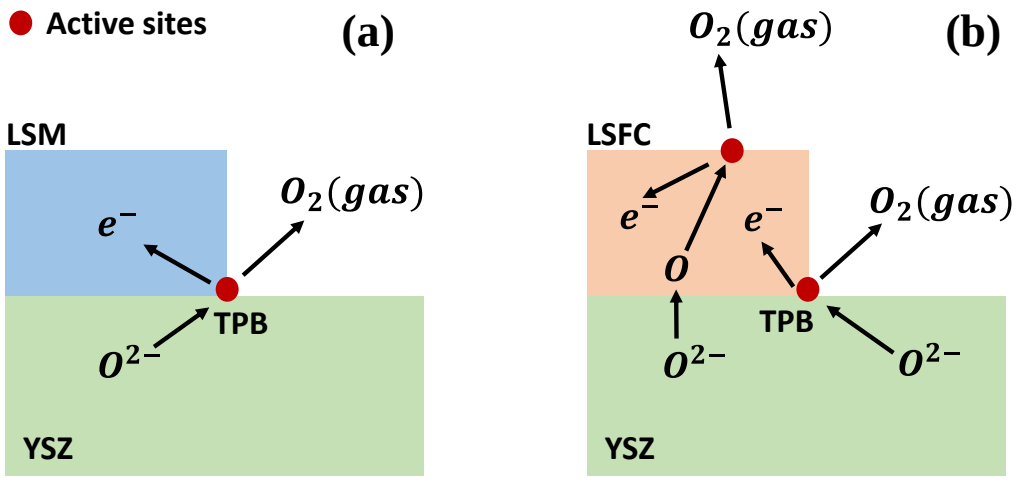

Fig. I-3 Comparison between the reaction mechanisms for a LSM-YSZ composite (a) and a LSCF (b) electrodes, respectively.

One of the most commonly used O_2-electrode material for Intermediate Temperature SOC (IT-SOC) is $La_{1-x}Sr_xCo_{1-y}Fe_yO_{3-\delta}$ (LSCF) [Menzler2010, Jiang2008, Sun2010]. A shown in Fig. I-4, the cell performances increase at low operating temperature (≤ 800 °C) using a LSCF electrode with respect to the traditional LSM-YSZ composite electrode [Tietz2006]. However, the use of LSCF-based electrodes implies the presence of an additional layer to mitigate the formation of non-conducting secondary phases with the YSZ electrolyte [Anderson2004]. For this reason, a thin barrier layer of $Ce_{1-x}Gd_xO_{2-\delta}$ (CGO) is usually added between these two materials [Sanchez

Ferreira2017]. Moreover, recent studies have shown that adding a high ionic conducting material like CGO into LSCF is liable to enhance the electrode performances [Aziz2020, Dusastre1999, Hwang2005]. Indeed, it has been reported [Leng2008, Wang2005] that the porous LSCF-CGO composite exhibits a higher effective ionic conductivity than the LSCF electrode. Moreover, a more compatible CTE with the electrolyte material reduces the risk of mechanical fractures by using a composite electrode [Laurencin2015, Wang2005].

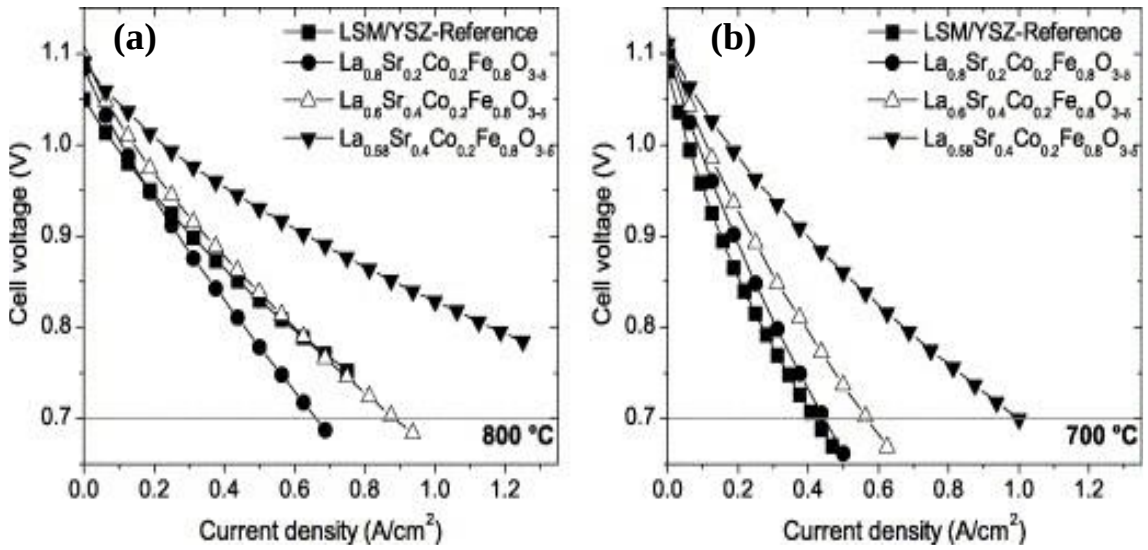

Fig. I-4 Polarization curves of complete cells with LSM and LSCF with different percentage of Sr dopant at the operating temperature of 800 °C (a) and 700 °C (b), respectively [Tietz2006].

Architecture – SOCs present two main types of architecture: planar or microtubular (Fig. I-5) [Jamil2015].

Planar SOCs are compact devices that present multiple layers with square or circular shape [Birss2017]. The cell can be self-supported or 'externally' supported. In the first case, SOCs can be classified as anode-, electrolyte- or cathode-supported, depending on which layer provides the mechanical strength. In the second case, an additional layer of metallic or ceramic material is added, while the other cell components are deposited as thin layers [Birss2017]. An electrode-supported or external supported structure is usually preferred since the electrolyte is maintained as thin reducing substantially the related Ohmic losses [Nozawa2008].

Microtubular SOCs (MT-SOCs) are made of concentric tubes which dimension goes from a few millimeters to sub-millimeter size [Panthi2014]. As well as planar SOCs, an electrode- or electrolyte-supported architecture can be designed [Lawlor2013]. MT-SOCs can be designed in

much smaller geometry than planar SOCs leading to some advantages such as a higher thermal shock resistance and an increased power per unit volume [Lawlor2013]. Both the possibility of a small size device and the resistance to multiple thermal cycling made this architecture very interesting for small portable fuel cell applications [Kendall2010]. However, the difficulty in positioning the sealing due to the reduced dimensions of the tubes enhances the risk of gas leakage [Lawlor2009].

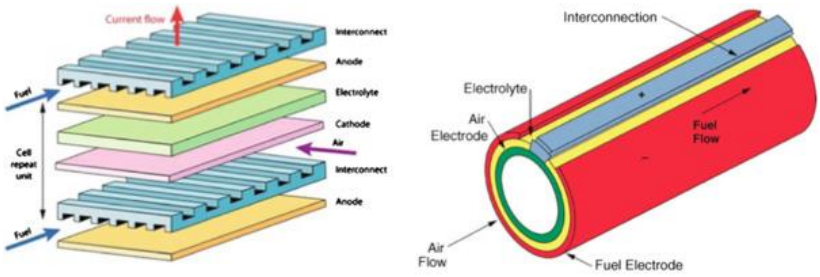

Planar SOFC [1] Tubular SOFC [2]

Fig. I-5 Different designs of SOCs: planar (on the left) and microtubular (on the right) [Jamil2015].

1.1.2 Operation in steady state condition

The efficiency of a SOC is represented by the corresponding polarization curve (i-V) showing the evolution of the cell voltage E^{cell} as a function of the current density (Fig. I-6a). The Open Circuit Voltage (OCV) corresponds to the cell voltage at the equilibrium state $E_{i=0}^{cell}$ (i = 0). This potential depends on temperature as well as the gas conditions and is expressed by the Nernst's equation in the case of a SOC fed by hydrogen and oxygen:

$$E_{i=0}^{cell} = E^0 + \frac{RT}{zF} \cdot ln\left(\frac{a_{H_2} \cdot \left(a_{O_2}\right)^{1/2}}{a_{H_2O}}\right) \quad (5)$$

where E^0 is the cell voltage in the standard conditions, R is the universal gas constant, T is the absolute temperature, F is the Faraday's constant, z is the number of exchanged electrons in the electrochemical reactions (i.e. 2 for a SOC fed by hydrogen and oxygen) and a_{H_2}, a_{O_2} and a_{H_2O} are the chemical activities of hydrogen, oxygen and steam, respectively, at the electroactive sites for i = 0.

Regardless of the operating mode, the cell voltage deviates from OCV under current (Fig. I-6a) since additional losses exist [O'Hayre2016, Patcharavorachot2008]. In SOEC mode, a sufficient cell voltage or current must be applied to trigger the non-spontaneous electrolysis reactions. In SOFC mode, the existence of a current implies that the cell voltage serves the irreversible phenomena related to the electrochemical reactions. Without emphasizing on any detailed electrode reaction mechanism, any electrochemical process implies mass transport of multi-components in a gas phase, mass transport through solid phases and charge transfer steps. Thus, additional losses are generated in a SOC that modify the cell voltage and are divided in three main contributions: Ohmic losses ($\eta_{ohm}(i)$), activation overpotentials ($\eta_{act}(i)$) and concentration overpotentials ($\eta_{conc}(i)$) [O'Hayre2016] (Fig. I-6b).

For SOFC mode ($i > 0$) and SOEC mode ($i < 0$), the cell potential is expressed as follows, respectively:

$$E^{cell} = E^{cell}_{i=0} - \eta_{ohm}(i) + \{\eta^{cathode}_{act}(i) - \eta^{anode}_{act}(i)\} + \{\eta^{cathode}_{conc}(i) - \eta^{anode}_{conc}(i)\} \quad (6)$$

$$E^{cell} = E^{cell}_{i=0} - \eta_{ohm}(i) + \{\eta^{anode}_{act}(i) - \eta^{cathode}_{act}(i)\} + \{\eta^{anode}_{conc}(i) - \eta^{cathode}_{conc}(i)\} \quad (7)$$

where $\eta^{cathode}_{act}(i)$, $\eta^{cathode}_{conc}(i)$, $\eta^{anode}_{act}(i)$ and $\eta^{anode}_{conc}(i)$ are the activation and concentration overpotentials for the cathode and the anode under a current *i*, respectively.

Ohmic losses – The Ohmic losses are related to the overall series resistance R_s due to the flow of electrons in the electrodes and current collectors and to the flow of ions in the electrolyte and the contact resistance R_c corresponding to the contact between the cell and the current collectors. By considering that the electronic resistances of both the electrodes and current collectors are negligible, R_s represents the sum of the electrolyte resistance $R_{electrolyte}$ and of R_c. The Ohmic losses are proportional to the current according the classical Ohm's law [Patcharavorachot2008]:

$$\eta_{ohm}(i) = i \cdot R_s \quad (8)$$

Accordingly, the contribution of Ohmic losses on the polarization curve is linear.

Activation overpotential – The activation overpotential is caused by a slow charge transfer reaction and reflects the irreversible phenomena related to electrochemical reactions. In this macroscopic description, it includes all the microscopic phenomena arising in the electrode active layers. This contribution is predominant for low polarizations and becomes higher when the operating

temperature is decreased. For an electrode reaction mechanism, the activation overpotential is usually expressed through a phenomenological equation using the Butler-Volmer relation [Patcharavorachot2008]:

$$i = i_0 \cdot \left\{ \exp\left(\frac{\alpha z F}{RT} \cdot \eta_{act}(i)\right) - \exp\left(-\frac{(1-\alpha) z F}{RT} \cdot \eta_{act}(i)\right) \right\} \quad (9)$$

where α is the symmetrical transfer coefficient (usually taken as 0.5) and i_0 is the 'apparent' exchange current density that depends on the operating temperature and the gas partial pressures [Godula-Jopek2015].

Concentration overpotential – The concentration overpotential is induced by the change of gas composition at the active sites that occurs under current [Godula-Jopek2015]. This overpotential can be considered as the sum of two contributions:

$$\eta_{conc}(i) = \Delta E_{rev} + \eta_{diff}(i) \quad (10)$$

where ΔE_{rev} are the gas conversion losses and $\eta_{diff}(i)$ are the diffusion overpotentials.

The gas conversion losses are reversible contributions related to the change of gas composition in the porous electrode due the species production or consumption all along the cell length [Laurencin2015]. They correspond to thermodynamic losses that cannot be avoided. On the other hand, the diffusion overpotentials are irreversible. Therefore, $\eta_{diff}(i)$ depend also to the microstructural properties of the electrode (such as porosity and tortuosity) that can play a central role on the gas diffusion in the electrode volume [Holzer2013]. The concentration overpotentials become predominant at high current density.

The Ohmic losses and the diffusion overpotentials can be reduced during the cell manufacturing or with experimental precautions. As an illustration, the increase of the gas flow in the porous electrode limits the resistance due to the mass transport, while the use of a thin electrolyte decreases the Ohmic losses. The situation is more complicated for the activation overpotential. Indeed, this loss is related to the electrode reaction mechanism that cannot be directly monitored. Therefore, the only possibility to limit this overpotential is a deep understanding of the phenomena that take place at a microscopic level. For this reason, the next section will be dedicated to a review of the coupled experimental-modelling approaches used to improve this knowledge.

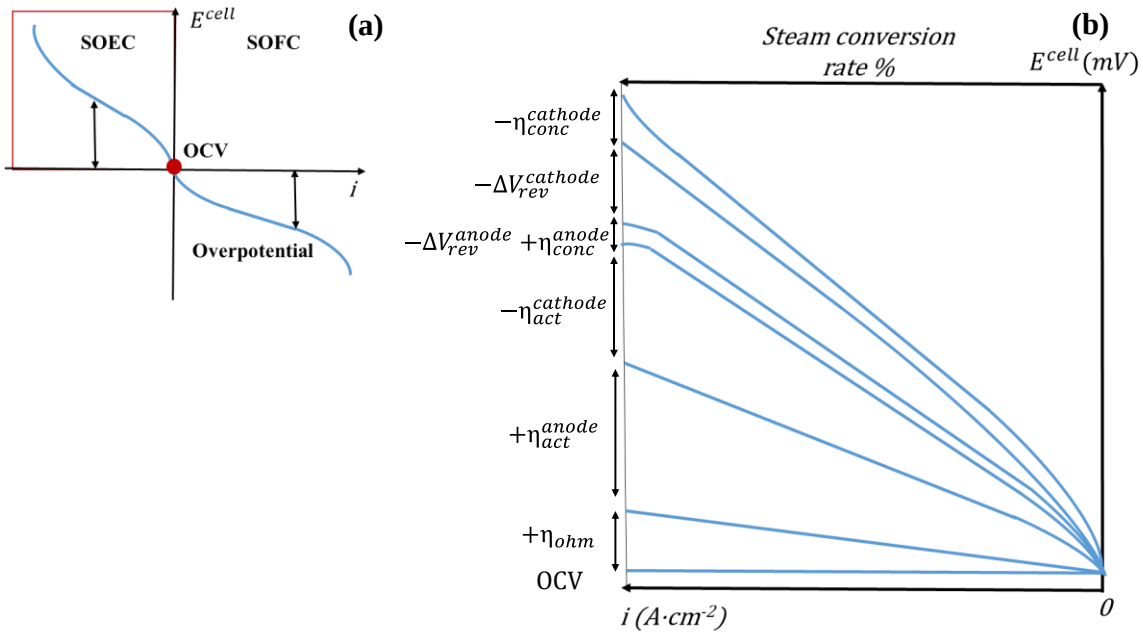

Fig. I-6 Example of a generic SOC polarization curve in SOFC and SOEC modes (a). Illustration of the voltage decomposition for a complete cathode-supported cell operated in electrolysis mode at T = 800 °C with air at the anode side and an inlet gas composition of 90% H_2O + 10% H_2 at the cathode side (b).

1.2 Review on the reaction mechanisms: electrodes functioning and degradation phenomena

Up to now, many efforts have been paid to achieve the full comprehension of SOCs reaction mechanisms. For this purpose, modelling coupled experimental approaches have been used. In these methods, the comparison between the experiments and the model simulations have allowed the validation or the discarding of the model assumptions towards a better understanding of the electrode reaction mechanisms. The most common electrochemical characterizations are the polarization curves and the Electrochemical Impedance Spectroscopy (EIS). Less usual experimental techniques as the Cyclic Voltammetry (CV) can be also found in the literature. However, despite the wide bibliography on the topic, the fundamental electrochemistry of both the hydrogen and oxygen electrodes still needs a deeper investigation. Indeed, as already mentioned, its knowledge is of primary importance to enhance the cell performances and to reduce the electrodes degradation. Accordingly, this work presents a review on the electrode reaction

mechanisms and on the most harmful degradation phenomena with the aim to report the main achievements in the field and to highlight the remaining open questions.

1.2.1 Hydrogen electrode reaction mechanism

Several experimental works have been devoted to the investigation of the reaction mechanism at the Ni-YSZ cermet by electrochemical characterizations (polarization curves and impedance diagrams) [Bieberle2000, 2001, Dasari 2013, Doppler2018, Grondin2011, Holtappels1999a, 1999b, Kek2001, Luo2017, Marina2007, Mizusaki1994a, 1994b, Pan2015a, Primdahl1997, Shin2016, Sonn2008]. Many of these studies have been carried out on electrodes with simplified geometries in order to relate more easily the morphological features of the electrode to the corresponding electrochemical response [Bieberle2000, 2001, Doppler2018, Kek2001, Luo2017, Mizusaki1994a, 1994b]. However, the real Ni-YSZ porous electrode exhibits a very complex microstructure that can strongly affect the reaction mechanism [Hanna2014]. For this reason, some authors have decided to perform experiments on classical porous electrodes in order to gather information under more realistic operating conditions [Dasari2013, Grondin2011, Holtappels1999a, 1999b, Marina2007, Pan2015a, Primdahl1997, Sonn2008]. Nevertheless, even in these cases, the exact microstructural properties of the tested electrodes were unknown. It is worth noting that most of the aforementioned studies concern mostly the Ni-8YSZ, while only very few experiments have been conducted on the Ni-3YSZ [Jiang1999, Kresse2000]. Finally, the majority of the experiments reported in the literature on the cermet electrode have been performed in SOFC mode, while only a few specific works have been focused on SOEC mode [Dasari2013, Grondin2011, Shin2016] among them only one at high steam partial pressures [Shin2016].

For the Ni-8YSZ cermet, it has been proposed that the charge transfer at the TPBls should limit the overall electrode response [Luo2017]. Indeed, it has been shown that the electrode reaction mechanism is strongly thermally activated and its kinetic rate is proportional to the density of active TPBls [Bieberle2000, Doppler2018, Mizusaki1994a, Pan2015a]. Moreover, a strong dissymmetry in the two branches/modes of the electrode polarization curve has been evidenced indicating that the activation of the electrode reaction depends on the operating mode [Dasari2013, Holtappels1999b, Luo2017, Marina2007, Mizusaki1994b, Pan2015a]. Finally, an important effect of the steam partial pressure on the kinetics has been found [Bieberle2001, Dasari2013,

Grondin2011, Holtappels1999a, Luo2017, Pan2015a, Shin2016], while the impact of the hydrogen partial pressure remains much less pronounced [Kek2001]. Therefore, it has been supposed that the interaction of steam molecules with the electrode surface could co-limit the global kinetics [Dasari2013].

In parallel with the experimental approach, the relevance of the electrode reaction mechanism has been investigated by using modelling tools. As an illustration, several authors have studied the interactions of steam and hydrogen with the Ni-YSZ system using Density Functional Theory (DFT) [Cadi-Essadek2016, Chaopradith2015, Cucinotta2011, Gorski2011, Kresse2000, Mohsenzadeh2014, Raz2001, Seenivasan2017, Shishkin2010]. From the determination of the most energetically favorable configuration, it has been deduced that H_2 molecules adsorb on the Ni surface as two hydrogen adatoms [Cadi-Essadek2016, Cucinotta2011, Kresse2000, Shishkin2010], whereas H_2O molecules can be adsorbed on both the Ni and YSZ surfaces. Based on both experimental results and DFT computations, three main reaction pathways (divided in a sequence of elementary steps) have been proposed in the literature. These pathways differ by the nature of the charge transfer across the Ni-YSZ interface: an interstitial process [Holtappels1999a], an oxygen spillover mechanism [Mizusaki1994b] or a hydrogen spillover mechanism [De Boer1998]. These reaction pathways have been implemented into micro-kinetic models and the simulations have been compared to the response of Ni patterned electrodes in order to identify the most relevant pathway [Bessler2010, 2007, Bieberle2002, Goodwin2009, Luo2019, Vogler2009]. The model computations have shown that the hydrogen spillover would be the most likely reaction mechanism for the Ni-8YSZ electrode [Bessler2010, Goodwin2009, Luo2019, Vogler2009]. However, some recent studies have suggested that the oxygen spillover mechanism could also be involved in the electrode response [Bredikhin2018, Fu2014, Ong2017].

To conclude, it appears that the reaction mechanism of hydrogen oxidation and steam reduction remains still unclear. In addition, it is necessary to apply these micro-kinetic models to porous cermet microstructures in order to achieve more representative results for real SOCs applications.

1.2.2 Oxygen electrode reaction mechanism

The present review is focused on the most common O_2-electrode materials: LSCF and the composite LSCF-CGO. Indeed, in spite of many studies, the reaction mechanisms related to LSCF-based electrodes are not yet fully understood. Nevertheless, it is generally admitted that the bulk path (related to the oxygen solid-state diffusion in LSCF and the oxygen exchange at the electrode surface) is predominant in SOFC mode [Adler1996, Baumann2007, Grunbaum2009, Prestat2007]. It has been more recently highlighted that a change of reaction mechanism arises at low overpotentials in SOEC mode, from the bulk to the surface path (defined by the direct charge transfer at the TPBls) [Laurencin2015, Monaco2018]. Regarding the LSCF-CGO composite, some studies have suggested that the reaction mechanism is entirely controlled by the surface path whatever the electrode polarization [Kim2019a].

To date, many models have been already published for the LSCF electrode [Adler1996, Baumann2006, Carraro2012, Çelikbilek2016, Deseure2005, Hubert2016, Laurencin2015, Monaco2018, Liu1998, Ma2018, Prestat2007, Simrick2012]. Adler and coworkers [Adler1996] were the first to propose an analytical model to express the impedance at Open Circuit Potential (OCP) for a porous MIEC electrode. These authors considered an equivalent homogenous electrode taking into account the bulk path with one global step of oxygen exchange between the gas and the MIEC, which was treated as a pure chemical reaction. With the simplification of a semi-infinite electrode thickness, the solution is equivalent to a Gerischer-type impedance [Boukamp2003] and is referred as the so-called 'ALS' model [Adler1996]. This approach has been used and improved by many authors for analytical or numerical models for the LSCF and LSCF-CGO electrodes [Çelikbilek2016, Carraro2012, Deseure2005, Nielsen2011, Mortensen2014]. For instance, Mortensen *et al.* [Mortensen2014] have proposed an analytical solution to compute the impedance diagrams for MIEC-CGO composite electrodes. In our group, numerical steady-state and dynamic models have been developed for porous LSCF and LSCF-CGO electrodes by taking into account the bulk and surface paths [Laurencin2015, Hubert2016]. The whole mechanism was splitted into four steps considering only neutral oxygen adatom species attached on the LSCF surface. Therefore, no interaction between the adsorbed species was assumed and the surface coverage at equilibrium was related to the oxygen partial pressure according to the Langmuir isotherm. It has been found that this approach is able to predict accurately the electrode polarization curves as well

as the impedance diagrams at P_{O_2} = 0.21 atm under cathodic and anodic dc currents [Monaco2018]. However, it is well known that charged oxygen species are likely to be found on oxide surfaces [Wang2013]. Fleig *et al.* [Fleig2005, 2007] have underlined that the charge of adsorbed oxygen ions on the surface could affect the global electrode kinetic and its dependence on the oxygen partial pressure because of electrostatic interactions. A model assuming an uniform double layer induced by the negative adsorbed species counterbalanced by the positive holes in LSCF was proposed to take into account these interactions.

From this context, the modeling with a full elementary description could improve the models predictability especially for the oxygen partial pressure dependence of the electrode kinetics. But it must be emphasized that the experimental validation remains questionable due to the large number of unknown parameters. Indeed, in the particular case of porous electrodes, in contrast to well-defined geometries such as patterned electrodes, it is essential to determine all the microstructural properties characterizing the electrode morphology (volume fractions, tortuosity factors, specific surface areas and density of TPBls). The measurements of these parameters from 3D electrode reconstructions allow decreasing the number of fitted parameters and enhance the relevance of the validation.

To date, very few full elementary models have been specifically dedicated to porous LSCF and LSCF-CGO electrodes. None of them has been validated with the knowledge of real microstructural parameters. Gong *et al.* [Gong2012] have proposed a steady-state model in which the reaction mechanism was divided in five reactions taking into account the presence of oxygen ions on the electrode surface. Even if the model was not experimentally validated, the authors found a transition from the bulk to the surface path arising under cathodic polarization when applied to LSM-type electrodes. Ma *et al.* [Ma2018] have recently published a steady-state elementary kinetic model for porous LSCF coupled with DFT simulations. The model was validated on one polarization curve taken from the literature at 800 °C under P_{O_2}= 1 atm. In contradiction to the statements reported in [Laurencin2015, Monaco2018], they claimed that the surface path is negligible even in the SOEC mode and all the kinetic simulations were carried out only considering the bulk path. Yurkiv *et al.* [Yurkiv2014] have proposed a dynamic elementary kinetic description of a LSCF-CGO composite in which the LSCF and CGO was modeled as an equivalent medium for oxygen solid-state diffusion and by neglecting the surface path. For the validation, simulated impedance diagrams at OCP under air were compared with experimental data recorded between

500 °C and 800 °C. However, although the three contributions in impedance diagrams at high, medium and low frequencies were identified, the agreement between the simulated and experimental spectra was not fully satisfactory. Finally, Donazzi *et al.* [Donazzi2020] have built a quasi-elementary model taking into account both surface and bulk paths for the LSCF-CGO composite. The authors have considered a dissociative adsorption step followed by an ionization on the LSCF surface. The model was validated for impedance diagrams recorded at OCP from 560 °C to 700 °C and three oxygen partial pressures (P_{O_2} = 0.05, 0.1 and 0.21 atm). In this case, it has been found that the reaction mechanism would be controlled by the surface path.

At this stage, it appears that a complete set of electrochemical characterizations is required for the interpretation of the complex LSCF reaction mechanism. As mentioned before, the most common technique used to study the electrochemical behavior of MIEC electrodes is EIS usually associated with the acquisition of polarization curves in steady-state conditions [Babelis2007, Leone2008, Chen2018]. In complementary with these methods, Cyclic Voltammetry (CV) measurements can be performed to analyze the non-linear part of the electrode response. Nevertheless, very few experimental data can be found in the literature on the response of MIEC materials involved in SOCs [Chen2003, Ding2009, Sapountzi2012] and even fewer are focused on the LSCF electrode [Bebelis2008, Kournoutis2011, Siebert2011]. Recently, Tezyk et al. [Tezyk2019] have investigated the dependence of the CV response on the microstructural parameters and the oxygen partial pressure, for the typical $La_{0.6}Sr_{0.4}Co_{0.2}Fe_{0.8}O_{3-\delta}$ composition deposited on a Ceria doped Gadolinium Oxide (CGO - $Ce_{0.9}Gd_{0.1}O_{2-\delta}$) electrolyte. The authors concluded that both the electrode specific surface area S_p^{LSCF} and the oxygen partial pressure P_{O_2} play a key role on the CV response. Indeed, when these two parameters are decreased, the reaction of oxygen exchange at the electrode surface becomes sufficiently limiting to allow the transient oxygen storage or depletion inside LSCF under dynamic polarization. This phenomenon results in the enhancement of both the intensity of the CV peaks and the series resistance R_s under cathodic dc bias. However, it is worth mentioning that (i) this previous experimental study was performed at lower temperatures than those used in the SOCs technology, and (ii) the electrolyte Ohmic drop, hard to compensate, was found to strongly distort the CV curves making the interpretation of experimental results very difficult. In this frame, a modelling approach could be an efficient tool to ensure a better analysis for the complex CV response.

Nevertheless, despite the several aforementioned models, none of them was extended to simulate CV curves as well. Only recently, our research group have proposed semi-analytical solutions for Linear Sweep Voltammetry (LSV) and Cyclic Voltammetry (CV) curves of porous MIEC electrodes [Montella2021]. These solutions have been established by extending the ALS-based model for non-linear potential solicitations and by neglecting the Ohmic losses in the electrolyte. However, to the best of our knowledge, no numerical tools exist up to now for the simulation of the results recorded by using this electrochemical technique.

To conclude, it appears that there is still a controversy on the dominant reaction pathway for LSCF and LSCF-CGO electrodes. Indeed, a full validation of the elementary model simultaneously applied to both the LSCF and LSCF-CGO porous electrodes is still missing with the knowledge of the microstructural properties and a set of relevant electrochemical characterizations. In this last frame, Cyclic Voltammetry can be regarded as a supplementary investigation technique whose implementation in the modelling tool may bring additional insights on the electrode reaction mechanism.

1.2.3 Main degradation phenomena

The degradation is defined as the loss in performances of a device over time. The high operating temperature of a SOC leads to many degradation phenomena that can imply the single cell component, the chemical reactivity between different layers or the contact with external components [Moçoteguy2013, Reisert2018, Wang2020]:

(i) Interdiffusion or formation of secondary phases,
(ii) Delamination of the oxygen electrode at the electrolyte interface,
(iii) Intergranular pores formation at the electrode/electrolyte interface,
(iv) Contamination by impurities,
(v) Microstructural evolutions such as agglomeration or migration,
(vi) Corrosion/oxidation of metal components,
(vii) Mechanical failures.

These degradation processes can result to an augmentation of the series resistance R_s, as for instance in the case of formation of voids at the interface with the electrolyte [Moçoteguy2013],

and/or to an increase in the polarization resistance R_{pol}, as in the case of poisoning of the electrode [Mehran2018]. Other phenomena can cause the deformation of the cell components due to mechanical effects [Nakajo2012]. Considering Ni-YSZ and the LSCF/LSCF-CGO as most common hydrogen and oxygen electrodes for SOCs applications, two degradation mechanisms are classified as the most detrimental in the literature: Ni agglomeration and migration in the cermet for the H_2 electrode and LSCF demixing for the O_2 electrodes.

The main problematic related to the cermet electrode is its microstructural evolution over time that yields both the Ni coarsening and the Ni migration in the electrode volume implying mass transport processes [Khan2020, Moçoteguy2013, Monaco2019]. This results in a decrease of the TPBls that deteriorates the global cell performances since TPBls are the hydrogen electrode active sites.

The Ni coarsening consists in the increase of the mean Ni particle dimension (Fig. I-7) [Hubert2018]. This process is strongly thermally activated since it is based on a sintering mechanism. However, thanks to the YSZ backbone that limits the massive Ni coarsening, the process tends to stabilize for long-term operations [Monaco2019]. As an illustration, Hubert *et al.* [Hubert2018] have shown that Ni agglomeration causes 30 % or 25 % of performance loss of a cell at 850 °C over the first 2000 h of operation in SOFC and SOEC modes, respectively, indicating that the Ni coarsening is likely to be independent on the operating mode (Fig. I-8) [Trini2020]. The mass transport in Ni-YSZ seems to be favored through the surface diffusion of Ni particle or $Ni(OH)_x$ species [Gao2014], but gas phase transport of $Ni(OH)_2$ species or by solid-state diffusion of vacancies is considered as possible [Hauch2011, Kröll2017]. Since the hydroxides plays a key role in the Ni transport, the water content influences substantially the Ni agglomeration mechanism [Lee2014, Khan2020]. As an illustration, Khan *et al.* [Khan2020] have observed a significant increase of the polarization resistance of two anode-supported flat-tubular cells at 800 °C in SOFC mode for a current density of 700 $mA \cdot cm^{-2}$ and 1000 $mA \cdot cm^{-2}$, respectively. Conversely, a negligible performance loss has been recorded for the cells operating at lower current densities. According to the authors, this behavior was supposed to be due to a decrease of the TPBls in the anode functional layer related the major water content produced at the highest current densities.

The agglomeration mechanism is usually described by the classical power-law coarsening model that mimics the sintering of two particles [Khan2018, Kröll2017]. Recently, it has been shown that the modeling approach can be used to accurately simulate the Ni agglomeration in the complex

cermet 3-D microstructure, since the process is based on the minimization of the Ni/gas surface energy [Trini2021].

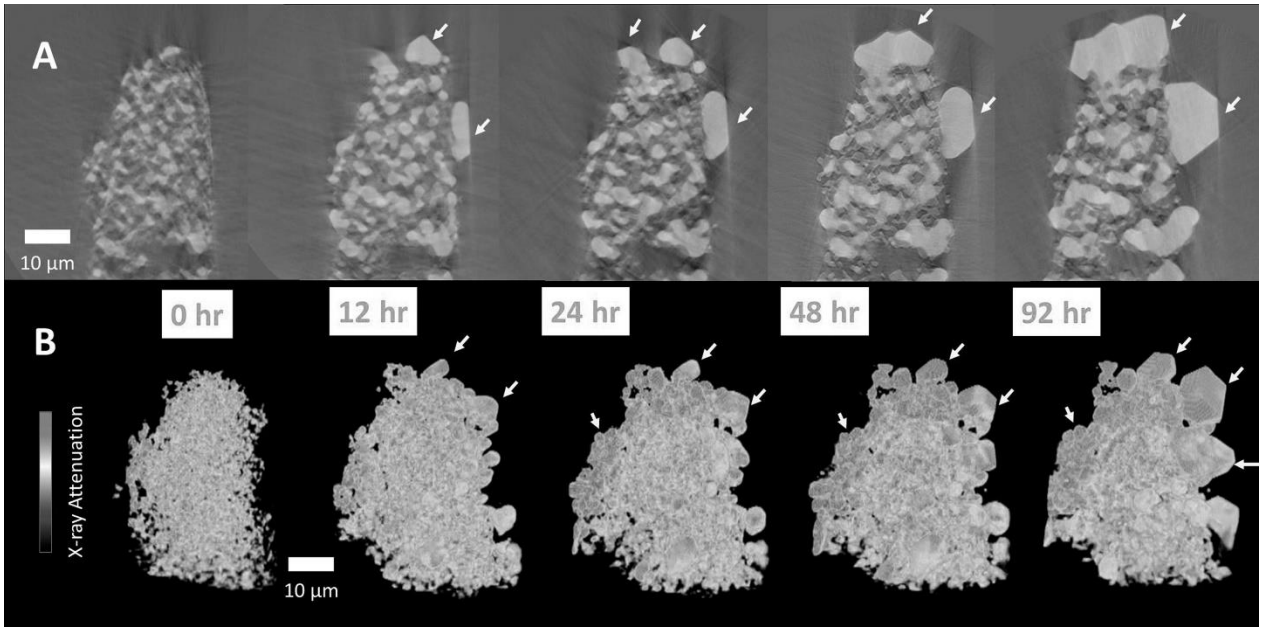

Fig. I-7 Evolution of the Ni coarsening on a cermet anode operated at 1050 °C as a function of time [Chen-Wiegart2016].

In parallel with the Ni coarsening, the Ni migration is the second process that affects strongly the degradation of the hydrogen electrode. It represents the change of the Ni distribution in the volume of the electrode due to the removal of Ni particles from the electrode/electrolyte interface in the SOEC mode [Hauch2008] and a potential Ni enrichment in the SOFC mode. However, conversely to the Ni agglomeration, the Ni migration is mainly activated in the SOEC mode [Lay-Grindler2014, Monaco2019, Trini2020]. For instance, Trini *et al.* [Trini2020] have observed the agglomeration in the cermet functional layer for two identical cells tested at 800 °C for 1000 h in SOFC and SOEC modes, respectively, while the Ni migration was detected only for the cell operated in SOEC mode (Fig. I-8).

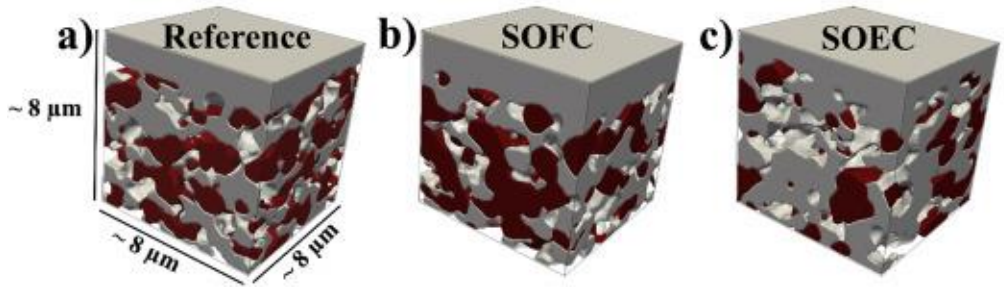

Fig. I-8 3D reconstructions of the rendering sub-volumes of a pristine cell (a), a cell operated in SOFC mode (b) and a cell operated in SOEC mode (c) at 800 °C during 1000 h each (Ni is red, YSZ is grey and the pores are transparent). By a pure visual inspection, it can be seen that the Ni microstructural evolution is higher for the cell operated in SOEC mode respect with the cell operated in SOFC mode [Trini2020].

Some authors have proposed that local cathodic overpotentials could drive this process in the hydrogen electrode [Mogensen2017, Monaco2019, Rinaldi2019]. Monaco *et al.* [Monaco2019] have suggested that an accumulation of oxygen vacancies at the interface Ni/YSZ under cathodic polarization could be the driving force of the Ni migration (Fig. I-9). Rinaldi *et al.* [Rinaldi2019] have related this behavior to a decrease of the Ni wettability on YSZ particles. However, this degradation mechanism is still unclear and remains a subject of investigation.

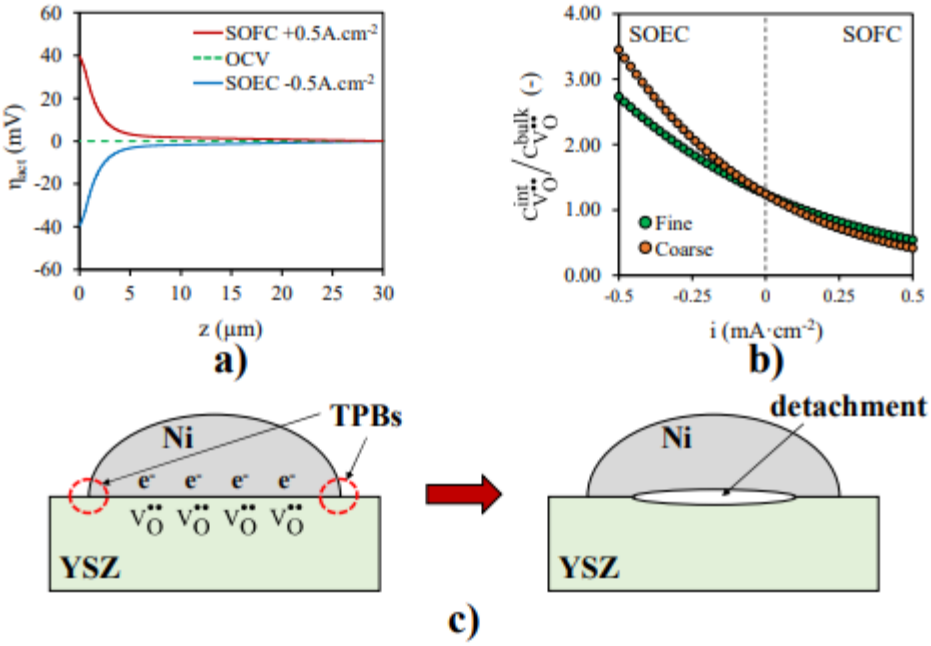

Fig. I-9 Proposed reaction mechanism for Ni depletion: in SOEC mode the overpotential at the interface Ni/YSZ (z = 0) becomes negative (a). This behavior is followed by an increase of oxygen vacancies (b) that could lead to the detachment of the Ni particles on the YSZ backbone in SOEC mode (c) [Ph.D. thesis Federico Monaco 2020].

Finally, it has been demonstrated that the initial microstructural parameters of the cermet Ni-YSZ play a key role on both the migration processes of nickel [Monaco2019]. As an illustration, a much higher degradation has been observed for an electrode with a coarse microstructure with respect to an electrode with initial fine particles size in SOEC mode [Monaco2019].

Nowadays, it is widely recognized that a significant part of the overall cell degradation originates from the oxygen electrode [Frey2018, Tietz2006]. Conversely to the cermet Ni-YSZ, post-test characterizations have shown that the LSCF microstructure remains stable in operation with only negligible evolutions [Lay-Grindler2013a, Shimura2019, Wang2016]. Indeed, LSCF-based electrodes suffer from degradation processes mostly related to the chemical reactivity of LSCF or to the diffusion of species from the perovskite lattice. Among all the underlying mechanisms that can affect the oxygen electrode stability, the LSCF demixing is considered as one of the most

detrimental [Laurencin2017]. It consists in the migration and segregation of strontium dopant cations $Sr_{La}^{'}$ from the perovskite lattice resulting in the formation of a SrO strontium oxide film at the LSCF surface. As SrO is an insulating phase, it blocks the oxygen exchange with the gas phase [Ding2013, Kim2019a, Pan2015b, Wang2018]. Wang *et al.* [Wang2018] have shown that the global exchange kinetic constant k_{chem} for $La_{0.6}Sr_{0.4}Co_{0.2}Fe_{0.8}O_{3-\delta}$ is decreased by an order of magnitude after ageing between 700 °C and 800 °C in SOFC mode. Kim *et al.* [Kim2019a] have also reported a significant degradation rate of k_{chem} (86 %) for $La_{0.6}Sr_{0.4}Co_{0.2}Fe_{0.8}O_{3-\delta}$ after an isothermal ageing at 800 °C for 800 h at OCP which was related to the strontium segregation on the LSCF surface. The estimated coverage of Sr segregation was estimated to be only around 15 %. Accordingly, the authors suggest that the strontium deficiency at the clean surface region more dominantly impacts the degradation process than the precipitation of SrO [Kim2019a]. Moreover, the oxygen chemical diffusivity (or ionic conductivity) of LSCF is decreased by the strontium loss in the volume but after operation for a few hundred hours at OCP [Ascolani-Yael2020, Fan2011, Kim2019a, Lay-Grindler2013a]. Indeed, strontium segregation was observed in $La_{0.6}Sr_{0.4}Co_{0.2}Fe_{0.8}O_{3-\delta}$ pellets that underwent a thermal anneal at 800 °C for 8 h in pure O_2 or ambient air [Niania2020]. But the authors claim that the oxygen transport properties remain unchanged in the compositional altered region where large changes in the A-site cation composition were detected. All these phenomena are expected to cause the degradation of the electrode performances even if their impact on the electrode response remains unclear. In this context, the exact role of the operating conditions (e.g. temperature, electrode polarization, duration) on the demixing mechanism is still under investigation. For instance, the formation of SrO is an increasing function of the temperature and the oxygen partial pressure [Oh2012]. Between 650 °C and 750 °C, the degradation of the polarization resistance of a LSCF electrode was found to increase with the current density in both SOFC and SOEC modes [Lu2019] and with time for temperatures above 650 °C [Wang2018]. Nevertheless, there are conflicting results on the effects of anodic versus cathodic polarization [Li2017] while keeping in mind that some operating conditions differ. Some studies have shown that a cathodic polarization facilitates the strontium segregation in LSCF-based electrodes [He2018, Matsui2019, Sun2021, Wang2014a] but other results suggest that operating in SOFC mode suppresses the strontium surface segregation [Finsterbusch2019, Liu2019].

It has been shown that the rate of the phase decomposition is strongly accelerated in SOEC mode [Laurencin2017]. Frey *et al.* [Frey2018] have shown that the demixing of the $La_{0.58}Sr_{0.4}Co_{0.2}Fe_{0.8}O_{3-\delta}$ material is enhanced for a stack in SOEC mode compared to stacks in SOFC mode (Fig. I-10). In this frame, Laurencin *et al.* [Laurencin2017] have proposed that the depletion of oxygen vacancies within $La_{0.6}Sr_{0.4}Co_{0.2}Fe_{0.8}O_{3-\delta}$ under anodic current drive the strontium segregation and the formation of SrO. It is worth noting that the accumulation of oxygen vacancies at the electrolyte surface close to the oxygen electrode has been recently invoked to explain the significant strontium segregation at the surface of $La_{0.6}Sr_{0.4}Co_{0.2}Fe_{0.8}O_{3-\delta}$ in SOFC mode [Na2018]. An accelerated migration of strontium under a constant anodic polarization was also evidenced for a $(La_{0.6}Sr_{0.4})_{0.95}Co_{0.2}Fe_{0.8}O_{3-\delta}$ - CGO composite electrode [Kim2021] suggesting that operating in SOEC mode facilitates the strontium accumulation [Finsterbusch2019, Pan2018]. According to Kim *et al.* [Kim2021], the driving force for the formation of strontium oxide increases under anodic polarization. At the opposite side, some reports indicate that an anodic current can improve the performance or mitigate the degradation of LSCF electrodes by suppressing strontium segregation and migration to the electrode/electrolyte interface [N2018, He2018, Pan2015b, 2016]. But it is worth mentioning that these last studies were performed without any CGO barrier layer. Accordingly, the chemical reactivity between YSZ and LSCF certainly interferes with the recorded results [Yang2021].

Besides, some authors [Ascolani-Yael2020, Bucher2011, Laurencin2017] have detected an increase in LSCF decomposition with the presence of steam in the O_2 side. Indeed, LSCF shows a relatively poor tolerance to H_2O even for long term operation in SOFC mode [Liu2011]. The strontium segregation rate was found to be significantly increased in the presence of H_2O as compared to dry pure O_2 and ambient air at OCP [Niania2020]. A decrease by a factor of 10 of the oxygen exchange kinetic constant was recorded for after 1000 h at 600 °C in a humidified atmosphere at OCP [Bucher2011].

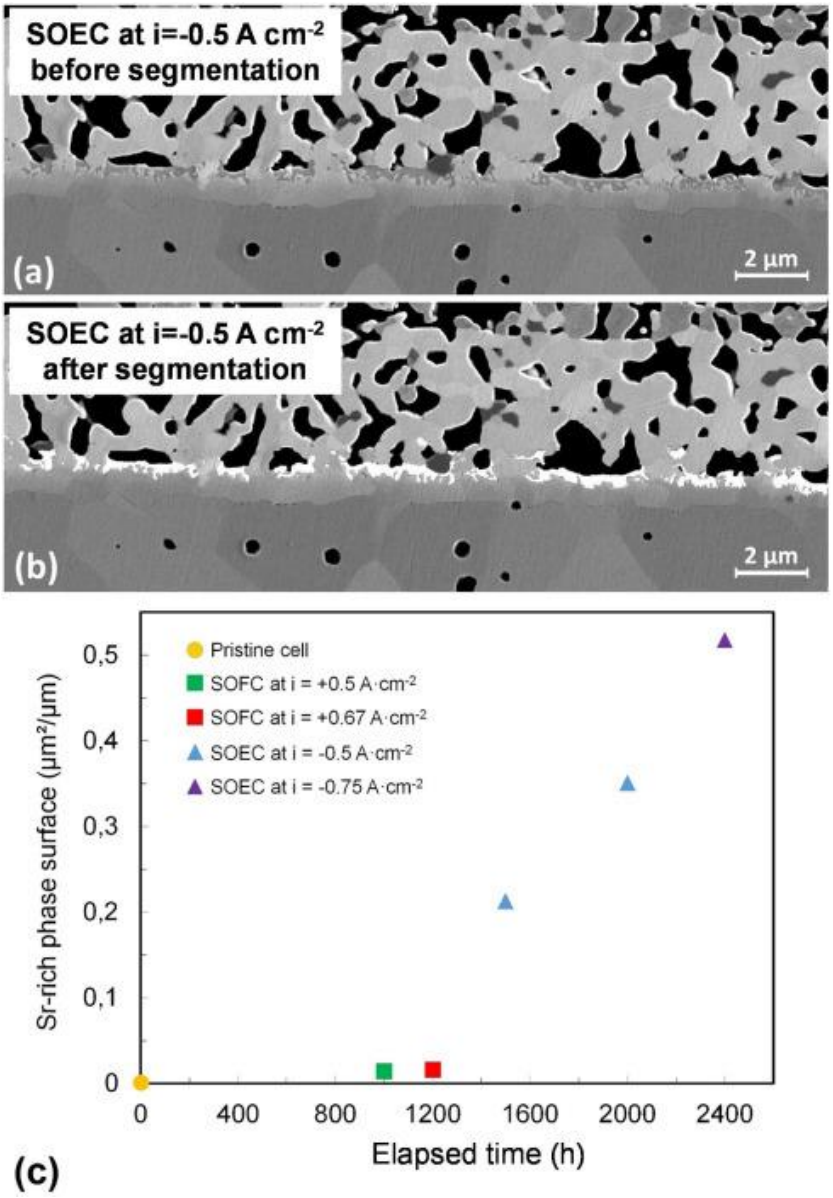

Fig. I-10 SEM cross-sections showing the zirconates for the cell operated in SOEC mode before (a) and after image segmentation (b). The amount of secondary phases (zirconates) measured at the CGO/YSZ interface has been plotted as a function of the operating time (c). This Sr-rich phase is detected mostly in SOEC mode, while the increase in SOFC mode is negligible. [Laurencin2017].

The LSCF demixing is usually completed by the formation of strontium zirconates $SrZrO_3$ at the interface between the CGO barrier layer and the YSZ electrolyte [De Vero2018, Frey2018, Laurencin2017, Rinaldi2017, The2015]. Since this secondary phase is also insulating, the

formation of this additional phase yields an increase the cell Ohmic resistance [Oh2012, Rinaldi2017, The2015]. It is worth mentioning that some authors have also detected the formation of $SrZrO_3$ during the cell manufacturing due to the high temperature of the electrode sintering [Kiebach2015, Sanchez2017, Villanova2019, The2015]. Moreover, the deposit of $SrZrO_3$ is likely to be accelerated in SOEC mode [Laurencin2017]. Kiebach *et al.* [Kiebach2015] found comparable amount of Sr enriched zones at the CGO/YSZ interface for a pristine cell and a cell operated in SOFC mode, suggesting that the formation of ziconates is not aggravated under cathodic polarization.

Finally, the initial LSCF and LSCF-CGO microstructural parameters can also affect the electrode degradation reducing consistently the formation of Sr-rich phases. On the one hand, Kim *et al.* [Kim2021] have shown that tailoring of a $(La_{0.6}Sr_{0.4})_{0.95}Co_{0.2}Fe_{0.8}O_{3-\delta}$-CGO composite electrode with the addition of graphite particles substantially improves the cell durability in SOEC mode thanks to the increased of well-distributed porosities. The authors have supposed that the higher surface area and the several pores at the interface LSCF/CGO helps the oxygen diffusion reducing the formation of Sr insulating phases. On the other hand, Yang *et al.* [Yang2021] have detected an improvement of the LSCF performances over time at OCP with the addition a compressive load in operation. The post-characterization analysis showed the suppression of the SrO layer at the top of the electrode during long-term tests may due to the slower Sr diffusion in the bulk.
To conclude, one can be stated from this overview that the roles of the operating mode and of the steam content on the degradation of LSCF-based electrodes remain still unclear. For this reason, a deep comprehension of the LSCF demixing is of fundamental importance in order to limit the degradation of the oxygen electrode.

1.2.3.1 LSCF demixing: study of the reaction mechanism

The demixing is a universal process concerning the LSCF electrodes operating at high temperatures regardless their microstructure or morphology. For this reason, many studies have been devoted to the understanding of the corresponding reaction mechanism [Heide2002, Laurencin2017, Oh2012, The2015,]. Although the operating conditions and the microstructural parameters differ depending on the literature reports, the electric field seems not be the dominant factor on the LSCF demixing [De Vero2018, Matsui 2019, Laurencin2017]. Indeed, according to Wang *et al*. [Wang2014a] the

direction of the electric field in SOFC mode should help the $SrZrO_3$ formation by accelerating the cations diffusion towards the oxygen electrode and slow down the reactivity in SOEC mode. This statement is in contradiction with the results of Laurencin *et al.* [Laurencin 2017]. Indeed, the driving force of this mechanism is usually associated to the variation of oxygen partial pressure or of the oxygen vacancies concentration in the perovskite material. As above mentioned, Oh *et al.* [Oh2012] have reported that the formation of SrO increases with the temperature and oxygen partial pressure. A defect chemistry model was thus proposed based on the observed phenomena: since SrO is thermodynamically stable [Königstein1998] and without taking into account the possible Cobalt segregation at the LSCF surface [Liu2019, Sun2021] or the change in the Co oxidation state as a charge compensation for the strontium loss from the perovskite volume [Lay-Grindler2013b], the formation of strontium precipitates can be written [Oh2012]:

$$Sr_{La}^{/} + \frac{1}{2}O_2(gas) \rightarrow SrO_{surface} + V_{La}^{///} + 2h^{\bullet} \quad (11)$$

If one considers the mixed valence of Cobalt ions, Eq. (11) can be written as [Laurencin2017]:

$$Sr_{La}^{/} + \frac{1}{2}O_2(gas) + 2\,CO_{Co}^{x} \rightarrow SrO_{surface} + V_{La}^{///} + 2\,Co_{Co}^{\bullet} \quad (12)$$

Because of the low variation of the local oxygen pressure in thin porous electrodes between SOFC and SOEC modes, reactions (11) and (12) cannot explain the higher degradation rate of $La_{0.6}Sr_{0.4}Co_{0.2}Fe_{0.8}O_{3-\delta}$ under anodic currents [Laurencin2017].

Therefore, my research group have proposed an alternative demixing mechanism that could explain the potential role of both the anodic polarization and steam content in aggravating the strontium precipitation and the formation of zirconates [Laurencin2017]. From the simulations of an inner house micro-scale model, the concentration of oxygen vacancies was found to depend on the electrode polarization. Indeed, a deep increase of oxygen ions has been retrieved in SOEC mode at the interface between the LSCF electrode and the electrolyte. Therefore, it has been suggested that the high oxygen content in LSCF under anodic polarization could accelerate the demixing and the SrO formation according [Laurencin2017]:

$$Sr_{La}^{/} + O_O^{x} \rightarrow SrO_{surface} + V_{La}^{///} + V_O^{\bullet\bullet} \quad (13)$$

At high temperatures, the presence of water molecules in the gas phase promotes the formation of secondary phases like SrO [Kim2019b]. Water molecules can react with the segregated SrO to form volatile $Sr(OH)_2$ in the electrode porosity [Kivi2017] according to the following reaction [Laurencin2017]:

$$SrO_{surface} + H_2O(gas) \rightarrow Sr(OH)_2(gas) \quad (14)$$

Thanks to a gas phase transport, the strontium hydroxide can thus react with zirconium cations at the electrolyte interface to form the zirconates in the porosity of the barrier layer at the electrolyte interface as shown in Fig. I-10a [Laurencin2017]:

$$Sr(OH)_2(gas) + Zr_{Zr}^{x}(YSZ) + 2O_O^x(YSZ) \rightarrow SrZrO_3 + H_2O(gas) + 2V_O^{\bullet\bullet}(YSZ) + V_{Zr}^{////} \quad (15)$$

This second part of the mechanism could explain the higher electrode degradation in presence of water. Nevertheless, it has been pointed out that supplementary experimental evidences are needed in order to validate the proposed degradation mechanism, especially for the role of the steam in the LSCF demixing.

1.3 Objectives and Methodology

In the current context of the global energetic change, SOC appears as a valuable candidate for a clean storage and production of energy. However, its high components degradation remains the bottleneck for the spread of this technology on the market place. Especially, the LSCF demixing appears as one of the most detrimental phenomena affecting the global cell performances and shortening the cell life time. Moreover, the reaction mechanism related to this kind of electrode is not fully understood yet.

In this frame, the present thesis aims a better comprehension of the oxygen electrode reaction mechanism and degradation phenomena. In particular, the work is focused on the modelling of the LSCF and LSCF-CGO reaction mechanisms with a special attention on the study of the LSCF decomposition. In order to reach this knowledge, a trifold methodology has been implemented (Fig. I-11): modelling, experiments and post-test characterizations. Indeed, to collect the data for the model validation, electrochemical characterizations (i-V curves, EIS and CV curves) have been

performed at the electrode level using symmetrical cells tested in a three-electrode set-up. The microstructural properties of studied electrodes have been extracted from their 3D electrodes reconstructions obtained through Focused Ion Beam Scanning Electron Microscope (FIB-SEM) tomography and subsequently implemented in the model as input parameters. The comparison between the measurements and the simulations have allowed the model validation.

As experimental evidences in support of the proposed LSCF degradation mechanism, one LSCF symmetrical cell has been tested over 1000 h with the working and counter electrodes operated in SOEC and SOFC modes, respectively. Post-test characterizations have been carried out on the tested electrodes and on a pristine cell through x-ray diffraction to observe the effect of the LSCF demixing on the electrode microstructure over operating time (collaboration with Federico Monaco). In parallel, long-term tests have been performed on complete cells with a LSCF oxygen electrode under both dry and humid air to verify the aggravated impact of the water on the O_2 electrode decomposition.

To conclude, the validated model has been used to study the electrode reaction mechanism and the impact of the LSCF demixing on the electrode response.

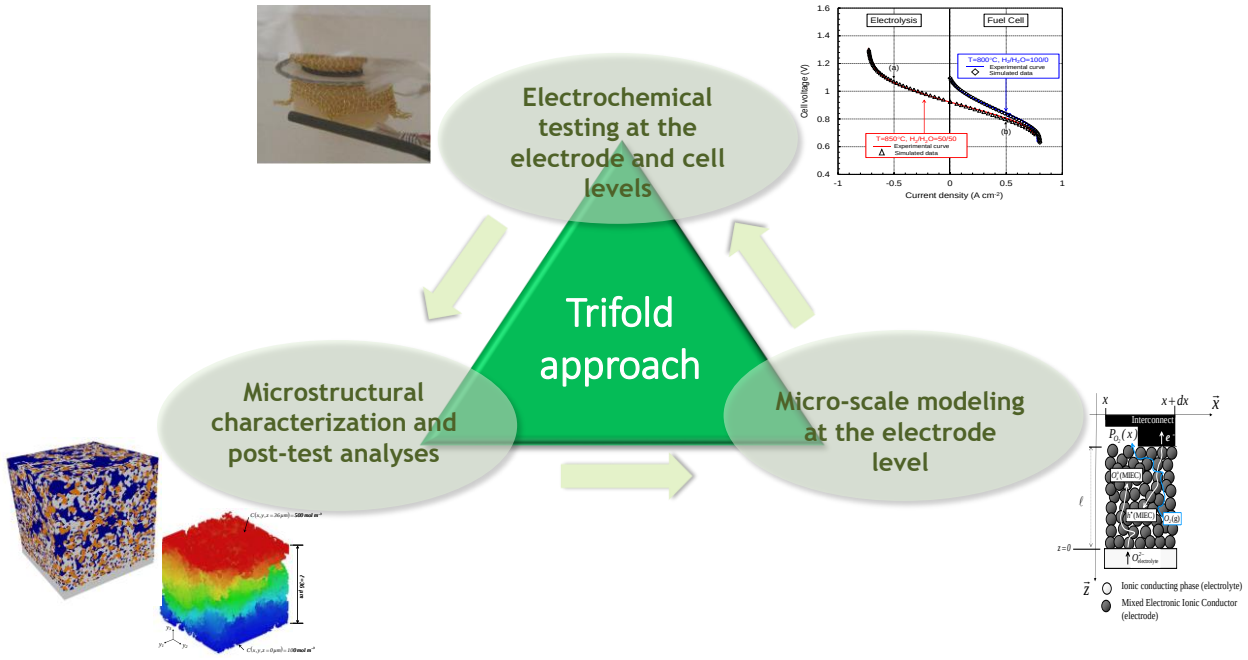

Fig. I-11 Schematic representation of the trifold methodology: (i) electrochemical characterizations at the electrode and complete cell levels, (ii) microstructural reconstructions and post-test characterizations of the samples and (iii) use of modeling tool to study the electrode response.

Chapter II. Experimental results

Any validation of an electrode reaction model requires to collect accurate and unambiguous experimental data. Thus, two campaigns of electrochemical characterizations have been carried out on symmetrical cells tested in a three-electrode set-up for validation of the hydrogen and oxygen electrodes models by using a three-electrode configuration. The first campaign was performed on Ni-3YSZ hydrogen electrode as part of a collaboration with Federico Monaco [Monaco Thesis 2020]. A special effort has been paid to optimize the current collecting, the tightness of the cell housing and the production of a stable steam flow to feed the cell. Thus, the effect of the water content on the electrode response could have been studied for a wide range of steam partial pressure.

The second set of characterizations has been performed on both LSCF and LSCF-CGO oxygen electrodes. In complementarity with polarization curves and EIS at OCP and under polarization, the effect of the oxygen partial pressure has also been investigated. Moreover, CV curves have been recorded at different operating temperatures and imposed scan rates.

The last part of the chapter is devoted to the long-term tests of single oxygen electrodes in SOEC and SOFC modes together with the corresponding post-test characterizations through micro X-ray diffraction using a synchrotron beamline at the Paul Scherrer Institute (PSI). Finally, the durability of two complete cells with a LSCF oxygen electrode has been investigated as a function of the steam content in the air flow at the anode side. All these results have been used as experimental support to investigate the mechanism of LSCF demixing.

2.1 Symmetrical cells testing for model validation

2.1.1 Introduction

2.1.1.1 Three-electrode configuration

The availability of an *in-situ* diagnostic tool to identify the rate limiting processes in solid oxide cells is of prime importance. The most common way to separate the contributions of the two electrodes of the total cell voltage is to use a reference electrode (RE). However, it has to be mentioned that the positioning of the electrodes is problematic for our cell configuration at high operating temperature.

The symmetry of the Working Electrode (WE) and the Counter Electrode (CE) positions is one of the key factors to determine the reliability of the three-electrode configuration in the case of a planar cell geometry. Indeed, even a slight dissymmetry between the two electrodes can yield significant errors on the impedance diagrams [Jiang2017, Jin2020]. It has been demonstrated that cells with a symmetric electrode geometry and RE located at the side of WE, as far as possible from WE, are suitable for performance evaluation [Adler2000, Rutman2008]. Accordingly, a special attention has been paid during the manufacturing of the tested cells to position both WE and CE (thickness = 35 µm, diameter = 11.3 mm) at the center of the electrolyte disk (thickness = 260 µm, diameter = 25 mm) (Fig. II-1). A platinum wire was used as RE and was placed at the periphery of the cell. The wire was glued with platinum ink (Metalor, ink 6082) dried at 100 °C and annealed at 800 °C (during the heating up of the cell for testing). For both hydrogen and oxygen electrodes, the symmetrical cell is composed of a thick electrolyte disk to ensure that RE probes accurate equipotential surfaces [Cimenti2007, Jiang2004]. It has to be specified that the electrolyte disk was sandwiched between two porous identical electrodes to avoid any dispersion of the measured impedance which may originate from the different electrode kinetics of WE and CE [Adler2002]. All these conditions have permitted to fulfill the geometrical rules of an accurate three-electrode configuration to ensure the reliability of the measurements [Jiang2017, Rutman2008].

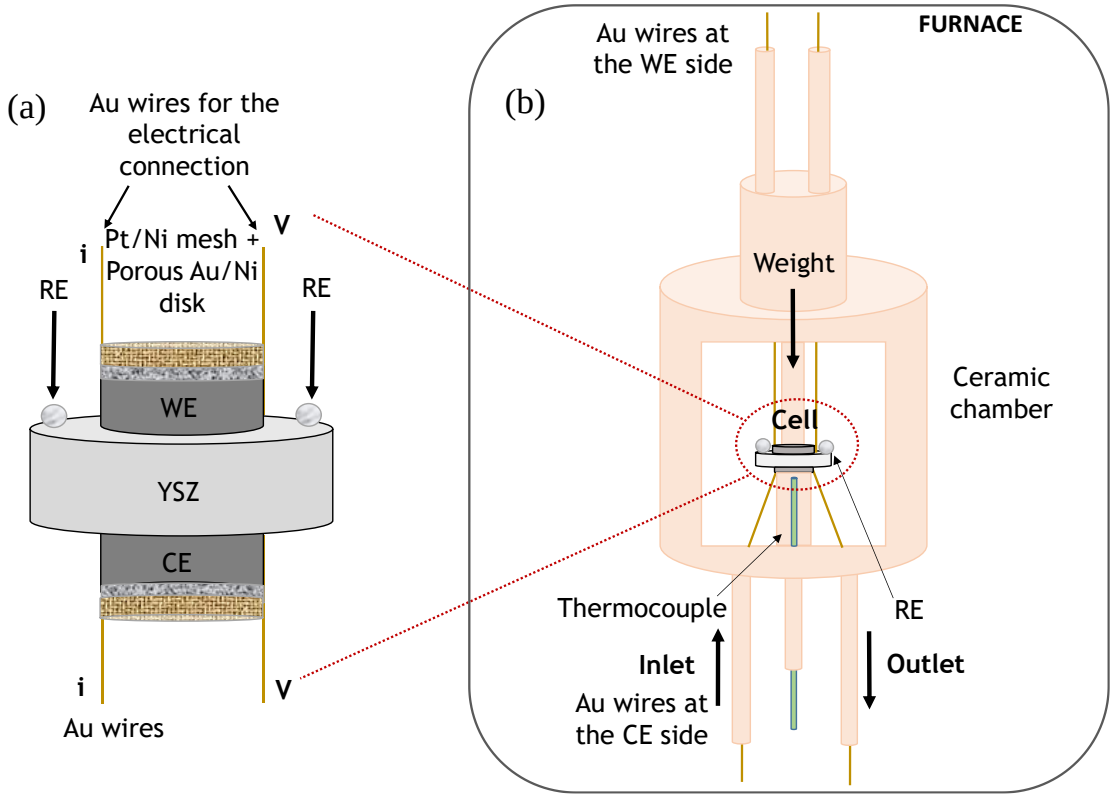

Fig. II-1 Schematic representation of the three-electrode cell (a) and of the alumina housing for tests in symmetrical configuration (b). Coarse grids in Ni or Au and fine grids in Ni or Pt for the hydrogen and oxygen electrodes, respectively.

As shown in Fig. II-1a, a perfect superposition has been found between the polarization curves recorded for a symmetrical cell with Ni-3YSZ cermet electrodes. Moreover, the impedance diagrams recorded for WE and CE (versus RE) are perfectly overlapped and the sum of these impedance diagrams corresponds to the one measured for the complete cell (between WE and CE) for both hydrogen and oxygen electrodes (Fig. II-1b and Fig. II-1c). This ensures that the impedance of RE is sufficiently small in such way that it does not affect the results. [Hsieh1996]. Therefore, it can be claimed that the positioning of RE was valid and that the reliability of the cell configuration was demonstrated for both hydrogen and oxygen electrodes [Pan2015b].

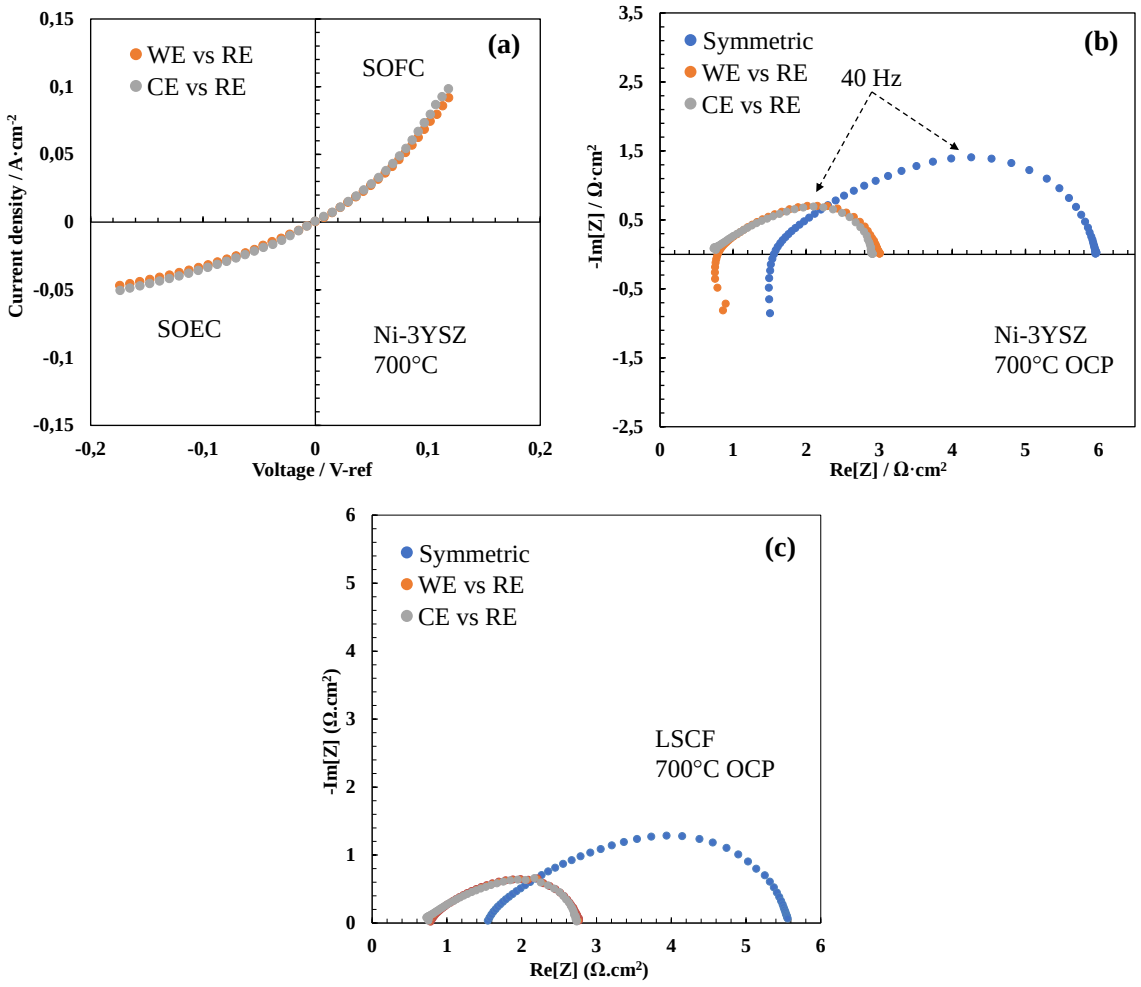

Fig.II-2 Illustration of the validity of the measurements in the three-electrode setup (with $\boldsymbol{P_{H_2}/P_{H_2O}}$ = 50/50 and T = 700 °C): i-V curves recorded for the WE and the CE vs the RE (a) and EIS diagrams at OCP recorded for the two electrodes and the complete symmetric cell (b), Experimental impedance diagrams at 700 °C at OCP for the WE-RE (red dots) and CE-RE (green dots), respectively, of the LSCF symmetrical cell (c).

2.1.1.2 Current collecting

The electrical contacts between an electrode and the interconnect material are identified as ones of the most important factors determining the performance loss since a continuous conduction path between two rigid components is extremely difficult to obtain [Shen2020, Zhu2017]. At a laboratory scale approach, a simple and effective way to form the electrode-interconnect contacts

is to incorporate metal grids or to deposit metallic layers because of their good electronic conductivity. Indeed, on the one hand, a paste layer can be easily deposited on the electrode material and the contact area can be accurately determined, while, on the other hand, a grid can mimic an interconnect material for the electrical contact and the gas feeding. In this procedure, it has to be considered that the contact area is one of the key parameters determining the good functionality of a current collector [Jiang2003a, Simner2005, Seo2018].

However, the metal structure can affect the current collecting efficiency and thus impact the performances. At the same time, adding metal pastes must be avoided because a metal particle diffusion through the electrode volume may affect the electrode resistance [Gao2017, Guillodo2000, Shin2013].

Concerning the metal grids, the mesh size influences the performance. Both Ohmic and electrode resistances decrease with the grid size, indicating an enhanced current collection by improving the charge drainage in the perovskite electrode volume [Noh2013]. The contact resistance between the current collector and the electrode can be improved by mechanical loading [Jiang2003b], or by increasing the operating temperature [Wang2014b]. Moreover, it has been observed that the electrochemical measurements are also sensitive to the chemical nature of the metal [Chervin2005, Guo2012, Rolle2012].

For a given cell geometry, the thickness and the microstructure of the current collector influence the gas transport and the charge transfer [Su2016]. A more homogeneous gas concentration at the electrode surface can be obtained with a thick porous current collector since it yields an extension of the active area in the electrode layer [Lin2003]. Accordingly, a coarse grid will provide an adequate gas distribution at the electrode surface [Canavar2015]. Nevertheless, larger current collector spacings, as well as thinner films, enhance deactivation of the electrode volume far from the current collector. Indeed, the resistance of an electrode can be several times its ideal value if the ratio of the current collector spacing to the electrode thickness increases [Lynch2010]. Thus, a fine metal grid can be inserted between a thick coarse grid and the electrode material to obtain the most homogeneous potential distribution within the electrode volume.

For this reason, a stack of grids with a coarse mesh (100 mesh·cm^{-2}; thickness = 1 mm) has been used as current collectors during the experiments. Nickel and Gold grids were used for the hydrogen and the oxygen electrodes, respectively. And a finer grid (3600 mesh·cm^{-2}) of surface

equal to that of the electrodes has been put in contact with the electrodes surface (Nickel for the hydrogen electrode and Platinum for the oxygen electrode) to ensure the good equipotentiality (Fig. II-1a).

2.1.2 Hydrogen electrode

2.1.2.1 Studied cell

The symmetrical cell is composed of a thick 8YSZ electrolyte (≈ 300 µm) sandwiched between two porous electrodes made of a Ni-3YSZ cermet. The WE and CE present a diameter of 11.3 mm for a surface area of 1 cm^2 (Fig. II-1a). The two electrodes have been screen-printed on the two sides of the solid membrane (disk with a diameter of 25 mm) and sintered under air above 1300 °C. Two Ni wires welded on the grids on each side of the cell were used to collect the current and to measure the voltage for the two electrodes (Fig. II-1a).

2.1.2.2 Experimental set-up

The tests have been conducted in a specific ceramic holder (Fig. II-1b) in which a mixture of H_2 and H_2O have been supplied with a well-controlled composition. The entire set-up was made of alumina to prevent from any contamination of the cell components under operation. A particular attention has been paid to ensure the gas tightness of the alumina cell housing to properly control the gas supplying the cell and recover the gas produced and non-consumed at the outlet. In addition, a specific solution has been chosen to generate a stable gas humidification even at high steam partial pressure in order to investigate a wide range of gas compositions. For this purpose, a system coupling a vapor mass flow meter (Brooks® 5850S) and a homemade steam generator has been installed and validated (Fig. II-3). The stability of the steam supply has been obtained in operation as shown by a very low noise voltage measurement and by the hygrometer located measured at the outlet of the cell chamber (Vaisala HMT330) (Fig. II-3). A second gas flowmeter was used for hydrogen, and the two fluxes (H_2 and H_2O) were mixed in the inlet pipe before entering the chamber (Fig. II-3). Moreover, a gas condenser has been added in series to collect the water (Fig. II-3). It is worth mentioning that all the tubes from the inlet to the outlet of the set-up were kept at ≈ 130 ºC to avoid any condensation of steam. In this bench, a pressure of 1 $kg \cdot cm^{-2}$ has been applied

on the cell to minimize the contact resistance between the electrodes and the grids (Fig. II-1b). This experimental set-up was placed in a furnace for which the temperature changes were applied using a slow heating rate of 1 ºC·min^{-1} to avoid any mechanical damage in the cell (Fig. II-b). It is worth noting that the setup was designed with the total volume of the gas chamber limited to ≈ 50 cm^3 while all the measurements were performed with a high inlet flow rate of reactants (1 – 6 NL·h^{-1}). These conditions were chosen to limit the concentration overpotentials. A thermocouple was positioned to the cell to monitor the temperature.

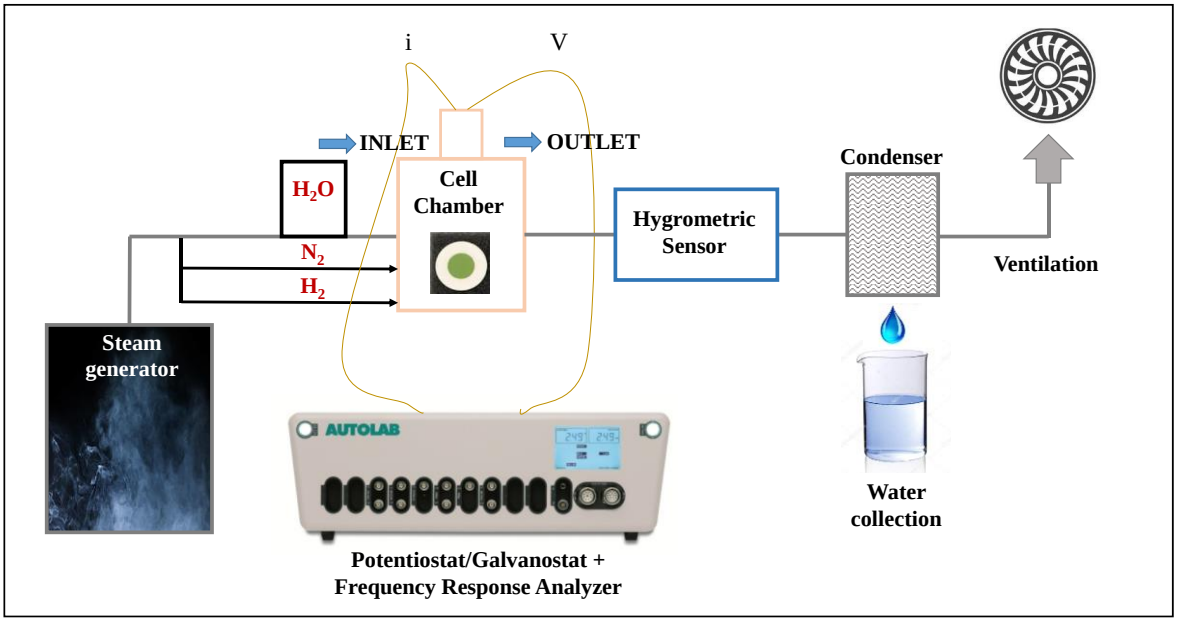

Fig. II-3 Schema of the test bench for the testing of cermet symmetrical cell. The experimental set-up includes the steam generator, the gas supply system and a hygrometric probe for the analysis of the steam content in series. Finally, a condenser has been placed after the outlet of the cell to collect the water, while the wasted gases have been sent to the vents.

2.1.2.3 Testing conditions

Firstly, the tested cell was fed with pure H_2 at 800 °C for a sufficient time (≈ 24 h) to guarantee the reduction of nickel oxide into pure nickel. The operating temperature was decreased and maintained at the reference temperature of 700 ºC for the whole duration of the experiments. In the first part of the characterization, the electrodes were tested under three reference gas compositions: P_{H_2}/P_{H_2O} = 25/75, 50/50 and 75/25. For each composition, the polarization curves measured between the electrodes and the reference one (WE/CE vs RE = E_{meas} (V/ref)) were recorded in a

potentiostatic mode between + 0.2 V and - 0.2 V with a step of 2 $mV \cdot s^{-1}$. Besides, the impedance spectra at OCP have been measured in a galvanostatic mode between 0.1 Hz and 10^6 Hz using a sinusoidal perturbation (i_{ac}) of +/- 5 $mA \cdot cm^{-2}$. From the EIS data, the series resistance and the polarization resistance have been obtained considering the intercepts of the diagram with the real axis at high frequency (R_s) and at low frequency ($R_{tot} = R_s + R_{pol}$), respectively. The overpotential of the WE at each current density (i-η curve) has been determined by subtracting the series contribution (= $R_s \cdot i$) to the overall voltage drop (i-V curve) (i.e. $\eta(V/Ref) = (E_{WE}^{meas}(V/Ref) - R_s \cdot i) - E_{WE}^{eq}(V/Ref)$).

The effect of the hydrogen and steam partial pressures on the impedance response of the electrodes at OCP has been studied in a large range of gas compositions: P_{H_2}/P_{H_2O}= 20/80, 30/70, 40/60, 50/50, 60/40, 70/30 and 80/20 maintaining the water flow constant. All the measurements have been performed with an Autolab potentiostat/ frequency response analyzer (PGSTAT302N/FRA2). For the sake of clarity, the series resistance R_s (corresponding to the resistive contribution of the YSZ pellet and the contact resistances) has been subtracted for all impedance diagrams.

2.1.2.4 Electrochemical characterizations

The polarization curves have been recorded for different steam partial pressures (P_{H_2}/P_{H_2O} = 50/50, 25/75 and 75/25) and they are provided in Fig. II-4a and II-4b. A strong dissymmetry in shape was detected for the i-η curves since a limiting current density was evidenced in SOEC mode (cathodic polarizations) while a potential-activated response was recorded in SOFC mode (anodic polarizations). This dissymmetry was still observed when varying the steam content regardless of the operating mode (Fig. II-4b). It suggests that the global reaction pathway could be modified when changing the operating mode from cathodic to anodic polarizations [Chen2016b, Dasari2013, Pan2015a].

At 700 °C, the performance of the studied Ni-3YSZ cermet increases with the steam partial pressure in both operating modes. Pan *et al.* [Pan2015a] have also reported that a Ni-8YSZ hydrogen electrode behaved better in SOEC mode by increasing the steam content for electrode potentials higher than -0.1 V at 800 °C, while no significant improvement was detected in SOFC mode. It can be noticed that this enhancement is more pronounced under cathodic polarization, indicating

that the interaction of steam with the electrode surface played a significant role on the kinetic limitation of the steam reduction process. This result further suggests that the polarization process is different in SOEC and SOFC modes.

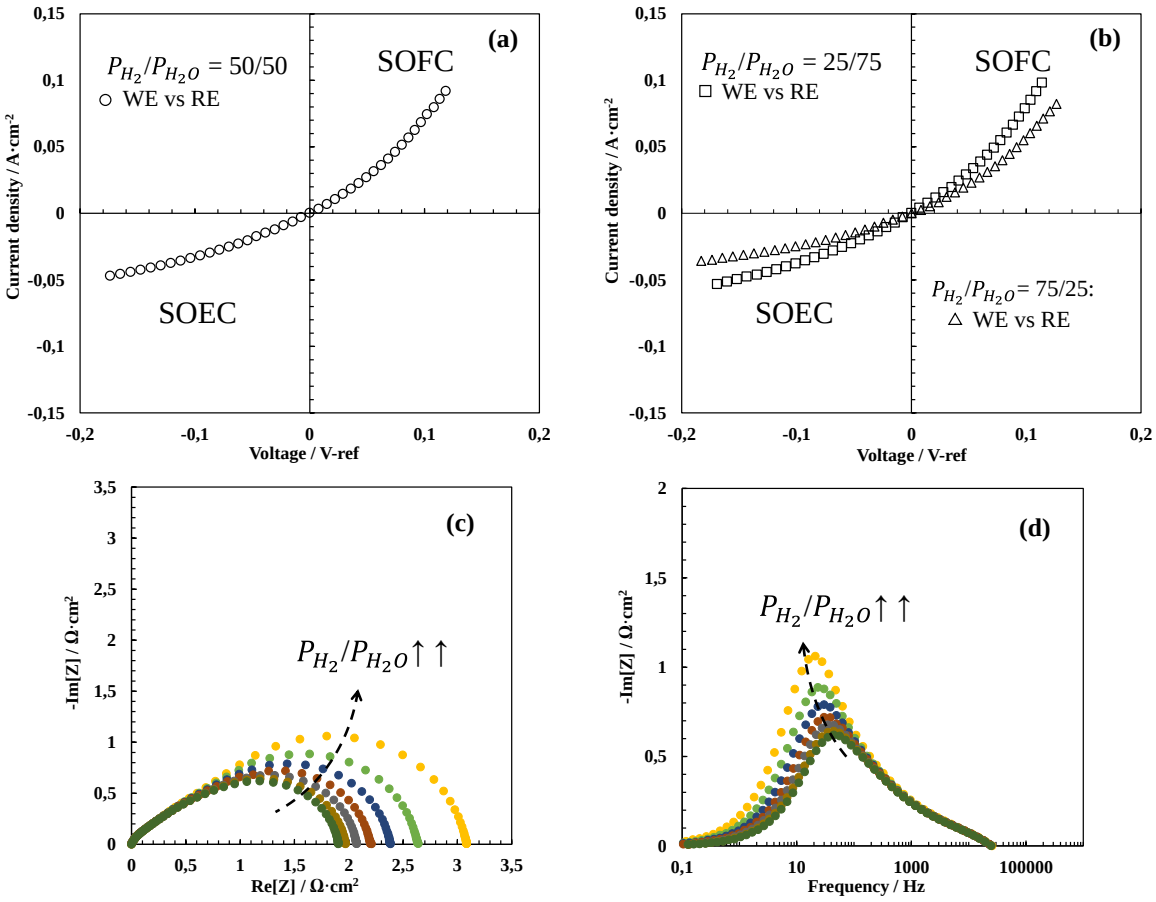

Fig. II-4 Experimental results at 700 ºC: experimental i-η curves with $\boldsymbol{P_{H_2}/P_{H_2O}}$= 50/50 (a) and experimental i-η curves with $\boldsymbol{P_{H_2}/P_{H_2O}}$ = 25/75 and $\boldsymbol{P_{H_2}/P_{H_2O}}$ = 75/25, respectively (b). Experimental Nyquist plot (c) and Bode plot (d) of the EIS diagrams at OCP measured at different $\boldsymbol{P_{H_2}/P_{H_2O}}$ (20/80, 30/70, 40/60, 50/50, 60/40, 70/30, 80/20 maintaining the water flow constant).

It can be noticed that impedance data are not perturbed by noise at low frequencies confirming the stability of the steam flow and, thus, the reliability of the experimental set-up (Fig.II-4a and Fig. II-4b). At OCP, the electrode impedance response can be identified to a Finite-Length Gerischer

(FLG) impedance (Fig. II-4c), in agreement with previous reports [Boukamp2006, Athanasiou2020]. A Gerischer element is generally used for fitting EIS data of MIEC electrodes and is characteristic of competing chemical and electrochemical processes. Without emphasizing on the electrode reaction mechanism, one can ensure that an oxygen transport step is involved as indicated by the high frequency straight line at 45 ° from the real axis in the Nyquist plane. Accordingly, one can consider an extension of the electrode reaction within the cermet volume [Nielsen2011]. As could be expected from the polarization curves, the polarization resistance at OCP decreased when increasing the steam content in the gas phase (Fig. II-4c). It is worth mentioning that the characteristic frequency peak decreases by only a factor of 2, suggesting that the electrode reaction mechanism remained nearly identical in the chosen experimental conditions (Fig. II-4d).

Since the polarization resistance depends on the ratio of the hydrogen partial pressure to the steam one, R_{pol} at OCP has been classically expressed according to Eq. (15) [Luo2017]:

$$R_{pol} = A \cdot pH_2^{-\alpha} \cdot pH_2O^{-\beta} \tag{15}$$

where A is a proportionality factor and the exponents α and β are the reaction orders with respect to H_2 and H_2O, respectively.

A least-square algorithm has been used to fit the exponents α and β for all tested compositions. A single solution for the two exponents has been found for all the experimental data in the investigated range of gas compositions. Single values (α = 0.035 and β = 0.38) for the reaction orders have been determined. This means that the reaction pathway is controlled by one single reaction mechanism at OCP whatever the steam content in the gas phase. As β is ten times higher than α, the global electrode reaction rate at OCP is clearly influenced by P_{H_2O}, while the effect of $P_{H_2}$is almost negligible. This impact of steam on a FLG-type element for the cermet could be attributed to a slow steam adsorption/desorption coupled with surface diffusion up to the TPBls [Atangulov1993, Boukamp2011].

The in-depth interpretation of these experimental results through the use of a micro-modelling tool for the hydrogen electrode can be found elsewhere [Monaco2020].

2.1.3 Oxygen electrode

2.1.3.1 Materials and studied cells

Two symmetrical cells made of $La_{0.6}Sr_{0.4}Co_{0.2}Fe_{0.8}O_{3-\delta}$ and $La_{0.6}Sr_{0.4}Co_{0.2}Fe_{0.8}O_{3-\delta}/Ce_{0.8}Gd_{0.2}O_{2-\delta}$ (50/50 wt. %), respectively, were prepared by screen-printing the electrodes (thickness = 35 µm, diameter = 12 mm) on both sides of a circular 8YSZ electrolyte (thickness = 260 µm, diameter = 25 mm). A CGO barrier layer (thickness = 2 µm) was also added by screen-printing between the electrodes and the electrolyte to prevent the formation of secondary phases [Uhlenbruck2009]. The current and voltage measurements of the two electrodes have been performed by using two Gold wires welded on the grids at each side of the cell (Fig. II-1a).

2.1.3.2 Experimental set-up

It is important to specify that the only difference between the alumina housing of the two test benches was related to the gas tightness of the cell chamber which is probably less good for the set-up operating under air. A pressure of 0.6 $kg \cdot cm^{-2}$ was applied on the top of the cell chamber in order to improve the electrical contact between the grids and electrodes (Fig. II-1b). The supplied gas was a synthetic mixture of nitrogen and oxygen, which was introduced in the chamber using inlet and outlet pipes as shown in Fig. II-1b (with a total O_2 and N_2 flow rates of 0.44 $Nl \cdot h^{-1}$ and 1.66 $Nl \cdot h^{-1}$, respectively). According to the design of the chamber, it is roughly estimated that around one third of the inlet flux was passing through each electrode (i.e. each electrode was fed with an inlet flux of around $F_{O_2}^{inlet} \approx 0.146$ $NL \cdot h^{-1} \cdot cm^{-2}$ and $F_{N_2}^{inlet} \approx 0.553$ $NL \cdot h^{-1} \cdot cm^{-2}$, respectively).

2.1.3.3 Testing conditions

Before starting the measurements, the cells were heated at a rate of 1 $°C \cdot min^{-1}$ up to 800 °C under synthetic air (with a total O_2 and N_2 flow rates of 0.44 $NL \cdot h^{-1}$ and 1.66 $NL \cdot h^{-1}$, respectively). This temperature was maintained for 48 h to anneal the platinum paste and mainly to improve the electrical contact between the electrodes and the current collectors. During this period, the cells were monitored periodically by EIS until the complete stabilization of the diagrams at OCP.

Polarization curves and EIS - The electrochemical measurements were carried out at 750 °C, 700 °C and finally 650 °C under air, keeping a high oxygen gas flow rate in order to limit as much as possible the electrode overpotential due to the gas conversion (P_{O_2} = 0.21 atm and $F_{O_2}^{inlet} \approx 0.146$ $NL \cdot h^{-1} \cdot cm^{-2}$). At each operating temperature, polarization curves were recorded in a galvanostatic mode with a current step of 1 $mA \cdot s^{-1}$ together with impedance diagrams at OCP. At the reference temperature of 700 °C, the experimental dataset was complemented by the acquisition of impedance diagrams under anodic (SOEC mode) and cathodic (SOFC mode) dc currents ($i_{dc} = \pm$ 50 $mA \cdot cm^{-2}$) for both studied cells, varying the oxygen partial pressure between 0.1 atm and 1 atm. These EIS diagrams were acquired in a frequency range of 10 kHz–0.01 Hz by applying a sinusoidal perturbation on the current with an optimized amplitude of $| i_{ac} | = \pm$ 10 $mA \cdot cm^{-2}$. For the sake of clarity, the series resistance has been subtracted for all impedance diagrams. As above mentioned, the electrode polarization curve was obtained by removing the Ohmic losses from the recorded voltage measurements.

Cyclic voltammetry – The electrochemical measurements were carried out at 700 °C and 650 °C under P_{O_2} = 0.1 atm. The CV experiments were conducted by imposing, between the WE and RE, a triangular potential waveform, as described in Fig. II-5, starting from OCP in the anodic direction, with a demi-amplitude of 0.3 V. The scan rate was applied with a potential step of 0.01 V from a minimum of 20 $mV \cdot s^{-1}$ up to a maximum of 1000 $mV \cdot s^{-1}$. Moreover, between each change of scan rate, the cell was maintained at OCP for a period of 30 minutes to allow the system returning to equilibrium before any subsequent measurement.

All the measurements were conducted using an Autolab potentiostat/impedance frequency analyzer (PGSTAT302N/FRA2).

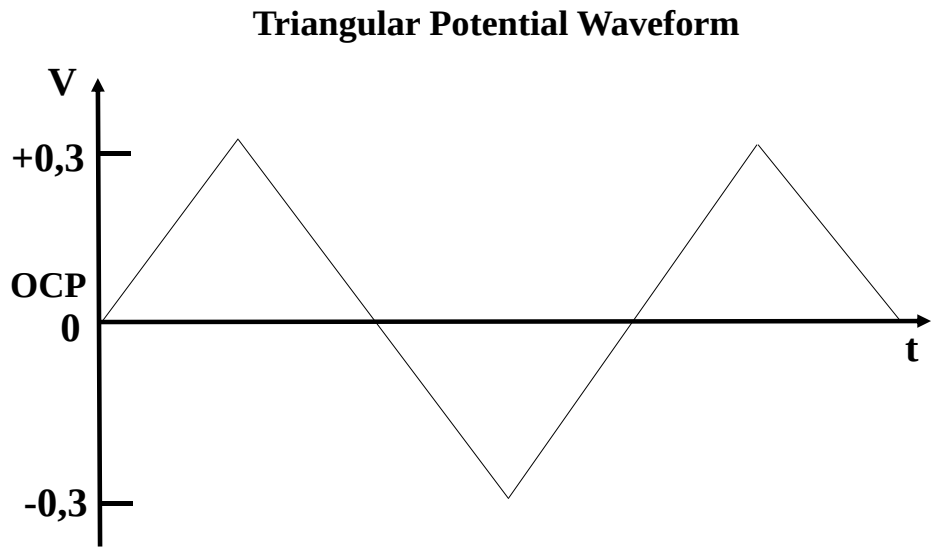

Fig. II-5 Representation of the triangular waveform with a demi-amplitude of = 0.3 V.

2.1.3.4 FIB-SEM reconstructions

The microstructural properties of the studied electrodes were quantified on the 3D reconstructions obtained by FIB-SEM tomography reconstruction. They have been subsequently implemented in the electrochemical model in order to reduce the number of unknown input parameters.

The samples were firstly impregnated under vacuum conditions in order to fill the pores with an epoxy resin. This enables to minimize the undesirable damage of the specimen, to avoid accumulation of gallium ions in the pores during the FIB milling and to improve the contrast between the porosity and the solid phases [Vivet2011].

The serial sectioning and the image acquisition were carried out in a FEG-SEM NVISION 40 from Carl ZEISS® microscope. For SEM observations, Energy selective Backscatter (EsB) detector with a low acceleration voltage of 1.5 kV was used in order to clearly distinguish the LSCF and CGO solid phases in the case of the composite electrode. Then, images with a pixel size of 10 nm were captured sequentially with a z-axis slice pitch of 10 nm using a milling current of 1.5 nA. For the LSCF electrode, a volume of 22.84 x 21.36 x 22.14 μm^3 has been acquired (Fig. II-6a), while for the LSCF-CGO electrode the reconstruction exhibited a dimension of 19.87 x 11.15 x 11.15 μm^3 (Fig. II-6b). It has to be specified that the two extracted volumes presented a voxel size of 10 nm.

For both reconstructions, the raw images have been segmented according to the procedure described in [Villanova2013] before extracting a cubic sub-volume of 10 x 10 x 10 μm^3 for the analyses. A set of numerical tools thoroughly detailed in [Moussaoui2018, Usseglio-Viretta2014] were used to compute all the microstructural required for the simulations. They correspond to the interfacial specific surface areas, the mean pores radius, the volume fractions, the tortuosity factors of the phases and the density of TPBls for the composite electrode. For what concerns the LSCF electrode, the density of TPBls and the LSCF/CGO interfacial specific surface area have been measured on a region of interest corresponding to a rectangular volume of 10 x 4 x 10 μm^3 taken at the CGO barrier layer.

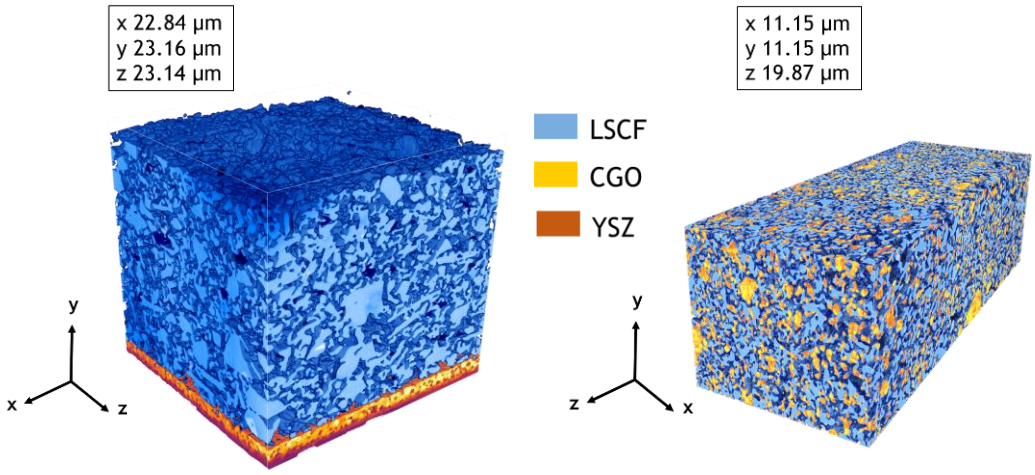

(a) LSCF (b) LSCF-CGO

Fig. II-6 FIB-SEM reconstruction for the LSCF electrode (a). The tomography includes also the CGO barrier layer (in yellow) and few micrometers of the YSZ electrolyte (in brown). FIB-SEM reconstruction for the LSCF-CGO electrode (b).

2.1.3.5 Electrode 3D reconstructions and electrochemical characterizations

The rendering volumes for the 3D reconstructions after segmentation are shown in Fig. II-6 for the two studied electrodes. The LSCF, CGO and YSZ phases appear in blue, yellow and orange, respectively. At a first sight, it can be noticed that the microstructures for the two electrodes seem well representative of classical SOC electrodes. To confirm this assertion, the microstructural

properties have been computed on the reconstructions and the corresponding data are listed in Tab. I. As expected, all the values lie in the range of the properties reported for classical LSCF and LSCF/CGO electrodes [He2017, Virkar2000]. The microstructure properties are used as input parameters for the model validation.

Table I Microstructural properties of the LSCF and LSCF-CGO electrodes computed on the FIB-SEM reconstructions (cf. List of symbols).

Microstructural properties	**LSCF**		**LSCF-CGO**	
	Values	**Unit**	**Values**	**Unit**
ε_{LSCF}	48.7	(%)	30.2	(%)
ε_{pores}	51.3	(%)	43.5	(%)
ε_{CGO}	-	-	26.4	(%)
$S_p^{LSCF/Gas}$	3.59 x10^{6}	(m^{-1})	2.20 x10^{6}	(m^{-1})
$S_p^{LSCF/CGO}$	2.08 x10^{-2}	(-)	1.06 x10^{6}	(m^{-1})
$\bar{r}_{pores}$	2.10 x10^{-7}	(m)	1.70 x10^{-7}	(m)
τ_{LSCF}	2.84	(-)	6.89	(-)
τ_{pores}	1.66	(-)	1.78	(-)
τ_{CGO}	-	-	13.17	(-)
ξ_{TPBls}	5.57 x10^{5}	(m^{-1})	9.06 x10^{12}	(m^{-2})

The same campaign of electrochemical characterization has been carried out for both the studied electrodes. The corresponding results are presented hereafter firstly for the LSCF electrode and after for the LSCF-CGO electrode.

For the LSCF electrode, the experimental polarization curves recorded under air are shown in Fig. II-7a. The electrode overpotential is lowered by increasing temperature as it could be expected from a thermal activation of the electrode reaction mechanism for LSCF-based electrodes

[Monaco2018, Brito2019, Loureiro2019]. Regardless of the operating mode (SOEC or SOFC), the evolution of the current density can be regarded as linear at all temperatures for electrode overpotentials below 0.05 V/air. An activation is evidenced for higher electrode overpotentials for temperatures up to 700 °C. At 750 °C, the polarization curve is symmetric and linear but it is likely to be due to the narrow overpotential range. These results are confirmed by the plot of the polarization resistance R_{pol} as a function of the current density i (Fig. II-7c to II-7e). Indeed, a strong dissymmetry of $R_{pol} = f(i)$ is observed at 650 °C that becomes less pronounced at 700 °C, while a constant value is found at 750 °C. These observations at 650 °C may suggest a change either in the reaction mechanism or in the rate-determining steps. This change turns into a gradual transition at 700 °C and, finally, into a unique dominant mechanism with the same co-limitations at 750 °C. However, as already mentioned in this case, the investigated range of current densities and overpotentials are restricted close to the equilibrium.

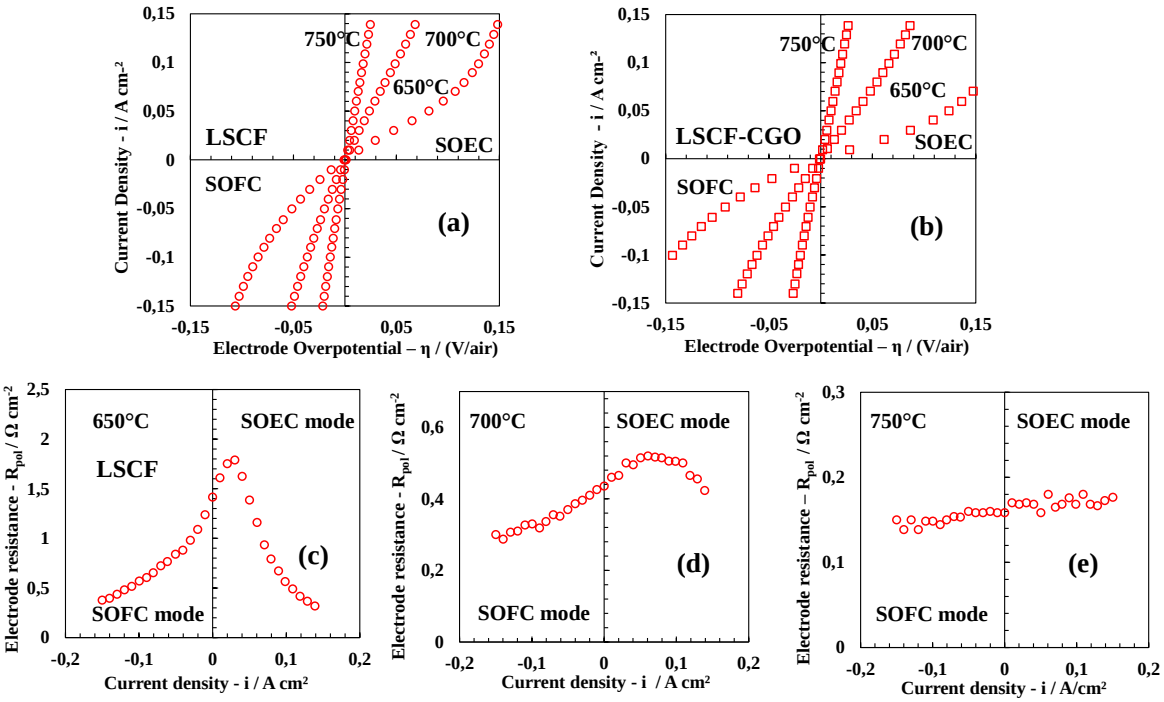

Fig. II-7 Experimental i-η curves under air for (a) the LSCF and (b) the LSCF-CGO electrodes, respectively. Experimental LSCF electrode polarization resistance plotted as a function of the current density at (c) 650 °C, (d) 700 °C and (e) 750 °C.

The EIS diagrams at OCP are plotted in the Nyquist representation in Fig. II-8a to II-8c. It is worth mentioning that the polarization resistance decreases with increasing the temperature. This result is in good agreement with the thermally activated behavior for this LSCF electrode. Besides, all the diagrams present a kind of Gerischer-type element whatever the investigated temperature. It can be noticed that a small contribution appears at low frequencies for the diagram at 750 °C. This contribution is ascribed to the limitation associated to the gas conversion and it is typically observed for electrodes exhibiting low polarization resistances at high temperatures [Nielsen2011]. As shown in the Bode plots reported in Fig. II-8d to II-8f, the frequency peak slightly increases with the operating temperature (i.e. f_c = 12 Hz, 19 Hz and 34 Hz at 650 °C, 700 °C and 750 °C, respectively). However, these values remain quite close to each other. To conclude, it can be stated that the unaffected shape of the impedance diagrams would suggest that the electrode is dominated at OCP by the same reaction mechanism in the range of studied temperatures.

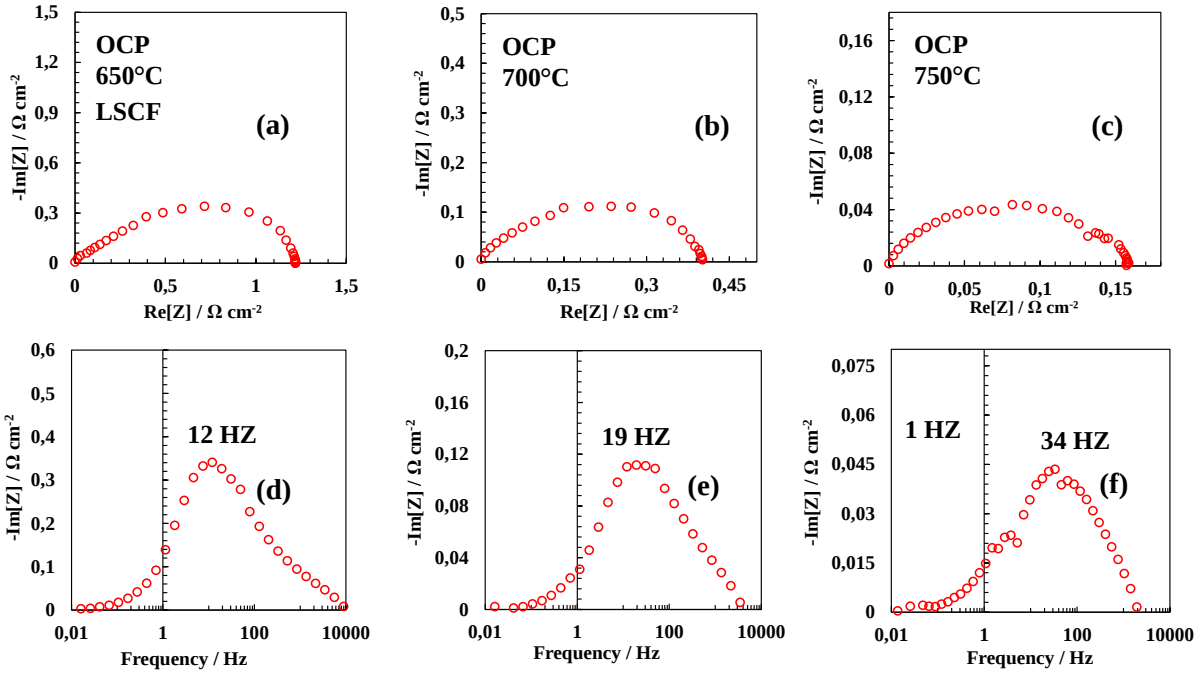

Fig. II-8 Experimental impedance diagrams for the LSCF electrode at OCP. Nyquist plots for (a) 650 °C, (b) 700 °C and (c) 750 °C. Bode plots for (d) 650 °C, (e) 700 °C and (f) 750 °C.

The EIS diagrams and Bode plots under dc current density at i_{dc} = +/- 50 mA·cm^{-2} are shown in Fig. II-9a to II-9d. As at OCP, the shape of the diagrams presents a kind of Gerischer-type element. The frequency distribution increases with increasing the dc current from cathodic to anodic polarization (f_c ≈ 7 Hz at i_{dc} = - 50 mA·cm^{-2} and f_c ≈ 24 Hz at i_{dc} = + 50 mA·cm^{-2}) as already observed by Monaco *et al*. [Monaco2018].

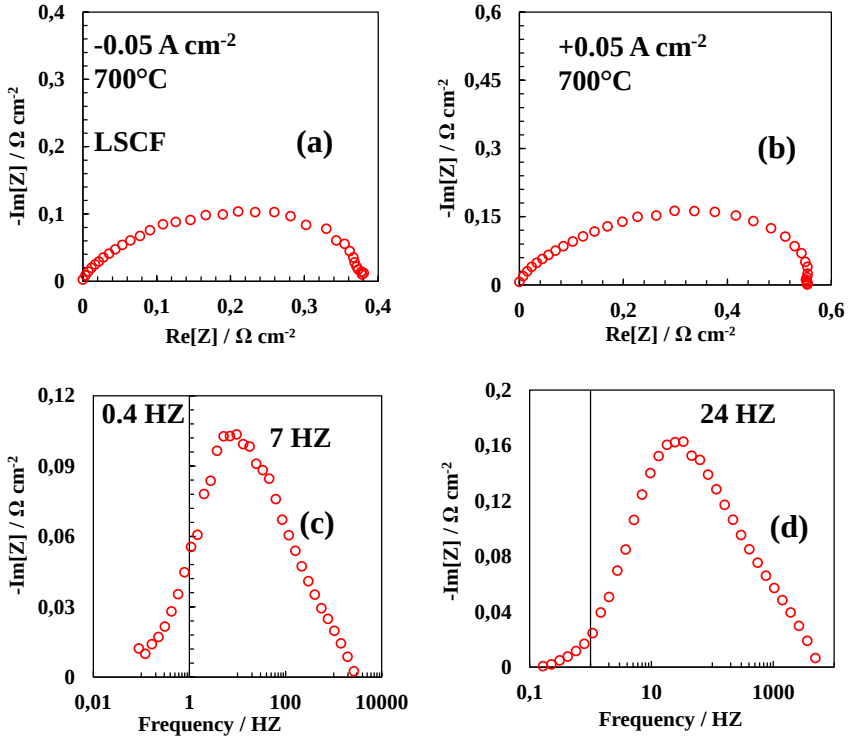

Fig. II-9 Experimental impedance diagrams for the LSCF electrode at 700 °C for i_{dc} = ± 50 mA·cm^{-2}. (a) and (b) Nyquist and (c) and (d) Bode plots.

The same electrochemical characterizations have been performed for the LSCF-CGO electrode. It can be remarked that the *i*-η curves recorded at 750 °C and 700 °C are symmetrical with respect to OCP (Fig. II-7b). This characteristic of the macroscopic electrode response suggests that the mechanism for the LSCF-CGO composite could be dominated by the same reaction pathway at 750 °C and 700 °C whatever the electrode polarization. In other words, the steady-state response of the electrode would indicate that there is no change in the reaction mechanism of the LSCF-CGO composite in SOEC and SOFC modes. In contrast to 750 °C and 700 °C, the *i*-η curve plotted at 650 °C in Fig. II-7b is clearly dissymmetric. This suggests that the global reaction pathway at

low temperature could be modified when changing the operating mode from cathodic to anodic polarization.

As shown in Fig. II-10a and Fig. II-10b, all the impedance diagrams exhibit a kind of 'classical' Gerischer-type element. This general shape at OCP have been already evidenced by many other authors for the LSCF-CGO composite electrodes [Choi2013, Hwang2005, Leng2008, Mortensen2014]. As for the LSCF electrode, the frequency peak f_c only slightly increases when increasing the temperature (i.e. $f_c \approx$ 2Hz, 8 Hz and 25 Hz at 650 °C, 700 °C and 750 °C, respectively). This trend consistent with that reported by Nielsen *et al.* [Nielsen2011] for a LSCF-CGO electrode. This further suggests that electrode reaction mechanism for the LSCF-CGO electrode at OCP does not change in the investigated temperature range.

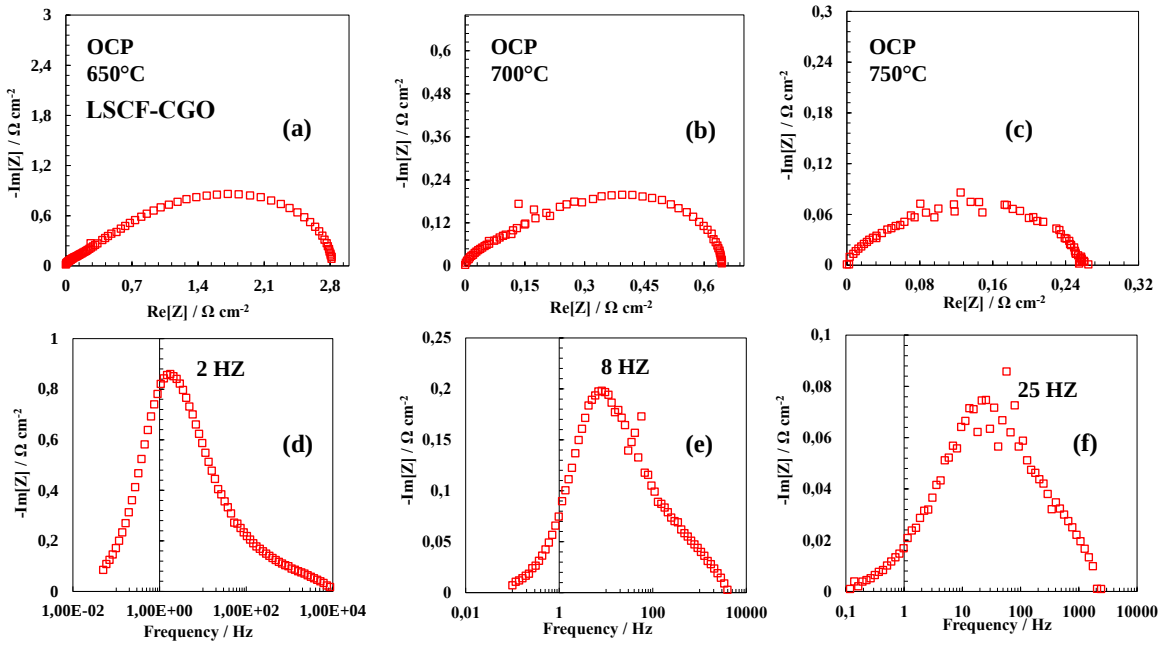

Fig. II-10 Experimental impedance diagrams for the LSCF-CGO electrode at OCP. Nyquist plots for (a) 650 °C, (b) 700 °C and (c) 750 °C. Bode plots for (d) 650 °C, (e) 700 °C and (f) 750 °C.

As evidenced for the LSCF electrode (Fig. II-9a), the electrode response is slightly depressed under cathodic polarization (Fig. II-11a), but it is worth noting that the global shape is not completely

modified under electrode polarizations. Moreover, the frequency peak (changing from $f_c \approx 6$ Hz at i_{dc} = - 50 mA·cm^{-2} to $f_c \approx 10$ Hz at i_{dc} = + 50 mA·cm^{-2}) is not strongly affected by the polarization as well. This statement tends to reinforce the claim that only one single reaction mechanism is dominant at this temperature for the LSCF-CGO composite.

It can be remarked that the performance of the LSCF-CGO composite is lower than the LSCF electrode (Fig. II-8). However, a direct comparison cannot be made since the two electrodes have very different microstructures because of different manufacturing conditions.

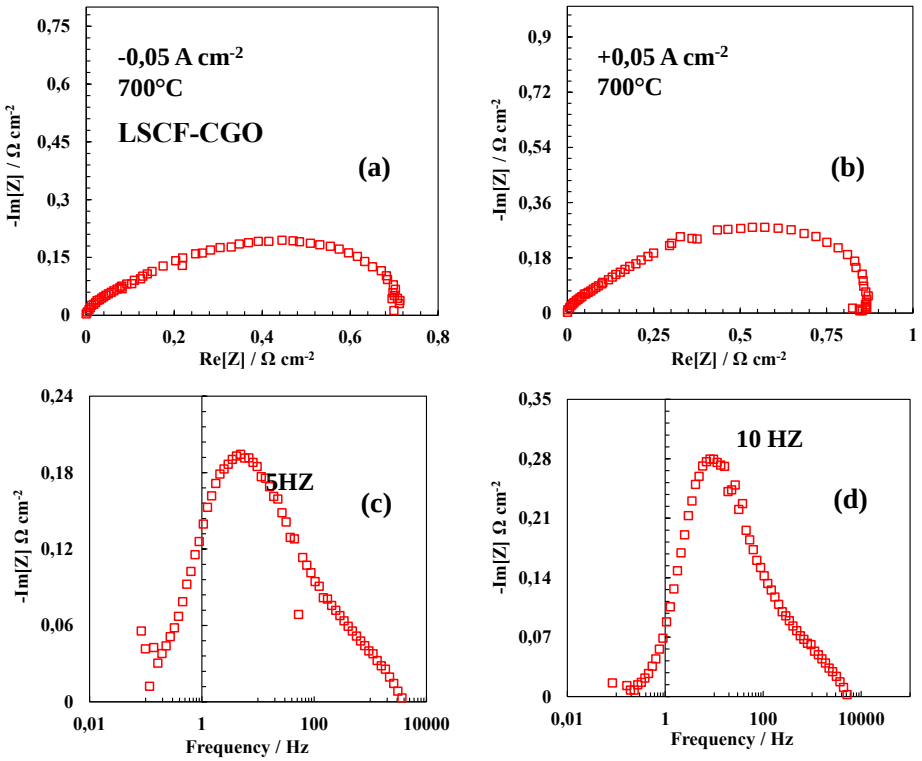

Fig. II-11 Experimental impedance diagrams for the LSCF-CGO electrode at 700 °C for i_{dc} = ± 50 mA·cm^{-2} (a) and (b) Nyquist and (c) and (d) Bode plots.

A specific attention has been paid on the effect of the oxygen partial pressure on the LSCF and the LSCF-CGO electrodes response (Fig. II-12a and Fig. II-12b). For oxygen partial pressures ranging from 0.1 to 1 atm, the polarization resistance of the LSCF-based electrodes significantly decreases when increasing the oxygen content, as already observed [Costamagna2019, Donazzi2020,

Hughes2015]. The reaction order *m* was estimated fitting the experimental data with the following relation:

$$R_{pol} = (P_{O_2})^{-m} \quad (16)$$

where R_{pol} is the polarization resistance extracted from the EIS at OCP.

For the LSCF electrode, a slight evolution of the reaction order is found with an exponent decreasing from 0.17 for 0.10 atm $\leq P_{O_2} \leq$ 0.21 atm down to 0.09 for $P_{O_2} >$ 0.21 atm (Fig. II-12a). These reaction orders are in rather good agreement with literature data. For instance, a value of 0.12 was deduced for a LSCF nanorod electrode operated at 717 °C between 0.10 and 0.20 atm [Costamagna2019]. For the LSCF-CGO composite, the evolution is less pronounced (Fig. II-12d). In this case, the reaction order decreased from 0.20 for 0.10 atm $\leq P_{O_2} \leq$ 0.21 atm down to 0.15 for $P_{O_2} >$ 0.21 atm (Fig. II-11d). Very few data are available in the literature for the composite electrode. To the best of our knowledge, no values are reported for an operating temperature close to 700 °C. Nevertheless, Murray *et al.* [Perry Murray2002] found a reaction order of 0.13 for a LSCF-CGO (40-60 wt. %) at 750 °C for $6.00 \cdot 10^{-4}$ atm $\leq P_{O_2} \leq$ 1.00 atm. Besides, Hughes *et al.* [Hughes2015] have reported a value of 0.20 for LSCF-CGO (50-50 wt. %) at 600 °C between 0.10 and 10 atm. Although these values were determined in different operating conditions, they are roughly consistent with the ones as obtained.

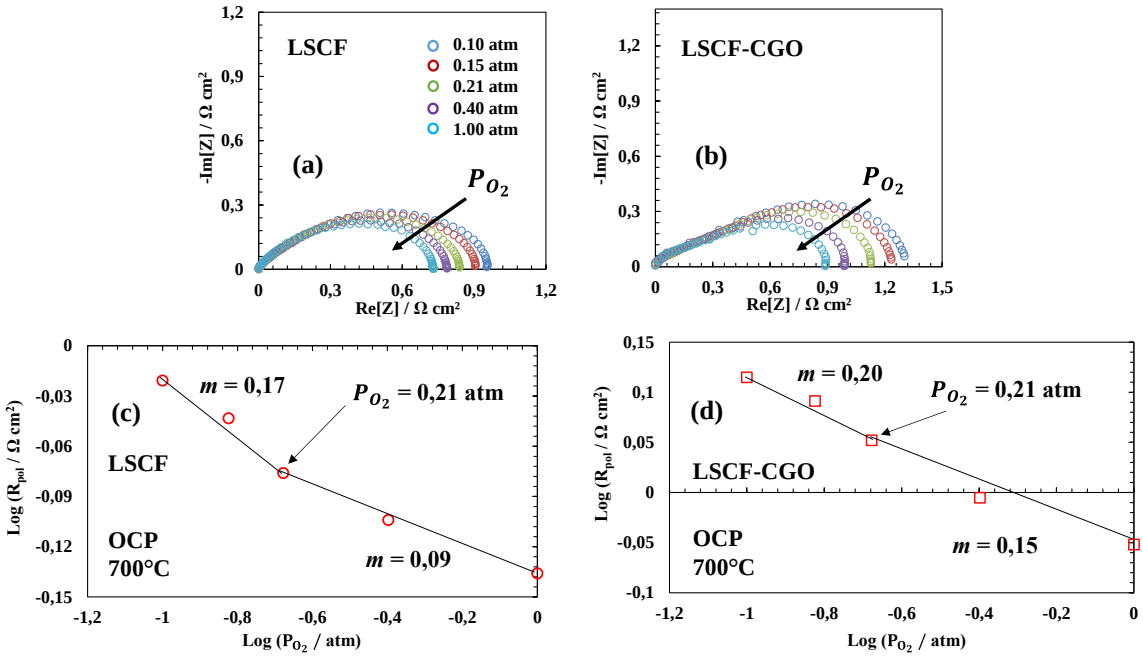

Fig. II-12 Nyquist plots as a function of the oxygen partial pressure at 700 °C for (a) the LSCF and (b) the LSCF-CGO electrode, respectively. Plot of the logarithm of the electrode polarization resistance as a function of the logarithm of the oxygen partial pressure for (c) the LSCF electrode and (d) the LSCF-CGO electrode.

Finally, cyclic voltammograms have been recorded at 700 °C and 650 °C for an oxygen partial pressure of 0.1 atm (Fig. II-13) only for the LSCF electrode. This oxygen partial pressure, slightly lower than the atmospheric condition, was chosen to enhance the hysteresis in the voltammograms. Indeed, it was shown in our previous experimental work performed at lower temperature [Tezyk2019] that the hysteresis is more pronounced at low P_{O_2}. However, whatever the temperature and the scan rate, the hysteresis remains rather limited at oxygen partial pressures close to P_{O_2} =0.21 atm, as already reported for LSCF electrodes [Kournoutis2011, Liu2006, Lust2010]. It can be noticed that a slightly higher hysteresis is found at 650 °C.

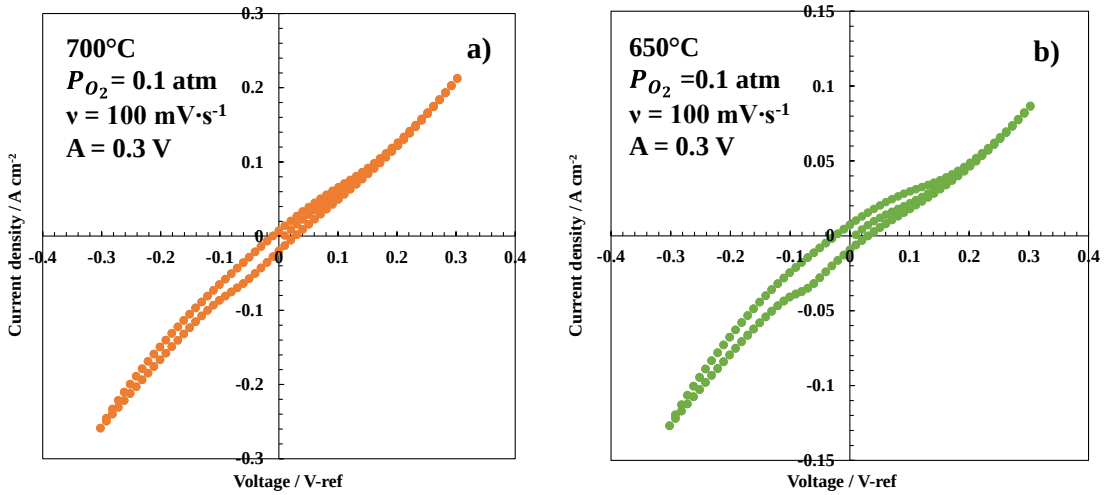

Fig. II-13 Experimental and simulated cyclic voltammetry curves, under P_{O_2}= 0.1 atm, at 700 °C (b) and 650 °C (c) for the potential waveform with ν = 100 mV·s^{-1} and A = 0.3 V (a).

In addition, experimental measurements have been conducted by varying the scan rate from 20 mV·s^{-1} up to 1000 mV·s^{-1} at the operating temperature of 650 °C and P_{O_2}= 0.1 atm (Fig. II-14). As expected, the hysteresis increases with the scan rate as classically observed in CV experiments [Tezyk2019]. This sensitivity of the CV response with the scan rate would be mainly explained by the slow diffusional process for the oxygen vacancies transport in LSCF material as mentioned in [Kournoutis2011].

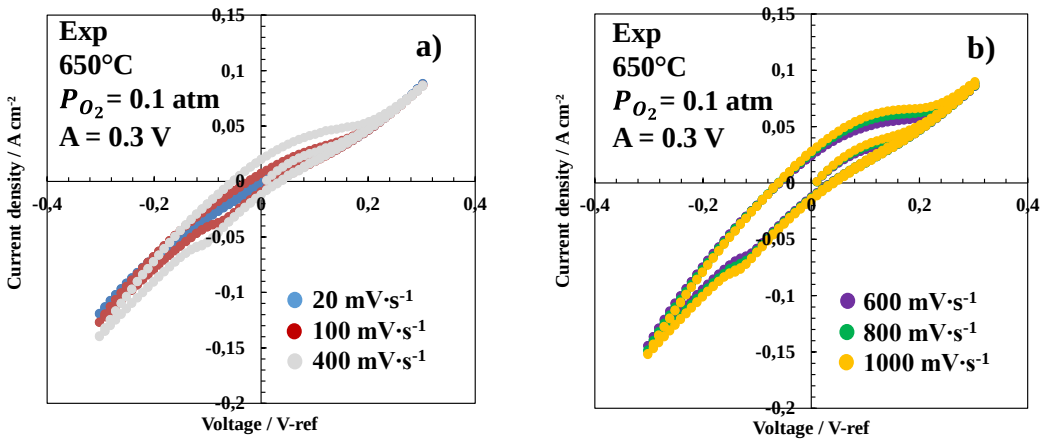

Fig. II-14 Experimental cyclic voltammetry curves as a function of the different scan rate: 20-100-400 mV·s^{-1} (a) and 600-800-1000 mV·s^{-1} (b) at 650 °C, P_{O_2} = 0.1 atm.

All these experimental results have been used for the validation of the full elementary model for the LSCF and LSCF-CGO electrodes together with the extension to the cyclic voltammetry simulation for the LSCF electrode model only (cf. Chapter III).

2.2 Long-term tests: study of the LSCF decomposition

2.2.1 LSCF symmetrical cells: effect of the anodic polarization

A durability test was carried out on a $La_{0.6}Sr_{0.4}Co_{0.2}Fe_{0.8}O_{3-\delta}$ symmetrical cell under dry air at the operating temperature of 750 °C for 1000 h (collaboration with Rakesh Sharma, post-doc at CEA). The evolution of the potential between the WE and the CE respect with the RE was recorded as function of the time and is reported in Fig. II-15. A positive current of + 0.75 A·cm^{-2} was imposed at the WE (SOEC mode, red curve) while the CE was operated under a negative current of -0.75 A·cm^{-2} (SOFC mode, bleu curve). As can be noticed in Fig. II-15, a higher degradation rate was detected for WE. In particular, an increase of the electrode potential of WE almost two times higher respect with the electrode potential of CE is recorded after 1000 h at 750 °C ($\Delta V^{WE} \approx 1400$ mV, while the of $\Delta V^{CE} \approx 650$ mV). This result means that a substantially higher degradation appeared for the LSCF electrode operated in galvanostatic SOEC mode. (Fig. II-15).

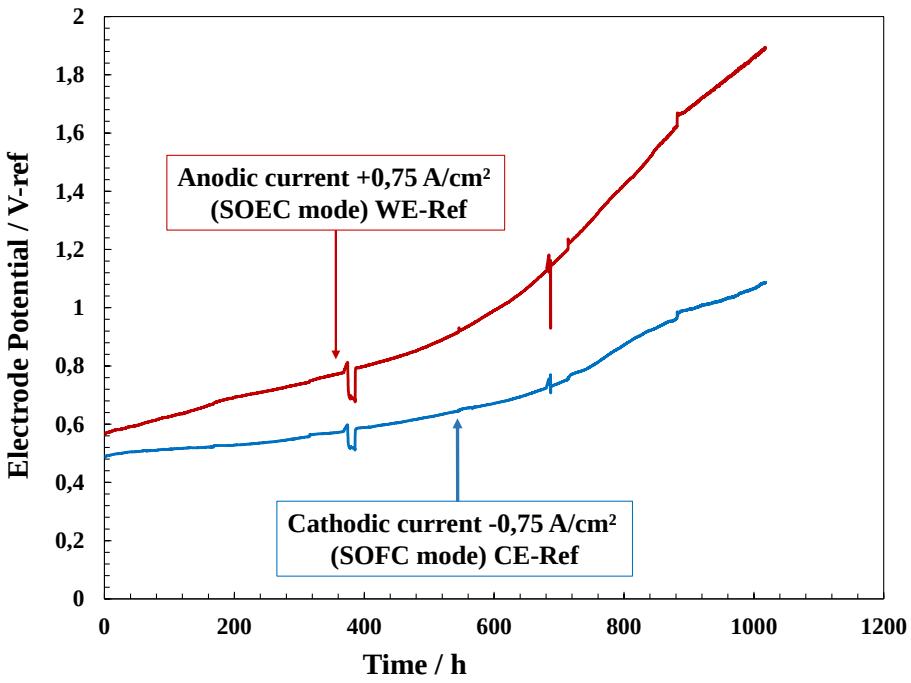

Fig. II-15 Durability curves of symmetrical cell electrodes in SOEC mode (WE versus REF) and SOFC mode (CE versus REF).

These experimental results confirm that degradation of the oxygen electrode is promoted in electrolysis mode, while its impact in the fuel cell mode is much less pronounced. This statement could be explained by the LSCF demixing mechanism proposed by Laurencin *et al.* [Laurencin2017].

In order to verify this hypothesis, post-test characterizations have been performed on the tested electrodes and on a pristine cell at the PSI facility (collaboration with Federico Monaco). Indeed, to highlight the Sr release from the LSCF structure, a useful indicator is the volume of unit cell of the LSCF crystal: it has been shown that that the volume of the unit cell increases when decreasing the strontium content in LSCF [Świerczek2009]. To characterize the samples, thin electrodes lamellas have been prepared by a plasma-Focused Ion Beam (p-FIB) for the pristine cell, the electrode operated in SOFC mode (anodic polarization) and the electrode operated in SOEC mode (cathodic polarization), respectively (Fig. II-16a to Fig. II-16c). They have been analyzed taking advantage of the high spatial resolution of the synchrotron light. The sample preparation and the micro XRD protocol are detailed in [Khamidy2020, Monaco2020]. To investigate the degree of destabilization of the material, the volume of the unit cell at each y position for the LSCF has been

determined *via* a Rietveld fitting of the XRD data. In Fig. II-16d the evolution of the unit cell volume with respect to the depth of the LSCF has been reported for the reference electrode (black dots) and the electrodes operated under anodic polarization (red dots) and under cathodic polarization (blue dots), respectively. The intercept with the y-axis (y = 0 µm) corresponds to the interface with the CGO barrier layer. First of all, it can be noticed that constant volume of ≈ 350.5 $Å^3$ was found for the reference cell (Fig. II-16d). This result is in good agreement with the attribution of this value to the unaltered LSCF structure. Interestingly, the aged electrodes showed a very different behavior: in the bulk of the electrode operated under cathodic polarization (SOFC mode), the volume of the unit cell remained similar to that of the reference electrode, while, at the interface with the barrier layer, an increase (≈ 351.5 $Å^3$) was evidenced which can be associated to a slight LSCF destabilization. This experimental observation is in good agreement with the durability curve of the CE electrode that showed a slight degradation over the time. On the other hand, for the electrode operated in SOEC mode, the volume of the unit cell is increased all along the electrode thickness indicating an overall higher destabilization of the material (≈ 353.5 $Å^3$). Moreover, also in this case, the variation of the unit cell was more pronounced at the LSCF/CGO interface (≈ 355.5 $Å^3$) indicating that the electrode destabilization was stronger in this zone regardless the electrode polarization. [Świerczek2009]. The results further support the proposed demixing mechanism of LSCF [Laurencin2017] that predicts a higher Sr precipitation from the LSCF bulk to the electrode surface under anodic polarization (Eq. 13). However, the exact impact of operating mode on the electrode performances has still to be clarified.

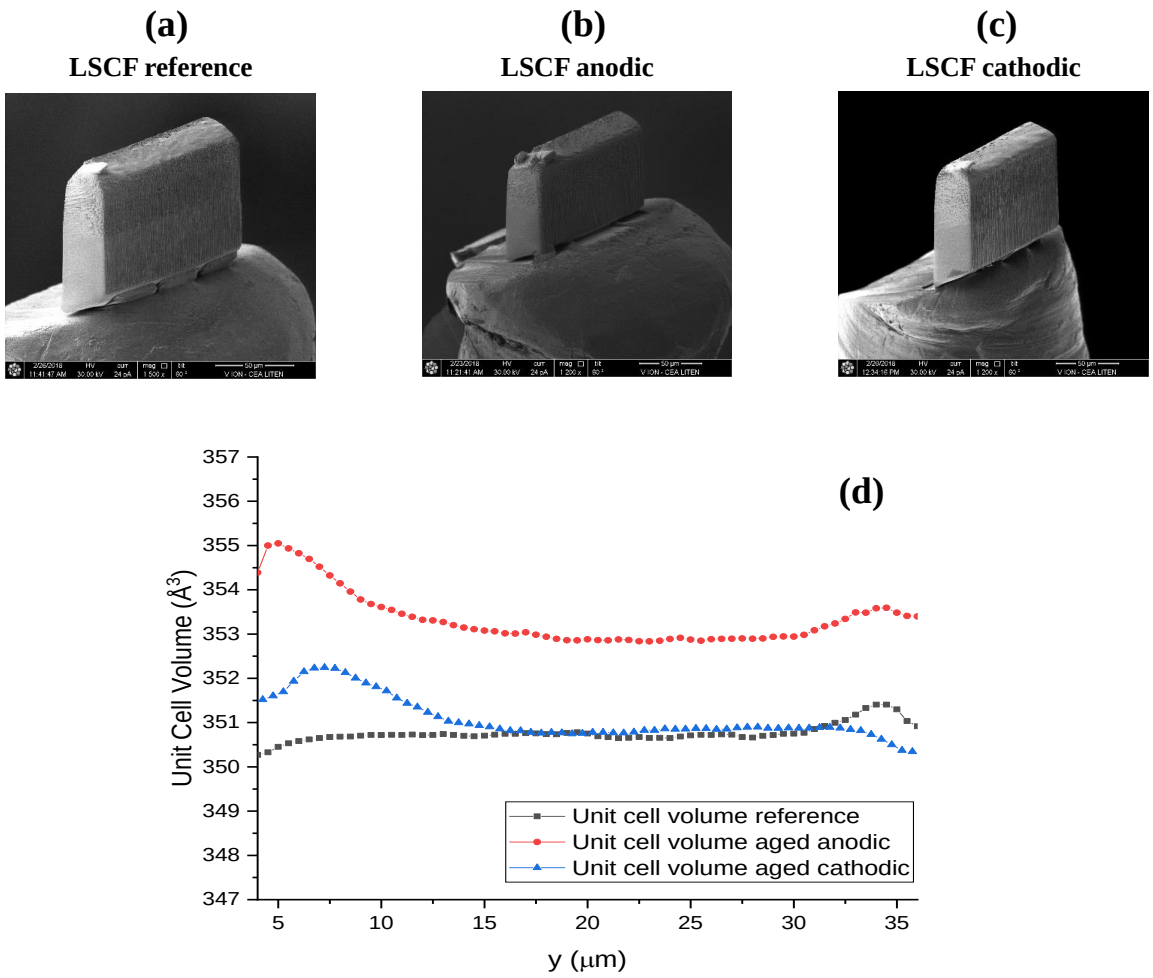

Fig. II-16 Lamella of the pristine electrode (a) and of the electrode operated in SOEC mode (b) and in SOFC mode (c), respectively. The graph represents the evolution of the unit cell through the depth of the LSCF electrode for the pristine cell (grey curve), the electrode operated under cathodic polarization (bleu curve) and the electrode operated in anodic polarization (red curve), respectively (d).

2.2.2 Complete cells: effect of the steam content

The objective was to evaluate the impact of moisture on the LSCF electrode degradation at a complete cell level. A first campaign of long-term SOEC tests has been carried out on two single cells in order to compare the degradation rates with and without the addition of humidity at the oxygen electrode side for 2000 h.

2.2.2.1 Studied cells, experimental set-up and testing conditions

Studied cells -. The tested cells were mechanically supported by a thick Ni-YSZ cermet layer. The hydrogen electrode and the electrolyte disks had a diameter = 5.0 cm on which the oxygen electrode (diameter = 3.4 cm) has been deposited by screen printing. This electrode had a multilayer structure composed by a LSCF-CGO layer, followed by a LSCF electrode and, finally, a LSC contact layer. A thin CGO barrier layer (diameter of 3.6 cm) has been added between YSZ and the oxygen electrode to limit the formation of secondary phases. It is important to underline that the LSCF material used for the complete bottom cells had the same stoichiometry of the one used for LSCF symmetrical cells ($La_{0.6}Sr_{0.4}Co_{0.2}Fe_{0.8}O_{3-\delta}$) since the stoichiometry can play a key role on the strontium release [Çelikbilek2019].

Experimental test bench - The set-up used for testing complete cells is described in Fig. II-16. The cell housing was composed by two plates that provided the connections to the gas delivery system. The oxygen electrode plate was made of alumina in order to avoid the electrode contamination (as by Cr for instance), whereas the hydrogen electrode plate was in Crofer22APU®. On the oxygen side, three grids of the same diameter of the electrode have been used: a fine Pt grid of 3600 mesh·cm^{-2} and two coarser Au grid of 100 mesh·cm^{-2}. The finer grid was placed in direct contact with the electrode surface to improve the current collection, while the two thick grids were used to reach a homogeneous potential distribution. In the hydrogen side, a nickel grid of 50 mm in diameter and a mesh density of 100 mesh·cm^{-2} was placed in contact with the cermet electrode. Four gold wires were welded to the coarser grids to allow the direct cell voltage measurements and current supply. Both the air and fuel gases were provided to the cell from the center of the housing and flowed through the grid meshes according to a radial co-flow configuration (Fig. II-17). The cell holder has been designed so that the pressure drop in the compartment that ensured gases collection up to the outlet is negligible compared to the one that arises through the current collecting meshes, thus yielding a homogenous gas distribution. The steam required for the cathode side has been produced by a homemade evaporator filled with deionized water coupled with a steam mass flow controller (Brooks® 5850S) (same system used for the testing of the cermet symmetrical cell, cf. par. 2.1.1.2). This device has allowed feeding the cell with a continuous flow rate of steam (up to 10 NL·h^{-1}) at atmospheric pressure without any gas carrier. To provide the moisture to the anode side, a warm up bubbler was used, while it was by-passed when the test was conducted in normal

condition (dry air). Commercial ceramic glass sealing Schott G018-311 was deposited on the edge of the cell to provide the gas tightness between the air and fuel sides in operation (Fig. II-17). Additionally, an alumina ring was positioned on the sealing agent improving gas tightness. At the hydrogen electrode side, the produced and non-consumed gases have been collected for safety reason and for gas analysis, if needed. At the oxygen electrode side, the produced O_2 and non-consumed air and steam were directly released into the furnace. Finally, a mechanical pressure has been applied on the housing to improve the electrical contacts between the grids and the electrodes (Fig. II-17).

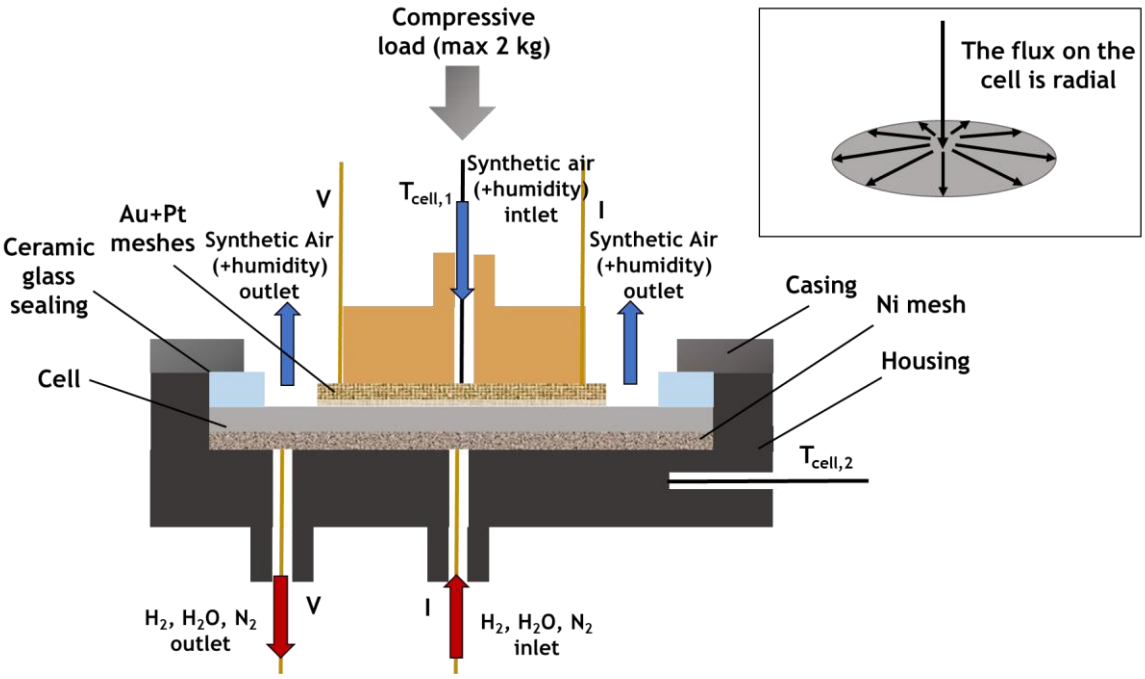

Fig. II-17 Schematic representation of the set-up for complete button cells used for the long-term tests both under dry and humid synthetic air at the oxygen electrode side.

Two cells have been tested in SOEC mode using the protocol described hereafter. Once positioned the cells in the test housing, a mechanical load was applied at room temperature with a pressure of 0.5 $kg \cdot cm^{-2}$. Then, the cells were heated up to the temperature required to form the glass sealing and then cooled down to 800 °C with a heating rate of 1 $°C \cdot min^{-1}$. The total flow rates of synthetic air and N_2 are 1 $NmL \cdot min^{-1} \cdot cm^{-2}$ in O_2 and H_2 compartments, respectively, during this step. It is worth noting that the purities of gases are the following: N58 for O_2, N51 for N_2 and N45 for H_2,

respectively, while the conductivity of the deionized water is less than 5 $S \cdot cm^{-1}$. These characteristics were similar to those used for symmetric cells tests.

Before durability tests – The reduction of the Ni-based cermet was performed at 800 °C by gradually increasing the amount of hydrogen while the amount of nitrogen was decreased. The total flow rate was maintained at the constant value of 4 $NmL \cdot min^{-1} \cdot cm^{-2}$. Each step lasted from 5 to 30 minutes until the OCV stabilization. At the end of the reduction process, 100 vol. % of H_2 and 100 vol. % of synthetic air were supplied at the hydrogen and oxygen sides, respectively, to check the quality of the cell in terms of tightness by measuring OCV and the cell temperature. After 12 hours, the gas flows have been modified to reach a total flow rate of 12 $NmL \cdot min^{-1} \cdot cm^{-2}$, with a composition of 90 vol. % H_2O and 10 vol. % H_2 on the cathode side. On the anode side, the sweeping gas flow rate (synthetic air, with or without addition of humidity at 8 %) was fixed to 36 $NmL \cdot min^{-1} \cdot cm^{-2}$.

Initial i-V curves were recorded at 800 °C in these gas conditions to check the quality of the cell in terms of performances. The current was increased continuously with a current ramping rate of 0.4 $A \cdot cm^{-2} \cdot min^{-}1$. The measurements were performed by starting at zero current, after going to the maximum magnitude and, finally, going back to zero. EIS measurements were performed at OCV and at -0.75 $A \cdot cm^{-2}$ under the same gas conditions with Autolab impedance frequency analyzer/potentiostat (FRA2/PGSTAT302N) coupled with a booster 20A. EIS measurements were performed in a frequency range from $2.0 \cdot 10^4$ Hz down to 10^{-2} Hz/10^{-3} Hz. Cycle repetitions have been performed for each frequency for reducing noise and improving data quality when considered as necessary. The current amplitude was optimized at 100 mA for measurement at OCP and 300 mA for measurements at 0.75 $A \cdot cm^{-2}$.

After the performance tests, the temperature was decreased down to 750 °C with a rate of 1 $°C \cdot min^{-1}$ which is the temperature chosen for the long-term tests. At this reference temperature, polarization curves and EIS diagrams have been recorded both at OCV and at - 0.75 $A \cdot cm^{-2}$.

Durability protocol - The durability tests were performed in a galvanostatic mode. A current density of - 0.75 $A \cdot cm^{-2}$ has been applied to the cell at the operating conditions previously reported (temperature and gas composition) which corresponds to a steam conversion of 48 %. A first durability test has been performed by supplying dry synthetic air at the anode side with an inlet

flow rate of 36 NmL·min^{-1}·cm^{-2}. At the cathode side, the total flow rate was 12 NmL·min^{-1}·cm^{-2} (90 vol. % H_2O and 10 vol. % H_2). The corresponding cell is thus referenced as *Cell-1*. A second test was performed in the same operating conditions by adding 8 vol. % of moisture at the air flow (referenced as *Cell-2*). The cells were tested for 2000 h.
During long-term tests, the EIS measurements have been performed at OCV and at - 0.75 A·cm^{-2} at periodic interval of time. After 2000 h of operation, final i-V curves and EIS diagrams have been recorded at 750°C in the same conditions of the initial characterizations.

After durability protocol - After switching off the current and once the humidity reached 0 vol. %, the fuel gas was gradually replaced by 3 vol. % H_2 and 97 vol. % N_2 in order to maintain the hydrogen electrode in the reduced state during the cooling of the furnace, while the air side was fed with pure N_2 to limit the risk of cermet oxidation if the cells broke during cooling. Then, the cells were cooled down to room temperature with a rate of 1 °C·min^{-1}.

Data evaluation - The cell performances were summarized in terms of Area Specific Resistance (ASR), series resistance (R_s), polarization resistance (R_{pol}), total resistance (R_{tot}) and of the cell voltage as a function of the various testing conditions. The ASR was taken as the slope of the i-V curve (ASR_{i-V}) at the operating point (- 0.75 A·cm^{-2}). For the presented i-V curves and EIS diagrams, the current density or resistance are normalized to the active area of the oxygen electrode surface, i.e. 9.08 cm². For durability measurements, the degradation rate of the cell voltage for times between t_1 (V_{t_1}) and t_2 (V_{t_2}), with $t_2 > t_1$, is defined as $\Delta V/V_{t_1} = (V_{t_2} - V_{t_1})/V_{t_1}$) and is expressed per 1000 hours (mV·kh^{-1}). The variations of the different resistive contributions can be determined from the comparison of i-V curves or EIS characteristics as a function of testing duration.

It is worth mentioning that a special effort has been paid to follow as much as possible the presented protocol even if some issues has been encountered during the measurements, mostly related to the stability of the steam generator. However, the reliability of the acquired data has been regarded as sufficient to ensure an exhaustive interpretation of the experimental results.

2.2.2.2 Durability under dry and humid air

Initial performances – After the reduction step, the two cells presented very close OCV values (≈ i.e. 1.18 V at 800 °C with 4 NL·h^{-1} of H_2 and air in the H_2 and O_2 side, respectively). This result confirms also the gas tightness of the experimental set-up, especially in the hydrogen compartment. Since the ASR values deduced from polarization curves and impedance diagrams are coherent, only the Nyquist and Bode plots of the investigated cells are reported (Fig. II-18). It can be noticed that the Nyquist plots present very similar shape and very close polarization resistance values (Fig. II-18a). Moreover, the frequency distribution is similar for both cells (Fig.II-18b). This confirms the good reproducibility of the tests. The slight difference in series resistance between the two cells could be related to the current collecting. For each cells, the high frequency inductive response is originated from the connecting wires for current and potential measurements.

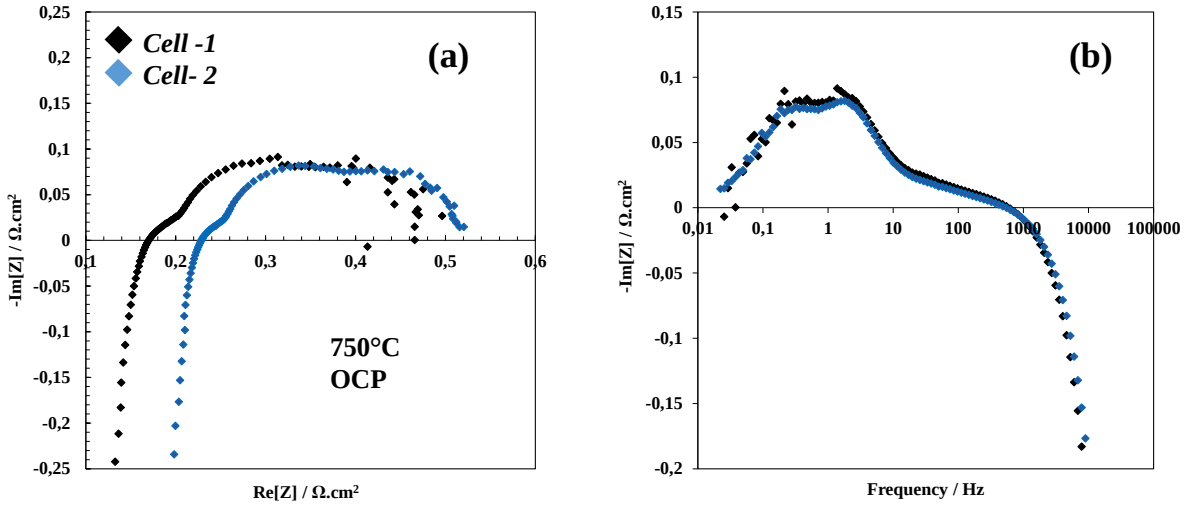

Fig. II-18 Initial impedance diagrams for *Cell-1* (black curve) and *Cell-2* (blue curve), respectively. Nyquist plots (a) and Bode plots (b). H_2O + H_2 (12 NmL·min^{-1}·cm^{-2}) at the cathode side, dry synthetic air (36 NmL·min^{-1}·cm^{-2}) at the anode side.

In addition, *Cell-2* was characterized with i-V curves at different steam percentages (0 vol. %-3 vol. %-8 vol. %, respectively) in the air flow. As could be expected (cf. Chapter I), the cell performances measured in this moisture range are very close (Fig. II-19).

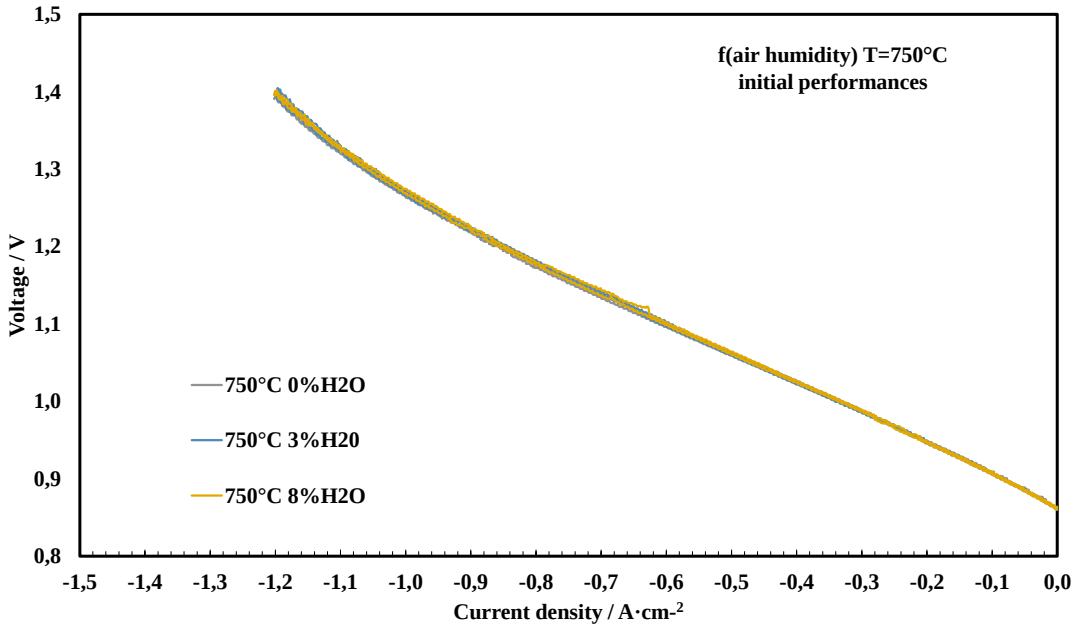

Fig. II-19 Initial i-V curves as a function of water content in the air flow at the anode side for *Cell-2*. $H_2O + H_2$ (12 NmL·min^{-1}·cm^{-2}) at the cathode side, dry synthetic air (36 NmL·min^{-1}·cm^{-2}) at the anode side.

Evaluation of degradation rates– The variations of cell voltages as a function of time during long-term SOEC tests for the two cells are shown in Fig. II-19. Regardless of the steam content, a steadily increase of the cell voltage has been evidenced in the chosen experimental conditions. The total variation of cell voltage (after 2000 h) has been found to be higher for *Cell-2* (ΔV = 45 mV·kh^{-1}) with respect to *Cell-1* (ΔV = 27 mV·kh^{-1}) (Tab. II). The total degradation rate was thus equal to 2.4 %·kh^{-1} and 3.9 %·kh^{-1} at 750 °C respectively. This suggests that the introduction of steam at the anode side is likely to accelerate the degradation rate of a hydrogen electrode supported cell Ni-YSZ/YSZ/CGO/LSCF-CGO/LSCF/LSC.

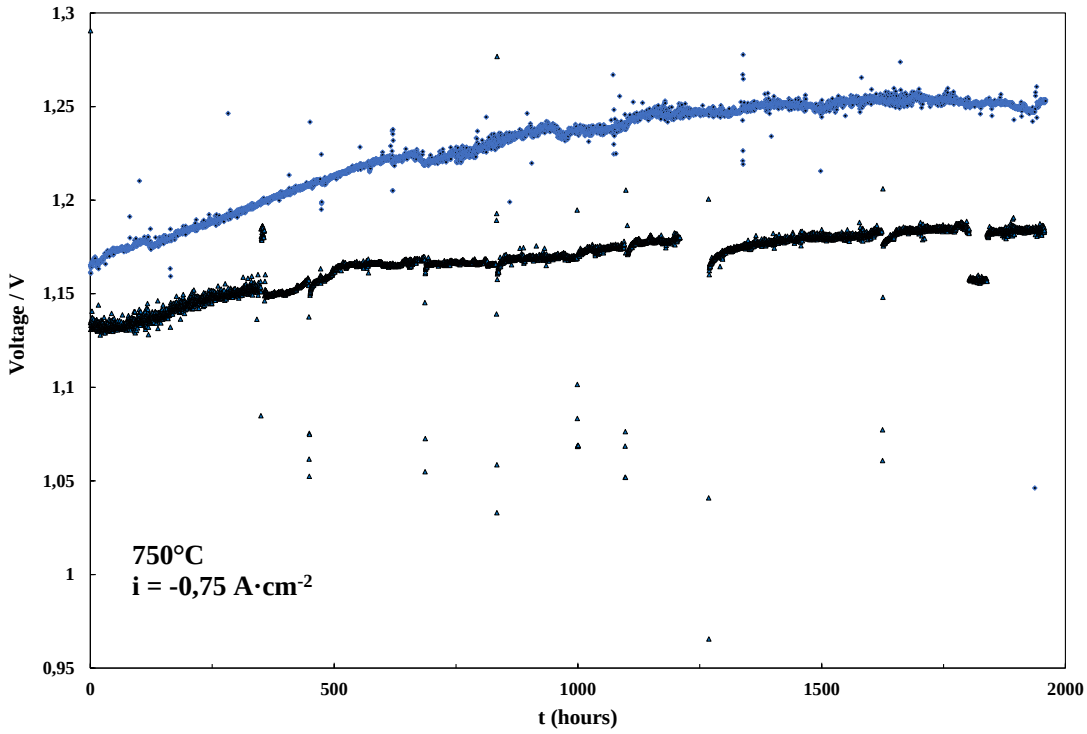

Fig. II-20 Time evolution of cell voltages in long-term SOEC tests for *Cell-1* (black squares) and *Cell-2* (blue squares) at 750 °C, H_2/H_2O 90/10 vol i = - 0.75 $A \cdot cm^{-2}$ with a steam conversion of 40%. $H_2O + H_2$ (12 $NmL \cdot min^{-1} \cdot cm^{-2}$) at the cathode side, dry synthetic air or humid (8 vol. %) air (36 $NmL \cdot min^{-1} \cdot cm^{-2}$) at the anode side.

It is worth noting that after 600 h of operation, the time dependence of the cell voltage slowed down for both cells (Fig. II-20). Accordingly, two different degradation rates can be considered: a steeper for the first 600 h and a smoother for the remaining 1400 h. Thus, the degradation rates of the cell voltage have also been expressed as voltage losses over time from 600 h to 2000 h (Tab. II). Even after an initial period of 500 h, the degradation rate of the cell voltage is higher under humid air at the anode side (0.6 $\% \cdot kh^{-1}$ for *Cell-1* and 1.0 $\% \cdot kh^{-1}$ for *Cell-2*).

Tab. II Degradation rates determined from durability tests after 2000 h (left) and after the first 600 h (right).

Tested gas conditions, i= -0.75 A/cm², at 750°C	$\Delta V_{V=f(t)}$ measured during the whole test mV·kh^{-1}	%/kh	$\Delta V_{V=f(t)}$ measured after an initial transient period of 600h mV·kh^{-1}	%/kh
Cell-1, dry synthetic air	27	2,4	7	0,6
Cell-2, synthetic air humidified at 8vol.%	45	3,9	12	1,0

The degradation rates of the cell potential and ASR have been determined after the durability SOEC tests (i.e. after 2000 h) for a current density of -0.75 A·cm^{-2} (operating point for the long-term tests) from the i-V curve. The corresponding values have been summarized in Tab. III as voltage losses (ΔU_{i-V}) and ASR (ΔASR_{i-V}).

Tab. III Degradation rates determined from i-V curves recorded at 750 °C.

Tested gas conditions, i = - 0.75 A/cm², at 750°C	$\Delta U_{i\text{-}V}$ mV·kh^{-1}	%/kh	ΔASR mΩ·cm²·kh^{-1}	$\%_{ASR}$/kh
Cell-1, dry synthetic air	25,0	2,2	36	8.3
Cell-2, synthetic air humidified at 8vol.%	45,9	4,0	97	27.1

The degradation rates of cell voltage determined from the i-V curves are equal to 25 and 46 mV·kh^{-1} at 750 °C for Cell-1 and Cell-2, respectively. These values are consistent with the

values deduced from the durability tests after 2000 hours (27 mV·kh^{-1} for Cell-1 and 45 mV·kh^{-1} for Cell-2, cf. Tab. II). These results confirm that the degradation of this type of cell is two times higher when air is humidified *at the anode side (*8 vol. %*)*. Regarding the ASR, the degradation is even three times higher (36 mΩ·cm²·kh^{-1} and 97 mΩ·cm²·kh^{-1} for Cell-1 and Cell-2, respectively). It is worth mentioning that higher degradation rates of ASR, with respect to that of the cell voltage, have been already reported in the literature [Fang2018, Schefold2017]. As for the cell voltage and ASR, the time evolutions of R_s, R_{pol} and R_{tot} during durability tests have been quantified by using the ratio of the difference between the resistance after 2000 hours ($R_{x\ t=2000}$) and the initial one at t = 0 ($R_{x,t=0}$) to the initial resistance ($R_{x,t=0}$) ($\Delta R_x/R_{x,t=0} = (R_{x,t=2000} - R_{x,t=0})/R_{x,t=0}$)). (Tab. IV).

The time evolutions of EIS diagrams recorded at 750 °C at OCV and for a current density of -0.75 A·cm^{-2} are shown in Fig. II-21 and Fig. II-22. As can be seen, the polarization and the series resistances of both cells increased as a function of the testing time in agreement with other studies on similar assemblies [Fang2018, Hauch2016, Zheng2015].

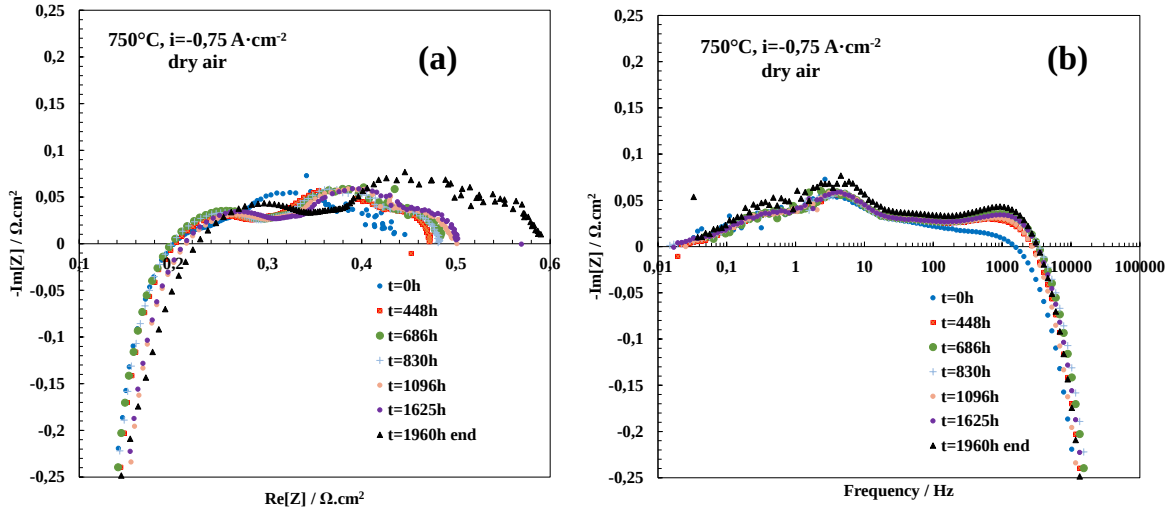

Fig. II-21 Time evolution of Nyquist (a) and Bode (b) plots in long-term SOEC tests for *Cell-1* at 750 °C and - 0.75 A·cm^{-2}. H_2O + H_2 (12 NmL·min^{-1}·cm^{-2}) at the cathode side, dry synthetic air (36 NmL·min^{-1}·cm^{-2}) at the anode side.

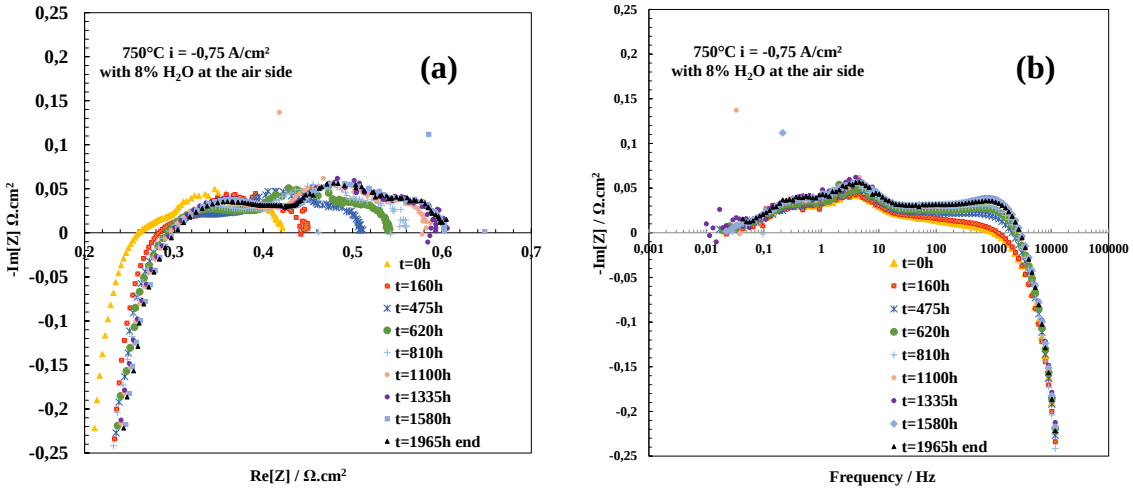

Fig. II-22 Time evolution of Nyquist (a) and Bode (b) plots in long-term tests SOEC tests for *Cell-2* at 750 °C and - 0.75 A·cm^{-}. H_2O + H_2 (12 NmL·min^{-1}·cm^{-2}) at the cathode side, humid (8 vol. %) synthetic air (36 NmL·min^{-1}·cm^{-2}) at the anode side.

As expected, the degradation of the series and polarization resistances, and thus of the total cell resistance, are enhanced in humid air (Tab. IV). Moreover, the degradations of R_{tot} are consistent with those determined for ASR_{i-V}. This further confirms the coherence of the experimental data recorded with the different characterization methods. From Fig. II-21 and Fig. II-22, one can deduce that the frequency distributions of the electrode responses remained nearly similar after a galvanostatic SOEC operation. For both tested cells, the faster increasing polarization resistance dominated the entire degradation process (Tab. IV) in agreement with the results of other groups [Zheng2015, Hauch2016], and this is even more important in the case of the cell-2 operating in humid air on the anode side.

Tab. IV Degradation rates of resistive contributions during long-term SOEC tests for *Cell-1* and *Cell-2*, at 750 °C in dry and humid synthetic air. ΔASR_{i-V} values have been reported as well for comparison with the degradation of R_{tot}. These values have been calculated in the tested gas conditions and i = - 0.75 A·cm^{-2}.

	ΔASR_{iV}		ΔR_t		ΔR_p		ΔR_s	
Cell-1 / Dry synthetic air	**mohm·cm²·kh^{-1}**	**%$_{ASR}$/kh**	**mohm·cm²·kh^{-1}**	**%$_{Rt}$/kh**	**mohm·cm²·kh^{-1}**	**%$_{Rp}$/kh**	**mohm·cm²·kh^{-1}**	**%$_{Rs}$/kh**
750°C	35,7	8,3	69,9	15,5	63,3	20,5	6,6	4,7
	ΔASR_{iV}		ΔR_t		ΔR_p		ΔR_s	
Cell-2 / Synthetic air humidified at 8%	**mohm·cm²·kh^{-1}**	**%$_{ASR}$/kh**	**mohm·cm²·kh^{-1}**	**%$_{Rt}$/kh**	**mohm·cm²·kh^{-1}**	**%$_{Rp}$/kh**	**mohm·cm²·kh^{-1}**	**%$_{Rs}$/kh**
750°C	97,4	27,1	91,6	21,8	73,8	35,1	17,8	8,5

Without emphasizing on the related degradation processes, one can stated that steam acted as an accelerating factor for the cell degradation. In particular, higher degradation rates of the serial and polarization resistances have been measured for this cell. The higher increase of the polarization resistance can be related to the loss of ionic conductivity in the LSCF bulk derived by the higher loss of strontium together with the effect of the surface passivation [Laurencin2017].

However, a specific study by EIS should be carried out on this cell to better identify the contribution of the O_2 electrode and assess performance loss over time by comparing the frequency responses in operation in dry air or humid air.

Moreover, post-test characterizations have still to be done on the samples to confirm or not the formation of zirconates. At the same time, it has to be considered that the formation of zirconates is thermally activated. It means that a higher presence could be expected at higher operating temperatures (i.e. 850 °C) [Monaco2020]. Moreover, the microstructure of the CGO barrier layer (porosity, grain size) could also play a significant role in hindering the formation of zirconates (without suppressing the demixing). Therefore, deeper investigations of this phenomenon are still needed.

2.3 Conclusions of the chapter

The electrochemical characterizations of both hydrogen and the oxygen electrodes have been presented. Concerning the hydrogen electrode, the experimental test bench was adapted to manage a wide range of steam partial pressure. Moreover, the very low noise on the recorded measurements has confirmed the stability of the steam flow. From the experimental data, the reaction orders for the hydrogen and steam partial pressures have been determined. These data together with the polarization curves have allowed calibrating and validating a microscale elementary model for the hydrogen electrode [Monaco2020].

In parallel, two types of oxygen electrode have been characterized (LSCF and LSCF-CGO). A wide range of operating conditions have been investigated in terms of temperature, polarization and oxygen partial pressure. Classical electrochemical techniques (such as polarization curves and EIS) have been employed together with cyclic voltammetry curves (which a less common method in the SOFC/SOEC field). All the presented data have been used for the validation of the elementary model for the oxygen electrode description extensively presented in the next chapter.

In order to obtain the experimental evidences for the LSCF demixing mechanism proposed by Laurencin *et al.* [Laurencin2017], long-term tests have been performed at the electrode and complete cell levels. From the durability curves performed on symmetrical cells, it has been demonstrated that the degradation of LSCF oxygen electrodes was higher when operating in SOEC mode than in SOFC mode. In addition, the XRD performed on the tested electrodes have shown a substantial increase of the cell unit volume for the oxygen electrode operated under SOEC mode (compared to the reference value measured on a pristine electrode). Since this behavior is usually related to a strontium loss from the perovskite lattice, this result is in good agreement with the proposed degradation mechanism that predicts a higher strontium precipitation under anodic polarization.

Finally, a campaign of long-term tests has been carried out on complete cells with LSCF oxygen electrode both in dry air and humid air at the anode side under SOEC mode. The durability curves have shown a higher degradation rate for the cell operated under moisture in the air flow. Nevertheless, further investigations are needed to fully validate the hypothesis of the steam as accelerating degradation factor under anodic polarization. In this frame, to complement this study,

another campaign of long-term tests has been planned to monitor the cell degradation for an operation in SOFC mode with the addition of steam at the air side.

Chapter III. Electrochemical model

A microscale electrochemical modelling has been developed for a better understanding of the electrode reaction mechanisms. For this reason, an already existing physically-based model for the representation of the porous LSCF and LSCF-CGO electrodes [Hubert2016, Laurencin2015] has been extended with a full elementary kinetic description including both the surface and bulk paths. The set of partial differential equations has been solved by keeping the full non-linearity of the system to compute the dynamic electrode response even for non-linear perturbations. Because of the large number of unknown parameters inherent to this kind of approach, a special attention has been paid to achieve a thorough and relevant model validation. For this purpose, the microstructural properties of the tested electrodes extracted from 3D reconstructions by FIB-SEM tomography (cf. Chapter II) have been implemented in the model as input parameters. Besides, in order to reduce as far as possible the uncertainties on the parameters estimation, a wide range of experimental conditions has been explored (polarization curves, impedance spectra at OCP and under dc currents at different temperatures and oxygen partial pressures).

Furthermore, the full elementary model was extended to compute the CV curves for a LSCF oxygen electrode and the capability of the model to reproduce experimental results was verified. In addition, a numerical version of a semi-analytical model presented by Montella *et al.* [Montella 2021] was also implemented. A comparison between the two models has been discussed to assess the relevance of the simplified approach (semi-analytical model) with respect to the detailed one (full elementary model).

To conclude, the validated full elementary model has been used to study the electrode reaction mechanisms with respect to the temperature, the polarization and the oxygen partial pressure. The corresponding results have permitted to identify the electrode limiting steps as a function of the different operating conditions. In parallel, the extension of the model to reproduce CV curves allowed evaluating the relevance of this electrochemical method for the LSCF characterization.

It is important to specify that the validation of the model for the Ni-3YSZ hydrogen electrode model has been developed and extensively described in the Ph.D. thesis of Federico Monaco [Monaco2020] and therefore not presented hereafter.

3.1 Model description

The model considers an equivalent homogeneous medium of an isothermal slice of porous LSCF or LSFC-CGO electrode including the CGO barrier layer (Fig. III-1a). The effective properties for the model are computed on the 3D reconstructions and are expressed through the electrode microstructural properties [Holzer2013]. The model was developed to simulate the electrode response for both steady-state and dynamic behaviors. The reaction mechanism, which is composed of the bulk and surface paths for the oxygen transfer, has been divided in a sequence of pure elementary steps. For this purpose, the presence of neutral oxygen atoms, adsorbed ions and molecules have been assumed on the LSCF surface [Che1983, Che1982].

3.1.2 Reaction mechanism

For the sake of clarity, the implemented reaction mechanism is described hereafter only for the LSCF-CGO electrode in anodic polarization. The model for the LSCF electrode can be deduced from the composite one by considering that the reactions occurring at the TPBls and at the LSCF/CGO interface do not extend in the whole electrode volume but are restricted at the interface with the electrolyte.

The detailed reaction mechanism is described in Fig. III-1b in which the blue and red arrows are related to the bulk and surface paths, respectively. All the reactions implemented in the model are listed in Table V using the "Kröger-Vink" notation along with the expressions of their kinetic rates. The bulk path is composed by the migration of the oxygen ions in CGO, followed by the ionic transfer at the LSCF/CGO interface (R1), the oxygen diffusion in the bulk and a final oxygen excorporation (R2). For this last step, the oxygen ion in LSCF reacts with a hole coming from the electrode to produce an oxygen ion attached on the surface. In parallel, the surface path is defined by the direct electrochemical oxidation at the TPBls (R3). The two parallel pathways merge in a common path depicted by green arrows in Fig. 3b. In this last part of the reaction mechanism, the oxygen ions diffuse on the LSCF surface and are further oxidized to form neutral oxygen ad-atoms (R4). After diffusion, these species can react to produce attached O_2 molecules (R5) that can also

diffuse before being released into the porosities (R6). Finally, the O_2 gaseous molecules can be transferred by gas diffusion in the porosity network up to the gas channel.

Because of this elementary kinetic description, the presence of adsorbed charged species (oxygen ions) is assumed on the LSCF surface. As proposed by Fleig *et al.* [Fleig2005], a double layer can arise at the LSCF/gas interface due to the accumulation of oxygen ad-ions whose charges are counterbalanced by holes in LSCF. This local double layer yields a surface electrostatic potential step χ which is characterized by a capacitance C_{dl}^{surface}:

$$\chi(\text{z}) = \chi_{LSCF}^{bulk} - \chi_{LSCF}^{surf} = \frac{\Gamma F\, \theta_{O^- - s_{LSCF}}(z)}{C_{dl}^{\text{surface}}} \tag{7}$$

where Γ is the density of available sites on the LSCF surface, F is the Faraday's constant and $\theta_{O^- - s_{LSCF}}$ the surface coverage of the oxygen ad-ions.

It is worth noting that Eq. (7) stands for a low concentration of adsorbed species (i.e. for a diluted solution) when there is no restriction on the number of available sites. This electrostatic potential is supposed to vary with the coverage rates all along the electrode thickness. On the other hand, the electrode potential *E* is classically expressed as the difference between the local electronic potential in LSCF (φ_{LSCF}) and the local ionic potential in CGO (φ_{CGO}):

$$E(z) = \varphi_{LSCF}(z) - \varphi_{CGO}(z) = +\frac{\tilde{\mu}_{h^\bullet}}{F} - \frac{\tilde{\mu}_{V_O^{\bullet\bullet}}}{2F} \tag{8}$$

where $\tilde{\mu}_{h^\bullet}$ and $\tilde{\mu}_{V_O^{\bullet\bullet}}$ denote the electrochemical potentials ($J \cdot mol^{-1}$) for the holes in LSCF and the oxygen vacancies in CGO. The transport equations for the fluxes and the mass and charge conservations are provided in Table VI.

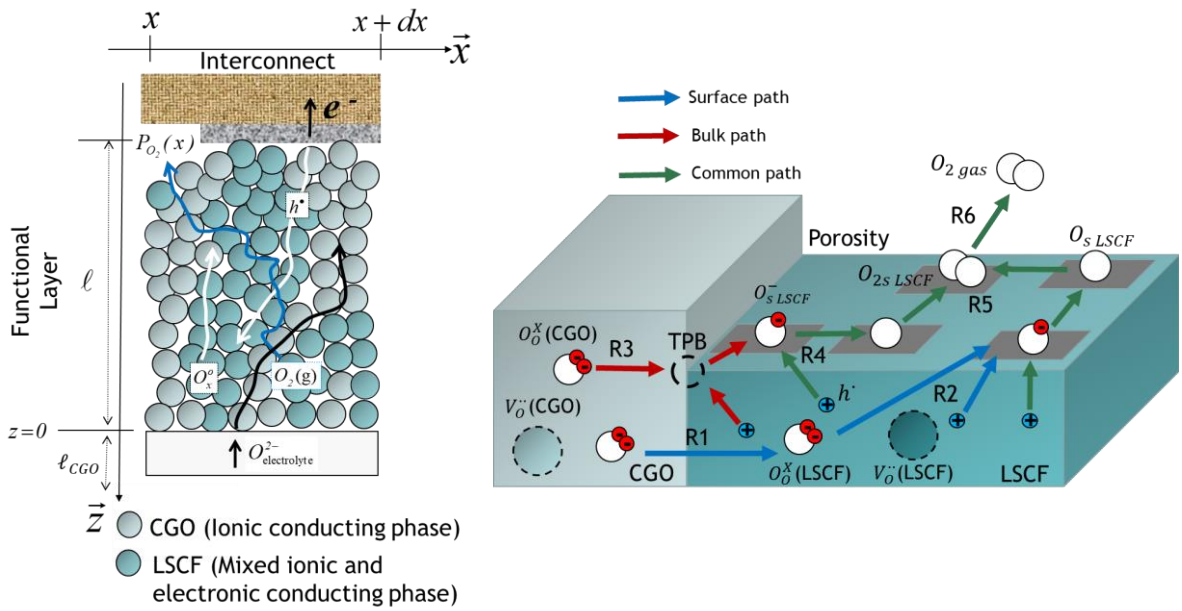

Fig. III-1 (a) Electrode slice considered for the LSCF-CGO model with the system of coordinates. (b) Schematic description of the two reaction pathways implemented in the elementary kinetic model. The “bulk path” and the “surface path” are represented with blue and red arrows, respectively, the “common path” with green arrows. The reaction mechanism is represented to occur in electrolysis mode.

Table V. Reactions and expressions of the kinetic rates (cf. list of symbols).

Electrode			
N°	**Reaction mechanisms**	**Kinetic rates**	
R1	$O_o^x(CGO) + V_o^{\bullet\bullet}(LSCF) \underset{k_-}{\overset{k_+}{\leftrightarrow}} O_o^x(LSCF) + V_o^{\bullet\bullet}(CGO)$	$\nu_{(1)} = S_p^{CGO/LSCF}\left\{k_+ exp\left(\frac{2\alpha_{(1)}^{ox}FE}{RT}\right)\left(\frac{C_{V_o^{\cdot\cdot}}}{C_{O_o^x}^{max}}\right) - k_- exp\left(\frac{-2\alpha_{(1)}^{red}FE}{RT}\right)\left(\frac{C_{O_o^x}^{max} - C_{V_o^{\cdot\cdot}}}{C_{O_o^x}^{max}}\right)\right\}$	(1)
R2	$O_o^x(LSCF) + 1h^{\bullet} + 1s_{LSCF} \underset{k_{red}^{LSCF/gas}}{\overset{k_{ox}^{LSCF/gas}}{\leftrightarrow}} V_o^{\bullet\bullet}(LSCF) + O^- - s_{LSCF}$	$\nu_{(2)} = S_p^{LSCF/gas}\left\{k_{ox}^{LSCF/gas} exp\left(\frac{\alpha_{(2)}^{ox}F\chi}{RT}\right)((C_{O_o^x}^{max} - C_{V_o^{\cdot\cdot}})\Gamma\theta_{s_{LSCF}}) - k_{red}^{LSCF/gas} exp\left(\frac{-\alpha_{(2)}^{red}F\chi}{RT}\right)(\Gamma\theta_{O^- - s_{LSCF}}C_{V_o^{\cdot\cdot}})\right\}$	(2)
R3	$O_o^x(CGO) + 1h^{\bullet} + 1s_{LSCF} \underset{k_{red}^{TPBls}}{\overset{k_{ox}^{TPBls}}{\leftrightarrow}} O^- - s_{LSCF} + V_o^{\bullet\bullet}(CGO)$	$\nu_{(3)} = \xi_{TPBs}\left\{k_{ox}^{TPBls} exp\left(\frac{\alpha_{(3)}^{ox}FE}{RT}\right)\Gamma\theta_{s_{LSCF}} - k_{red}^{TPBls} exp\left(\frac{-\alpha_{(3)}^{red}FE}{RT}\right)\Gamma\theta_{O^- - s_{LSCF}}\right\}$	(3)
R4	$O^- - s_{LSCF} + 1h^{\bullet} \underset{k_{ion}}{\overset{k_{deion}}{\leftrightarrow}} O - s_{LSCF}$	$\nu_{(4)} = S_p^{LSCF/gas}\left\{k_{deion} exp\left(\frac{\alpha_{(4)}^{ox}F\chi}{RT}\right)(\Gamma\theta_{O^- - s_{LSCF}}) - k_{ion} exp\left(\frac{-\alpha_{(4)}^{red}F\chi}{RT}\right)(\Gamma\theta_{O - s_{LSCF}})\right\}$	(4)
R5	$2O - s_{LSCF} \underset{k_{diss}}{\overset{k_{ass}}{\leftrightarrow}} O_2 - s_{LSCF} + 1s_{LSCF}$	$\nu_{(5)} = S_p^{LSCF/gas}\{k_{ass}\Gamma^2\theta_{O - s_{LSCF}}{}^2 - k_{diss}\Gamma^2\theta_{O_2 - s_{LSCF}}\theta_{s_{LSCF}}\}$	(5)
R6	$O_2 - s_{LSCF} \underset{k_{ads}}{\overset{k_{des}}{\leftrightarrow}} O_2(gas) + 1s_{LSCF}$	$\nu_{(6)} = S_p^{LSCF/gas}\{k_{des}\Gamma\theta_{O_2 - s_{LSCF}} - k_{ads}P_{O_2}\Gamma\theta_{s_{LSCF}}\}$	(6)

3.1.3 Kinetic rates and transport phenomena

Expression for the kinetic rates – As shown in Tab. V for Eqs. (1-6), all the kinetic rates $\nu_{(i)}$ have been expressed as the difference between the forward and backward reactions. It can be noticed that the charge transfer at TPBls (R3) is an electrochemical reaction and its kinetic depends on the

local electrode potential *E(z)* through the classical Butler-Volmer equation (Eq. (3)). Even if there is no change in the oxidation state between the products and reactants for the ionic transfer R1, this reaction is still supposed to be affected by the electrode potential at the LSCF/CGO interface. Its kinetic is thus written using a Butler-Volmer formalism as reported in Eq. (1) [Laurencin2015]. The oxidation/reduction steps (R2 and R4) arising at the LSCF surface are two electrochemical reactions and their kinetic rates are also assumed to be affected by the surface potential step $\chi(z)$ (cf. Eqs. (2) and (4)) [Fleig2007]. Finally, the association and desorption steps (R5 and R6) are pure chemical reactions and their kinetics is written in classical way (Eqs. (5) and (6)). The activity for all the surface species *i* is given by the product of the number of available sites on the LSCF surface Γ and the surface coverage θ_i considering an ideal solution. In other words, a Langmuir isothermal hypothesis is adopted assuming a monolayer of adsorbed species on the LSCF surface without interaction:

$$\theta_{O^- - s_{LSCF}} + \theta_{O - s_{LSCF}} + \theta_{O_2 - s_{LSCF}} + \theta_{s_{LSCF}} = 1 \quad (9)$$

where the subscripts $O^- - s_{LSCF}$, $O - s_{LSCF}$ *and* $O_2 - s_{LSCF}$ denote the oxygen ad-ions, neutral ad-atoms and ad-molecules.

All the kinetics have been multiplied by the corresponding microstructural parameter in order to take into account the local geometry of the porous electrode. Therefore, the velocity for all the surface steps is dependent on the LSCF/gas specific surface area. The rate for the reaction R3 occurring at the gas, LSCF and CGO triple line is proportional to the TPBls density while the one for the ionic transfer R1 is scaled by the LSCF/CGO interfacial specific surface area. Finally, it is worth noting that all the reactions are supposed to be thermally activated. The kinetic constant k_i in Table V are thus dependent on the temperature according to a classical Arrhenius' law:

$$k_i = \mathrm{k}_{0,i} exp\left(-\frac{E_{act,i}}{RT}\right) \quad (10)$$

where $E_{act,i}$ is the activation energy for the reaction *i*.

Expressions for the mass and charge transfers – Regarding the transport phenomena, the fluxes of the surface species follow a classical Fick's law according to Eqs. (13-15) in Table VI. The oxygen vacancies transport in the LSCF network (cf. Eq. (12)) is also expressed as a pure diffusional process through a chemical diffusivity depending on the oxygen partial pressure [Elshof1997]:

$$D_{chem} = -\frac{D_{V_O^{\bullet\bullet}}}{2}\frac{\partial(\ln P_{O_2})}{\partial(\ln C_{V_O^{\bullet\bullet}})} \quad (27)$$

where $D_{V_O^{\bullet\bullet}}$ is the oxygen vacancy self-diffusivity and $\frac{\partial(\ln P_{O_2})}{\partial(\ln C_{V_O^{\bullet\bullet}})}$ is the thermodynamic factor.

The thermodynamic factor is calculated using the dependence of the oxygen under-stoichiometry with the oxygen partial pressure measured in [Bouwmeester2004] by thermogravimetry on the studied $La_{0.6}Sr_{0.4}Co_{0.2}Fe_{0.8}O_{3-\delta}$ compound.

The gas transport in the porosities is simulated in the frame of the dusty gas model (DGM) combining a molecular and Knudsen diffusion (Eq. (16)). The binary coefficient D_{O_2,N_2} for the molecular diffusion is expressed according to Fuller's Theory while the Knudsen coefficient D_{k,O_2} is proportional to the mean pore radius $\bar{r}_{pores}$:

$$D_{O_2,N_2} = \frac{0.00143}{P_{tot}\cdot\left(\left(V_{O_2}\right)^{1/3}+\left(V_{N_2}\right)^{1/3}\right)^2\cdot\sqrt{\frac{2}{\frac{1}{M_{O_2}}+\frac{1}{M_{N_2}}}}}\cdot T^{1.75} \quad (28)$$

$$D_{k,O_2} = \bar{r}_{pores}\cdot\frac{2}{3}\sqrt{\frac{8\cdot RT}{\pi M_i}} \quad (29)$$

where M_i is the molar mass for the gas species and V_i the Fuller diffusion volume tabulated in [Todd2002].

Finally, the ionic and electronic currents obey to the classical Ohm's law for LSCF and CGO in the electrode (Eqs. (11) and (17)) and for the CGO barrier layer as well (Eq. (18)). To account for the effect of microstructure in the electrode, the intrinsic diffusivities and conductivities are corrected by the ratio of the phase volume fraction to the tortuosity factor to express the effective properties ($D_i^{eff} = (\varepsilon_i/\tau_i)D_i$ and $\sigma_i^{eff} = (\varepsilon_i/\tau_i)\sigma_i$).

All the surface and oxygen vacancies diffusions together with the ionic conduction in CGO are supposed to be thermally activated and expressed using an Arrhenius' law. The temperature dependence for the LSCF electronic conduction has been neglected while its evolution with the oxygen partial pressure has been taken into account in the model as follows [Laurencin2015]:

$$\sigma_{h^{\bullet}_{LSCF}} = \sigma_0 \left(P_{O_2}\right)^n \quad (30)$$

where n is an exponent that can depend on the P_{O_2} [Lane2000].

A set of mass and charge balance equations (Tab. VI) was written for each species in the electrode and in the electrolyte. Each equation is formed by source/sink terms that consider the reaction rates for which the species is formed (positive sign) or consumed (negative sign). Moreover, a transient term is added to allow simulating the time-dependent response of the electrode. For the vacancies in LSCF and the adsorbed species, this temporal term is associated to the transient storage in the considered phase (Eqs. (20-24)). Regarding the charge balance for the ionic and electronic currents, the temporal term is related to the charging/discharging effect of the capacitor associated to the double layer at the LSCF/CGO interface (Eqs. (19) and (25)).

Lastly, the impact of the gas conversion in the EIS diagrams was also considered in the model. For this purpose, the gas channel is modeled as a Continuous Stirred Tank Reactor (CSTR) for which the inlet and outlet fluxes are linked according to the following mass balance [Bessler2006, Donazzi2020]:

$$V_{CSTR}\frac{dC_{O_2}(z=\ell)}{dt} = F_{Tot}^{inlet}\cdot y_{O_2}^{inlet}(z=\ell) - F_{Tot}^{outlet}\cdot y_{O_2}(t,z=\ell) \pm \left|\vec{N}_{O_2}(t,z=\ell)\right| \times S_{el.} \quad (31)$$

where $\left|\vec{N}_{O_2}(t,z=\ell)\right|$ is the oxygen flux taken at the top of the electrode while V_{CSTR} represents the volume of the CSTR. The terms F_{Tot}^{inlet} and F_{Tot}^{outlet} denote the inlet and outlet fluxes for the gas channel, respectively.

In the chosen model, these latter terms have been assumed independent of time and calculated using the stationary version of the model (i.e. $F_{Tot}^{outlet}\cdot y_{O_2}(z=\ell) = F_{Tot}^{inlet}\cdot y_{O_2}^{inlet}(z=\ell) \pm \left|\vec{N}_{O_2}(z=\ell)\right| \times S_{el.}$) [Yurkiv2014]. It is worth noting that this approach can be considered valid only if the concentration overpotentials are limited (that is to say at OCP or under small dc current with a high inlet oxygen flux as considered in the experiments). Otherwise, a 2D model description constituted by a series of electrode slices would be required to account the oxygen partial pressure evolution along the electrode length [Bessler2006].

Table VI. Equations of charge and mass conservations associated to the current and the fluxes taken into account in the physically-based model together with the expression of the transport phenomena (given for the LSCF-CGO electrode).

Electrode			
Transport phenomena (fluxes)		**Conservation equations**	
$\vec{i}_{io} = -\frac{\varepsilon_{CGO}}{\tau_{CGO}}\sigma_{io,CGO}\times\vec{\nabla}\varphi_{CGO}$	(11)	$\vec{\nabla}\cdot\vec{i}_{io} = +2F(\nu_{(1)}+\nu_{(3)}) - S_p^{CGO/LSCF}C_{dl}^{CGO/LSCF}\frac{\partial E}{\partial t}$	(19)
$\vec{N}_{V_o^{\bullet\bullet}} = -\frac{\varepsilon_{LSCF}}{\tau_{LSCF}}\tilde{D}_{chem}\times\vec{\nabla}C_{V_o^{\bullet\bullet}}$	(12)	$\vec{\nabla}\cdot\vec{N}_{V_o^{\bullet\bullet}} = (\nu_{(2)} - \nu_{(1)}) - \varepsilon_{LSCF}\frac{\partial C_{V_o^{\bullet\bullet}}(z,t)}{\partial t}$	(20)
$\vec{N}_{O\text{-}s_{LSCF}} = -S_p^{LSCF/gas}D_{O-s_{LSCF}}\Gamma\times\vec{\nabla}\theta_{O-s_{LSCF}}$	(13)	$\vec{\nabla}\cdot\vec{N}_{O-s_{LSCF}} = (\nu_{(4)} - 2\nu_{(5)}) - S_p^{LSCF/gas}\Gamma\frac{\partial\theta_{O-s_{LSCF}}(z,t)}{\partial t}$	(21)
$\vec{N}_{O^{-}\text{-}s_{LSCF}} = -S_p^{LSCF/gas}D_{O^{-}-s_{LSCF}}\Gamma\times\vec{\nabla}\theta_{O^{-}-s_{LSCF}}$	(14)	$\vec{\nabla}\cdot\vec{N}_{O^{-}-s_{LSCF}} = (\nu_{(2)}+\nu_{(3)} - \nu_{(4)}) - S_p^{LSCF/gas}\Gamma\frac{\partial\theta_{O^{-}-s_{LSCF}}(z,t)}{\partial t}$	(22)
$\vec{N}_{O_2\text{-}s_{LSCF}} = -S_p^{LSCF/gas}D_{O_2-s_{LSCF}}\Gamma\times\vec{\nabla}\theta_{O_2-s_{LSCF}}$	(15)	$\vec{\nabla}\cdot\vec{N}_{O_2-s_{LSCF}} = (\nu_{(5)} - \nu_{(6)}) - S_p^{LSCF/gas}\Gamma\frac{\partial\theta_{O_2-s_{LSCF}}(z,t)}{\partial t}$	(23)
$\vec{\nabla}y_{O_2} = -\frac{RT}{P_t}\frac{\tau_{pores}}{\varepsilon_{pores}}\left(\frac{\vec{N}_{O_2}}{D_{k,O_2}} + \frac{\vec{N}_{O_2}y_{N_2}}{D_{O_2,N_2}}\right)$	(16)	$\vec{\nabla}\cdot\vec{N}_{o_2} = \nu_{(6)} - \frac{\varepsilon_{pores}}{RT}P_t\frac{\partial y_{O_2}(z,t)}{\partial t}$	(24)
$\vec{i}_{e^-} = -\frac{\varepsilon_{LSCF}}{\tau_{LSCF}}\sigma_{h^{\bullet}_{LSCF}}\times\vec{\nabla}\varphi_{LSCF}$	(17)	$\vec{\nabla}\cdot\vec{i}_{e^-} = -F(\nu_{(2)}+\nu_{(3)}+\nu_{(4)}) + S_p^{CGO/LSCF}C_{dl}^{CGO/LSCF}\frac{\partial E}{\partial t}$	(25)
Electrolyte			
$\vec{i}_{io} = -\sigma_{io,CGO}\times\vec{\nabla}\varphi_{CGO}$	(18)	$\vec{\nabla}\cdot\vec{i}_{io} = 0$	(26)

3.1.4 Thermodynamic description

In the model, the forward and backward kinetic constants for each reaction are linked through the thermodynamic equilibrium constant according to the set of equations reported in Table VII. In Eq. (33), it can be noticed that the superficial potential step at equilibrium χ^{eq} is proportional to the coverage rate of the oxygen ions at equilibrium $\theta_{O^{2-}-s_{LSCF}}^{eq}$ according to Eq. (7) (i.e. $\chi^{eq} = \left(\Gamma F \theta_{O^{2-}-s_{LSCF}}^{eq}\right)/\left(C_{dl}^{\text{surface}}\right)$) [Fleig2005]. Moreover, the electrode potential at equilibrium E^{eq} in Eqs. (32) and (34) is equal to the chemical potential of oxygen in the gas phase taken at the reference electrode (i.e. $E^{eq} = \frac{\tilde{\mu}_{O_2(gas)}^{ref}}{4F}$ knowing that $E_{WE}^{eq}(V/Ref) \approx 0$ [Monaco2021]).

The equilibrium constants were not directly calculated from the thermodynamic data since there is still a large uncertainty on the entropies and enthalpies especially for the attached species on LSCF [Choi2010, Yurkiv2014]. As a consequence, the surface coverage at equilibrium ($\theta_{O^{2-}-s_{LSCF}}^{eq}$, $\theta_{O-s_{LSCF}}^{eq}$ and $\theta_{O_2-s_{LSCF}}^{eq}$) were considered as model inputs parameters at P_{O_2} = 0.21 atm and thus fitted using the dc experimental data. Furthermore, they were supposed to be independent on the temperature. This last assumption is rather well justified considering the low surface coverage assumed in Eq. (7) by neglecting the surface site restriction. Once the surface coverage of the three adsorbed species fitted at P_{O_2}= 0.21 atm, the thermodynamic constants for the surface reactions $K_e^{(4)}$, $K_e^{(5)}$ and $K_e^{(6)}$ were determined.

To compute the composition at equilibrium, the concentration of oxygen vacancies $C_{V_O^{\cdot\cdot}}^{eq}$ was determined as a function of the temperature and the oxygen partial pressure using the oxygen under-stoichiometry δ and the pseudo cubic lattice parameter for $La_{0.6}Sr_{0.4}Co_{0.2}Fe_{0.8}O_{3-\delta}$ taken from Bouwmeester *et al.* [Bouwmeester2004] and Hashimoto *et al.* [Hashimoto2011], respectively. Besides, using the previously determined constants $K_e^{(4)}$, $K_e^{(5)}$ and $K_e^{(6)}$, the system of Eqs. (35-37) were solved numerically to compute the evolutions of $\theta_{O^{2-}-s_{LSCF}}^{eq}$, $\theta_{O-s_{LSCF}}^{eq}$ and $\theta_{O_2-s_{LSCF}}^{eq}$ as a function of the oxygen partial pressure.

Finally, the determination of the thermodynamic constants $K_e^{(1)}$, $K_e^{(2)}$ and $K_e^{(3)}$, involving bulk species, were calculated with Eqs. (32-34) using the data at equilibrium.

Table VII. Equations of the thermodynamic equilibrium constants (cf. List of symbols).

N°	Thermodynamic equilibrium constants				
R1	$K_e^{(1)} = \frac{C_{O_O^x}^{max} - C_{V_O^{\cdot\cdot}}^{eq}}{C_{V_O^{\cdot\cdot}}^{eq}} exp\left(\frac{-2FE^{eq}}{RT}\right)$	(32)	R4	$K_e^{(4)} = \frac{\theta_{O-s_{LSCF}}^{eq}}{\theta_{O^{--}s_{LSCF}}^{eq}} exp\left(\frac{-F\chi^{eq}}{RT}\right)$	(35)
R2	$K_e^{(2)} = \frac{\theta_{O^{--}s_{LSCF}}^{eq} C_{V_O^{\cdot\cdot}}^{eq}}{\theta_{s_{LSCF}}^{eq}(C_{O_O^x}^{max} - C_{V_O^{\cdot\cdot}}^{eq})} exp\left(\frac{-F\chi^{eq}}{RT}\right)$	(33)	R5	$K_e^{(5)} = \frac{\theta_{s_{LSCF}}^{eq}}{(\theta_{O_2-s_{LSCF}}^{eq} \theta_{O-s_{LSCF}}^{eq})^2}$	(36)
R3	$K_e^{(3)} = \frac{\theta_{O^{--}s_{LSCF}}^{eq}}{\theta_{s_{LSCF}}^{eq}} exp\left(\frac{-FE^{eq}}{RT}\right)$	(34)	R6	$K_e^{(6)} = \frac{\theta_{s_{LSCF}}^{eq} P_{O_2}^{eq}}{\theta_{O_2-s_{LSCF}}^{eq}}$	(37)

3.1.5 Boundary conditions and input parameters

The thermodynamic computation allows obtaining the equilibrium constants used to express the backward kinetic constants and the composition at equilibrium used as initial values for the time dependent simulations. For the kinetic computation, the charge and mass balances (Eqs. (19-26) and Eq. (31)) combined with the expressions for the fluxes (Eqs. (11-18)) and the reaction rates (Eqs. (1-6)) constitute a set of Partial Differential Equations (PDEs) which are solved in the time domain by Finite Element Method (FEM). The methodology for the calculations of the EIS diagrams has been already described [Hubert2016].

For a sake of clarity, the boundary conditions are only summarized hereafter for the LSFC-CGO composite electrode model. On the one hand, the ionic current is imposed in the barrier layer and is nil at the top of the electrode: $i_{io}(z = 0) = \text{imposed}$; $i_{io}(z = \ell_{CGO} + \ell) = 0$. On the other, the electronic potential in LSCF is taken at zero at the top of the electrode while the electronic current is nil at the interface with the barrier layer: $\varphi_{el}(z = \ell_{CGO} + \ell) = 0$; $i_{el}(z = \ell_{CGO}) = 0$. The flux of vacancies in LSCF is equal to zero on each side of the electrode: $\vec{N}_{V_O^{\cdot\cdot}}(z = \ell_{CGO}) = \vec{N}_{V_O^{\cdot\cdot}}(z = \ell_{CGO} + \ell) = 0$ and the fluxes for all the adsorbed species on LSCF are nil on each side of the electrode: $\vec{N}_{i\text{-}s_{LSCF}}(z = \ell_{CGO}) = \vec{N}_{i\text{-}s_{LSCF}}(z = \ell_{CGO} + \ell) = 0$. Finally, the oxygen gas flux is

imposed at the inlet of the gas channel and is nil at the barrier layer interface: $F_{O_2}^{inlet}(z = \ell_{CGO} + \ell) = imposed; \vec{N}_{O_2}(z = \ell_{CGO}) = 0$.

Regarding the input parameters for the simulations, all the microstructural properties were extracted from the 3D reconstructions (cf. section 4.1). The gas diffusivities were evaluated with Eqs. (28) and (29)) while the electronic conductivity in the LSCF was estimated with Eq. (30). In this case, the exponent *n* was considered to vary from *n* = + 1/5 to *n* = + 1/20 according to the data reported by Lane and Kilner [Lane2000]. The evolution of CGO ionic conductivity with the temperature was determined in the model using an activation energy of 65 kJ·mol^{-1} [Takana2012]. The oxygen vacancy self-diffusivity for LSCF was taken in order to obtain a chemical diffusivity of 3.7·10^{-10} m^2·s^{-1} at 700 °C under air with an activation energy of 156 kJ·mol^{-1}. It can be noticed that these values are consistent with data reported in the literature [Bouwmeester2014, Yashiro2011]. The capacitance of the LSCF/CGO double layer was taken at 0.5 F·m^{-2} as estimated by Monaco *et al.* [Monaco2018]. For what concerns the surface capacitance C_{dl}^{surface}, a wide range of data spreading from 0.1 F·m^{-2} up to 100 F·m^{-2} is reported in the literature [Donazzi2020]. In the present model, a low value of 0.2 F·m^{-2} was chosen for the simulations to be consistent with the assumption of the low oxygen ions coverage at the LSCF surface. All the mentioned input parameters are provided in Tab. VIII at the reference temperature of 700 °C at P_{O_2} = 0.21 atm. The microstructural properties of both studied electrodes are reported in Table I.

Table VIII. Model input parameters for the LSCF material given here at 700°C under P_{O_2}=0.21 atm.

Parameter at 700°C, P_{O_2}=0.21 atm	**Value**	**Unit**
Maximum oxygen concentration in the LSCF ($C_{O_O^x}^{max}$)	83108	(mol·m^{-3})
Equilibrium oxygen concentration in the LSCF ($C_{O_O^x}^{eq}$)	82491	(mol·m^{-3})
Electronic conductivity of LSCF ($\sigma_{h^{\bullet}_{LSCF}}$)	33738	(S·m^{-1})
Ionic conductivity of CGO ($\sigma_{io,CGO}$)	2.9	(S·m^{-1})
Density of available adsorption sites (Γ)	1·10x10^{-5}	(mol·m^{-2})
LSCF chemical diffusivity (D_{chem})	3.7 x10^{-10}	(m²·s^{-1})
LSCF/CGO double layer capacitance ($C_{dl}^{LSCF/CGO}$)	0.5	(F·m^{-2})
Surface double layer capacitance ($C_{dl}^{surface}$)	0.2	(F·m^{-2})
Knudsen diffusion coefficient (D_{k,O_2})	535	(m²·s^{-1})
Molecular diffusion coefficient (D_{O_2,N_2})	1.65 x10^{-4}	(m²·s^{-1})
Charge transfer coefficient (α^{ox})	0.5	(-)

In order to reduce further the number of unknown parameters, two supplementary assumptions have been considered. Firstly, as generally observed and admitted for the studied electrodes [Adler2004], the oxygen ionic transfer (R1) across LSCF/CGO interface was supposed as not limiting ($k_+ \gg 0$). In addition, the associative reaction (R5) on the LSCF surface was considered very fast and near the equilibrium as justified by Yurkiv *et al.* [Yurkiv2014] ($k_{ass} \gg 0$).
Finally, the LSCF surface properties including the surface coverages at equilibrium at P_{O_2} = 0.21 atm, the surface diffusivities and the kinetic constants for the surface reactions along with their related activation energies correspond to the missing input parameters fitted on the experimental data (cf. section 3.2.1).

3.1.6 Extension to the Cyclic Voltammetry simulation

The full elementary model for the LSCF electrode has been extended to simulate CV curves. Besides, a numerical version of the semi-analytical ALS-based model proposed by Montella *et al.* [Montella2021] for the CV response of the porous LSCF electrode has also been developed. The comparison between the two approaches will be discussed in section 3.4.3.

ALS-based model – As this semi-analytical model has been already thoroughly detailed in [Montella2021], only a brief description, with the main assumptions, is reminded hereafter. The model considers a 1D homogenous electrode film connected from one side to the electrolyte (z=0) and to the opposite side to the current collector ($z = \ell$) (Fig. III-2a). The oxygen partial pressure is assumed as constant all along the electrode thickness. Therefore, the incorporated oxygen and vacancies in LSCF are the only species that can vary. The reaction mechanism is simply composed by the ionic transfer at the electrode/electrolyte interface (38), followed by a solid-state diffusion coupled with a pure chemical reaction of the oxygen exchange between the gas and LSCF (39) (Fig. III-2b):

$$O^{2-}(electrolyte) + V_o^{\bullet\bullet}(LSCF) \leftrightarrow O_o^x(LSCF) \text{ at the electrolyte interface } (z = 0) \quad (38)$$

$$O_o^x(LSCF) \leftrightarrow V_o^{\bullet\bullet}(LSCF) + 1/2O_2(gas) + 2e^- \text{ in the electrode thickness } (0 < z < \ell) \quad (39)$$

where $O_o^x(LSCF)$ and $V_o^{\bullet\bullet}(LSCF)$ denote the incorporated oxygen and vacancies in LSCF.

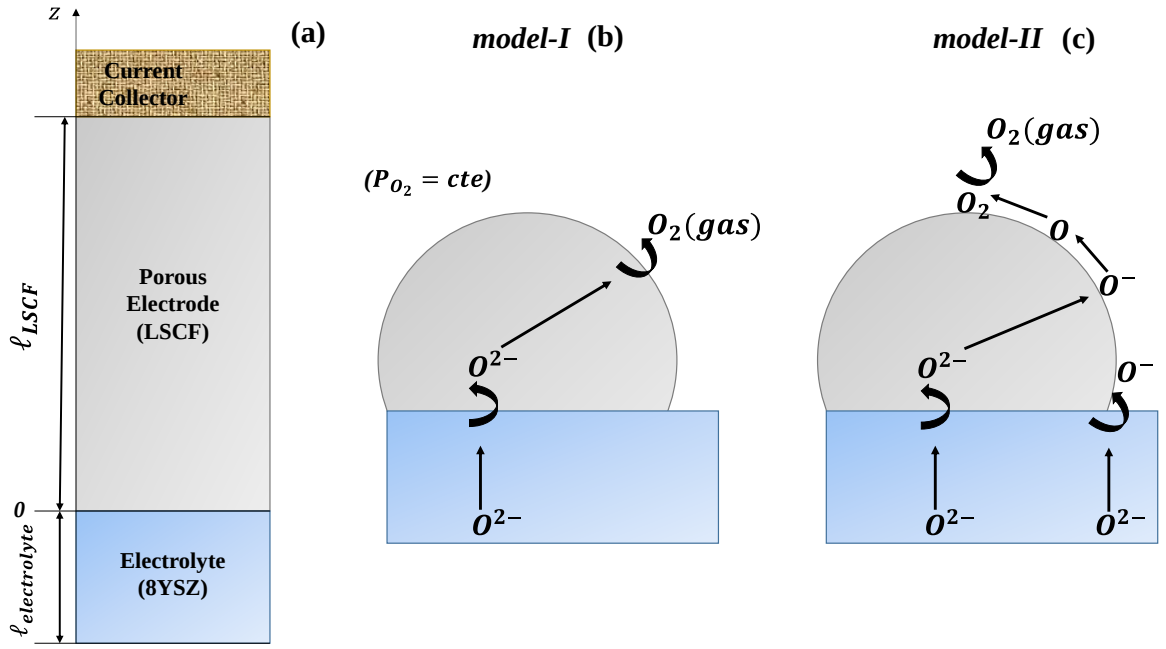

Fig. III-2 Schematic representation of the simulated domain (a) with a focus on the reaction mechanism for *model-I* (b) and *model-II* (c). For the sake of clarity, the electrons have been omitted.

In this approach, the double layer capacitance at electrode/electrolyte interface as well as the Ohmic drop in the electrolyte are neglected. Because of the high operating temperature, the reaction of ionic transfer is considered to occur in a quasi-equilibrium state. This condition allows expressing the concentration of oxygen in LSCF at the electrolyte interface ($z = 0$) through the Nernst's equation (used as a first boundary condition):

$$C_{O_o^x}(0,t) = C_{O_o^x}^{max} / \{1 + exp[-(\xi(t))]\} \quad \text{with} \quad C_{O_o^x}(0,t) = C_{O_o^x}^{max} - C_{V_o^{\bullet\bullet}}(0,t) \qquad (40)$$

where $C_{V_o^{\bullet\bullet}}(0,t)$ and $C_{O_o^x}(0,t)$ represent the time dependent interfacial concentration of vacancies and oxygen in LSCF, respectively, while $C_{O_o^x}^{max}$ is the maximum concentration of oxygen in the material. The dimensionless parameter $\xi(t)$ is related to the electrode potential as follows:

$$\xi(t) = \frac{2F}{RT}(E(t) - E^0) \qquad (41)$$

where F is the Faraday's constant, R the universal gas constant and T the absolute temperature. The terms $E(t)$ and E^0 are referred as the time-dependent electrode potential and the standard potential,

respectively. It is worth noting that equilibrium conditions are supposed to be fulfilled at t = 0 in such a way that $C_{O_o^x}^{eq} = C_{O_o^x}(z,0)$, $E^{eq} = E(0)$ and $\xi^{eq} = \xi(0)$.

The kinetic rate for the oxygen exchange reaction between the electrode and the gas phase is written as a function of the incorporation level:

$$v_{chem}(z,t) = S_p^{LSCF}\, k_{chem} \left(C_{o_o^x}(z,t) - C_{O_o^x}^{eq}\right) \text{ for } 0 < z < \ell \tag{42}$$

where k_{chem} and S_p^{LSCF} are the chemical exchange rate constant and the electrode specific surface area, respectively. The flux of oxygen in the LSCF bulk is expressed with the classical Fick's law:

$$J_{o_o^x}(\mathrm{z,t}) = -\frac{\varepsilon_{LSCF}}{\tau_{LSCF}} D_{chem} \frac{\partial C_{O_o^x}(z,t)}{\partial z} \text{ for } 0 < z < \ell \tag{43}$$

where D_{chem}, ε_{LSCF} and τ_{LSCF} are related to the chemical diffusivity, the volume fraction and the tortuosity factor for the LSCF phase, respectively. The flux $J_{o_o^x}(z,t)$ is considered to be nil at the top of the electrode ($z = \ell$) (condition used as the second boundary condition). The two last equations are combined in the mass balance for the oxygen in LSCF. In other words, the local variation in the flux is controlled by the kinetic rate of the oxygen exchange reaction together with a dynamic term related to the transient accumulation/depletion of oxygen in LSCF:

$$\frac{\partial J_{O_o^x}(z,t)}{\partial z} = -v_{chem}(z,t) - \varepsilon_{LSCF} \frac{\partial C_{O_o^x}(z,t)}{\partial t} \text{ for } 0 < z < \ell \tag{44}$$

The Faradaic current density is derived from the interfacial diffusion and it is calculated at the electrode/electrolyte interface as follows:

$$j_{e^-}(0,t) = 2F \frac{\varepsilon_{LSCF}}{\tau_{LSCF}} D_{chem} \frac{\partial C_{o_o^x}(z,t)}{\partial z}\Big]_{z=0} \tag{45}$$

By combining Eqs. (42-45) with the two boundary conditions, it is possible to derive an explicit semi-analytical solution for the CV response, expressed through the following equation [Montella2021]:

$$j_{e^-}(t) = 2F C_{O_o^x}^{max} \cdot \mathcal{L}^{-1}\left(\frac{1}{s \cdot M(s)}\right) * \frac{dh[\xi(t)]}{dt} \tag{46}$$

where the symbol $(*)$ denotes the convolution product, $\mathcal{L}$ is the Laplace transform operator and s is the Laplace variable. The term $M(s)$ is the so-called 'mass transfer function', defined as the ratio

in the Laplace domain between the incremental changes of oxygen concentration and flux at the electrolyte interface ($M(s) = \mathcal{L}\Delta C_{O_o^x}(x = 0, t)/\mathcal{L}\Delta J_{O_o^x}(x = 0, t)$). The term $h[\xi(t)]$ is referred as the potential-dependent function that depends on the controlled-potential technique ($h[\xi(t)] = \frac{1}{1+exp(-\xi(t))} - \frac{1}{1+exp(-\xi^{eq})}$).

In order to simplify the analyses, the electrochemical input parameters are replaced by dimensionless variables. In this approach, the chemical rate constant k_{chem} and the electrode thickness ℓ_{LSCF} are respectively substituted by the dimensionless parameters λ and L, as follows:

$$\lambda = \frac{S_p^{LSCF} k_{chem}}{2f\nu\varepsilon_{LSCF}} \tag{47}$$

$$L = \ell_{LSCF}\left(\frac{2f\nu}{D_{chem}/\tau_{LSCF}}\right)^{1/2} \tag{48}$$

where ν is the imposed scan rate for the voltammetry computation and $f = F/(RT)$. In function of these two variables, it is possible to build the so-called 'zone diagram' as detailed in [Montella2021]. By imposing limit conditions on λ and L, specific shapes of the cyclic voltammograms can be obtained with simplified closed-form expressions for the dimensionless current density. Moreover, the type of kinetic and/or mass transport control for the reaction is identified for each individual limiting zone. It is worth mentioning that the zone diagram reported in [45] is plotted for LSV starting in the cathodic direction for the special case where $\xi^{eq} \to \infty$. This hypothesis means that a full oxygen occupation in LSCF is reached at equilibrium (i.e. $\delta \to 0$ and $C_{O_o^x} \to C_{O_o^x}^{max}$).

In order to investigate the impact of the Ohmic loss in the electrolyte on the CV response, the assumptions listed before have been taken into account to propose a numerical version of the ALS-based model. However, some slight differences have to be underlined. In the numerical version, the CV simulations have been performed starting at OCP, corresponding to $\xi_{eq} = 4.896$. Nevertheless, the condition $\xi^{eq} \to \infty$ is almost fulfilled, as the concentration of oxygen at OCP differs by less than 1% from the maximum concentration in LSCF in the chosen experimental conditions [Hashimoto2011]. Moreover, the Nernst's equation at the electrode/electrolyte interface

has been replaced with a fast and non-limiting reaction of ionic transfer (Eq. (38)). In this condition, the expression of the oxygen concentration at the interface given in Eq. (40) is still satisfied. This alternative expression for Eq. (40) has been adopted in order to introduce in the model a description of the electrolyte. In this case, the oxygen migration in the electrolyte is modeled using a classical Ohm's law. This numerical version of the ALS-based model is referred as '*model-I*' thereafter.

Elementary numerical model extension– The full elementary model for the description of the LSCF electrode described above has been extended to simulate the CV curves as well.

In contrast to the ALS-based model, it can be noticed that the charging/discharging effect of the double layer capacitance at the LSCF/CGO interface was taken into account. It must also be emphasized that the set of partial differential equations related to the mass and charge balances are solved in the time domain by keeping the full nonlinearity of the system. Therefore, the model can be directly employed for the CV simulation. In this case, the difference in electronic potential at the top of the electrode, $\varphi_{e^-}(z = \ell_{LSCF})$ and ionic potential in the electrolyte, $\varphi_{io}(z = -\ell_{electrolyte})$ (i.e. $\varphi_{e^-}(z = \ell_{LSCF}) - \varphi_{io}(z = -\ell_{electrolyte}) \approx -\varphi_{io}(z = -\ell_{electrolyte})$), varies with a triangular waveform starting from OCP:

$$\varphi_{io}(t, z = -\ell_{electrolyte}) = 0 \pm wv(t) \tag{49}$$

where $\ell_{electrolyte}$ is the electrolyte thickness. The term $wv(t)$ is the wave function, which depends on the chosen demi-amplitude A and angular frequency ω. The scan rate was changed in the simulation by varying the period T_w of the wave function ($\omega = 2\pi/T_w$).

Since the full elementary model has shown a very good agreement between the simulations and the experiments without any additional fitting (both in terms of polarization curves and impedance diagrams), it is considered as a reliable representation of the LSCF electrochemical behavior. Therefore, this predictive model has been used for the extension of the cyclic voltammetry without any adaption of the input parameters, knowing that the same type of LSCF electrode has been used for the voltammetry measurements as well.

For the sake of clarity, a comparison of the two reaction mechanisms is reported in Fig. III-2 to highlight the difference between the semi-analytical and full elementary approach in terms of kinetic description. Moreover, in order to distinguish the two numerical versions for the

voltammetry computation, the semi-analytical model is referred as '*model-I*' hereafter, while the extension of the full elementary model is referred as '*model-II*'.

3.2 Elementary model calibration and validation

3.2.1 Model calibration on polarization curves

The unknown parameters for the elementary model (cf. section 3.1.5) were determined by fitting the simulated data on the experimental polarization curves at the three investigated temperatures. In other words, the computed i-η curves have been adjusted on the experimental data through an iterative process. Because of the non-symmetrical shape of the electrode response (especially at 700 °C and 650 °C), it is worth mentioning that this process has led to determine a unique value for each of the missing parameters. The results of the fitting procedure are shown in Fig. III-3a and Fig. III-3b for the LSCF and LSCF-CGO electrodes, respectively. As expected, the calibrated model is able to simulate accurately the shape of the i-η curves at each operating temperature for both studied electrodes.

All the model fitted parameters are reported in Tab. IX. Firstly, it can be noticed that low values were obtained for the surface coverage at equilibrium (for P_{O_2} = 0.21 atm) in good agreement with the assumption of a diluted solution considered for Eq. (46). Moreover, the activation energies for the diffusivities and kinetic constants are quite consistent between the two electrodes. Indeed, a good agreement is found for these fitted parameters with a mismatch of less than 18 % except for the activation energy associated to the charge transfer at TPBls. In this case, the difference increases up to 39 %. Besides, the diffusion coefficients as well as the kinetic constants for the oxygen ionization and adsorption, which are reported in Tab. IX at 700 °C, are also coherent between the two investigated electrodes. However, a discrepancy was found for the excorporation kinetic constant. This unexpected result could be explained by different surface states for LSCF in the two types of electrode affecting the reaction of excorporation/incorporation. Finally, it can be noticed that the kinetic constants for the charge transfer at TPBls cannot be compared since they do not have the same dimension. As a general matter, in spite of some differences, it can be claimed that the parameters fitted on the i-η curves are consistent between the LSCF and LSCF-CGO electrodes.

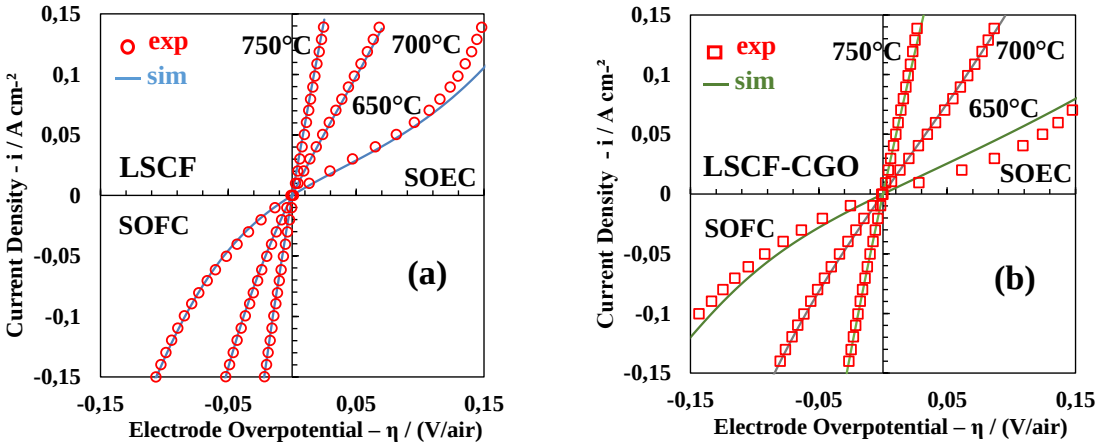

Fig. III-3 Experimental and simulated i-η curves under air for (a) the LSCF and (b) the LSCF-CGO electrode, respectively.

Table IX. Model parameters fitted on the i-V curves for LSCF and LSCF-CGO electrodes at 700 °C.

Parameters at 700°C	**LSCF**			**LSCF-CGO**		
Diffusivities	**Value**	**Unit**	**E_{act} (kJ·mol^{-1})**	**Value**	**Unit**	**E_{act} (kJ·mol^{-1})**
Diffusion coefficient of the oxygen ad-ions ($D_{O^- - s_{LSCF}}$)	9x10^{-8}	(m²·s^{-1})	184	4x10^{-7}	(m²·s^{-1})	218
Diffusion coefficient of the oxygen ad-atoms ($D_{O-s_{LSCF}}$)	3x10^{-7}	(m²· s^{-1})	153	3x10^{-7}	(m²·s^{-1})	153
Diffusion coefficient of the oxygen ad-molecules ($D_{O_2-s_{LSCF}}$)	3x10^{-7}	(m²·s^{-1})	153	3x10^{-7}	(m²·s^{-1})	153
Kinetic constants	**Value**	**Unit**	**E_{act} (kJ·mol^{-1})**	**Value**	**Unit**	**E_{act} (kJ·mol^{-1})**
Kinetic constant for excorporation $k_{ox}^{LSCF/gas}$	1 x10^{-4}	(m^3·mol^{-1}·s^{-1})	148	2 x10^{-5}	(m^3·mol^{-1}·s^{-1})	149
Kinetic constant for deionization k^{deion}	6.8 x10^4	(s^{-1})	212	5.1 x10^4	(s^{-1})	245
Kinetic constant for desorption k^{des}	2.8 x10^5	(s^{-1})	178	2.8 x10^5	(s^{-1})	178
Kinetic constant for oxidation at TPBls k_{ox}^{TPBls}	2.3 x10^{-3}	(m·s^{-1})	206	4.6 x10^{-5}	(s^{-1})	286
Kinetic constant for charge transfer at LSCF/CGO k_+	NOT LIMITING	(mol · m^{-1}·s^{-1})	-	NOT LIMITING	(mol · m^{-2}·s^{-1})	-
Kinetic constant for association k_{ass}	NOT LIMITING	(m^2·mol^{-1}·s^{-1})	-	NOT LIMITING	(m^2·mol^{-1}·s^{-1})	-
LSCF surface coverage at equilibrium for P_{O_2}= 0.21 atm	Value			Unit		
Oxygen ions coverage at equilibrium $\theta_{O^- - s_{LSCF}}^{eq}$	6 x10^{-3}			(-)		
Oxygen atoms coverage at equilibrium $\theta_{O-s_{LSCF}}^{eq}$	1 x10^{-3}			(-)		
Oxygen molecules coverage at equilibrium $\theta_{O_2-s_{LSCF}}^{eq}$	1 x10^{-4}			(-)		

3.2.2 Model validation

3.2.2.1 Impedance diagrams

In order to validate the model, impedance diagrams were computed in the same conditions of the experiments without any additional fitting. The comparison between the simulated and measured EIS diagrams for the LSCF electrode at OCP is reported in Fig. III-4. From the diagrams represented in Figs. III-4a and III-4b at 650 °C and 700 °C, it can be seen that the model is able to predict quite accurately the shape of the experimental EIS diagrams characterized by a Gerischer type-element (cf. Chapter II). It is worth noting that the agreement between experimental and simulated impedance diagrams in the low frequency range at high temperature (Fig. III-4c) suggests that the CSTR model (Eq. (31)) is well adapted to capture the effect of gas conversion that appears at 750 °C. In Fig. III-5, the impedance diagrams recorded under polarization are compared to the simulated ones at 700 °C. As shown in Fig. III-5a and III-5b, the model is also able to reproduce quite correctly the global shape of the impedance diagrams under cathodic and anodic polarizations. It can be noticed that, in the range of investigated polarizations, the EIS diagrams still exhibit a Gerischer type-element behavior suggesting that the LSCF electrode mechanism remains unchanged in these operating conditions.

The computed and experimental frequency distributions are compared at OCP in Figs. III-4d to III-4f and under polarization at 700 °C in Fig. III-5c and III-5d for the diagrams plotted in the Bode plan. It can be observed that the increase of the peak frequency with the temperature and the polarization is well retrieved with the model. This evolution of the peak frequency at OCP with the temperature and under polarization at 700 °C is explained by a higher contribution of the surface path as detailed in section 3.3.1. Nevertheless, a frequency lag between the simulations and the measurements is obtained for all the diagrams. Indeed, the computed frequency distribution is systematically lower than the experimental one. The precise origin of this frequency shift is still unclear. The disagreement may come from an uncertainty on the determination of the microstructural properties using a 3D reconstruction that could be not fully representative of potential inhomogeneities in the whole electrode volume. Indeed, the electrode microstructure can play a major role on the frequency response of the electrode [Çelikbilek2017, Marinha2011, Nielsen2011,]. Moreover, it could be also mentioned that even a slight change in the bulk to surface ratio for the reaction mechanism could have a strong impact on the simulated frequency distribution

as discussed in section 5.1. Besides, the experimental conditions could affect the measurements of the frequency distribution partially explaining the discrepancy between the simulations and the experimental data.

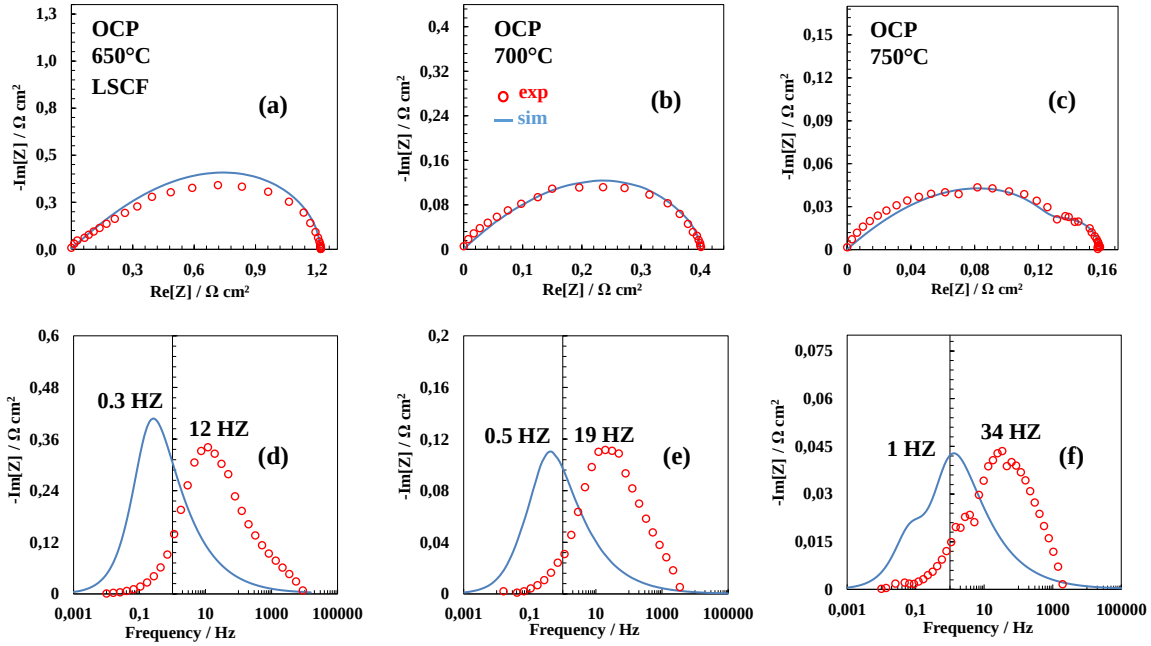

Fig III-4 Experimental and simulated impedance diagrams for the LSCF electrode at OCP. Nyquist plots for (a) 650 °C, (b) 700 °C and (c) 750 °C. Bode plots for (d) 650 °C, (e) 700 °C and (f) 750 °C.

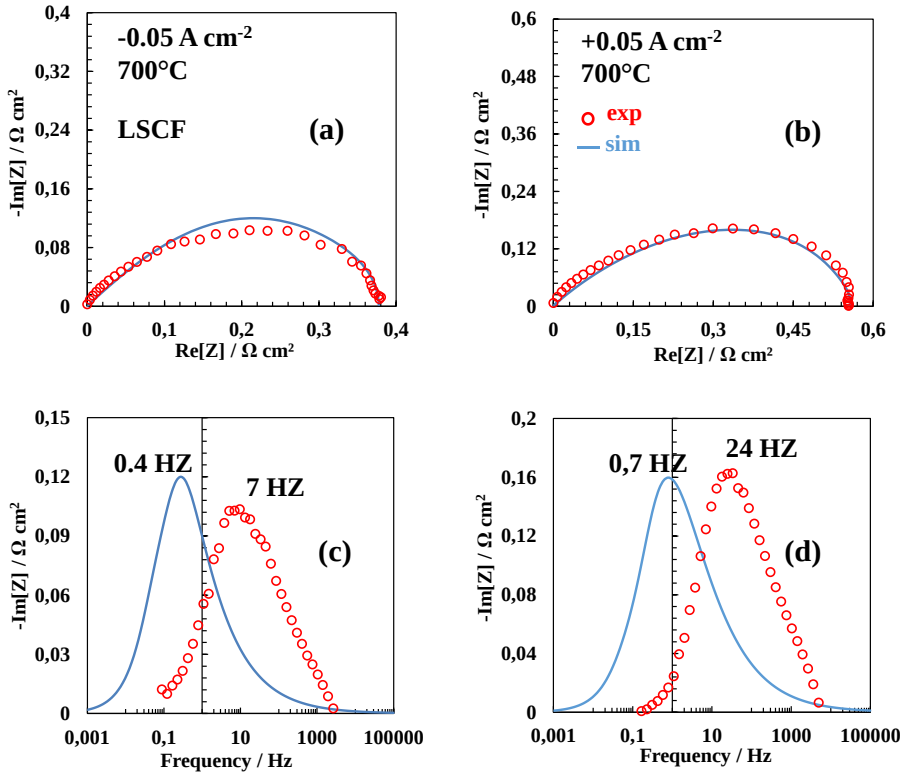

Fig. III-5 Experimental and simulated impedance diagrams for the LSCF electrode at 700 °C for i_{dc} = ± 50 mA cm^{-2}. (a) and (b) Nyquist and (c) and (d) Bode plots.

The same results have been obtained for the LSCF-CGO electrode. The full elementary model is also able to reproduce correctly the shape of the experimental impedance diagrams whatever the temperature or the polarization (Fig. III-6 and Fig. III-7). All the evolutions of the frequency distribution with the operating conditions are also well retrieved with the model even though a frequency shift is also observed for the composite electrode. To conclude, despite the systematic error on the frequency distribution, it can be asserted that, without supplementary fitting, the model is able to predict quite correctly the impedance response for the two types of studied electrodes.

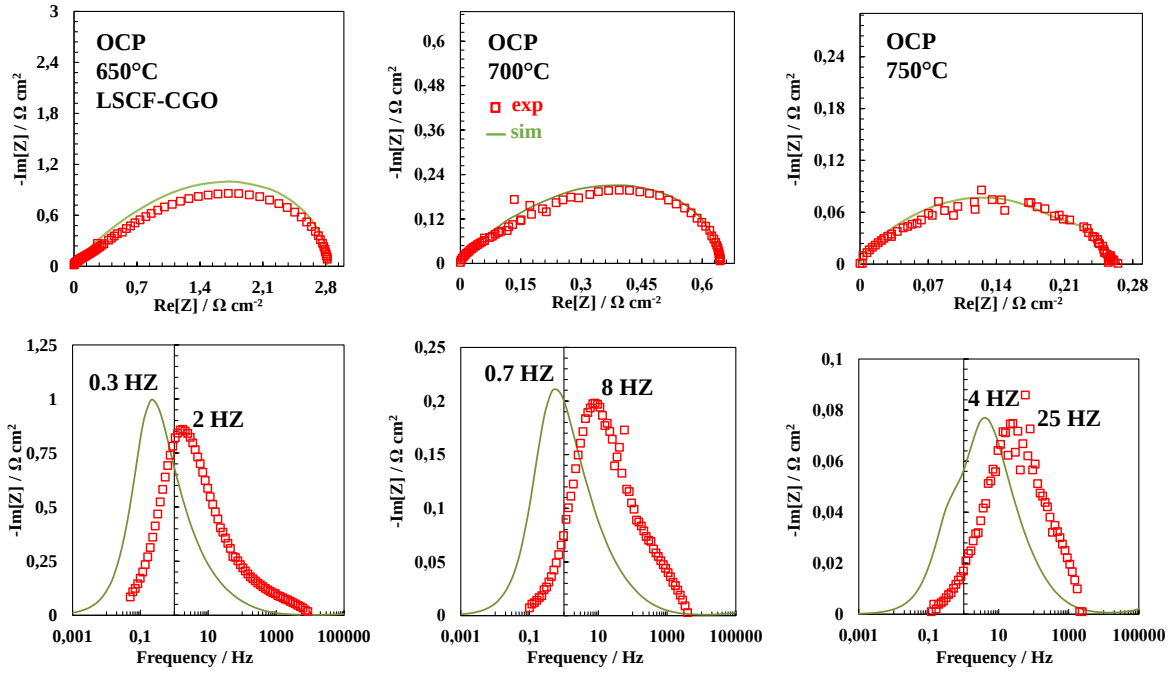

Fig. III-6 Experimental and simulated impedance diagrams for the LSCF-CGO electrode at OCP. Nyquist plots for (a) 650 °C, (b) 700 °C and (c) 750 °C. Bode plots for (d) 650 °C, (e) 700 °C and (f) 750 °C.

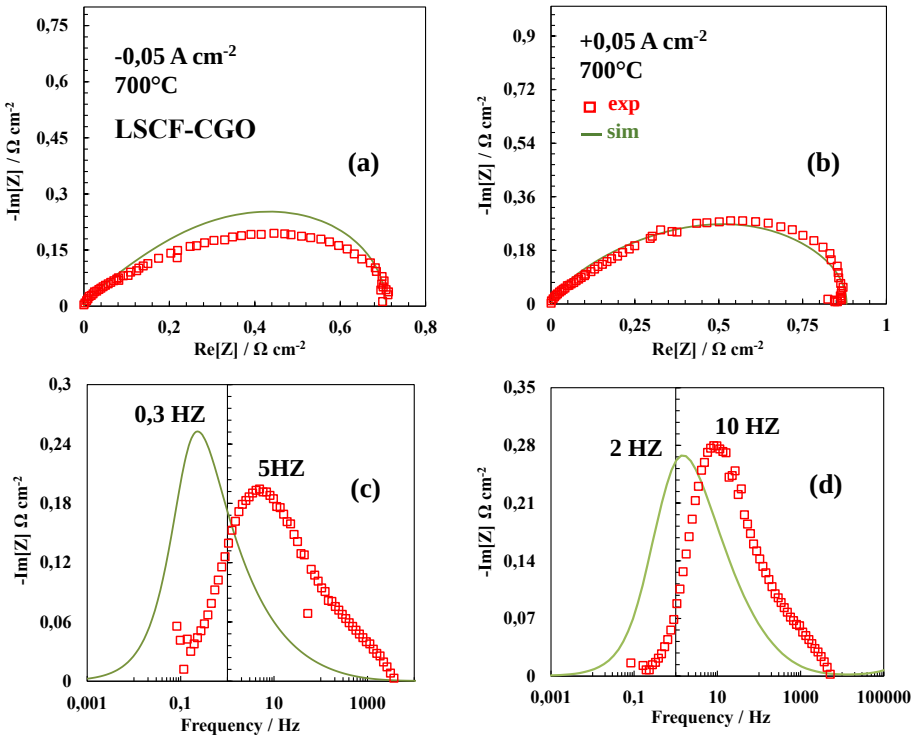

Fig. III-7 Experimental and simulated impedance diagrams for the LSCF-CGO electrode at 700 °C for i_{dc} = ± 50 mA cm^{-2}. (a) and (b) Nyquist and (c) and (d) Bode plots.

3.2.2.2 Effect of the oxygen partial pressure

To go further in the model validation, its capability to simulate the dependency of the electrode response on the oxygen partial pressure has been investigated for both studied electrodes. For this purpose, impedance diagrams at OCP have been computed changing the oxygen content in the gas (without fitting). The graphs of R_{pol} as a function of P_{O_2} have been plotted in logarithmic coordinates and compared to the experimental data in Fig. III-8 for the LSCF and LSCF-CGO electrodes, respectively. In the two cases, it can be seen that the model predicts accurately the gradual increase of the polarization resistance when decreasing the oxygen partial pressure. Moreover, the model also captures correctly the higher dependency with P_{O_2} for the LSCF electrode compared to the composite one. A slight distortion of the low frequency part of the impedance diagram recorded for the LSCF electrode at 700 °C can be detected at low P_{O_2} values (Fig. III-7a),

as it was evidenced at 750 °C under air (Fig. III-5c). This contribution was also observed by Mosialek *et al.* [Mosialek1998] in the same experimental conditions confirming that a gas conversion impedance arises also at low oxygen partial pressures.

This good agreement between the model and the experiments is also confirmed by the reaction order *m* drawn from the simulated data for both studied electrodes. Regarding the LSCF electrode, the fitted value was found to be equal 0.15 for $0.10\ \text{atm} \leq P_{O_2} \leq 0.21\ \text{atm}$ and to 0.09 for $P_{O_2} > 0.21\ \text{atm}$ (Fig. III-8a). For the LSCF-CGO electrode, a fitted value of 0.27 was calculated for $0.10\ \text{atm} \leq P_{O_2} \leq 0.21\ \text{atm}$ while a value of 0.16 was obtained for $P_{O_2} > 0.21\ \text{atm}$ (Fig. III-8b). All these exponents are very close to the ones fitted on the experimental data (cf. section 2.1.3.5). For instance, the error on the reaction orders for the LSCF electrode is less than 12 %. The consistency between the experimental and computed exponents would indicate the relevance of the model assumption regarding the reaction mechanism and the presence of oxygen ions on the LSCF surface. Therefore, as pointed out by Fleig *et al*. [Fleig2007], the description of the reaction mechanism with elementary reactions in the porous electrode allows the good prediction of the electrode response as a function of the P_{O_2}.

As a general comment, it was possible using the same model to reproduce the experimental polarization curves for the LSCF and LSCF-CGO electrodes by identifying for the two cases a set of consistent data (kinetic constants and surface diffusivities). Moreover, the model is able to predict without any fitting the LSCF and LSCF-CGO electrodes behavior with the change of P_{O_2} and the shape of the impedance diagrams depending on the temperature and polarization. In spite of a systematic frequency lag in the impedance spectra, the capacity of the model to reproduce the response for the two types of electrode allows validating the main model assumptions.

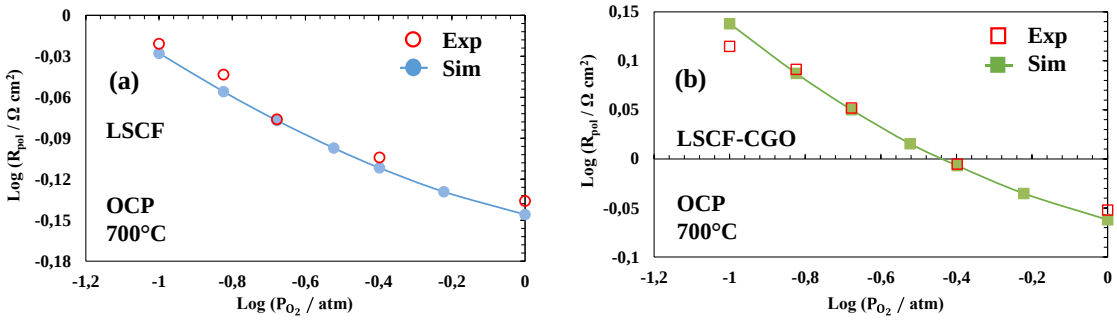

Fig. III-8 Plot of the logarithm of the electrode polarization resistance as a function of the logarithm of the oxygen partial pressure for (a) the LSCF electrode and (b) the LSCF-CGO electrode.

3.3 Analysis of the reaction mechanism

3.3.1 Effect of polarization and temperature on the reaction pathway under air condition

To study the reaction pathway in air at the three studied temperatures, the ratio of the surface to the bulk path has been computed as a function of the current density for LSCF (Fig. III-9a) and LSCF-CGO (Fig. III-9b), respectively. The ratio is defined by the integration of R3 and R2 over the electrode thickness for the LSCF-CGO composite, while R3 is limited at the electrolyte interface for the LSCF electrode.

For both electrodes, this ratio is an increasing function of the anodic current, regardless of the operating temperature (Fig. III-9). This behavior is associated to the concentration of the oxygen vacancies in the LSCF material. Indeed, as already discussed by Laurencin and co-workers [Hubert2016, Laurencin2015], the LSCF under-stoichiometry tends to zero by increasing the anodic polarization. In this condition, the bulk path becomes more and more limited, while the direct oxidation at the TPBls is promoted (without limitation due to the accumulation of adsorbed oxygen species on the LSCF since the surface coverage of the adsorbed oxygen species at equilibrium is low). This evolution is illustrated for the LSCF electrode in Fig. III-9c by plotting the kinetic rates of both the charge transfer at TPBls and the oxygen incorporation/excorporation (integrated along the electrode thickness). Accordingly, the reaction of oxygen excorporation becomes bounded under anodic polarization while the charge transfer at TPBls is strongly activated. On the contrary, an opposite behavior is highlighted under cathodic polarization (i.e. the

incorporation step is activated while the reaction at TPBls is bounded). As already shown for the LSCF electrode [Monaco2018], a transition from the bulk to the surface path occurs by increasing the anodic polarization at all the operating temperatures. Even if a slight increase of the ratio is detected as a function of the operating temperature, the bulk path appears to be the dominant pathway for the LSCF electrode at OCP (Fig. III-9a). This result is in good agreement with the Gerischer type-element observed for the diagrams obtained in this condition [Adler1998] (Fig. III-4). Moreover, a steep variation of the ratio is found at 650 °C indicating a well-defined threshold for the transition from the bulk to the surface path. However, this evolution and the transition become smoother by increasing the operating temperature. This behavior is in accordance with the derivatives of the polarization curves as a function of the current density. Indeed, a clear dissymmetry occurs close to the OCP at 650 °C, while a more linear evolution is observed at 750 °C (see Fig. II-6 in Chapter II). From the analysis of the ratio at 750 °C (Fig. III-9a), it can be stated that the constant value measured experimentally is due to the fact that the investigated range of current density is not sufficiently extended to detect the transition to the surface path (taking place at a higher anodic dc current ≈ + 200 mA·cm^{-2}). At 700 °C, the ratio starts to be higher than the unity only at ≈ + 90 mA·cm^{-2}. This result explains why no change in the impedance diagrams was observed since the experiments were conducted for a lower dc current (± 50 mA·cm^{-2}: cf. section 2.1.3.5).

The ratio has also been computed at 800 °C for the LSCF electrode taking advantage of the fitted activation energies. As it can be noticed in Fig. III-9a, the ratio increases very slowly with the current density, probably due to the small overpotential values. Thereby, the transition to the surface path is much less abrupt and is decayed at high anodic current density (≈ + 300 mA·cm^{-2}). This result may explain the apparent discrepancy between our statements and the conclusions of Ma *et al.* [Ma2018] who claimed that the LSCF remains dominated by the bulk path in both anodic and cathodic polarizations at 800°C. Furthermore, it is worth noting that in their model, the chemical diffusivity depends exponentially on the concentration of oxygen vacancies in the LSCF ($D_{chem} = A\exp\left(B\left(C_{V_O^{\bullet\bullet}} - C_{V_O^{\bullet\bullet}}^{eq}\right)\right)$). With this model, the steep increase of D_{chem} at the electrolyte interface prevents the limitation of the bulk path under anodic current. In our case, the dependence of the chemical diffusivity with the concentration of vacancies is given by the thermodynamic factor computed using the local oxygen partial pressure in the electrode and the thermogravimetric

data from Bouwmeester *et al.* [Bouwmeester2004] (cf. Eq. (27)). With this approach, the chemical diffusivity increases only slightly in the investigated range of oxygen partial pressure (i.e. $P_{O_2} \geq$ 0.10 atm). This evolution is in good agreement with several articles that have referred only a very slight evolution of D_{chem} for $P_{O_2} \geq 0.10$ atm [Bouwmeester2004, Elshof1997, Lane2000, Laurencin2016, Yashiro2011].

As shown in Fig. III-9b, the reaction mechanism for the LSCF-CGO electrode is completely dominated by the surface path whatever the polarization at 750 °C and 700 °C. This result could have been anticipated since the surface pathway is favored by the multiplication of the active sites in the whole electrode volume. However, the reaction mechanism starts to be fully controlled by the bulk path under low cathodic overpotentials when the temperature is lowered down to 650°C (Fig. III-9b). This change in the reaction pathway is also experimentally confirmed by the dissymmetric shape of the i-η curve recorded at 650 °C (Fig. III-3b).

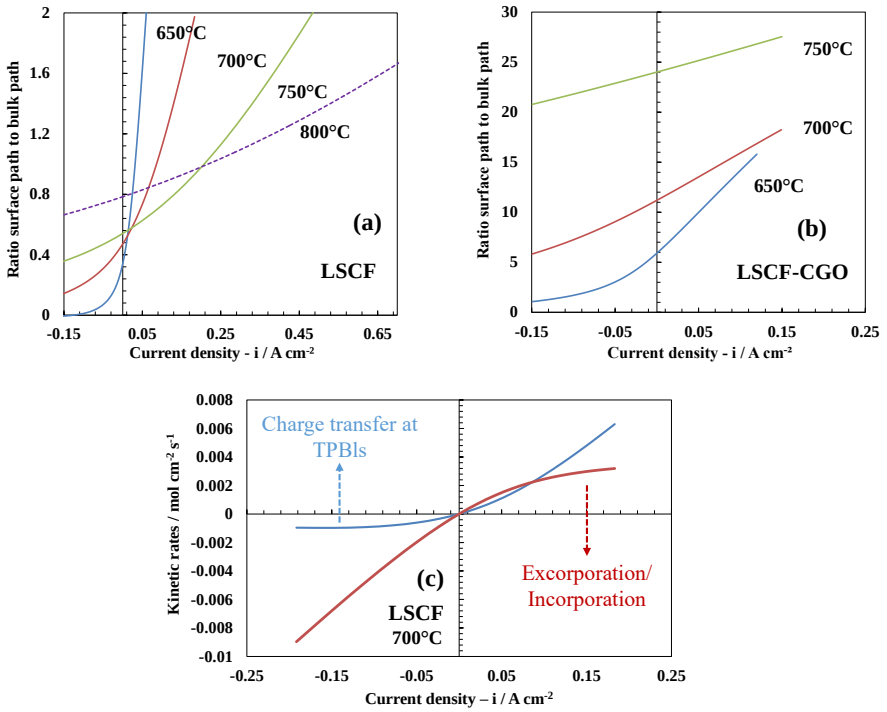

Fig. III-9 Ratio of the surface to the bulk path under air for (a) the LSCF electrode and (b) the LSCF-CGO electrode. The kinetic rates for the charge transfer at TPBs and the oxygen incorporation/excorporation (integrated along the electrode thickness) are plotted versus the current density in (c) for the LSCF electrode at 700°C.

3.3.2 Impact of the ratio on the impedance response

Impedance diagrams have been computed below and above the transition at 700 °C under air for i_{dc} = + 50, + 90, + 120 and + 150 mA·cm^{-2} to gain insight on the effect of the predominant reaction path on the electrode impedance response. The corresponding diagrams plotted in the Nyquist and Bode plans are given in Fig. III-10. A change in the shape of the diagram has been highlighted with an evolution starting from a slightly depressed Gerischer type-element towards a complete flattened semi-circle at i_{dc} = + 150 mA·cm^{-2}. This evolution is in good agreement with the experimental results reported in [Monaco2018]. Furthermore, a sharp increase of the peak frequency has been found when the dc current is raised above the threshold (at around + 90 mA·cm^{-2}). Indeed, the peak frequency is augmented from 0.7 Hz at i_{dc} = + 50 mA·cm^{-2} up to 13 Hz at i_{dc} = + 150 mA·cm^{-2} (with 1.9 Hz and 4.9 Hz for the intermediate values corresponding to + 90, + 120 mA·cm^{-2}, respectively). This statement shows that the simulated frequency distribution is strongly impacted even by a slight change in the ratio of the surface to bulk path for the reaction mechanism. Therefore, the mismatch between the computed and experimental frequencies highlighted in section 3.2.2.1 could be partly due to a slight under-estimation of the surface path in the modeling results.

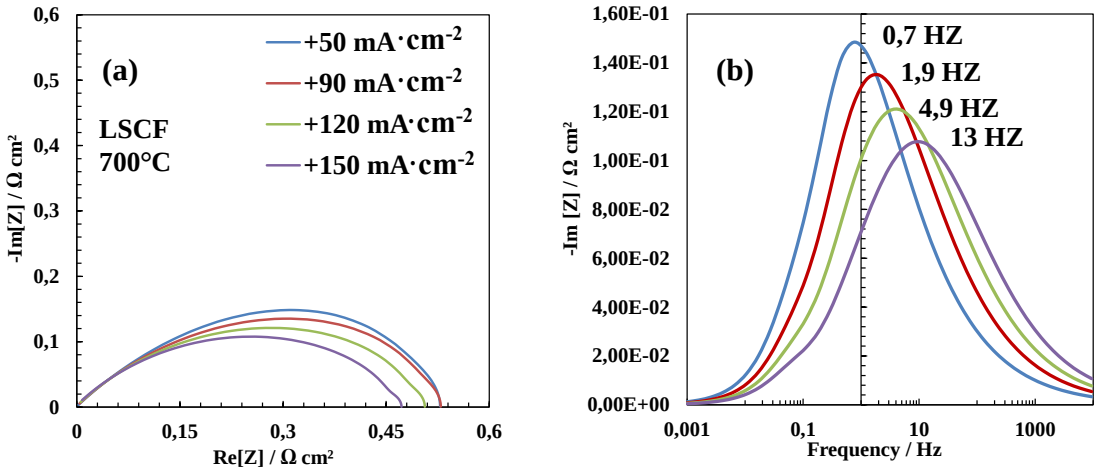

Fig. III-10 Simulated impedance diagrams for the LSCF electrode at 700 °C under air for i_{dc} = + 50, + 90, + 120 and + 150 mA·cm^{-2} (a) Nyquist and (b) Bode plots. It has to be reminded that the surface area of the electrode is ≈ 1 cm^2.

3.3.3 Effect of oxygen partial pressure on the reaction mechanism at OCP

Taking advantage of the full elementary model capability to predict the electrode response depending on P_{O_2}, the effect of oxygen partial pressure on the reaction mechanism for the LSCF electrode has been investigated at OCP. For this purpose, simulations have been carried out at 700 °C changing step by step the oxygen partial pressure from P_{O_2}= 0.1 atm to 1 atm. As shown in Fig. III-11a, the increase of oxygen content in the gas phase enhances gradually the contribution of the surface path in the reaction mechanism. For instance, the ratio of the surface path to the bulk path close to the OCP rises from 0.29 at P_{O_2}= 0.1 atm up to 1.05 at P_{O_2}= 1 atm. On the one hand, this evolution can be explained by the decrease of the LSCF under-stoichiometry at equilibrium when the oxygen partial pressure is increased. As for an anodic polarization, the low concentration of vacancies at high oxygen partial pressure tends to block the bulk path towards a lower bound (Fig. III-11b). As expected, the integrated reaction rate of oxygen incorporation/excorporation (R2) is a decreasing function of the oxygen partial pressure. On the other hand, the increase of P_{O_2} also leads to enhance the oxygen activities for the adsorbed species promoting the reaction kinetics involved in the surface path. This statement is illustrated in Fig. III-11b by the continuous increase of the rate of charge transfer at TPBls (R3) with the oxygen partial pressure. As a result, it can be noticed that the sum of the two contributions increases with P_{O_2} explaining the continuous decrease of the electrode polarization resistance as previously discussed (cf. section 3.2.2.2).

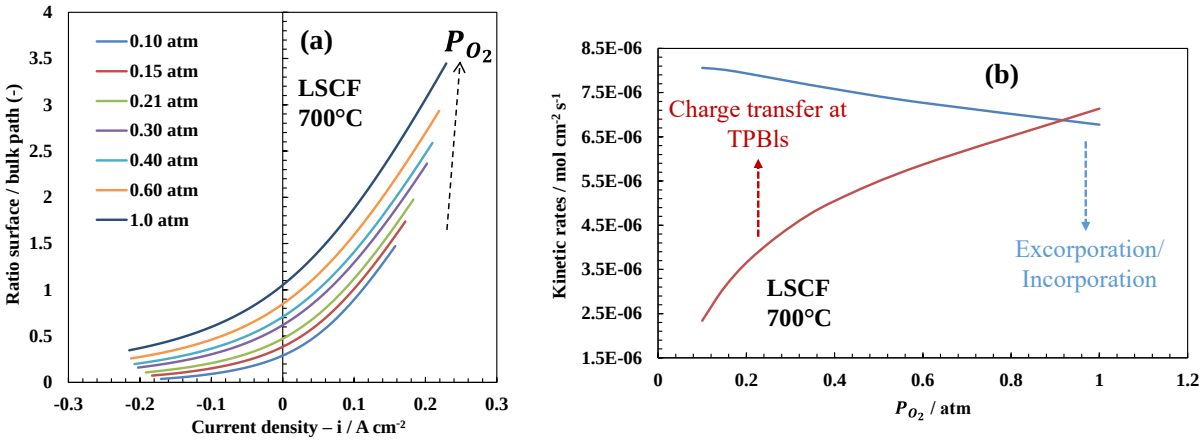

Fig. III-11. Ratio of surface/bulk path as a function of the current density for each investigated oxygen partial pressure at 700 °C for the LSCF electrode (a). Kinetic rates of the oxygen excorporation/incorporation (blue) and the charge transfer at TPBls (red) as a function of the oxygen partial pressure computed close to the OCP (at + 0.225 mA·cm^{-2}) (b).

It can be mentioned that the same explanation stands for the LSCF-CGO electrode. Nevertheless, the promotion of the reactions involved in the surface path is less sensitive to oxygen activities on the surface since, in this case, there is not a limitation in the density of available TPBls for the reaction step R3. Therefore, the improvement of the electrode performances with the oxygen partial pressure is less pronounced than for the LSCF electrode. Indeed, the ratio of the surface path to the bulk path rises at OCP only by a factor of 2.2 for the LSCF-CGO electrode when P_{O_2} varies between 0.1 and 1 atm at 700 °C (Fig. III-12).

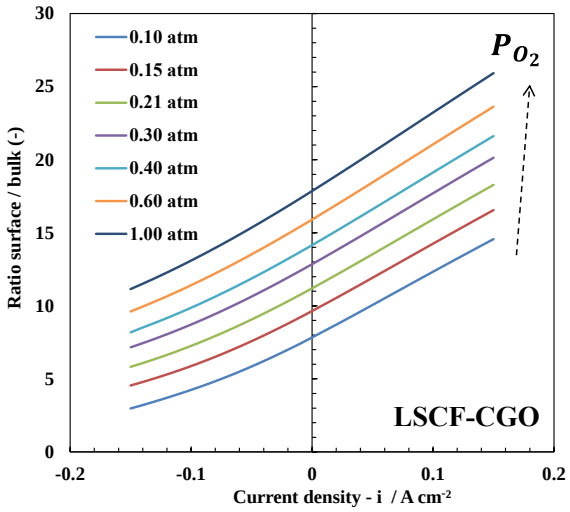

Fig. III-12 Ratio of the surface/bulk path as a function of the current density for each investigated oxygen partial pressure at 700 °C for the LSCF-CGO electrode.

To identify the rate-determining steps for the LSCF electrode at OCP, a sensitivity analysis has been conducted with the model changing the kinetic constant one after the other. The impedance simulations have been performed at 700 °C for two oxygen partial pressures at P_{O_2} = 0.15 and 0.30 atm. For the chosen conditions, the ratio of the surface path to the bulk path is equal to 0.39 and 0.58, respectively (Fig. III-11a). For both oxygen partial pressures, it has been found that the adsorption R6 and ionization R4, which belong to the common path, co-limits the reaction mechanism. Indeed, the division by two of their respective kinetic constants leads to raise significantly the polarization resistance, i.e. the relative increase of the polarization resistance $\Delta R_{pol}/R_{pol}$ is found equal to 8 % (resp. 6 %) for $k_{ads}/2$ and to 14 % (resp. 11 %) for $k_{ion}/2$ at P_{O_2} = 0.15 atm (resp. 0.30 atm). When the mechanism is dominated by the bulk path at low oxygen partial pressure, the reaction of oxygen incorporation/excorporation (R2) is identified as an additional rate-determining step whereas the role of the reaction at TPBls (R3) becomes more and more negligible. Indeed, the division by two of their kinetic constants yields an increase of R_{pol} of 17 % for $k_{ox}^{LSCF/gas}/2$ and 5 % for $k_{ox}^{TPBls}/2$. As expected, this result tends to be reversed when increasing the oxygen partial pressure to 0.3 atm. In that case, the diminution of the electrode performances due to the decrease of $k_{ox}^{LSCF/gas}$ is of 15 % whereas it reaches almost 10 % when reducing the charge transfer at TPBls. In this case, the reaction mechanism becomes also more and

more dependent on the surface diffusion coefficient of the oxygen ions (hindering the oxygen transport away from the TPBls restricted at the electrolyte interface).

3.4 Cyclic Voltammetry study

3.4.1 Validation of *model-II* for the CV computation: effect of temperature and scan rate

The capability of the full elementary model to predict the voltammograms has been checked by comparing the simulated and the experimental curves as functions of the operating temperature and applied scan rate. As previously mentioned, all the computations have been carried out using the input data used for the model validation on the impedance diagrams and on the effect of the oxygen partial pressure. Nevertheless, for the present CV simulations, the Ohmic loss in the CGO barrier has been neglected because of its low thickness (2 µm) and only the 8YSZ electrolyte has been considered with an ionic conductivity equal to 2.3 $S{\cdot}m^{-1}$ and 1.4 $S{\cdot}m^{-1}$ at 700 °C and 650 °C, respectively (data provided by the electrolyte supplier (Kerafol®)). Besides, since the measurements were performed using a three-electrode setup in a symmetrical cell configuration, the electrolyte thickness in the simulation has been chosen to the half of the whole electrolyte thickness (i.e. $\ell_{electrolyte}$ = 125 µm) [Rutman2007]. Moreover, the contact resistance between the platinum grids (used as current collectors) and the electrodes surface has been also considered in the model as an additional Ohmic loss. This resistance, R_c, was determined from the experimental impedance diagrams recorded at OCP and was obtained by subtracting the electrolyte resistance $R_{electrolyte}$ from the series resistance R_s. This contact resistance has been found to increase from $R_c = 0.96\ \Omega \cdot cm^2$ to $R_c = 1.82\ \Omega \cdot cm^2$ by decreasing the temperature from 700 °C down to 650 °C. This temperature dependence of R_c, which has been already reported by other authors [Wang2014a], may be explained by a higher viscoplastic accommodation of the metallic grids at higher temperatures.

Regarding the effect of the temperature on the CV response, the comparison between the experimental data and the curves simulated with *model-II* has been reported in Fig. III-13. It can be seen that the model is able to reproduce quite correctly the general shape of the voltammograms at both operating temperatures. As for the experiments, a slightly higher hysteresis is found at 650 °C with the model.

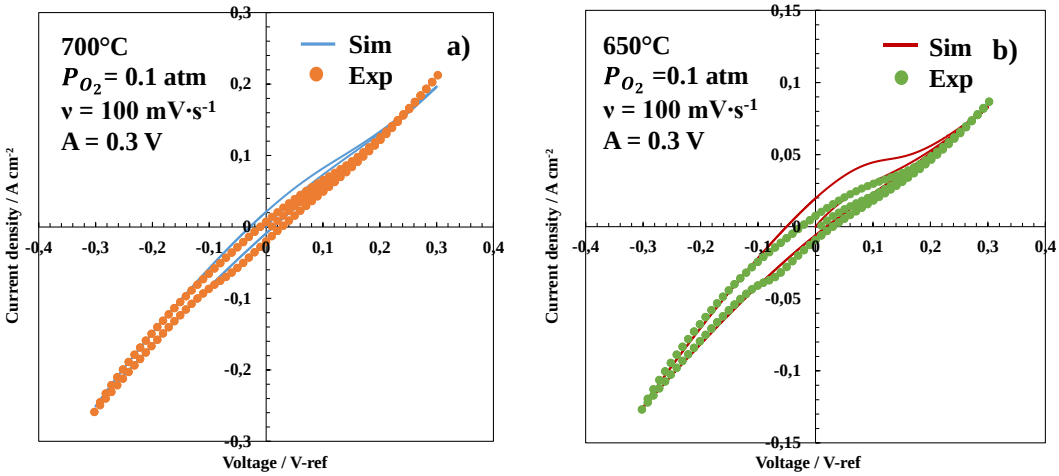

Fig. III-13 Experimental and simulated (*model-II*) cyclic voltammetry curves at (a) 700 °C and (b) 650 °C at P_{O_2} = 0.1 atm with ν = 100 mV·s^{-1} and A = 0.3 V.

As a further element of validation, the model capability to capture the evolution of the CV response when changing the potential scan rate has been investigated. As it can be noticed in Figs. III-14b and III-14d, the model is able to retrieve quite precisely the evolution of the CV response with the scan rate. Therefore, it has been stated that the computed voltammograms with *model-II* are quite in good agreement with the experimental curves obtained under various operating conditions. Since all these results were obtained without fitting, the model can be considered as validated to predict the CV response of the LSCF electrode.

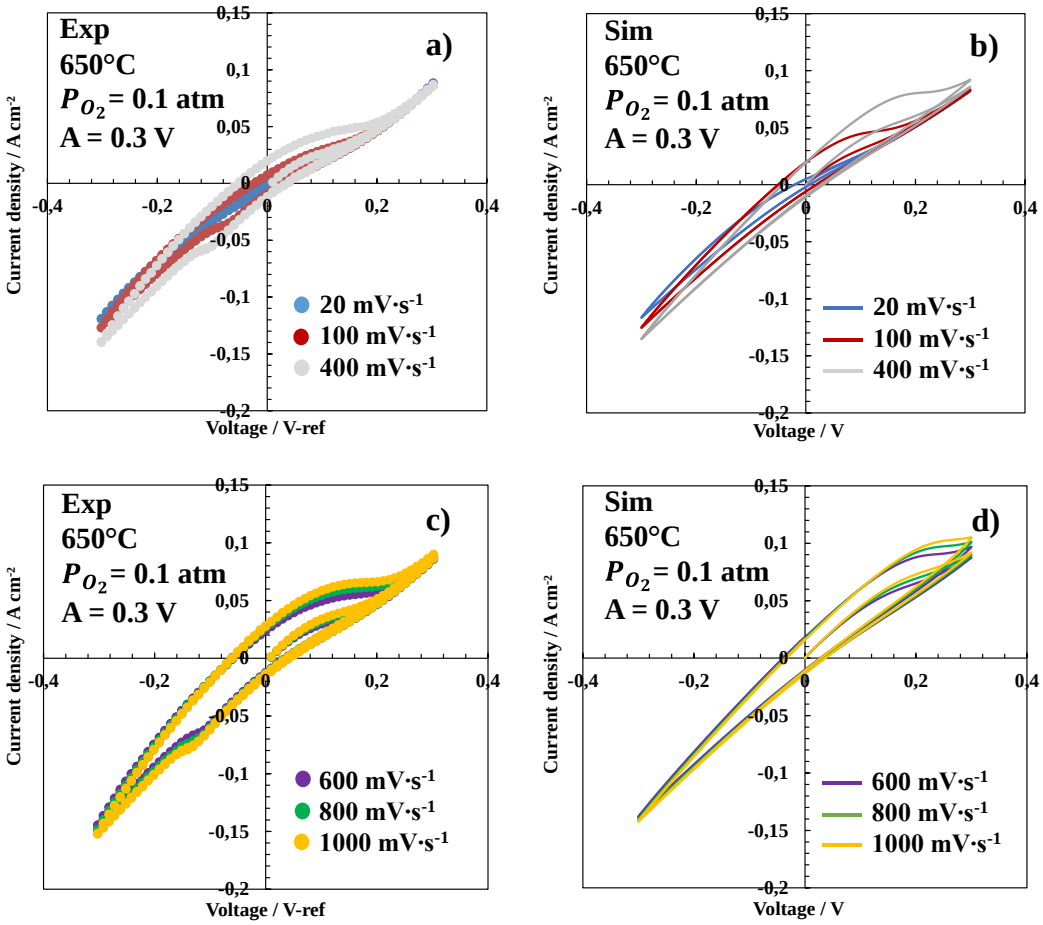

Fig III-14 Experimental (a) and (c) and simulated (*model-II*) (b) and (d) cyclic voltammetry curves as a function of the scan rate: 20-100-400 mV·s^{-1} (a) and 600-800-1000 mV·s^{-1} (b) at 650 °C, P_{O_2} = 0.1 atm and A = 0.3.

3.4.2 Calibration of *model-I*

The implemented numerical version of the ALS-based model (*model-I*) has been calibrated using simulations obtained with the full elementary model (*model-II*). The input parameters used for *model-I* are reported in Table X. The microstructural parameters and thermodynamic data correspond to the ones taken for the elementary model. As mentioned in section 3.1.6, the kinetic constant of the ionic transfer R1 has been considered as not limiting, in order to fulfill the boundary condition of a quasi-equilibrium state at the electrode/electrolyte interface. Therefore, the chemical rate constant k_{chem} for the global oxygen exchange between LSCF and gas remains the only unknown parameter. This parameter has been determined, by fitting with *model*-I, the impedance

diagram obtained at OCP, 700 °C and P_{O_2}= 0.1 atm, using *model-II* (Fig. III-15a). As reported in Table X, a value of $1.23 \cdot 10^{-7} m \cdot s^{-1}$ has been obtained in these conditions. It can be noticed that the computed impedance diagrams present the same polarization resistance R_{pol} and a quite good match in terms of shape, especially at high frequencies. As expected, the diagram related to *model-I* is a perfect Gerischer element as predicted by the ALS-based model. On the other hand, the one simulated with the full elementary model is slightly depressed, due to the more complex reaction mechanism, which better reflects the real behavior of the LSCF electrode. However, despite the good superposition of the impedance diagrams, it can be noticed in Fig. III-15b that the consistency between the two i-V curves, corrected from the Ohmic drop, is valid only near OCP. Indeed, it diverges highly for anodic potentials since a limiting current is evidenced for *model-I*. This behavior is linked to the fact that the ALS-based approach neglects the contribution of the surface path in the reaction mechanism, which has been demonstrated to be the dominant pathway for the LSCF electrode under SOEC mode [Laurencin2015, Monaco2018]. From this point of view, the electrode modelling under polarization requires a more detailed description of the reaction mechanism that is not taken into account in the ALS-based approach.

Tab. X Model input parameters for the LSCF material given here at 700°C under P_{O_2}=0.1 atm for the numerical version of the semi-analytical model (*model-I*).

Analytical model: parameter at 700°C, P_{O_2}=0.1 atm	**Value**	**Unit**
Maximum oxygen concentration in the LSCF ($C_{O_O^x}^{max}$)	83108	(mol·m^{-3})
Equilibrium oxygen concentration in the LSCF ($C_{O_O^x}^{eq}$)	82491	(mol·m^{-3})
LSCF chemical diffusivity (D_{chem})	3.7 x10^{-10}	(m²·s^{-1})
Ionic transfer kinetic constant (k_+)	NOT LIMITING	(mol·m^{-1}·s^{-1})
Chemical constant (k_{chem})	1.23x10^{-7}	m·s^{-1}
Charge transfer coefficient (α)	0.5	(-)
Electrolyte thickness (ℓ_{YSZ})	1.25 x10^{-4}	(m)
Contact resistance (R_c)	0.96	(Ω·cm²)
Ionic conductivity of YSZ (σ_{YSZ})	2.3	(S·m^{-1})
Electrode thickness (ℓ_{LSCF})	3.5 x10^{-5}	(m)
Volume fraction (ε_{LSCF})	48.7	(%)
Tortuosity factor (τ_{LSCF})	2.84	(-)
LSCF specific surface area ($S_p^{LSCF/gas}$)	3.59 x10^{6}	(m^{-1})

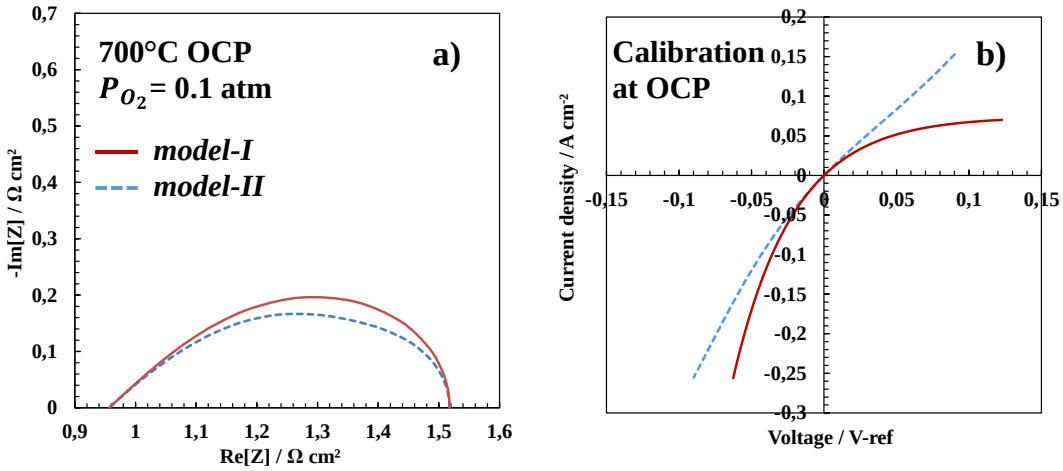

Fig. III-15 Comparison of the impedance spectra at OCP, 700 °C and P_{O_2} = 0.1 atm (a) and corresponding calibration on the polarization curve (b). The red solid lines represent the simulations obtained with *model-I*, while the blue dashed lines represent the simulation with *model-II*.

3.4.3 Comparison between *model-I* and *model-II* for the CV response

3.4.3.1 Microstructural effect: from a porous to a dense electrode

As the electrode microstructural parameters play a significant role on experimental CV curves [Tezyk2019], their effect on the voltammetry response have been investigated with both models at 700 °C and P_{O_2} = 0.1 atm. In this first part of the study, it is worth emphasizing that the Ohmic losses due to the electrolyte and the contact resistances have been neglected by considering $\ell_{electrolye} \rightarrow 0$ and $R_{contact} \rightarrow 0$. The analysis has been performed by starting from the classical porous electrode used for the model validation with a scan rate of 100 mV·s^{-1} (i). The procedure has consisted to simulate the additive effects of four successive steps: division of the specific electrode surface area by a factor of 10 (ii), increase of the LSCF volume fraction up to 90 % (iii), reduction of the electrode thickness from 35 µm down to 5 µm (iv), and finally, lowering the scan rate down to 1 mV·s^{-1} (v). The first four conditions have allowed passing from the case of a porous 'thick' electrode to a quasi-dense 'thin' film, while the last step has allowed investigating the electrode response in a quasi-steady state regime. The CV curves obtained at each step of the procedure have been interpreted through the zone diagram established in [Montella2021].

For *model-I*, the trajectory in the zone diagram can be predicted using Eqs. (47) and (48) as shown in Fig. III-16a. The solid circles on this trajectory correspond to each step of the procedure. For the standard 'thick' porous electrode, the voltammogram falls in zone 3 (blue curve), indicating that the CV response is controlled by both the chemical reaction of oxygen exchange and the oxygen diffusion in LSCF under semi-infinite conditions as detailed in [Montella2021]. Both the decrease of the specific surface area of LSCF S_p^{LSCF} (orange curve) and the increase of the volume fraction of LSCF ε_{LSCF} (green curve) yield a horizontal translation to the left in zone 3 since the dimensionless parameter λ is lowered (Eq. (47)). As expected when the electrode is getting dense (i.e. ε_{LSCF} is increased and S_p^{LSCF} is decreased), the effect of the chemical process decreases up to reach a response with no chemical effect and only a control by diffusion in a semi-infinite medium (translation in zone $1 \cap 3$ for an even a denser electrode). Subsequently, the decrease of the electrode thickness ℓ_{LSCF} (yellow curve) yields a vertical translation due to the decrease of the dimensionless thickness L, according to Eq. (48). Consequently, the voltammograms move towards zone 4 as shown by the more symmetrical shape of the CV curve in Fig. III-16a (yellow curve). In this zone, the CV response is governed by both the chemical oxygen exchange and the diffusion in a finite medium as expected for a thin film [Montella2021]. Finally, the decrease of the scan rate down to 1 $mV \cdot s^{-1}$ (purple curve) shifts the response at the intersection of zone 4 and zone $2 \cap 4$. The resulting curve, whose enlargement is reported in the corner of Fig. III-16a, corresponds to an almost steady-state condition with a sigmoidal shape.

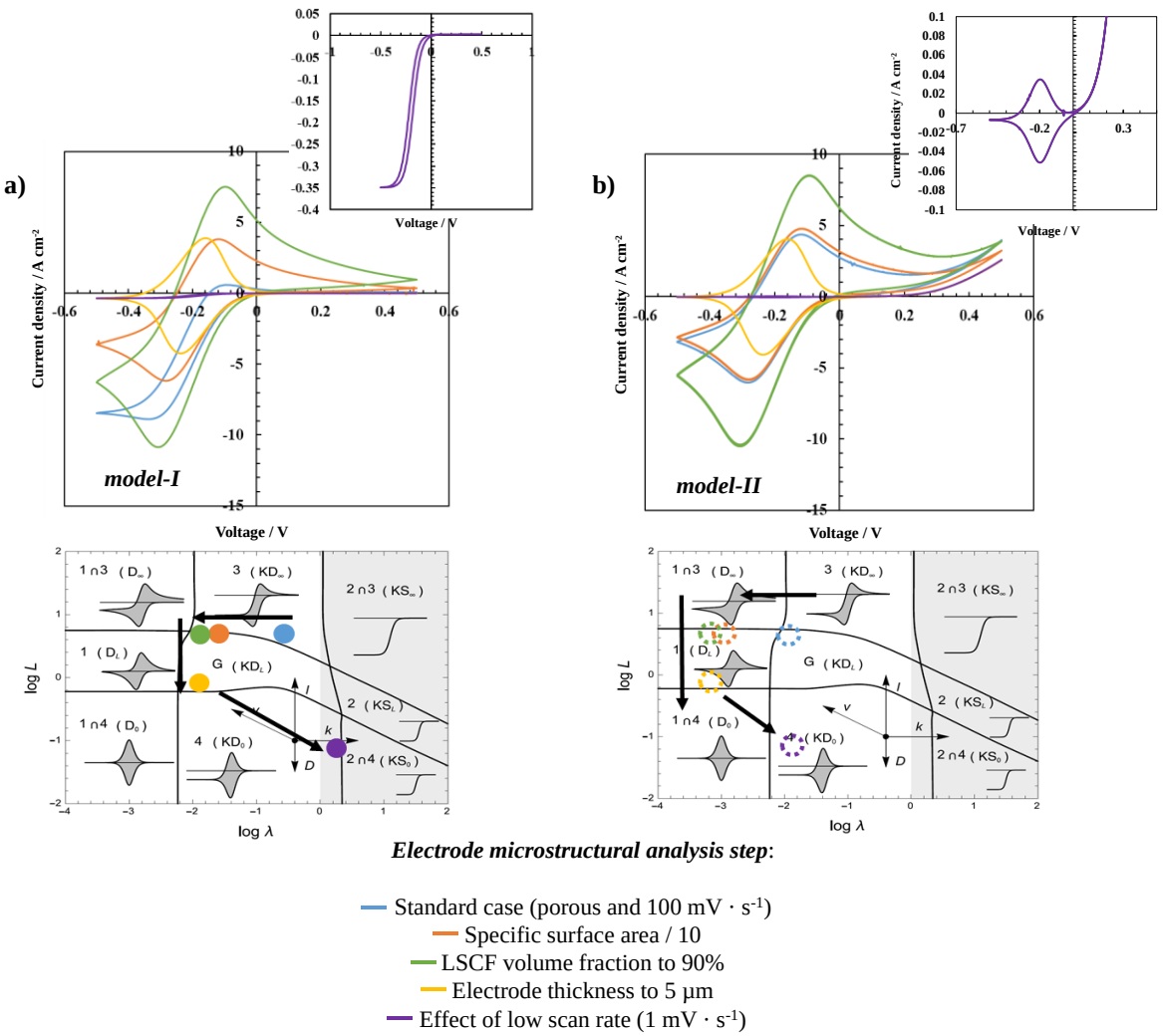

Fig. III-16 Evolution of the cyclic voltammetry curves from the case of a porous electrode to the case of a quasi-dense electrode for *model-I* (a) and *model-II* (b) without the Ohmic losses ($\ell_{YSZ} \rightarrow 0$ and $R_c \rightarrow 0$) at 700 °C, P_{O_2} = 0.1 atm and A = 0.5 V. The last curve at low scan rate has been magnified and reported in second quarter of both figures. The full circles represent the calculated values of λ and L for the semi-analytical model, while the empty circles represent the zone in which the CV curves of the full elementary model can be located after visual identification.

All the reported results are in quite good agreement with the semi-analytical solutions determined by Montella et al. [Montella2021], ensuring the reliability of this implemented numerical version (*model-I*). The comparison between *model-I* and the semi-analytical solution is detailed in

Fig. III-17. It is shown that the CV curves obtained from the semi-analytical ALS-based model developed in [Montella2021] have the same shape as those reported in Fig. III-16a. Moreover, the values of the cathodic and anodic peak current density are exactly the same. However, there is a slight mismatch on the values of the peak potential difference, defined by: $\Delta E_p = E_{pa} - E_{pc}$, where E_{pc} and E_{pa} are the cathodic and anodic peak potentials, respectively. Indeed, it has been found that ΔE_p is always about 50 mV higher with *Model-I* compared to the semi-analytical ALS-based model. The reason to explain difference is still unclear. It could be due to some numerical uncertainties in the numerical simulations for large perturbations.

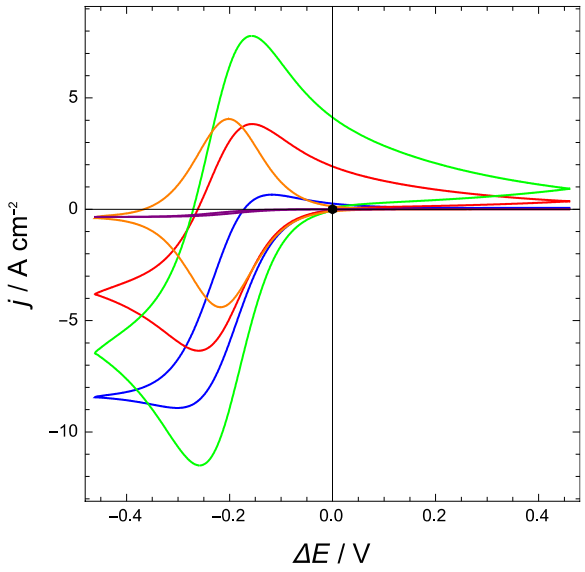

Fig. III-17. Cyclic voltammetry curves plotted with the semi-analytical model for the characteristic points of the zone diagram shown in Fig. III-16a. The color code is the same as in Fig. III-16.

The same study has been performed with the elementary model (*model-II*). The corresponding CV curves are reported in Fig. III-16b. It can be seen that this model does not change significantly the shape of the CV response. Therefore, it can be proposed that the zone diagram can still be used to analyze the results. Visual analysis shows that the CV curves obtained with *model-II* are only translated to the left in the zone diagram with respect to *model-I*. The value of this shift, $\Delta \log \lambda$, was estimated considering the purple curves, plotted at 1 mV. s^{-1}, in Fig. III-16a and III-16b, as

their shape is highly modified from *model-I* to *model-II*. For this purpose, the voltammograms obtained with *model-II* has been roughly retrieved with the semi-analytical solution (knowing the voltammograms obtained with this model are quite well representative of those obtained with the elementary description as pointed out in the next section). Fig. III-18 shows the CV curves plotted from the semi-analytical model for the coordinate point in the zone diagram log λ= -1.29 and log L=-1.17 (curve on the left). It can be seen that the curve is very similar to that obtained with *Model-II* (purple curve in Fig. III-16b). Moreover, if we increase log λ by 1.6 (curve on the right), we find the curve of Fig. III-16a, corresponding to *Model-I*. One can thus propose that, in the experimental conditions of Fig. III-16a, the results from *Model-II* can be deduced from *Model-I* by translating from -1.6 on the x-axis in the zone diagram.

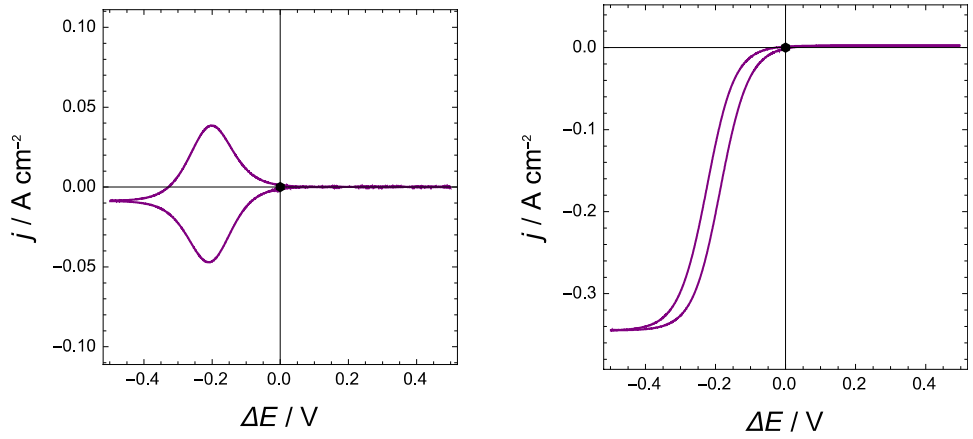

Fig. III-18 Cyclic voltammetry curve plotted with the semi-analytical model for the coordinate point [-1.29; -1.17] (left) and by translating from 1.6 on the x-axis (right). The color code is the same as in Fig. III-16.

This result is confirmed in Fig. III-19, which shows the CV curves plotted from the semi-analytical model for the characteristics points calculated in Fig. III-16a and translated from -1.6 on the x-axis. It can be noticed that the voltammograms are very similar to those in Fig. III-16b, obtained from *Model-II*.

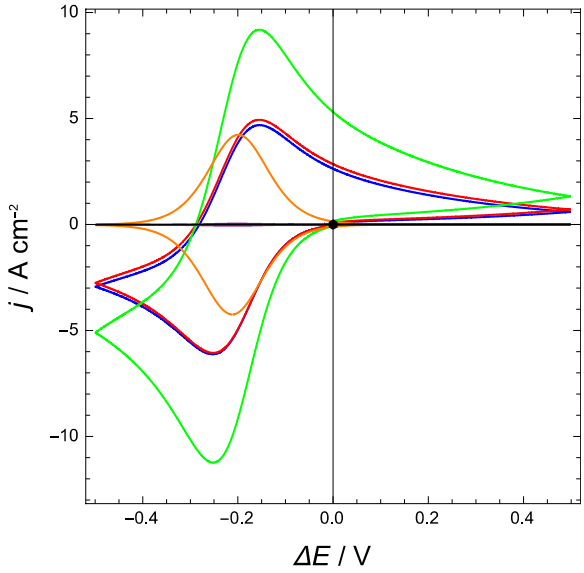

Fig. III-19 Cyclic voltammetry curves plotted with the semi-analytical model by translating the point of Fig. III-16a from -1.6 on the x-axis. The color code is the same as in Fig. III-16.

The translation on the x-axis in the zone diagram was found to be almost equal to $\Delta \log \lambda$ =-1.6. The corresponding points, related to this translation, are represented by empty circles in Fig. III-16b. Thanks to this positioning, it can be noticed that, for each circle, the global shape of the simulated voltammograms is well consistent with the one reported in the zone diagram. Therefore, for the standard case (blue curve), it is found that the voltammogram drops in the left part of zone 3, in a region very close to zone 1∩3. As expected, the decrease of S_p^{LSCF} (orange curve) yields to move the CV curve at the intersection of zone 1 and zone $1 \cap 3$ of the diagram, where the voltammogram is only slightly impacted by the decrease of the effective chemical constant. This result would thus confirm that the CV response is positioned in the left part of the zone diagram with no effect of the global reaction of oxygen exchange (including in this model several elementary steps). After increasing ε_{LSCF} (green curve), the CV curve is only slightly translated horizontally to the left. When ℓ_{LSCF} is decreased (yellow curve), the voltammogram is translated vertically in zone 1 near zone $1 \cap 4$, as suggested by the limiting current falling to zero. This localization of the voltammetry curve for the quasi-dense thin film means that the CV response is characteristics of a uniform insertion reaction with no chemical reaction effect. Finally, the decrease of the scan rate shifts the CV response to zone 4 as shown by the purple peak shaped-curve in the corner of Fig. III-16b, indicating an increase of the chemical reaction effect.

In summary, the results of Fig. III-16 allow suggesting that:

(i) The simulated voltammograms with *model-II*, which are representative of the real behavior of the LSCF electrode, are consistent with the ones predicted by *model-I*, keeping in mind that the surface path is neglected in this ALS-based model (cf. section 3.1.6). This statement indicates that the semi-analytical solution and the corresponding zone diagram must provide a rather good estimation of the CV response for the LSCF electrode when the Ohmic losses are negligible. Thus, in the investigated conditions of the study, the attached species on the LSCF surface along with the gaseous oxygen in the porosity are not likely to play a major role in the CV response. This remark suggests that the CV behavior is mainly controlled by the transient accumulation or depletion of oxygen vacancies in LSCF as already pointed out in [Tezyk2019].

(ii) The positions in the zone diagram of the voltammograms obtained with *model-I* are shifted to the right compared to those obtained with the elementary model (*model-II*). As shown in Figs. III-16a and III-16b, it seems that a simple translation along the x-axis in the zone diagram is sufficient to recover the results of *model-II*. We can therefore suggest that the shift between the two models could come from a too large value of log λ and thus from an overestimation of k_{chem}. Indeed, the value of k_{chem} in *model-I* was determined using impedance spectra at OCP, while the accuracy of the i-V curves fitting under dc current was ignored (cf. Fig. III-15). In order to improve the match of the polarization curves under cathodic dc current, the value of k_{chem} was determined by fitting the cathodic polarization curve, as shown in Fig. III-20.

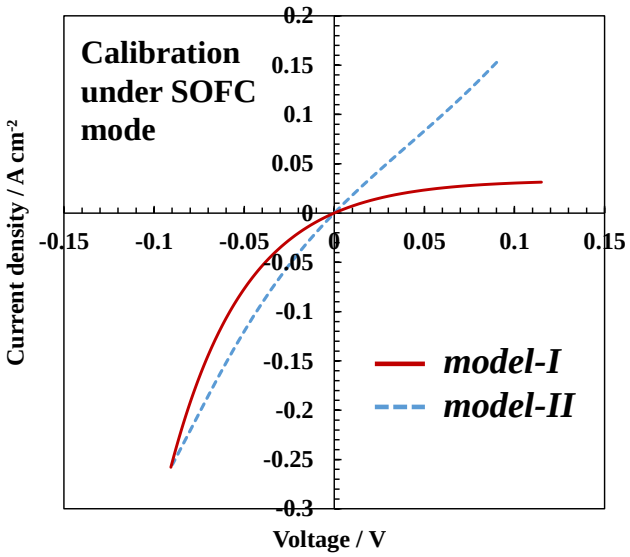

Fig. III-20. Calibration of *model-I* on the cathodic branch of the i-V curve obtained with *model-II* (at 700°C, P_{O_2} = 0.1 atm) (a). The red solid line represents the simulations with the *model-I*, while the blue dashed line represents the simulation with *model-II*.

One must remind that the discrepancy for the anodic polarizations can be related to the contribution of the dominant surface path in the reaction mechanism under SOEC mode. With this new fitting procedure, a lower value of k_{chem} has been obtained: typically, it is equal to $3.0 \cdot 10^{-8}$ m·s^{-1} when the parameter is determined in the potential range from 0 to - 0.1 V (this value is 4 times lower than the one determined from the fitting of the impedance diagram at OCP). The analysis to mimic the passage from a porous standard electrode to a quasi-dense film has been then repeated with *model-I*. As expected, the lower value of the kinetic constant has shifted the electrode response on the left in the zone diagram with a CV response closer to the one found with the elementary model (Fig. III-21).

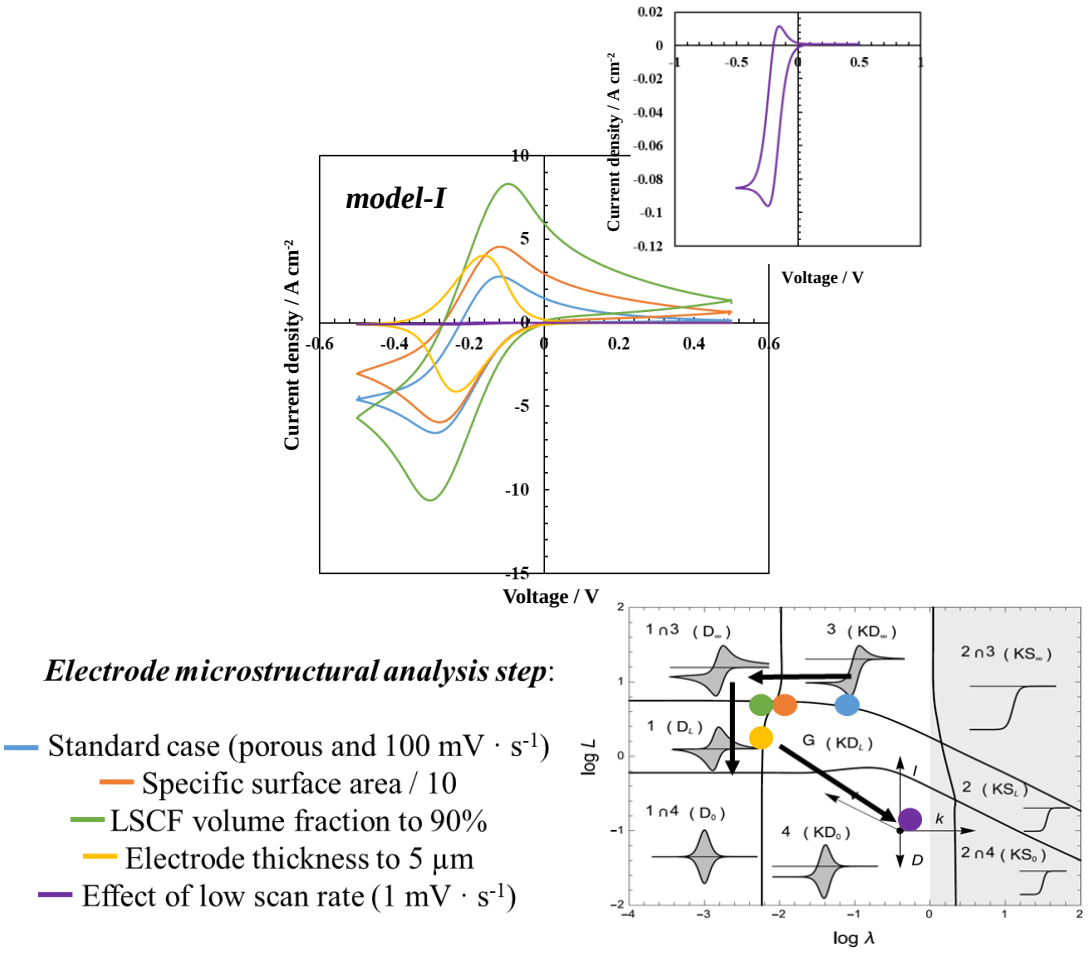

Fig. III-21 Cyclic voltammetry curves at 700 °C and P_{O_2}= 0.1 atm calculated with the second calibration of *model-I* (for k_{chem}=3.0·10^{-8} m·s^{-1}) without Ohmic losses ($\ell_{YSZ} \rightarrow 0$ and $R_c \rightarrow 0$). The passage from a porous electrode to a quasi-dense electrode has been simulated. The last curve at low scan rate has been magnified and reported in the quarter of the figure. The triangular potential waveform starts in the cathodic direction with A = 0.5V.

With the same hypothesis considering a translation on the x axis, the shift in the zone diagram has been estimated to $\Delta \log \lambda = -0.6$. For a perfect agreement between the two models, a lower value of k_{chem} would be thus necessary. This lower value could be obtained by fitting the polarization curves on a larger range of cathodic polarizations. Nevertheless, these results confirm that the difference between the two models is mostly related to an overestimation of k_{chem}. Therefore, as long as the Ohmic losses can be neglected, the semi-analytical model developed in our previous work [Montella2021] can be used to analyze the CV response of the LSCF electrode. For this

purpose, the chemical constant must be determined on the cathodic polarization curve and not only at OCP.

3.4.3.2 Cyclic voltammetry peaks evolution

The evolution of the voltammetry peaks has been investigated as a further comparison between the two models. In the ALS-based model (*model-I*), this evolution is determined by theoretical expressions that link the peak coordinates with the model input parameters. For instance, the current density for the cathodic peak j_{pc} in zone 1∩3 is expressed as followed [Montella2021]:

$$j_{pc}^{model-I} = -0.4463 \times 2FC_{O_o^x}^{max}\varepsilon_{LSCF}\left(2f\nu\frac{D_{chem}}{\tau_{LSCF}}\right)^{1/2} \quad (50)$$

This zone was selected as it corresponds to the behavior classically observed for the reversible electron transfer reaction with diffusion of the electroactive species in a planar semi-infinite medium [Bard2001]. This theoretical evolution of j_{pc} with the oxygen chemical diffusivity has been compared to the simulated data obtained with the elementary model (*model-II*) when the voltammograms is located in zone $1 \cap 3$. It means that we started from the orange curve in Fig. III-16b, located in zone 1 near zone $1 \cap 3$ and that we decreased the value of D_{chem} in order to rapidly enter in zone $1 \cap 3$. As it can be seen in Fig. III-22a, the peak current simulated with *model-II* evolves quite perfectly with the square root of the chemical diffusivity D_{chem} as predicted by Eq. (50). Indeed, the following expression has been fitted on the simulated data:

$$j_{pc}^{model-II} = -0.4200 \times 2 \cdot FC_{O_o^x}^{max}\varepsilon_{LSCF}\left(2f\nu\frac{D_{chem}}{\tau_{LSCF}}\right)^{1/2} \quad (51)$$

The numerical pre-factor identified with *model-II* for $j_{pc}^{model-II}$ is almost the same than the one in Eq. (50). This slight discrepancy between both slopes could come from the fact that the assumption $\xi^{eq} \to \infty$ used for establishing Eq. (50) is not fulfilled when E_{eq} is taken to zero in the numerical implementation of the two models (cf. section 3.1.6). Indeed, $\xi^{eq} = 4.896$ results in a slightly lower value of the coefficient 0.4463, as shown by the simulations in the supplementary document of our previous work [Montella2021] (see page 37, Fig. I.9).

In order to confirm the consistency between the two models, the CV response obtained with *model-I* has also been compared to the voltammogram simulated with the full elementary model (*model-II*) when both are calculated in the same 1 ∩ 3 zone. It can be shown in Fig. III-22b that the two types of voltammograms are almost superimposed since they are independent on k_{chem} in this zone. The current densities of the peaks are especially quite identical. This result reinforces the claim that the CV behavior for the LSCF material is practically only governed by the transient evolution of the oxygen under-stoichiometry (without a significant impact of the other species taken into account in *model-II*). This change in the oxygen vacancies in the material is obviously controlled by the fast ionic transfer at the electrolyte interface, the solid-state diffusion within the electrode thickness and the rate of oxygen exchange with the gas phase [Laurencin2015].

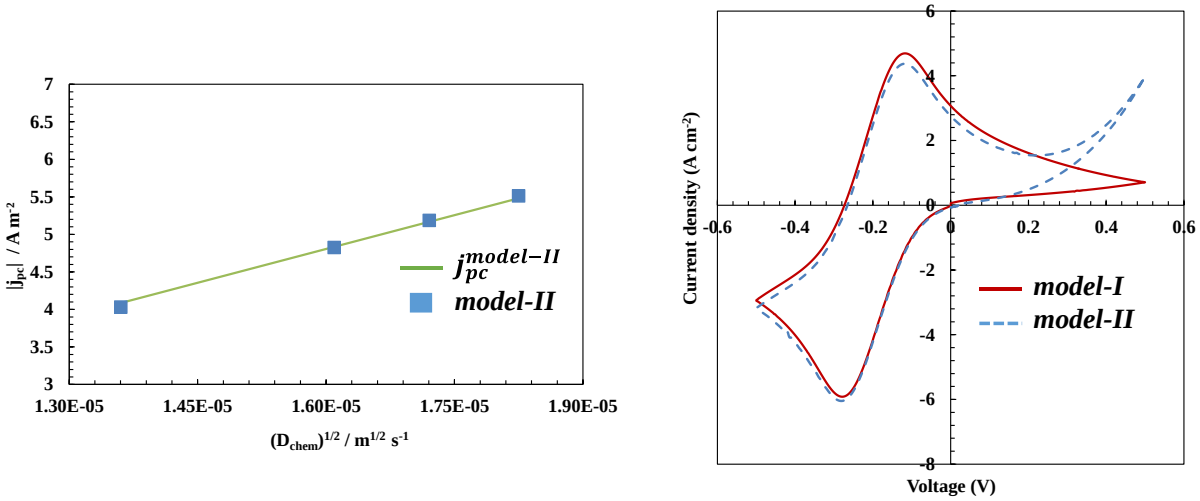

Fig. III-22 Current density of the cathodic peak as a function of the square root of the chemical diffusivity simulated with *model-II* (blue squares) and fitted with Eq. (50) (solid green line) (a). Comparison of the analytical solution (solid red curve) and full elementary model (dotted blue curve) (b) in zone 1 ∩ 3 (700 °C, P_{O_2} = 0.1 atm, A = 0.5 V, ν = 100 mV·s^{-1} without the Ohmic losses ($\ell_{YSZ} \rightarrow 0$ and $R_c \rightarrow 0$).

3.4.3.3 Impact of the Ohmic losses

The same approach as in section 3.4.3.1 has been repeated by taking into account the electrolyte thickness $\ell_{electrolyte}$ = 125 µm and the contact resistance $R_{contact}$ = 0.96 Ω.cm^2, at 700 °C and

P_{O_2} = 0.1 atm. This study was carried out to evaluate the effect of the Ohmic losses on the CV response with the two models. From Fig. III-23, it can be observed that the addition of the electrolyte and contact resistances in the models results in a complete distortion of the voltammograms. These simulations are obviously coherent with the experimental data reported in Fig. II-13 and Fig. II-14. Therefore, the information related to the voltammetry peaks is completely lost especially under cathodic polarization. This statement is in good agreement with the conclusion reported by Tezyk et al. [Tezyk2019]. Indeed, the authors have suggested that the Ohmic drop is a major limitation for the interpretation of CV experiments. Indeed, it cannot be compensated accurately because of variation of the series resistance with the polarization, meaning that the Ohmic drop compensation function of the classical electrochemical equipment is not efficient.

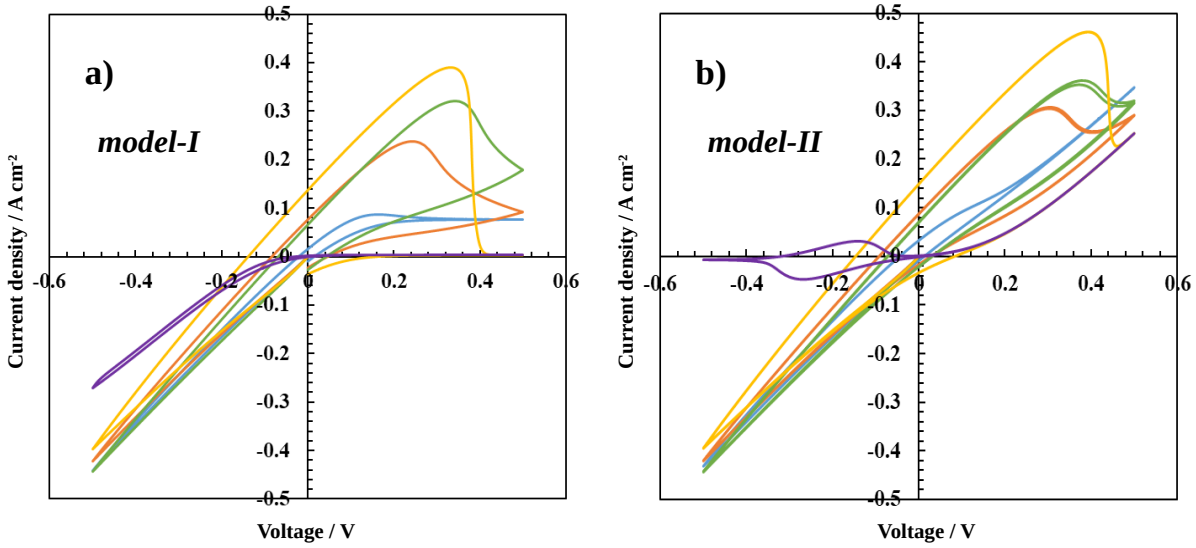

Fig. III-23 Evolution of the cyclic voltammetry curves from the case of a porous electrode to the case of a dense electrode for *model-I* (a) and *model-II* (b) at 700 °C, P_{O_2} = 0.1 atm and A = 0.5 V by taking into account the Ohmic losses (electrolyte and contact resistances). The same color code than in Fig. III-16 has been used.

From the comparison of the voltammograms obtained with the two models (Fig. III-23a and III-23b), it can be noticed that the global shape is quite similar except for the quasi-dense thin film simulated at a low scan rate (purple curves). In this case, one cathodic peak and a reverse anodic one are detected on the voltammogram simulated with *model-II*, whereas the curve obtained with *model-I* exhibits no peak (Fig. III-23a and III-23b). It is worth noting that the

curve obtained with the full elementary model is consistent with the results reported by Tezyk et al. [Tezyk2019] on a quasi-dense LSCF thin electrode deposited by Electrostatic Spray Deposition (ESD). Indeed, two voltammetry peaks were observed in this condition in contrast to the curves obtained for a more classical 'thick' porous LSCF electrode deposited by screen-printing. Therefore, this result also participates to highlight the reliability of the elementary model to predict accurately the CV curves. It can be noticed that the peak shaped voltammogram for the quasi-dense 'thin' film obtained with *model-II* is located in zone 4 (Fig. III-23b). Regarding *model-I*, the absence of peaks in the voltammogram confirms that the chemical constant fitted on the impedance diagram at OCP is overestimated as already mentioned. Indeed, the voltammogram obtained with this model without Ohmic losses is located near the shaded area of the zone diagram, corresponding to a sigmoidal shape of the CV response. It is worth emphasizing that it has been checked that the absence of limiting current density under catholic polarization is due to the use of too low voltage amplitude A for the simulation. Moreover, as the voltammogram is shifted to the left toward the zone 4 with the second model calibration (i.e. k_{chem} = 3.0·10^{-8} m·s^{-1}), the simulations have confirmed that the anodic and cathodic peaks start to appear in the CV response (Fig. III-24).

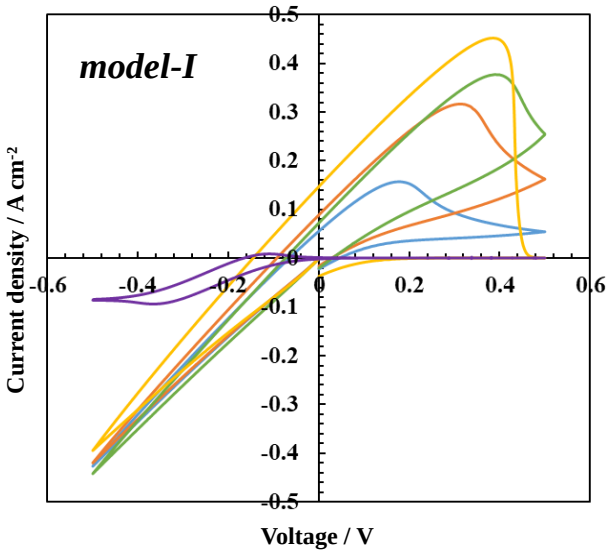

Fig. III-24 Cyclic voltammetry curves at 700°C , P_{O_2}= 0.1 atm calculated with the second calibration of *model-I* (for k_{chem}=3.0·10^{-8} m·s^{-1}) by taking into account the Ohmic losses (electrolyte thickness and contact resistances). The same color code than in Fig. 5 has been used for each step of the analysis. The potential waveform is the same as in Fig. III-16.

Since the Ohmic losses are the major limitation for the interpretation of the CV experiments, a sensitivity analysis has been carried out with *model-II* by changing the electrolyte thickness. The study has been performed considering the standard porous electrode by imposing two scan rates of 100 $mV \cdot s^{-1}$ and 5 $mV \cdot s^{-1}$. For the sake of clarity, the contact resistance has also been set to zero ($R_{contact} \rightarrow 0$). As shown in Fig. III-25, we observe the existence of a quasi-invariant point during the reverse scan whatever the scan rate. As expected, the dependency of the voltammograms with the Ohmic loss is less pronounced at low scan rate, due to lower current density values. For instance, the cathodic and reverse anodic peaks start to be detected for an electrolyte thickness of around 10 µm at 5 $mV \cdot s^{-1}$ whereas, in this condition, the voltammogram is still strongly distorted at 100 $mV \cdot s^{-1}$. Therefore, as expected, there is an optimum in terms of scan rate to detect the voltammetry peaks. Nevertheless, even at low scan rate, an electrolyte thickness of less than 10 µm is required to observe well-defined anodic and cathodic peaks. This statement demonstrates that, even with a very thin electrolyte without contact resistance, the CV measurements can be still strongly affected by the Ohmic losses. Therefore, in the operating conditions of the SOCs technology, there is no realistic experimental configuration that would allow avoiding this artifact for a clear highlight of the voltammetry peaks (i.e. by using the classical three-electrode setup since the electrolyte thickness is at least equal to 100 µm).

To overcome the problem of the ohmic drop compensation, the data analyses with a numerical tool could be a relevant strategy for studying the CV response of LSCF. Indeed, the modelling approach can be used to deconvoluate the effect of the Ohmic losses from the experimental voltammograms. For this purpose, after the prior model calibration on the experimental CV curves, the simulation just needs to be run a second time without the Ohmic losses. For this 'data post-processing', *model-I*, which is much easier to implement than *model-II*, can be used since it provides a rather good approximation of the CV response. Before this processing, it is obvious that the electrolyte resistance must be determined accurately at OCP with two-electrode measurements.

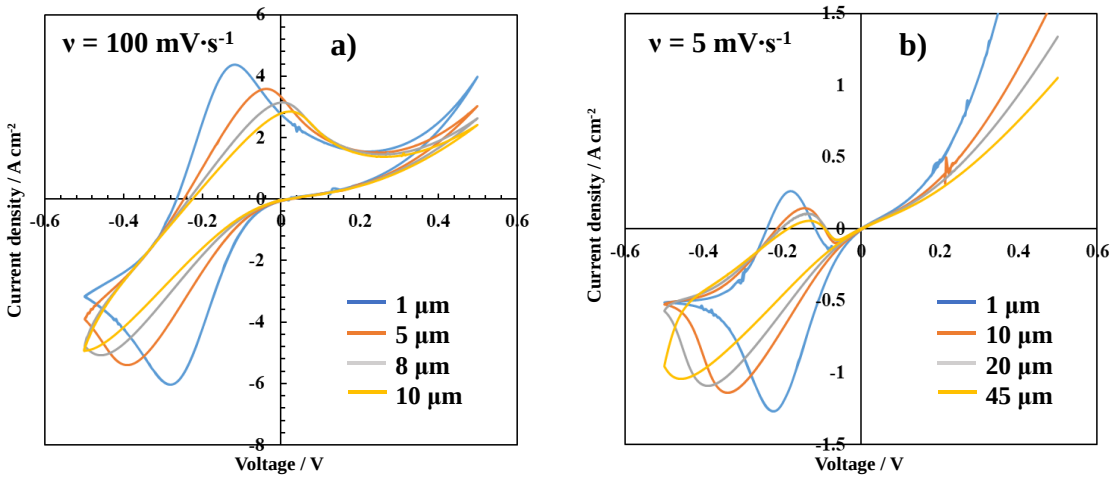

Fig. III-25 Effect of the electrolyte thickness on the cyclic voltammetry curves for the standard porous electrode, at 700 °C and P_{O_2} = 0.1 atm, simulated with *model-II* with a scan rate of 100 mV·s^{-1} (a) and 5 mV·s^{-1} (b), without contact resistance ($R_{contact} \rightarrow 0$). The potential waveform is the same as in Fig. III-16.

3.4 Conclusions

A full elementary kinetic model was developed to predict the electrochemical response of the LSCF and LSCF-CGO porous electrodes. The model describes the mass and charge fluxes in the porosity and in the bulk of the solid phases along with the transport of adsorbed species at the surface of the electrode particles. In this frame, the presence of oxygen ad-ions has been assumed onto the LSCF particles leading to take into account a surface electrostatic potential. For impedance simulations, the mass and charge conservations are solved in the time domain by taking into account the kinetic rates and the transient terms for all the considered species.

The elementary model was validated thanks to experiments performed on symmetrical cells using a three-electrode configuration. The missing parameters corresponding to the kinetic constants and surface diffusivities have been determined by fitting the polarization curves obtained at three temperatures (650 °C, 700 °C and 750 °C). It is worth mentioning that it was possible to identify a single solution of the fitted parameters for both electrodes thanks to the dissymmetry of the curves,

especially at low temperature. Besides, the two sets of values have been found to be consistent between the two types of studied electrodes. After the calibration, it has been shown that, without additional fitting, the model is able to simulate accurately the experimental EIS diagrams at OCP and under polarization of LSCF and LSCF-CGO oxygen electrodes for all the investigated temperatures. Moreover, the evolution of the electrode polarization resistance with the oxygen partial pressure is also well captured by the model. Indeed, a very good agreement has been found between the experimental and simulated reaction orders for both electrodes. Nevertheless, it can be mentioned that a systematic frequency lag was obtained between the measured and simulated diagrams. For this reason, further investigations are still required to elucidate the origin of this discrepancy.

Once validated, the model has been used to analyze deeply the LSCF and LSCF-CGO reaction mechanisms. It has been confirmed that, at low and intermediate temperatures (≤ 700 °C), the LSCF exhibits a net change of reaction pathway from the bulk to the surface path at low anodic polarization. However, this transition has been found to be smoother and delayed at higher anodic current with increasing the temperature (≥ 800 °C), probably due to the small overpotential value. On the contrary, the LSCF-CGO electrode remains fully controlled by the surface path except at low temperature and high cathodic polarization. Besides, the dependency of the reaction mechanism with the oxygen partial pressure has been also studied at 700 °C. For both electrodes, the decrease of the electrode polarization when increasing P_{O_2} is associated to a higher contribution of the surface path in the reaction mechanism. This behavior has been ascribed to the combined evolution of oxygen at the surface and in the bulk of LSCF as a function of P_{O_2}. In addition, the rate-determining steps at OCP have been identified for the LSCF depending on the oxygen partial pressure. When the reaction mechanism is mainly controlled by the bulk path at low P_{O_2}, the global kinetic rate is co-limited by the oxygen excorporation, the surface ionization and the desorption. For a higher contribution of the surface path at higher P_{O_2}, the charge transfer at TPBls and the surface diffusion of oxygen ad-ions become more and more co-limiting while the ionization and desorption remain two rate-determining steps.

Furthermore, the validated elementary model for the LSCF electrode has been extended to simulate cyclic voltammetry curves. In parallel, a numerical version of a semi-analytical model for the

voltammetry response for porous mixed conducting electrode has been implemented in the same modelling tool. The model takes into account the solid-state diffusion in LSCF coupled with a global reaction of oxygen exchange with the gas phase while the ionic transfer at the electrode/electrolyte interface is considered at equilibrium.

The relevance of the elementary model to predict the voltammograms has been checked using experimental data obtained by testing a symmetrical LSCF cell in a three-electrode configuration at different operating temperatures and scan rates. The good agreement between the measurements and the simulations has allowed validating the model capability to predict accurately the CV response.

A first sensitivity analysis has been performed with the two models by neglecting the Ohmic losses in the computation of the cyclic voltammetry at 700 °C and P_{O_2} = 0.1 atm. The microstructural properties and the thickness of the electrode have been successively changed to evolve from a classical porous electrode to a thin quasi-dense LSCF film. The results have been interpreted in the frame of the so-called zone diagram method. It has been found that the voltammograms obtained with the two models are very similar, confirming that the CV behavior of the LSCF material is mainly governed by the transient evolution of the oxygen content in LSCF. This evolution is mainly controlled by the solid-state diffusion within the electrode along with the chemical oxygen exchange with the gas phase taken account in the semi-analytical approach. In this condition, it has been established that this simplified model can provide a satisfactory approximation of the CV curves for the LSCF electrode.

Finally, the same study for porous and quasi-dense electrodes have been repeated taking into account the Ohmic losses in the simulations. It has been shown that they induce a strong distortion of the voltammograms making their interpretations impossible in practice. In this frame, it has been established that an electrolyte thickness as low as 10 µm is needed to reveal the voltammetry peaks at low scan rates (without any contact resistance). To overcome this issue, a methodology using the modeling approach has been proposed. It consists in the post-processing of the experimental data with the semi-analytical model to remove the Ohmic losses and thus highlight the voltammetry peaks, once the electrolyte resistance was accurately determined.

Chapter IV. Impact of the LSCF demixing

Once the full elementary model has been validated and its reliability has been ensured (cf. Chapter III), this model has been used to investigate the impact of the LSCF decomposition on the electrode response. In particular, the effects of the surface passivation and loss of ionic conductivity have been studied by decreasing the electrode surface area and the chemical diffusivity, respectively. The sensitivity analysis has been carried out by simulating the increase of the polarization resistance of the simulated impedance diagrams due to the degradation both at OCP and under anodic or cathodic polarizations. Indeed, even if experimental evidences have suggested that the LSCF decomposition could be higher in SOEC mode (cf. section 2.2.1), the exact impact of the operating mode on the electrode performances remains still unclear.

The same analysis has been undertaken for the cyclic voltammetry response of LSCF still using the full elementary model. This study was performed to evaluate the relevance of this technique for investigating the degradation of porous MIEC electrodes without any Ohmic losses.

4.1 Impact of the LSCF decomposition on the impedance diagrams

As mentioned in Chapter II, the LSCF decomposition upon operation is liable to decrease the global exchange kinetic constant k_{chem} due to the LSCF surface passivation. Besides, the loss of strontium can affect the oxygen chemical diffusion coefficient D_{chem} by modifying the oxygen stoichiometry in the bulk of the material. To date, few data are reported in the literature to estimate the decay of k_{chem} and D_{chem} due to the demixing for the classical $La_{0.6}Sr_{0.4}Co_{0.2}Fe_{0.8}O_{3-\delta}$ compound. Wang *et al.* [Wang2016] have estimated a decrease of D_{chem} and k_{chem} of 50 % after an isothermal ageing of symmetric cells at 800 °C for 800 hours under air. However, the same authors have also reported a decrease of around 85 % for k_{chem} with no significant change in D_{chem} for LSCF electrodes annealed at 700-800 °C for the same period under air [Wang2018]. In addition, Kim *et al*. [Kim2019a] have found a severe decrease of k_{chem} estimated to 85 % whereas the deviation in the chemical diffusivity is only of 8 % for sintered LSCF pellets after a thermal ageing at 800 °C for 800 h under air. For an ageing at 750 °C during 1012 h using complete cells, Endler-Schuck *et al*. [Endler-Schuck2015] have found that the 'performance degradation in the LSCF electrode seems to be caused by a decrease of the bulk diffusion while the exchange coefficient remains almost

constant'. At 600 °C, they have found that both parameters decreased with the operating time. Therefore, there is still a large uncertainty on the real impact of the LSCF demixing on the values of D_{chem} and k_{chem}. Wang *et al.* [Wang2018] have proposed that this apparent discrepancy could be explained by a potential slight deficiency on the A-site of the perovskite that could lead to different Sr segregation. Furthermore, it can be suspected that the experimental conditions such as the presence of residual steam in the gas stream may also influence the results [Lu2019].

In spite of this scattering of the published results, the full elementary model has been used to assess the impact of the LSCF demixing on the electrode response. Firstly, the electrode surface passivation was simulated by decreasing the specific surface area between the LSCF and the gas phase ($S_p^{LSCF/gas}$). Indeed, the kinetics of the surface reactions for the common path as well as the reaction of oxygen incorporation/excorporation (R2) for the bulk path are proportional to this parameter (cf. Table I in Chapter III). It is worth noting that the combination of all these reaction kinetics results in the global exchange kinetic constant k_{chem} usually estimated at OCP according to the 'ALS' model [Endler-Schuck2015, Wang2018, 2016]. Secondly, the loss of ionic conductivity due to the Sr release from the perovskite lattice was simulated by decreasing the oxygen chemical diffusion coefficient (D_{chem}). The sensitivity analysis was carried out for the LSCF electrode computing the impedance diagrams at 750 °C under air at OCP and for a dc current of ± 50 mA·cm^{-2}. The electrode degradation was simulated by decreasing each parameter by step of 10 % up to 50%. This range was chosen since a decrease of 10 % can be roughly seen as a lower bound for the degradation, while a decrease of 50 % remains in the scale of the reasonable published values. Finally, it can be mentioned that the bulk path is prevailing in the chosen conditions for the simulations (cf. section 3.3.1). Indeed, the bulk path must be favored to determine the effect of the oxygen chemical diffusivity on the polarization resistance of LSCF.

4.1.2 Analysis of the degradation at OCP

The evolutions of the impedance diagrams and frequency distributions in the Nyquist and Bode plots are shown in Fig. IV-1a and IV-1b as a function of the surface passivation at OCP. An enlargement of the diagram for the contribution at low frequencies is found (Fig. IV-1a), which is accompanied by a slight shift of the frequency distribution towards lower values (Fig. IV-1b). These evolutions are expected since the LSCF/gas specific surface area impacts the excorporation

(R2), deionization (R4) and desorption (R6) identified as the rate-determining steps at OCP. Indeed, it has been observed that all these reactions are at the origin of the skewed semicircle arising at low frequencies in the spectrum. Regarding the loss of ionic conductivity, the decrease of D_{chem} induces a swelling of the contribution at intermediate frequency in the Gerischer type-element (Fig. IV-1c). This behavior is associated to the diffusion of the oxygen vacancies in LSCF co-limiting the electrode response [Hubert2016]. This evolution is concomitant with a very slight increase of the peak frequency in the Bode plots (Fig. IV-1d). At OCP, it can be noticed that the impact of the specific surface area on R_{pol} (Fig. IV-1e) is higher with respect to the loss of ionic conductivity (Fig. IV-1f). Considering a decrease of 30 % for both studied parameters, the polarization resistance is increased by 25 % for the surface passivation, while an augmentation of only 12 % was simulated for the loss of ionic conductivity. This result means that the co-limitation at OCP due to the reactions involved in the bulk path is higher than the resistance induced by the diffusion of oxygen vacancies diffusion in LSCF.

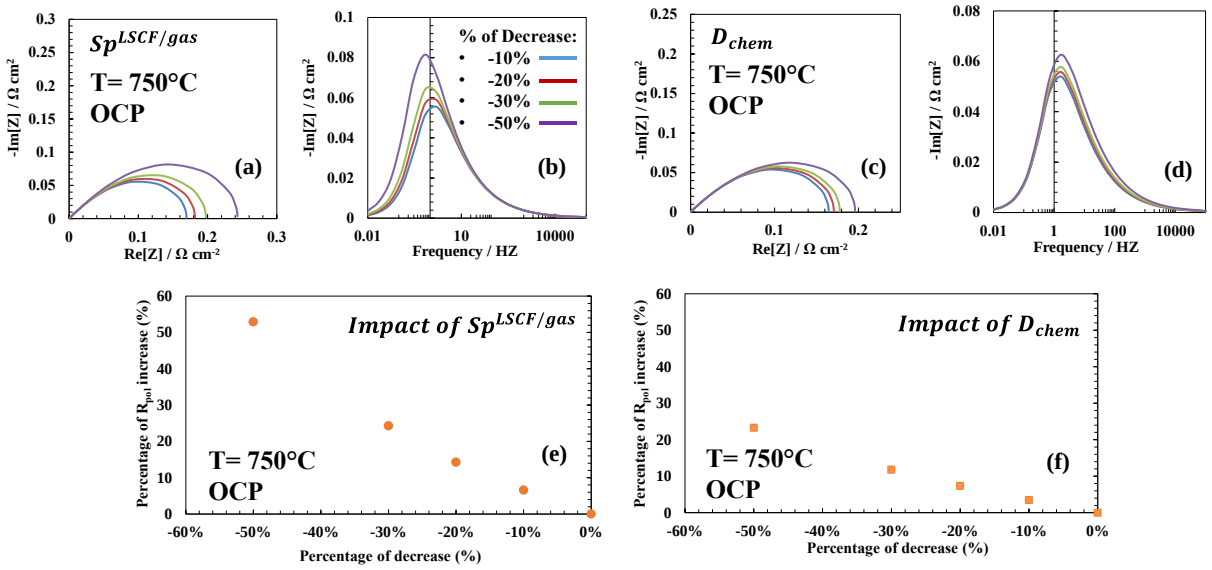

Fig. IV-1. Sensitivity analysis on the surface passivation ($S_p^{LSCF/gas}$) and on the loss of ionic conductivity (D_{chem}) at 750 °C under air at OCP. Nyquist and Bode plots evolution (a) and (b) for the surface passivation and (c) and (d) for the loss of ionic conductivity, respectively. Evolution of the polarization resistance with the decrease of (e) the specific surface area and of (f) the chemical diffusivity.

4.1.3 Analysis of the degradation under polarization

As expected (cf. section 3.3.1), the same trends have been observed for the evolutions of the impedance diagrams under dc currents. The degradation of the electrode polarization resistance due to the surface passivation in SOFC and SOEC modes is given in Fig. IV-2a, while the impact of the loss of ionic conductivity is shown Fig. IV-2b. It is found that the decrease of the specific surface area is more impacting when the electrode is operated in SOEC mode compared to SOFC mode. This result can be correlated with the higher contribution of the surface path under anodic polarization. In this condition, the two pathways become co-limited by decreasing the surface reaction belonging to the common path. Besides, it is worth reminding that the flux of the adsorbed oxygen ions, which have been identified as a rate-determining step for the surface path (cf. section 3.3.1), also depends on the LSCF/gas specific surface area. Therefore, the decrease of this flux due to the surface passivation prevents the activation of the surface path.

In contrast to the passivation, the electrode performances are more impacted by the decrease of D_{chem} when it is operated in SOFC mode. Indeed, as already mentioned, the bulk path is co-limited by the oxygen solid-state diffusion in the perovskite. Therefore, the decrease of the ionic conductivity due to the LSCF demixing is especially harmful when this reaction pathway is predominant.

It can be noticed in Fig. IV-2 that the impact of the surface passivation on the electrode response seems to be higher than the one induced by the loss of ionic conductivity. This result would indicate that the contribution of the LSCF demixing on the loss of electrode performances is more related to the surface deactivation than to an evolution of the LSCF bulk properties. This suggestion is in good agreement with the statement made by some authors who have observed an electrode recovery thanks to an LSCF surface etching treatment after aging [Lu2019, Pan2015b]. Therefore, the present modeling result would strengthen the claim that 'the degradation is most likely due to the emergence of surface inhibited species on LSCF electrode' [Pan2015b].

Moreover, the sum of the degradation due to the surface passivation and the loss of ionic conductivity, is higher in SOEC mode (Fig. IV-2). In other words, the impact of LSCF degradation is higher under anodic polarization, addressing a double penalty for this operating mode since the Sr segregation seems to be also promoted in this operating mode [Chen2015, Huber2012, Li2017, Laurencin2017]. Finally, it is worth mentioning that, even for the considered lower bound for the LSCF decomposition, the impact on the electrode performance is not negligible meaning that the demixing remains an important issue for the durability of SOCs.

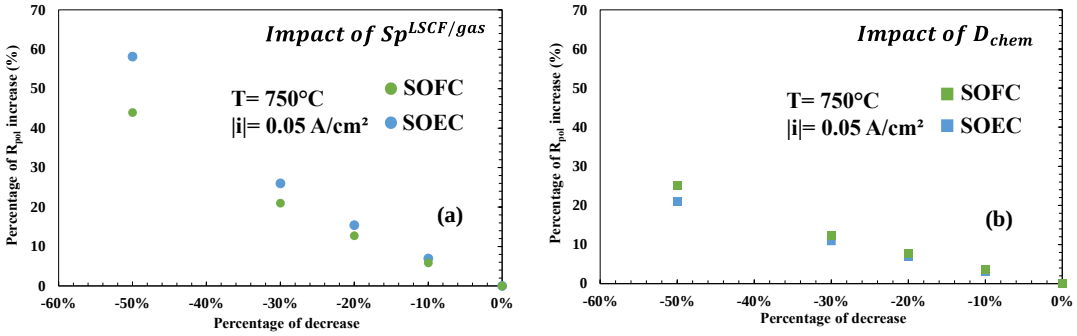

Fig. IV-2. Sensitivity analysis on (a) and (b) the surface passivation ($S_p^{LSCF/gas}$) and the loss of ionic conductivity (D_{chem}) at 750 °C under air with a dc current of +/- 50 mA·cm^{-2}. The green points represent the values computed under cathodic polarization, while the blue points represent the values computed under anodic polarization.

4.2 Analysis of the degradation on the cyclic voltammetry response

The impact of the LSCF decomposition on the CV response has been investigated with the elementary model (*model-II*) without electrolyte. The analysis has been conducted considering the classical porous electrode as the standard case numerically tested at 700 °C, P_{O_2}= 0.1 atm, A = 0.5 V and v = 100 mV·s^{-1}. To mimic the impact of the surface passivation and the loss of ionic conductivity, the electrode specific surface area S_p^{LSCF} and the oxygen chemical diffusion coefficient D_{chem} have been respectively decreased up to 50 % of their original values. This evolution can be seen as an upper bound for the material degradation as mentioned above. The simulated cyclic voltammograms have been interpreted in the frame of the zone diagram. As mentioned in section 3.4.3, the CV curve for the standard case falls in proximity of zone 1 ∩ 3 (Fig. III-16b). In this zone, the electrode behavior is mainly controlled by the oxygen diffusion with no effect of the global reaction of oxygen exchange. Therefore, no evolution in the CV curves has been found when decreasing S_p^{LSCF} (Fig. IV-3a). To highlight the impact of this microstructural parameter, the scan rate was lowered down to 5 mV·s^{-1} to shift the CV response in a zone where the electrode behavior is controlled by the reaction of oxygen exchange with the gas phase. In this condition, the effect of the surface passivation is clearly shown in Fig. IV-3b. According to the shape of the voltammograms in this figure, the CV behavior would be located in zone 4 of the diagram (this new location is explained since the decrease of the scan rate induces an increase of λ

and a decrease of L (cf. Eqs. (47) and (48) in Chapter III). Moreover, it is found that the limiting current density under cathodic polarization is decreased by decreasing the electrode specific surface area, as expected from the analytical solution (indeed, this evolution is due to the progressive displacement to the left in the zone diagram when S_p^{LSCF} is decreased).

Considering the loss of ionic conductivity, the voltammograms are substantially affected by the decrease of D_{chem} (Fig. IV-3c). Indeed, the voltammetry curve depends only on the oxygen solid-state diffusion in LSCF in zone 1∩3 for the standard case. Moreover, the current density for the cathodic peak is increased with D_{chem}, in agreement with Eq. (51).

Once the Ohmic losses have been subtracted, it appears from the present study that the LSCF decomposition can be potentially detected using the cyclic voltammetry (at least after substantial material degradation). The analysis of the variation of the CV curves would thus provide useful insights on the effect of LSCF demixing on both the surface passivation and the change in the material properties. From a qualitative point of view, the existence of a limiting current density under cathodic polarization for peak shaped voltammograms will suggest an increase of the chemical reaction effect meaning that a mixed chemical-kinetic and diffusion control should be anticipated. It is worth mentioning that a variation of the oxygen chemical diffusivity will affect the magnitude of the polarization resistance without any significant modification of the shape of EIS diagrams. From transient cyclic voltammetry, one can expect a variation of dissymmetry between cathodic and anodic peaks (see Fig. III-16). Moreover, CV measurements are not sensitive to the cell symmetry and no artifacts could be anticipated as compared to impedance measurements [Guo2018]. For these reasons, cyclic voltammetry can give a new insight on the characterization of LSCF-based electrodes under operating conditions.

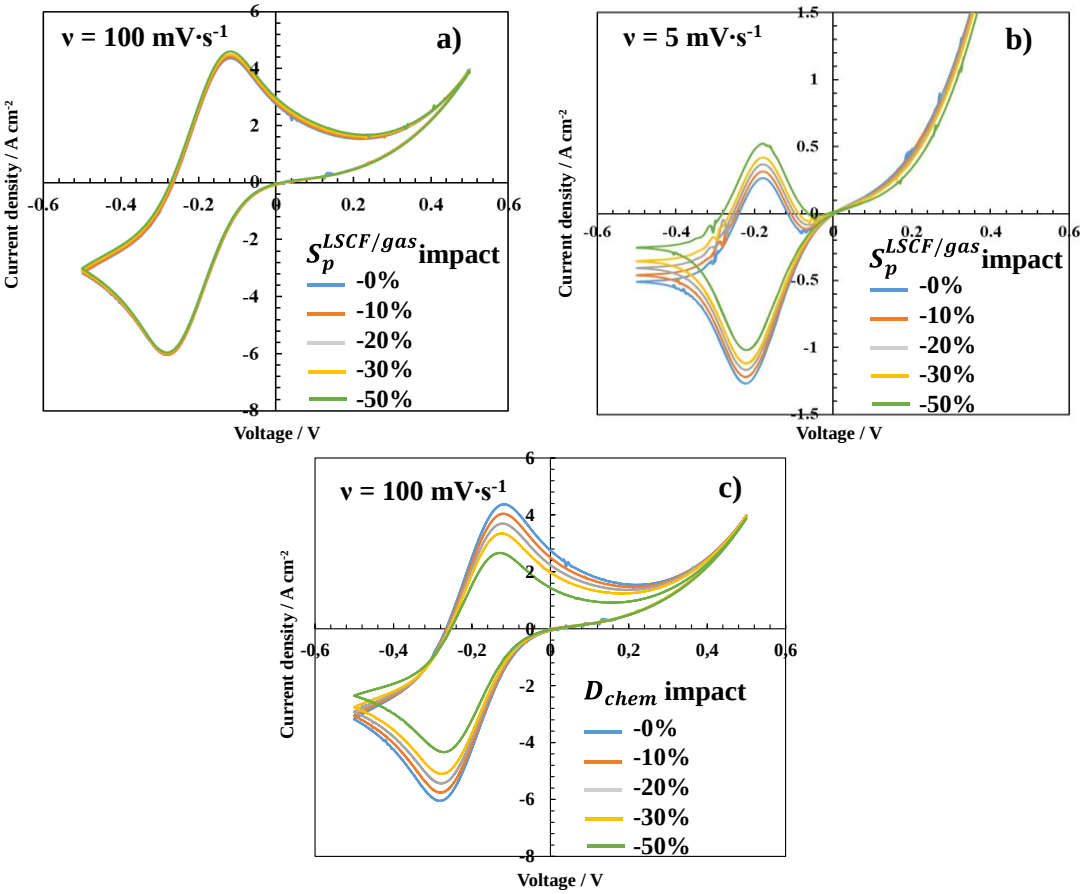

Fig. IV-3 Study of the impact of surface passivation ($S_p^{LSCF/gas}$) at 100 mV·s^{-1} (a) and 5 mV·s^{-1} (b) and of the loss of ionic conductivity (D_{chem}) (c). The simulations have been performed with *model-II* at 700 °C, P_{O_2} = 0.1 atm and A = 0.5 V for the porous LSCF electrode without the Ohmic losses ($\ell_{YSZ} \rightarrow 0$ and $R_c \rightarrow 0$).

4.3 Conclusions of the chapter

The impact of the perovskite decomposition on the LSCF electrode response has been studied with the model at OCP and under anodic and cathodic dc currents. The surface passivation and the loss of ionic conductivity have been simulated by decreasing the specific surface area and the chemical diffusivity, respectively. At OCP, the impact of the demixing on the evolution of the impedance diagrams have been discussed. It has been shown that the passivation affects the contribution at

low frequency in the Gerischer-type element while the loss of ionic conductivity enlarges the contribution at intermediate frequency.

It has been stated that the surface passivation is more affecting the electrode response when the performances are evaluated in SOEC mode. On the contrary, the electrode polarization resistance is more sensitive to the decrease of ionic conductivity when the response is evaluated in SOFC mode. Finally, whatever the conditions, it appears that the surface passivation would be more impacting than the decrease of the ionic conductivity. Moreover, the sum of the degradation induced by the two phenomena is higher when the electrode response is computed in anodic polarization. Therefore, the LSCF decomposition would be more detrimental for the electrode performances in SOEC mode.

Finally, the impact of the LSCF demixing has been studied on the CV response as well using the full elementary model. Both the surface passivation for a low scan rate and the decrease of the chemical diffusivity have been found to change significantly the voltammograms. Therefore, this technique could be seen as a supplementary method to complement the more conventional electrochemical characterizations used for the application of SOCs.

Chapter V. Conclusions and Outlooks

In this study, a microscale modelling has been developed considering reaction mechanisms decomposed in elementary steps for oxygen electrodes in LSCF and LSCF-CGO. For each electrode, the model calibration has been performed on the polarization curves recorded in specific gas conditions at three different operating temperatures. One single solution has been found for the set of fitted parameters (reaction kinetic constants, surface coverage rates at equilibrium and surface diffusivities) thanks to the non-symmetrical shape of the i-V curve at low temperature. After the calibration, the model has been validated on a large set of experimental data with impedance diagrams at OCP and under polarization. Moreover, the effect of the oxygen partial pressure has also been studied by taking advantage of the detailed surface reaction mechanism. As expected, a very good agreement has been found between the simulated and the experimental reaction orders for both studied electrodes thanks to the implemented elementary approach.

The validated model has been used to investigate the electrode reaction mechanisms as a function of the different operating conditions. It has been confirmed that the LSCF-CGO electrode is dominated by the surface path whatever the polarization (except under high cathodic polarization at low operating temperature). On the other hand, a transition between the surface and the bulk paths has been found for the LSCF electrode that becomes more and more delayed at high anodic polarization with the increase of the operating temperature. Besides, the dependency of the reaction mechanism with the oxygen partial pressure has been studied at 700 °C. Both electrodes exhibited an increase in performances with the increasing of the oxygen partial pressure associated to a higher contribution of the surface path in the reaction mechanism. In addition, the rate-determining steps at OCP have been identified for the LSCF electrode depending on the oxygen partial pressure. It has been found that, at low P_{O_2}, the reaction mechanism is mainly controlled by the bulk path and the global kinetic rate is co-limited by the oxygen excorporation, the surface ionization and the desorption. Conversely, at higher P_{O_2}, the contribution of the surface path gradually increases. In this case, the charge transfer at TPBls along with the surface diffusion of oxygen ad-ions become more and more co-limiting, while the ionization and desorption remain rate-determining steps.

Furthermore, the non-linear response of the electrodes has been studied modelling the cyclic voltammetry. For this purpose, the LSCF elementary model has been extended to simulated CV curves and the corresponding simulations have been validated on the experimental data recorded

at different operating temperatures and scan rates. A good agreement has been found between the computation and the measurements. At the same time, an ALS based model, for which semi-analytical solutions are existing, has been implemented on the same modelling tool. The comparison between this semi-analytical model and the elementary one has highlighted the relevance of a simplified approach for the description of the LSCF CV curves. To conclude, a methodology to remove the Ohmic drop with the use of a numerical tool has been proposed that allows overcoming the issues related to the distortion of the experimental voltammograms.

As a general comment, a very good agreement has been found for both studied electrodes in all the investigated operating conditions. This result allows considering the methodology (modelling coupled microstructural and electrochemical characterizations) as a valid approach to study the electrochemical behavior of porous oxygen electrode. Thus, it could be extended to other types of materials such as the nickelates.

As an outlook, a third surface charged species (O_2^{2-}) will be introduced in the model as a further refinement of the LSCF electrode reaction mechanism. Nevertheless, in order to ensure its presence on the electrode surface, ab initio computations are necessary. For this reason, the Density Functional Theory Calculations (DFT) will be used to complement the methodology. Indeed, this technique will permit to study the electrode at the atomic scale and to calculate the diffusivities of the species on the LSCF surface, the activation energies and the surface reaction kinetic constants reducing the large number of unknown parameters, which is typical of the elementary kinetic approach (thesis of Giuseppe Sassone).Concerning the hydrogen electrode, the experimental data presented in Chapter II obtained by testing a cermet symmetrical cell in a three-electrode set-up have been used in the thesis of Federico Monaco to validate a microscale model. In the frame of the present work, a special effort has been paid to the testing set-up capable to provide a controlled and stable steam flow over a large range of steam partial pressure. The low noise in the impedance spectra and the good tightness of the cell housing have confirmed the reliability of the experimental set-up. The validated model has been used to discriminate the reaction pathway for porous Ni-3YSZ electrodes that would be controlled by a double hydrogen spillover mechanism. However, the electrochemistry of this electrode material is less clear with respect to the oxygen electrode. Therefore, the use of DFT calculations would be also a meaningful tool that could help the validation of the proposed reaction mechanism for the hydrogen electrode (thesis of Léa Rorato).

In addition, the hydrogen model has been used to study the electrode microstructural evolution over the time. In particular, a mechanism for the Ni migration has been proposed which could explains the aggravating degradation under electrolysis conditions. In this mechanism, the accumulation of oxygen vacancies at the Ni/YSZ interface that occurs under cathodic polarization may justify the migration away from the electrolyte interface. However, the precise course of this phenomenon remains still an open question. For this reason, further investigations based on long-term tests coupled with simulations at both electrode and complete cell levels are planned in order to confirm the proposed mechanism. Moreover, the Ni migration is strictly related to the electrochemistry of the electrode since it is activated by the cathodic overpotential. In this perspective, DFT calculations will be used to find the law linking the Ni wettability angle and the accumulation of vacancies in the double layer. Finally, in complementary with the classical electrochemical characterization techniques, the cyclic voltammetry could be used to obtain more valuable informations on the hydrogen electrode behavior (thesis of Léa Rorato).

To take advantage of the reliability of the extensively validated model for the oxygen electrode, the impact of the LSCF demixing has been studied in this study through a sensitivity analysis carried out on (i) the decrease of the surface passivation and (ii) the loss of ionic conductivity. It has been confirmed that the surface passivation remains the most detrimental phenomenon both at OCP and anodic polarization, while the decrease of the oxygen chemical diffusivity is more affecting in SOFC mode. Interestingly, it has been shown that the increase of the polarization resistance is substantially higher in electrolysis mode respect with the fuel cell mode at the same level of material decomposition. This result means that not only the LSCF demixing is aggravated under SOEC mode (as already observed experimentally), but that its impact on the electrode performances is also higher.

The same analysis has been repeated with the cyclic voltammetry technique. An evident change in the voltammograms shapes has been detected with the decrease of both the specific surface area and the chemical diffusivity. This result has allowed considering the CV as a supplementary electrochemical technique for the studying of the oxygen electrode degradation.

From the experimental point of view, a long-term test performed on a LSCF symmetrical cell has confirmed the acceleration of the degradation for the electrode operated under anodic polarization.

The post-test characterizations through micro x-ray diffraction have revealed an enlargement of the unit cell volume correlated to the release of strontium. This result is in good agreement with the degradation mechanism proposed by our group that predicts a higher precipitation of Sr cations under electrolysis mode. On the other hand, two durability tests carried out on complete cells with the oxygen electrode in LSCF have been carried out under dry air and by adding moisture at the anode side both in SOEC mode. From the recorded endurance curves, a stronger degradation rate has been found for the cell operated with the addition of water in the sweeping air flow. However, a second campaign of long-term tests in fuel cell mode is still needed before concluding on the aggravating effect of the steam on the LSCF performances. For this purpose, the same tests will be performed also in SOFC mode and post-test characterizations of all tested cells will be performed.

To conclude, as last perspective related to this thesis work, the phenomenological and physical laws for the description of the LSCF degradation phenomena (strontium segregation, formation of secondary phases etc.) will be implemented in the model to further improve its predictability (thesis of Giuseppe Sassone). Indeed, while the impact of the degradation on the electrode performances is clear (i.e. Chapter IV), the degradation mechanisms themselves remain still subjects of investigation. In this frame, long-term tests will be performed at the electrode and complete cell levels. Several techniques will be used for the post-test characterizations of the aged samples, in order to collect the parameters necessary to simulate of the evolution of the material decomposition. Finally, as well as for the study of the reaction mechanisms, also the DFT will be used to investigate the electrode behavior at the atomic scale. This methodology will be subsequently extended to other kinds of oxygen electrode material.

References

[Aziz2020] Aziz A., Junaida A., Baharuddin N. A., Somalu M. R., and Muchtar A. "Review of Composite Cathodes for Intermediate-Temperature Solid Oxide Fuel Cell Applications." *Ceramics International* 46, no. 15 (October 15, 2020): 23314–25. https://doi.org/10.1016/j.ceramint.2020.06.176.

[Adler1998] Adler S. B. "Mechanism and Kinetics of Oxygen Reduction on Porous $La_{1-x}Sr_xCoO_{3-\delta}$ Electrodes." *Solid State Ionics* 111, no. 1 (August 1, 1998): 125–34. https://doi.org/10.1016/S0167-2738(98)00179-9.

[Adler2002] Adler S. B. "Reference Electrode Placement in Thin Solid Electrolytes." *Journal of The Electrochemical Society* 149, no. 5 (April 2, 2002): E166. https://doi.org/10.1149/1.1467368.

[Adler2000] Adler S. B., Henderson B. T., Wilson M. A., Taylor D. M., and Richards R. E. "Reference Electrode Placement and Seals in Electrochemical Oxygen Generators." *Solid State Ionics*, Festschrift dedicated to Prof. Brian Steele, 134, no. 1 (October 1, 2000): 35–42. https://doi.org/10.1016/S0167-2738(00)00711-6.

[Adler1996] Adler, S. B., Lane J. A., and Steele B. C. H. "Electrode Kinetics of Porous Mixed-Conducting Oxygen Electrodes." *Journal of The Electrochemical Society* 143, no. 11 (November 1, 1996): 3554. https://doi.org/10.1149/1.1837252.

[Adler2004] Adler S.B. "Factors Governing Oxygen Reduction in Solid Oxide Fuel Cell Cathodes." *Chemical Reviews* 104, no. 10 (October 1, 2004): 4791–4844. https://doi.org/10.1021/cr020724o.

[Al Daroukh2015] Al Daroukh M., F. Tietz, D. Sebold, H. P. Buchkremer. "Post-Test Analysis of Electrode-Supported Solid Oxide Electrolyser Cells." *Ionics* 21, no. 4 (April 2015): 1039–43. https://doi.org/10.1007/s11581-014-1273-2.

[Anderson2004] Anderson M. D., J. W. Stevenson, S. P. Simner. "Reactivity of Lanthanide Ferrite SOFC Cathodes with YSZ Electrolyte." *Journal of Power Sources* 129, no. 2 (April 22, 2004): 188–92. https://doi.org/10.1016/j.jpowsour.2003.11.039.

[Ascolani-Yael2020] Ascolani-Yael J., Montenegro-Hernández A., Garcés D., Liu Q., Wang H., Yakal-Kremski K., Barnett S., Mogni L. "The Oxygen Reduction Reaction in Solid Oxide Fuel Cells: From Kinetic Parameters Measurements to Electrode Design." *Journal of Physics: Energy* 2, no. 4 (October 9, 2020): 042004. https://doi.org/10.1088/2515-7655/abb4ec.

[Atangulov1993] Atangulov, R. U., Murygin I. V. "Gas Electrode Impedance with Slow Adsorption and Surface Diffusion." *Solid State Ionics* 67, no. 1 (December 1, 1993): 9–15. https://doi.org/10.1016/0167-2738(93)90302-J.

[Athanasiou2020] Athanasiou M., Niakolas D.K., Bebelis S., Neophytides S. G. "Steam Effect on Gerischer Impedance Response of a Ni/GDC|YSZ|LSM Fuel Cell / Anode." *Journal of Power Sources* 448 (February 1, 2020): 227404. https://doi.org/10.1016/j.jpowsour.2019.227404.

[Bard2001] Bard A. and Faulkner L. Wiley.com. "Electrochemical Methods: Fundamentals and Applications, 2nd Edition | Wiley." Accessed May 21, 2021.

[Baumann2007] Baumann F. S., Fleig J., Cristiani G., Stuhlhofer B., Habermeier H.-U., Maier J. "Quantitative Comparison of Mixed Conducting SOFC Cathode Materials by Means of Thin Film Model Electrodes." *Journal of The Electrochemical Society* 154, no. 9 (July 17, 2007): B931. https://doi.org/10.1149/1.2752974.

[Baumann2006] Baumann F. S., Fleig J., Habermeier H.-U., Maier J. “Impedance Spectroscopic Study on Well-Defined (La,Sr)(Co,Fe)$O_{3-\delta}$ Model Electrodes.” *Solid State Ionics* 177, no. 11 (April 1, 2006): 1071–81. https://doi.org/10.1016/j.ssi.2006.02.045.

[Bebelis2006] Bebelis, S., Kotsionopoulos N., Mai A., Tietz F. “Electrochemical Characterization of Perovskite-Based SOFC Cathodes.” *Journal of Applied Electrochemistry* 37, no. 1 (December 14, 2006): 15–20. https://doi.org/10.1007/s10800-006-9215-y.

[Bebelis2008] Bebelis, S., Kournoutis V., Mai A., Tietz F. “Cyclic Voltammetry of $La_{0.78}Sr_{0.2}FeO_{3-\delta}$ and $La_{0.78}Sr_{0.2}Co_{0.2}Fe_{0.8}O_{3-\delta}$ Electrodes Interfaced to CGO/YSZ.” *Solid State Ionics*, Solid State Ionics 16: Proceedings of the 16th International Conference on Solid State Ionics (SSI-16), Part I, 179, no. 21 (September 15, 2008): 1080–84. https://doi.org/10.1016/j.ssi.2008.02.028.

[Bessler2006] Bessler W. G. “Gas Concentration Impedance of Solid Oxide Fuel Cell Anodes: I. Stagnation Point Flow Geometry.” *Journal of The Electrochemical Society* 153, no. 8 (June 7, 2006): A1492. https://doi.org/10.1149/1.2205150.

[Bessler2007] Bessler, W. G., Gewies S., Vogler M. “A New Framework for Physically Based Modeling of Solid Oxide Fuel Cells.” *Electrochimica Acta*, POLYMER ELECTROLYTES Selection of papers fromThe 10th International Symposium (ISPE-10)15-19 October 2006, Foz do Iguaçú-PR, Brazil, 53, no. 4 (December 31, 2007): 1782–1800. https://doi.org/10.1016/j.electacta.2007.08.030.

[Bessler2010] Bessler G. W., Vogler M., Störmer H., Gerthsen D., Utz A., Weber A., Ivers-Tiffée E. “Model Anodes and Anode Models for Understanding the Mechanism of Hydrogen Oxidation in Solid Oxide Fuel Cells.” *Physical Chemistry Chemical Physics* 12, no. 42 (2010): 13888–903. https://doi.org/10.1039/C0CP00541J.

[Bieberle2000] Bieberle A. and Gauckler L. J. “Reaction Mechanism of Ni Pattern Anodes for Solid Oxide Fuel Cells.” *Solid State Ionics*, Proceedings of the 12th International Conference on Solid State, 135, no. 1 (November 1, 2000): 337–45. https://doi.org/10.1016/S0167-2738(00)00462-8.

[Bieberle2002] Bieberle A. and Gauckler L. J. “State-Space Modeling of the Anodic SOFC System Ni, H2–H2O|YSZ.” *Solid State Ionics* 146, no. 1 (January 1, 2002): 23–41. https://doi.org/10.1016/S0167-2738(01)01004-9.

[Bieberle2001] Bieberle A., Meier L. P., Gauckler L. J. “The Electrochemistry of Ni Pattern Anodes Used as Solid Oxide Fuel Cell Model Electrodes.” *Journal of The Electrochemical Society* 148, no. 6 (June 1, 2001): A646. https://doi.org/10.1149/1.1372219.

[Birss2017] Birss V., El Sawy E., Ketabi S., Keyvanfar P, Li X, and Young J. “Electrochemical Energy Production Using Fuel Cell Technologies,” 1729–79, 2017. https://doi.org/10.1007/978-3-319-52287-6_32.

[Boer1998] Boer B. de. “SOFC Anode. Hydrogen Oxidation at Porous Nickel and Nickel/Zirconia Electrodes,” October 9, 1998. https://research.utwente.nl/en/publications/sofc-anode-hydrogen-oxidation-at-porous-nickel-and-nickelzirconia.

[Boukamp2006] Boukamp B. A., Verbraeken M., Blank D. H. A., and Holtappels P. “SOFC-Anodes, Proof for a Finite-Length Type Gerischer Impedance?” *Solid State Ionics*, Solid State Ionics 15: Proceedings of the 15th International Conference on Solid State Ionics, Part II, 177, no. 26 (October 31, 2006): 2539–41. https://doi.org/10.1016/j.ssi.2006.03.002.

[Boukamp2003] Boukamp B. A., and Bouwmeester H. J. M. “Interpretation of the Gerischer Impedance in Solid State Ionics.” *Solid State Ionics*, Proceedings of the 6th International Symposium on Systems with Fast Ionic Transport (ISSFIT), 157, no. 1 (February 1, 2003): 29–33. https://doi.org/10.1016/S0167-2738(02)00185-6.

[Bouwmeester2004] Bouwmeester, H. J. M., Den Otter M. W., Boukamp B. A. "Oxygen Transport in $La_{0.6}Sr_{0.4}Co_{1-y}Fe_yO_{3-\delta}$." *Journal of Solid State Electrochemistry* 8, no. 9 (August 2004): 599–605. https://doi.org/10.1007/s10008-003-0488-3.

[Bredikhin2018] Bredikhin S. I., Agarkov D. A., Aronin A. S., Burmistrov I. N., Matveev D. V., and Kharton V. V. "Ion Transfer in Ni-Containing Composite Anodes of Solid Oxide Fuel Cells: A Microstructural Study." *Materials Letters* 216 (April 1, 2018): 193–95. https://doi.org/10.1016/j.matlet.2018.01.022.

[Brito2019] Brito M. E., Morishita H., Yamada J., Nishino H., Uchida H. "Further Improvement in Performances of $La_{0.6}Sr_{0.4}Co_{0.2}Fe_{0.8}O_{3-\delta}$ - Doped Ceria Composite Oxygen Electrodes with Infiltrated Doped Ceria Nanoparticles for Reversible Solid Oxide Cells." *Journal of Power Sources* 427 (July 1, 2019): 293–98. https://doi.org/10.1016/j.jpowsour.2019.04.066.

[Bucher2011] Bucher E., and Sitte W.. "Long-Term Stability of the Oxygen Exchange Properties of $(La,Sr)_{1-z}(Co,Fe)O_{3-\delta}$ in Dry and Wet Atmospheres." *Solid State Ionics*, Proceedings of the 17th International Conference on Solid State Ionics, 192, no. 1 (June 16, 2011): 480–82. https://doi.org/10.1016/j.ssi.2010.01.006.

[Cadi-Essadek2016] Cadi-Essadek A., Roldan A., de Leeuw N. H. "Density Functional Theory Study of the Interaction of H_2O, CO_2 and CO with the ZrO_2 (111), Ni/ZrO_2 (111), YSZ (111) and Ni/YSZ (111) Surfaces." *Surface Science* 653 (November 1, 2016): 153–62. https://doi.org/10.1016/j.susc.2016.06.008.

[Canavar2015] Canavar M, and Kaplan Y. "Effects of Mesh and Interconnector Design on Solid Oxide Fuel Cell Performance." *International Journal of Hydrogen Energy*, Hydrogen and Fuel Cell Systems for Clean Energy Applications, 40, no. 24 (June 29, 2015): 7829–34. https://doi.org/10.1016/j.ijhydene.2014.11.101.

[Carraro2012] Carraro T., Joos J., Rüger B, Weber A., Ivers-Tiffée E. "3D Finite Element Model for Reconstructed Mixed-Conducting Cathodes: I. Performance Quantification." *Electrochimica Acta* 77 (August 30, 2012): 315–23. https://doi.org/10.1016/j.electacta.2012.04.109.

[Çelikbilek2019] Çelikbilek Ö., Thieu C.-A., Agnese F., Calì E., Lenser C., Menzler N.H., Son J.-W., Skinner S. J., Djurado E. "Enhanced Catalytic Activity of Nanostructured, A-Site Deficient $(La_{0.7}Sr_{0.3})_{0.95}(Co_{0.2}Fe_{0.8})O_{3-\delta}$ for SOFC Cathodes." *Journal of Materials Chemistry A* 7, no. 43 (November 5, 2019): 25102–11. https://doi.org/10.1039/C9TA07697B.

[Çelikbilek2016] Çelikbilek Ö., Jauffrès D., Siebert E., Dessemond L., Burriel M., Martin C. L., Djurado E. "Rational Design of Hierarchically Nanostructured Electrodes for Solid Oxide Fuel Cells." *Journal of Power Sources* 333 (November 30, 2016): 72–82. https://doi.org/10.1016/j.jpowsour.2016.09.156.

[Chaopradith2015] Chaopradith D. T., Scanlon D. O., Richard C., Catlow A. "Adsorption of Water on Yttria-Stabilized Zirconia." *J. Phys. Chem. C*, (September 3, 2015): 119, 39, 22526–22533. https://doi.org/10.1021/acs.jpcc.5b06825

[Che1982] Che M., and Tench A. J. "Characterization and Reactivity of Mononuclear Oxygen Species on Oxide Surfaces." In *Advances in Catalysis*, edited by D. D. Eley, Herman Pines, and Paul B. Weisz, 31:77–133. Academic Press, 1982. https://doi.org/10.1016/S0360-0564(08)60453-8.

[Che1983] Che, M., and A.J. Tench. "Characterization and Reactivity of Molecular Oxygen Species on Oxide Surfaces." In *Advances in Catalysis*, 32:1–148. Elsevier, 1983. https://doi.org/10.1016/S0360-0564(08)60439-3.

[Chen2018] Chen J., Wan D., Sun X., Li B., Lu M. "Electrochemical Impedance Spectroscopic Characterization of Impregnated $La_{0.78}Sr_{0.2}Co_{0.2}Fe_{0.8}O_{3-\delta}$ Cathode for Intermediate-Temperature SOFCs." *International Journal of Hydrogen Energy* 43, no. 20 (May 17, 2018): 9770–76. https://doi.org/10.1016/j.ijhydene.2018.03.223.

[Chen2016] Chen K. and Jiang S. P. "Review—Materials Degradation of Solid Oxide Electrolysis Cells." *Journal of The Electrochemical Society* 163, no. 11 (June 15, 2016): F3070. https://doi.org/10.1149/2.0101611jes.

[Chen2003] Chen X. J., Chan S. H., Khor K. A. "Cyclic Voltammetry of (La,Sr)MnO_3 Electrode on YSZ Substrate." *Solid State Ionics* 164, no. 1 (October 1, 2003): 17–25. https://doi.org/10.1016/j.ssi.2003.08.006.

[Chen2002] Chen X. J, Khor K. A, Chan S. H, Yu L. G. "Influence of Microstructure on the Ionic Conductivity of Yttria-Stabilized Zirconia Electrolyte." *Materials Science and Engineering: A* 335, no. 1 (September 25, 2002): 246–52. https://doi.org/10.1016/S0921-5093(01)01935-9.

[Chen-Wiegart2016] Chen-Wiegart Y.-C. K., Kennouche D., Cronin J. S., Barnett S. A., Wang J. "Effect of Ni Content on the Morphological Evolution of Ni-YSZ Solid Oxide Fuel Cell Electrodes." *Applied Physics Letters* 108, no. 8 (February 22, 2016): 083903. https://doi.org/10.1063/1.4942459

[Chervin2005] Chervin C., Glass R. S., Kauzlarich S. M. "Chemical Degradation of $La_{1-x}Sr_xMnO_3/Y_2O_3$-Stabilized ZrO_2 Composite Cathodes in the Presence of Current Collector Pastes." *Solid State Ionics* 176, no. 1 (January 14, 2005): 17–23. https://doi.org/10.1016/j.ssi.2004.06.004.

[Choi2013] Choi M.-B., Singh B., Wachsman E. D., Song S.-J. "Performance of $La_{0.1}Sr_{0.9}Co_{0.8}Fe_{0.2}O_{3-\delta}$ and $La_{0.1}Sr_{0.9}Co_{0.8}Fe_{0.2}O_{3-\delta}$–$Ce_{0.9}Gd_{0.1}O_2$ Oxygen Electrodes with $Ce_{0.9}Gd_{0.1}O_2$ Barrier Layer in Reversible Solid Oxide Fuel Cells." *Journal of Power Sources* 239 (October 1, 2013): 361–73. https://doi.org/10.1016/j.jpowsour.2013.03.154.

[Choi2010] Choi Y.-M., Lin M. C., Liu M. "Rational Design of Novel Cathode Materials in Solid Oxide Fuel Cells Using First-Principles Simulations." *Journal of Power Sources* 195, no. 5 (March 1, 2010): 1441–45. https://doi.org/10.1016/j.jpowsour.2009.09.017.

[Cimenti2007] Cimenti M., Co A. C., Birss V. I., Hill J. M. "Distortions in Electrochemical Impedance Spectroscopy Measurements Using 3-Electrode Methods in SOFC. I – Effect of Cell Geometry." *Fuel Cells* 7, no. 5 (2007): 364–76. https://doi.org/10.1002/fuce.200700019.

[Costamagna2019] Costamagna P., Sanna C., Campodonico A., Sala E. M., Sažinas R., Holtappels P. "Electrochemical Impedance Spectroscopy of Electrospun $La_{0.78}Sr_{0.2}Co_{0.2}Fe_{0.8}O_{3-\delta}$ Nanorod Cathodes for Intermediate Temperature – Solid Oxide Fuel Cells." *Fuel Cells* 19, no. 4 (2019): 472–83. https://doi.org/10.1002/fuce.201800205.

[Cucinotta2011] Cucinotta C. S., Bernasconi M., Parrinello M. "Hydrogen Oxidation Reaction at the Ni/YSZ Anode of Solid Oxide Fuel Cells from First Principles." *Physical Review Letters* 107, no. 20 (November 8, 2011): 206103. https://doi.org/10.1103/PhysRevLett.107.206103.

[Dasari2013] Dasari H. P., Park S.-Y., Kim J., Lee J.-H., Kim B.-K., Je H.-J., Lee H.-W., K. J. Yoon. "Electrochemical Characterization of Ni–Yttria Stabilized Zirconia Electrode for Hydrogen Production in Solid Oxide Electrolysis Cells." *Journal of Power Sources* 240 (October 15, 2013): 721–28. https://doi.org/10.1016/j.jpowsour.2013.05.033.

[De Vero2018] De Vero J. C., Develos-Bagarinao K., Kishimoto H., Ishiyama T., Yamaji K. Horita T., Yokokawa H. "Enhanced Stability of Solid Oxide Fuel Cells by Employing a Modified Cathode-Interlayer Interface with a Dense $La_{0.78}Sr_{0.2}Co_{0.2}Fe_{0.8}O_{3-\delta}$ Thin Film."

Journal of Power Sources 377 (February 15, 2018): 128–35. https://doi.org/10.1016/j.jpowsour.2017.12.010.

[Deseure2005] Deseure J., Bultel Y., Dessemond L., Siebert E. "Modelling of Dc and Ac Responses of a Planar Mixed Conducting Oxygen Electrode." *Solid State Ionics* 176, no. 3 (January 31, 2005): 235–44. https://doi.org/10.1016/j.ssi.2004.07.018.

[Ding2013] Ding H., Virkar A. V., Liu M., Liu F. "Suppression of Sr Surface Segregation in $La_{1-x}Sr_xCo_{1-y}Fe_yO_{3-\delta}$: A First Principles Study." *Physical Chemistry Chemical Physics* 15, no. 2 (2013): 489–96. https://doi.org/10.1039/C2CP43148C.

[Ding2009] Ding X., Kong X., Jiang J., Cui C. "Evaluation of Sr Substituted Nd_2CuO_4 as a Potential Cathode Material for Intermediate-Temperature Solid Oxide Fuel Cells." *International Journal of Hydrogen Energy*, 4th Dubrovnik Conference, 34, no. 16 (August 1, 2009): 6869–75. https://doi.org/10.1016/j.ijhydene.2009.06.041.

[Donazzi2020] Donazzi A., Cordaro G., Baricci A., Ding Z.-B., Maestri M. "A Detailed Kinetic Model for the Reduction of Oxygen on LSCF-GDC Composite Cathodes." *Electrochimica Acta* 335 (March 1, 2020): 135620. https://doi.org/10.1016/j.electacta.2020.135620.

[Doppler2018] Doppler M. C., Fleig J., Bram M., Opitz A. K. "Hydrogen Oxidation Mechanisms on Ni/Yttria Stabilized Zirconia Anodes: Separation of Reaction Pathways by Geometry Variation of Pattern Electrodes." *Journal of Power Sources* 380 (March 15, 2018): 46–54. https://doi.org/10.1016/j.jpowsour.2018.01.073.

[Dusastre1999] Dusastre V. and Kilner J. A. "Optimisation of Composite Cathodes for Intermediate Temperature SOFC Applications." *Solid State Ionics* 126, no. 1 (November 1, 1999): 163–74. https://doi.org/10.1016/S0167-2738(99)00108-3.

[Eguchi2002] Eguchi K., Kojo H., Takeguchi T., Kikuchi R., Sasaki K. "Fuel Flexibility in Power Generation by Solid Oxide Fuel Cells." *Solid State Ionics*, Vol. 152–153 (December 1, 2002): 411–16. https://doi.org/10.1016/S0167-2738(02)00351-X.

[Elshof1997] Elshof, J. E. ten, Lankhorst M. H. R., Bouwmeester H. J. M. "Chemical Diffusion and Oxygen Exchange of $La_{0.78}Sr_{0.2}Co_{0.2}Fe_{0.8}O_{3-\delta}$." *Solid State Ionics* 99, no. 1 (August 1, 1997): 15–22. https://doi.org/10.1016/S0167-2738(97)00263-4.

[Endler-Schuck2015] Endler-Schuck C., Joos J., Niedrig C., Weber A., Ivers-Tiffée E. "The Chemical Oxygen Surface Exchange and Bulk Diffusion Coefficient Determined by Impedance Spectroscopy of Porous $La_{0.58}Sr_{0.4}Co_{0.2}Fe_{0.8}O_{3-\delta}$ (LSCF) Cathodes." *Solid State Ionics* 269 (January 1, 2015): 67–79. https://doi.org/10.1016/j.ssi.2014.11.018.

[Eriksson2017] Eriksson E. L. V. and Gray E. MacA. "Optimization and Integration of Hybrid Renewable Energy Hydrogen Fuel Cell Energy Systems – A Critical Review." *Applied Energy* 202 (September 15, 2017): 348–64. https://doi.org/10.1016/j.apenergy.2017.03.132.

[Fan2011] Fan B., Yan J., Yan X. "The Ionic Conductivity, Thermal Expansion Behavior, and Chemical Compatibility of $La_{0.54}Sr_{0.44}Co_{0.2}Fe_{0.8}O_{3-\delta}$ as SOFC Cathode Material." *Solid State Sciences* 13, no. 10 (October 1, 2011): 1835–39. https://doi.org/10.1016/j.solidstatesciences.2011.07.007.

[Fang2018] Fang Q., Frey C. E., Menzler N. H., Blum L. "Electrochemical Performance and Preliminary Post-Mortem Analysis of a Solid Oxide Cell Stack with 20,000 h of Operation." *Journal of The Electrochemical Society* 165, no. 2 (January 9, 2018): F38. https://doi.org/10.1149/2.0541802jes.

[Fergus2006] Fergus J. W. "Electrolytes for Solid Oxide Fuel Cells." *Journal of Power Sources* 162, no. 1 (November 8, 2006): 30–40. https://doi.org/10.1016/j.jpowsour.2006.06.062.

[Finsterbusch2012] Finsterbusch M., Lussier A., Schaefer J. A., Idzerda Y. U. "Electrochemically Driven Cation Segregation in the Mixed Conductor $La_{0.6}Sr_{0.4}Co_{0.2}Fe_{0.8}O_{3-\delta}$." *Solid State Ionics* 212 (March 29, 2012): 77–80. https://doi.org/10.1016/j.ssi.2012.02.006.

[Fleig2007] Fleig, J., Merkle R., Maier J. "The p(O2) Dependence of Oxygen Surface Coverage and Exchange Current Density of Mixed Conducting Oxide Electrodes: Model Considerations." *Physical Chemistry Chemical Physics* 9, no. 21 (2007): 2713–23. https://doi.org/10.1039/B618765J.

[Fleig2005] Fleig J. "On the Current–Voltage Characteristics of Charge Transfer Reactions at Mixed Conducting Electrodes on Solid Electrolytes." *Phys. Chem. Chem. Phys.* 7, no. 9 (2005): 2027–37. https://doi.org/10.1039/B501086A.

[Frey2018] Frey C. E., Fang Q., Sebold D., Blum L., Menzler N. H. "A Detailed Post Mortem Analysis of Solid Oxide Electrolyzer Cells after Long-Term Stack Operation." *Journal of The Electrochemical Society* 165, no. 5 (April 6, 2018): F357. https://doi.org/10.1149/2.0961805jes.

[Fu2014] Fu Z., Wang M., Zuo P., Yang Z., Wu R. "Importance of Oxygen Spillover for Fuel Oxidation on Ni/YSZ Anodes in Solid Oxide Fuel Cells." *Physical Chemistry Chemical Physics* 16, no. 18 (April 9, 2014): 8536–40. https://doi.org/10.1039/C3CP55076A.

[Gao2017] Gao C., Liu Y., Zhao T., Wang W., Tomov R. I., Kumar R. V. "The Effect of Silver Current Collector on Metal Oxide Infiltrated $La_{0.78}Sr_{0.2}Co_{0.2}Fe_{0.8}O_{3-\delta}$ /$Ce_{0.9}Gd_{0.1}O_2$ in Solid Oxide Fuel Cells Application." *Nano-Structures & Nano-Objects* 12 (October 1, 2017): 91–97. https://doi.org/10.1016/j.nanoso.2017.09.004.

[Gao2014] Gao S., Li J., Lin Z. "Theoretical Model for Surface Diffusion Driven Ni-Particle Agglomeration in Anode of Solid Oxide Fuel Cell." *Journal of Power Sources* 255 (June 1, 2014): 144–50. https://doi.org/10.1016/j.jpowsour.2014.01.033.

[Godula-Jopek2015] Godula-Jopek A. *Hydrogen Production: By Electrolysis*. John Wiley & Sons, 2015.

[Gong2012] Gong M., Gemmen R. S., Liu X. "Modeling of Oxygen Reduction Mechanism for 3PB and 2PB Pathways at Solid Oxide Fuel Cell Cathode from Multi-Step Charge Transfer." *Journal of Power Sources* 201 (March 1, 2012): 204–18. https://doi.org/10.1016/j.jpowsour.2011.11.002.

[Goodwin2009] Goodwin D. G., Huayang Zhu, Andrew M. Colclasure, and Robert J. Kee. "Modeling Electrochemical Oxidation of Hydrogen on Ni–YSZ Pattern Anodes." *Journal of The Electrochemical Society* 156, no. 9 (July 6, 2009): B1004. https://doi.org/10.1149/1.3148331.

[Gorski2011] Gorski A., Yurkiv V., Starukhin D., Volpp H.-R. "H_2O Chemisorption and H_2 Oxidation on Yttria-Stabilized Zirconia: Density Functional Theory and Temperature-Programmed Desorption Studies." *Journal of Power Sources*, Proceedings of 2010 European Solid Oxide Fuel Cell Forum, 196, no. 17 (September 1, 2011): 7188–94. https://doi.org/10.1016/j.jpowsour.2010.09.090.

[Grondin2011] Grondin D., Deseure J., Ozil P., Chabriat J. -P., Grondin-Perez B., Brisse A. "Computing Approach of Cathodic Process within Solid Oxide Electrolysis Cell: Experiments and Continuum Model Validation." *Journal of Power Sources* 196, no. 22 (November 15, 2011): 9561–67. https://doi.org/10.1016/j.jpowsour.2011.07.033.

[Grunbaum2009] Grunbaum N., Dessemond L., Fouletier J., Prado F., Mogni L., Caneiro A. "Rate Limiting Steps of the Porous $La_{0.78}Sr_{0.2}Co_{0.2}Fe_{0.8}O_{3-\delta}$ Electrode Material." *Solid State Ionics* 180, no. 28 (November 12, 2009): 1448–52. https://doi.org/10.1016/j.ssi.2009.09.005.

[Guaitolini2018] Guaitolini S. V. M., Yahyaoui I., Fardin J. F.,. Encarnação L. F, Tadeo F.. "A Review of Fuel Cell and Energy Cogeneration Technologies." In *2018 9th International Renewable Energy Congress (IREC)*, 1–6, 2018. https://doi.org/10.1109/IREC.2018.8362573.

[Guillodo2000] Guillodo M., Vernoux P., Fouletier J. "Electrochemical Properties of Ni–YSZ Cermet in Solid Oxide Fuel Cells: Effect of Current Collecting." *Solid State Ionics* 127, no. 1 (January 1, 2000): 99–107. https://doi.org/10.1016/S0167-2738(99)00254-4.

[Guo2012] Guo Y., Liu Y., Cai R., Chen D., Ran R., Shao Z. "Electrochemical Contribution of Silver Current Collector to Oxygen Reduction Reaction over $Ba_{0.5}Sr_{0.5}Co_{0.8}Fe_{0.2}O_{3-\delta}$ Electrode on Oxygen-Ionic Conducting Electrolyte." *International Journal of Hydrogen Energy*, HYFUSEN, 37, no. 19 (October 1, 2012): 14492–500. https://doi.org/10.1016/j.ijhydene.2012.07.031.

[Guo2018] Guo S., Puleo F., Wang L., Wu H., and Liotta L. F. "La0.6Sr0.4Co0.2Fe0.79M0.01O3−δ (M = Ni, Pd) Perovskites Synthesized by Citrate-EDTA Method: Oxygen Vacancies Effect on Electrochemical Properties." *Advanced Powder Technology* 29, no. 11 (November 1, 2018): 2804–12. https://doi.org/10.1016/j.apt.2018.07.029.

[Hanna2014] Hanna J., W. Y. Lee, Y. Shi, and A. F. Ghoniem. "Fundamentals of Electro- and Thermochemistry in the Anode of Solid-Oxide Fuel Cells with Hydrocarbon and Syngas Fuels." *Progress in Energy and Combustion Science* 40 (February 1, 2014): 74–111. https://doi.org/10.1016/j.pecs.2013.10.001.

[Hashimoto2011] Hashimoto S., Fukuda Y., Kuhn M., Sato K., Yashiro K., Mizusaki J. "Thermal and Chemical Lattice Expansibility of $La_{0.6}Sr_{0.4}Co_{1-y}Fe_yO_{3-\delta}$ (y=0.2, 0.4, 0.6 and 0.8)." *Solid State Ionics* 186, no. 1 (March 25, 2011): 37–43. https://doi.org/10.1016/j.ssi.2011.01.014.

[Hauch2016] Hauch A., Brodersen K., Chen M., Mogensen M. B. "Ni/YSZ Electrodes Structures Optimized for Increased Electrolysis Performance and Durability." *Solid State Ionics* 293 (October 1, 2016): 27–36. https://doi.org/10.1016/j.ssi.2016.06.003.

[Hauch2008] Hauch A., Ebbesen S. D., Jensen S. H., Mogensen M. "Solid Oxide Electrolysis Cells: Microstructure and Degradation of the Ni/Yttria-Stabilized Zirconia Electrode." *Journal of The Electrochemical Society* 155, no. 11 (2008): B1184. https://doi.org/10.1149/1.2967331.

[Hauch2011] Hauch A., Mogensen M., Hagen A. "Ni/YSZ Electrode Degradation Studied by Impedance Spectroscopy — Effect of p(H_2O)." *Solid State Ionics*, Proceedings of the 17th International Conference on Solid State Ionics, 192, no. 1 (June 16, 2011): 547–51. https://doi.org/10.1016/j.ssi.2010.01.004.

[Hawkes2007] Hawkes A. D., Aguiar P., Croxford B., Leach M. A., Adjiman C. S., Brandon N. P. "Solid Oxide Fuel Cell Micro Combined Heat and Power System Operating Strategy: Options for Provision of Residential Space and Water Heating." *Journal of Power Sources* 164, no. 1 (January 10, 2007): 260–71. https://doi.org/10.1016/j.jpowsour.2006.10.083.

[He2017] He A., Kim Y., Shikazono N. "Numerical Simulation of LSCF-GDC Composite Cathodes with Various Microstructures." *ECS Transactions* 78, no. 1 (May 30, 2017): 2751. https://doi.org/10.1149/07801.2751ecst.

[He2018] He S., Saunders M., Chen K., Gao H., Suvorova A., Rickard W. D. A., Quadir Z., Cui C. Q, Jiang S. P. "A FIB-STEM Study of Strontium Segregation and Interface Formation of Directly Assembled $La_{0.78}Sr_{0.2}Co_{0.2}Fe_{0.8}O_{3-\delta}$ Cathode on Y_2O_3-ZrO_2 Electrolyte of Solid Oxide Fuel Cells." *Journal of The Electrochemical Society* 165, no. 7 (April 20, 2018): F417. https://doi.org/10.1149/2.0151807jes.

[Heide2002] Heide P. A. W. van der. "Systematic X-Ray Photoelectron Spectroscopic Study of $La_{1-x}Sr_x$-Based Perovskite-Type Oxides." *Surface and Interface Analysis* 33, no. 5 (2002): 414–25. https://doi.org/10.1002/sia.1227.

[Holtappels1999a] Holtappels P., de Haart L. G. J., Stimming U. "Reaction of Hydrogen/Water Mixtures on Nickel-Zirconia Cermet Electrodes: I. DC Polarization Characteristics." *Journal of The Electrochemical Society* 146, no. 5 (May 1, 1999): 1620–25. https://doi.org/10.1149/1.1391816.

[Holtappels1999b] Holtappels P., Vinke I. C., de Haart L. G. J., Stimming U. "Reaction of Hydrogen/Water Mixtures on Nickel-Zirconia Cermet Electrodes: II. AC Polarization Characteristics." *Journal of The Electrochemical Society* 146, no. 8 (August 1, 1999): 2976–82. https://doi.org/10.1149/1.1392038.

[Holzer2011] Holzer L., Iwanschitz B., Hocker Th., Münch B., Prestat M., Wiedenmann D., Vogt U. "Microstructure Degradation of Cermet Anodes for Solid Oxide Fuel Cells: Quantification of Nickel Grain Growth in Dry and in Humid Atmospheres." *Journal of Power Sources* 196, no. 3 (February 1, 2011): 1279–94. https://doi.org/10.1016/j.jpowsour.2010.08.017.

[Holzer2013] Holzer, L., Wiedenmann D., Münch B., Keller L., Prestat M., Gasser Ph., Robertson I., Grobéty B. "The Influence of Constrictivity on the Effective Transport Properties of Porous Layers in Electrolysis and Fuel Cells." *Journal of Materials Science* 48, no. 7 (April 2013): 2934–52. https://doi.org/10.1007/s10853-012-6968-z.

[Hossain2017] Hossain S., Abdalla A. M., Jamain S. N. B., Zaini J. H., Azad A. K. "A Review on Proton Conducting Electrolytes for Clean Energy and Intermediate Temperature-Solid Oxide Fuel Cells." *Renewable and Sustainable Energy Reviews* 79 (November 1, 2017): 750–64. https://doi.org/10.1016/j.rser.2017.05.147.

[Hsieh1996] Hsieh G., Mason T. O., Pederson L. R. "Experimental Limitations in Impedance Spectroscopy: Part II — Electrode Artifacts in Three-Point Measurements on Pt/YSZ." *Solid State Ionics* 91, no. 3 (October 2, 1996): 203–12. https://doi.org/10.1016/S0167-2738(96)83020-7.

[Hubert2018] Hubert M., Laurencin J., Cloetens P., Morel B., Montinaro D., Lefebvre-Joud F. "Impact of Nickel Agglomeration on Solid Oxide Cell Operated in Fuel Cell and Electrolysis Modes." *Journal of Power Sources* 397 (September 1, 2018): 240–51. https://doi.org/10.1016/j.jpowsour.2018.06.097.

[Hubert2016] Hubert M., Laurencin J., Cloetens P., da Silva J. C., Lefebvre-Joud F., Bleuet P., Nakajo A., Siebert E. "Role of Microstructure on Electrode Operating Mechanisms for Mixed Ionic Electronic Conductors: From Synchrotron-Based 3D Reconstruction to Electrochemical Modeling." *Solid State Ionics* 294 (October 15, 2016): 90–107. https://doi.org/10.1016/j.ssi.2016.07.001.

[Hughes2015] Hughes G., Railsback J., Butts D., Barnett S. A. "Electrochemical Performance of Solid Oxide Cell Oxygen Electrodes Under Pressurization." *ECS Transactions* 68, no. 1 (June 2, 2015): 687. https://doi.org/10.1149/06801.0687ecst.

[Hwang2005] Hwang H. J., Moon J.-W., Lee S., Lee E. A. "Electrochemical Performance of LSCF-Based Composite Cathodes for Intermediate Temperature SOFCs." *Journal of Power Sources*, Selected papers presented at the Fuel Cells Science and Technology Meeting, 145, no. 2 (August 18, 2005): 243–48. https://doi.org/10.1016/j.jpowsour.2005.02.063.

[Ivers-Tiffée2001] Ivers-Tiffée, E., Weber A., Herbstritt D. "Materials and Technologies for SOFC-Components." *Journal of the European Ceramic Society* 21, no. 10 (January 1, 2001): 1805–11. https://doi.org/10.1016/S0955-2219(01)00120-0.

[Jamil2015] Jamil S. M., Othman M. H. D., Rahman M. A., Jaafar J., Ismail A. F., Li K. "Recent Fabrication Techniques for Micro-Tubular Solid Oxide Fuel Cell Support: A Review." *Journal of the European Ceramic Society* 35, no. 1 (January 1, 2015): 1–22. https://doi.org/10.1016/j.jeurceramsoc.2014.08.034.

[Jiang2003a] Jiang, S. P, Love J. G, Apateanu L. "Effect of Contact between Electrode and Current Collector on the Performance of Solid Oxide Fuel Cells." *Solid State Ionics* 160, no. 1 (May 1, 2003): 15–26. https://doi.org/10.1016/S0167-2738(03)00127-9.

[Jiang2003b] Jiang S. P. "Issues on Development of (La,Sr)MnO_3 Cathode for Solid Oxide Fuel Cells." *Journal of Power Sources* 124, no. 2 (November 24, 2003): 390–402. https://doi.org/10.1016/S0378-7753(03)00814-0.

[Jiang2008] Jiang S. P. "Development of Lanthanum Strontium Manganite Perovskite Cathode Materials of Solid Oxide Fuel Cells: A Review." *Journal of Materials Science* 43, no. 21 (November 2008): 6799–6833. https://doi.org/10.1007/s10853-008-2966-6.

[Jiang2017] Jiang S. P. "Placement of Reference Electrode, Electrolyte Thickness and Three-Electrode Cell Configuration in Solid Oxide Fuel Cells: A Brief Review and Update on Experimental Approach." *Journal of The Electrochemical Society* 164, no. 7 (May 31, 2017): F834. https://doi.org/10.1149/2.1331707jes.

[Jiang2004] Jiang, S.P. "Cell Configurations for Performance Evaluation in Planar Solid Oxide Fuel Cells." *Journal of Applied Electrochemistry* 34, no. 10 (October 1, 2004): 1045–55. https://doi.org/10.1023/B:JACH.0000042671.56349.da.

[Jin2020] Jin X. and Huang K. "Precautions of Using Three-Electrode Configuration to Measure Electrode Overpotential in Solid Oxide Electrochemical Cells: Insights from Finite Element Modeling." *Journal of The Electrochemical Society* 167, no. 12 (August 6, 2020): 124501. https://doi.org/10.1149/1945-7111/aba876.

[Kek2001] Kek D., Mogensen M., Pejovnik S. "A Study of Metal (Ni, Pt, Au)/Yttria-Stabilized Zirconia Interface in Hydrogen Atmosphere at Elevated Temperature." *Journal of The Electrochemical Society* 148, no. 8 (July 3, 2001): A878. https://doi.org/10.1149/1.1383069.

[Kendall2010] Kendall K. "Progress in Microtubular Solid Oxide Fuel Cells." *International Journal of Applied Ceramic Technology* 7, no. 1 (2010): 1–9. https://doi.org/10.1111/j.1744-7402.2008.02350.x.

[Khamidy2020] Khamidy N.I., Laurencin J., Ferreira Sanchez D., Monaco F., Charlot F., Djurado E. "Durability of Nanostructured $LaPrNiO_{4+\delta}$ Electrode for Solid Oxide Cells: Electrochemical, Microstructural, and Structural Investigation." *Journal of Power Sources* 450 (February 29, 2020): 227724. https://doi.org/10.1016/j.jpowsour.2020.227724.

[Khan2018] Khan M. Z., Mehran M. T., Song R.-H., Lee J.-W., Lee S.-B., and Lim T. H. "A Simplified Approach to Predict Performance Degradation of a Solid Oxide Fuel Cell Anode." *Journal of Power Sources* 391 (July 1, 2018): 94–105. https://doi.org/10.1016/j.jpowsour.2018.04.080.

[Kiebach2015] Kiebach R., Zhang W.-W., Zhang W., Chen M., Norrman K., Wang H.-J., Bowen J. R., Barfod R., Hendriksen P. V. "Stability of $La_{0.6}Sr_{0.4}Co_{0.2}Fe_{0.8}O_{3-\delta}$ /$Ce_{0.9}Gd_{0.1}O_2$ Cathodes during Sintering and Solid Oxide Fuel Cell Operation." *Journal of Power Sources* 283 (June 1, 2015): 151–61. https://doi.org/10.1016/j.jpowsour.2015.02.064.

[Kim2019a] Kim D., Park J. W., Yun B.-H., Park J. H., Lee K. T. "Correlation of Time-Dependent Oxygen Surface Exchange Kinetics with Surface Chemistry of $La_{0.6}Sr_{0.4}Co_{0.2}Fe_{0.8}O_{3-\delta}$ Catalysts." *ACS Applied Materials & Interfaces* 11, no. 35 (September 4, 2019): 31786–92. https://doi.org/10.1021/acsami.9b06569.

[Kim2019b] Kim M., Muroyama H., Matsui T., Eguchi K.. "Influence of Water Vapor on Performance Degradation and Microstructural Change of (La,Sr)(Co,Fe)$O_{3-\delta}$ Cathode." *Journal of The Electrochemical Society* 166, no. 16 (2019): F1269–74. https://doi.org/10.1149/2.0641915jes.

[Kim2021] Kim S., Joh D. W., Lee D.-Y., Lee J., Kim H. S., Khan M. Z., Hong J. E. "Microstructure Tailoring of Solid Oxide Electrolysis Cell Air Electrode to Boost Performance and Long-Term Durability." *Chemical Engineering Journal* 410 (April 15, 2021): 128318. https://doi.org/10.1016/j.cej.2020.128318.

[Kivi2017] Kivi I., Aruväli J., Kirsimäe K., Möller P., Heinsaar A., Nurk G., Lust E. "Influence of Humidified Synthetic Air Feeding Conditions on the Stoichiometry of $(La_{1-X=x}Sr_x)_yCoO_{3-\delta}$ and $La_{0.6}Sr_{0.4}Co_{0.2}Fe_{0.8}O_{3-\delta}$ Cathodes under Applied Potential Measured by Electrochemical in Situ High-Temperature XRD Method." *Journal of Solid State Electrochemistry* 21, no. 2 (February 1, 2017): 361–69. https://doi.org/10.1007/s10008-016-3379-0.

[Königstein1998] Königstein M. and Catlow C. R. A "Ab InitioQuantum Mechanical Study of the Structure and Stability of the Alkaline Earth Metal Oxides and Peroxides." *Journal of Solid State Chemistry* 140, no. 1 (October 1, 1998): 103–15. https://doi.org/10.1006/jssc.1998.7871.

[Kournoutis2011] Kournoutis V. Ch., Tietz F., Bebelis S. "Cyclic Voltammetry Characterization of a $La_{0.8}Sr_{0.2}Co_{0.2}Fe_{0.8}O_{3-\delta}$ Electrode Interfaced to CGO/YSZ." *Solid State Ionics* 197, no. 1 (August 25, 2011): 13–17. https://doi.org/10.1016/j.ssi.2011.06.007.

[Kröll2017] Kröll L., de Haart L. G. J., Vinke I., Eichel R.-A. "Degradation Mechanisms in Solid-Oxide Fuel and Electrolyzer Cells: Analytical Description of Nickel Agglomeration in a Ni/YSZ Electrode." *Physical Review Applied* 7, no. 4 (April 17, 2017): 044007. https://doi.org/10.1103/PhysRevApplied.7.044007.

[Lane2000] Lane, J. A. and Kilner J. A. "Measuring Oxygen Diffusion and Oxygen Surface Exchange by Conductivity Relaxation." *Solid State Ionics*, Proceedings of the 12th International Conference on Solid State Ionics, 136–137 (November 2, 2000): 997–1001. https://doi.org/10.1016/S0167-2738(00)00554-3.

[Laurencin2015] Laurencin J., Hubert M., Couturier K., Le Bihan T., Cloetens P., Lefebvre-Joud F., Siebert E. "Reactive Mechanisms of LSCF Single-Phase and LSCF-CGO Composite Electrodes Operated in Anodic and Cathodic Polarisations." *Electrochimica Acta* 174 (August 20, 2015): 1299–1316. https://doi.org/10.1016/j.electacta.2015.06.080.

[Laurencin2017] Laurencin J., Hubert M., Ferreira Sanchez D., Pylypko S., Morales M., Morata A., Morel B., Montinaro D., Lefebvre-Joud F., Siebert E. "Degradation Mechanism of $La_{0.6}Sr_{0.4}Co_{0.2}Fe_{0.8}O_{3-\delta}/Gd_{0.1}Ce_{0.9}O_{2-\delta}$ Composite Electrode Operated under Solid Oxide Electrolysis and Fuel Cell Conditions." *Electrochimica Acta* 241 (July 1, 2017): 459–76. https://doi.org/10.1016/j.electacta.2017.05.011.

[Lawlor2013] Lawlor V. "Review of the Micro-Tubular Solid Oxide Fuel Cell (Part II: Cell Design Issues and Research Activities)." *Journal of Power Sources* 240 (October 15, 2013): 421–41. https://doi.org/10.1016/j.jpowsour.2013.03.191.

[Lawlor2009] Lawlor, V., Griesser S., Buchinger G., Olabi A. G., Cordiner S., Meissner D. "Review of the Micro-Tubular Solid Oxide Fuel Cell: Part I. Stack Design Issues and Research Activities." *Journal of Power Sources* 193, no. 2 (September 5, 2009): 387–99. https://doi.org/10.1016/j.jpowsour.2009.02.085.

[Lay-Grindler2013a] Lay-Grindler E., Laurencin J., Delette G., Aicart J., Petitjean M., Dessemond L. "Micro Modelling of Solid Oxide Electrolysis Cell: From Performance to Durability." *International Journal of Hydrogen Energy* 38, no. 17 (June 10, 2013): 6917–29. https://doi.org/10.1016/j.ijhydene.2013.03.162.

[Lay-Grindler2013b] Lay-Grindler E., Laurencin J., Villanova J., Kieffer I., Usseglio-Viretta F., Le Bihan T., Bleuet P., Aurore Mansuy, and Gérard Delette. “Degradation Study of the $La_{0.6}Sr_{0.4}Co_{0.2}Fe_{0.8}O_{3-\delta}$ Solid Oxide Electrolysis Cell (SOEC) Anode after High Temperature Electrolysis Operation.” *ECS Transactions* 57, no. 1 (October 6, 2013): 3177. https://doi.org/10.1149/05701.3177ecst.

[Lay-Grindler2014] Lay-Grindler E., Laurencin J., Villanova J., Cloetens P., Bleuet P., Mansuy A., Mougin J., Delette G. “Degradation Study by 3D Reconstruction of a Nickel–Yttria Stabilized Zirconia Cathode after High Temperature Steam Electrolysis Operation.” *Journal of Power Sources* 269 (December 10, 2014): 927–36. https://doi.org/10.1016/j.jpowsour.2014.07.066.

[Lee2014] Lee Y.-H., Muroyama H., Matsui T., Eguchi K. “Degradation of Nickel–Yttria-Stabilized Zirconia Anode in Solid Oxide Fuel Cells under Changing Temperature and Humidity Conditions.” *Journal of Power Sources* 262 (September 15, 2014): 451–56. https://doi.org/10.1016/j.jpowsour.2014.03.031.

[Leng2008] Leng Y., Chan S. H., Liu Q. “Development of LSCF–GDC Composite Cathodes for Low-Temperature Solid Oxide Fuel Cells with Thin Film GDC Electrolyte.” *International Journal of Hydrogen Energy*, TMS07: Symposium on Materials in Clean Power Systems, 33, no. 14 (July 1, 2008): 3808–17. https://doi.org/10.1016/j.ijhydene.2008.04.034.

[Leone2008] Leone P., Santarelli M., Asinari P., Calì M., and Borchiellini R.. “Experimental Investigations of the Microscopic Features and Polarization Limiting Factors of Planar SOFCs with LSM and LSCF Cathodes.” *Journal of Power Sources* 177, no. 1 (February 15, 2008): 111–22. https://doi.org/10.1016/j.jpowsour.2007.11.021.

[Li2017] Li Y., Zhang W., Zheng Y., Chen J., Yu B., Chen Y., Liu M. “Controlling Cation Segregation in Perovskite-Based Electrodes for High Electro-Catalytic Activity and Durability.” *Chemical Society Reviews* 46, no. 20 (2017): 6345–78. https://doi.org/10.1039/C7CS00120G.

[Lin2003] Lin Z., Stevenson J. W., Khaleel M. A. “The Effect of Interconnect Rib Size on the Fuel Cell Concentration Polarization in Planar SOFCs.” *Journal of Power Sources* 117, no. 1 (May 15, 2003): 92–97. https://doi.org/10.1016/S0378-7753(02)00726-7.

[Liu2006] Liu J., Co A. C., Paulson S., Birss V. I. “Oxygen Reduction at Sol–Gel Derived $La_{0.8}Sr_{0.2}Co_{0.8}Fe_{0.2}O_3$ Cathodes.” *Solid State Ionics* 177, no. 3 (January 31, 2006): 377–87. https://doi.org/10.1016/j.ssi.2005.11.005.

[Liu1998] Liu M. and Wu Z. “Significance of Interfaces in Solid-State Cells with Porous Electrodes of Mixed Ionic–Electronic Conductors.” *Solid State Ionics* 107, no. 1 (March 1, 1998): 105–10. https://doi.org/10.1016/S0167-2738(97)00528-6.

[Liu2011] Liu, R. R., S. H. Kim, S. Taniguchi, T. Oshima, Y. Shiratori, K. Ito, and K. Sasaki. “Influence of Water Vapor on Long-Term Performance and Accelerated Degradation of Solid Oxide Fuel Cell Cathodes.” *Journal of Power Sources*, Proceedings of 2010 European Solid Oxide Fuel Cell Forum, 196, no. 17 (September 1, 2011): 7090–96. https://doi.org/10.1016/j.jpowsour.2010.08.014.

[Liu2019] Liu Y., Zhao X., Yang Z., Wang Z., Chen X., Yang S., Wei M. “New Insights into Element Migration on $La_{0.6}Sr_{0.4}Co_{0.2}Fe_{0.8}O_{3-\delta}$ Cathodes of Intermediate Temperature Solid Oxide Fuel Cells.” *Solid State Ionics* 334 (June 1, 2019): 145–51. https://doi.org/10.1016/j.ssi.2019.02.011.

[Loureiro2019] Loureiro F. J. A., Macedo D. A., Nascimento R. M., Cesário M. R., Grilo J. P. F., Yaremchenko A. A., Fagg D. P. “Cathodic Polarisation of Composite LSCF-SDC IT-SOFC Electrode Synthesised by One-Step Microwave Self-Assisted Combustion.” *Journal of the*

European Ceramic Society 39, no. 5 (May 1, 2019): 1846–53. https://doi.org/10.1016/j.jeurceramsoc.2019.01.013.

[Lu2019] Lu M. Y., Railsback J. G., Wang H., Liu Q., Chart Y. A., Zhang S.-L., Barnett S. A. "Stable High Current Density Operation of $La_{0.6}Sr_{0.4}Co_{0.2}Fe_{0.8}O_{3-\delta}$ Oxygen Electrodes." *Journal of Materials Chemistry A* 7, no. 22 (June 4, 2019): 13531–39. https://doi.org/10.1039/C9TA04020J.

[Luo2017] Luo Y., Li W., Shi Y., Wang Y., Cai N. "Reversible H_2/H_2O Electrochemical Conversion Mechanisms on the Patterned Nickel Electrodes." *International Journal of Hydrogen Energy* 42, no. 40 (October 5, 2017): 25130–42. https://doi.org/10.1016/j.ijhydene.2017.08.138.

[Luo2019] Luo Y., Shi Y., Li W., Cai N. "Mechanism of Rate-Limiting Step Switchover for Reversible Solid Oxide Cells in H2/H2O Atmosphere." *Electrochimica Acta* 326 (December 5, 2019): 135003. https://doi.org/10.1016/j.electacta.2019.135003.

[Lust2010] Lust E., Küngas R., Kivi I., Kurig H., Möller P., Anderson E., Lust K., Tamm K., Samussenko A., Nurk G. "Electrochemical and Gas Phase Parameters of Cathodes for Intermediate Temperature Solid Oxide Fuel Cells." *Electrochimica Acta*, Selection of papers from the 7th ISE Spring Meeting22-25 March 2009, Szczyrk, Poland, 55, no. 26 (November 1, 2010): 7669–78. https://doi.org/10.1016/j.electacta.2009.11.007.

[Lynch2010] Lynch M. E. and Liu M. "Investigation of Sheet Resistance in Thin-Film Mixed-Conducting Solid Oxide Fuel Cell Cathode Test Cells." *Journal of Power Sources* 195, no. 16 (August 15, 2010): 5155–66. https://doi.org/10.1016/j.jpowsour.2010.03.017.

[Ma2018] Ma L., Priya P., Aluru N. R.. "A Multiscale Model for Electrochemical Reactions in LSCF Based Solid Oxide Cells." *Journal of The Electrochemical Society* 165, no. 14 (November 6, 2018): F1232. https://doi.org/10.1149/2.0921814jes.

[Mahato2015] Mahato N., Banerjee A., Gupta A., Omar S., Balani K. "Progress in Material Selection for Solid Oxide Fuel Cell Technology: A Review." *Progress in Materials Science* 72 (July 1, 2015): 141–337. https://doi.org/10.1016/j.pmatsci.2015.01.001.

[Marina2007] Marina O. A., Pederson L. R., Williams M. C., Coffey G. W., Meinhardt K. D., Nguyen C. D., Thomsen E. C. "Electrode Performance in Reversible Solid Oxide Fuel Cells." *Journal of The Electrochemical Society* 154, no. 5 (2007): B452. https://doi.org/10.1149/1.2710209.

[Marinha2011] Marinha D., Dessemond L., Cronin J. S., Wilson J. R., Barnett S. A., Djurado E. "Microstructural 3D Reconstruction and Performance Evaluation of LSCF Cathodes Obtained by Electrostatic Spray Deposition." *Chemistry of Materials* 23, no. 24 (December 27, 2011): 5340–48. https://doi.org/10.1021/cm2016998.

[Marinha2012] Marinha D., Dessemond L., Djurado E. "Electrochemical Investigation of Oxygen Reduction Reaction on $La_{0.6}Sr_{0.4}Co_{0.2}Fe_{0.8}O_{3-\delta}$ Cathodes Deposited by Electrostatic Spray Deposition." *Journal of Power Sources* 197 (January 1, 2012): 80–87. https://doi.org/10.1016/j.jpowsour.2011.09.049.

[Matsui2019] Matsui T., Li S., Inoue Y., Yoshida N., Muroyama H., Eguchi K. "Degradation Analysis of Solid Oxide Fuel Cells with $(La,Sr)(Co,Fe)O_{3-\delta}$ Cathode/Gd_2O_3–CeO_2 Interlayer/Y_2O_3–ZrO_2 Electrolyte System: The Influences of Microstructural Change and Solid Solution Formation." *ECS Transactions* 91, no. 1 (July 10, 2019): 1247. https://doi.org/10.1149/09101.1247ecst.

[Mehran2018] Mehran M. T., Khan M. Z., Lee S.-B., Lim T.-H., Park S., Song R.-H. "Improving Sulfur Tolerance of Ni-YSZ Anodes of Solid Oxide Fuel Cells by Optimization of

Microstructure and Operating Conditions." *International Journal of Hydrogen Energy* 43, no. 24 (June 14, 2018): 11202–13. https://doi.org/10.1016/j.ijhydene.2018.04.200.

[Menzler2010] Menzler N. H., Tietz F., Uhlenbruck S., Buchkremer H. P., Stöver D. "Materials and Manufacturing Technologies for Solid Oxide Fuel Cells." *Journal of Materials Science* 45, no. 12 (June 2010): 3109–35. https://doi.org/10.1007/s10853-010-4279-9.

[Mihn2021] Mihn N. Q. "Ceramic Fuel Cells - Minh - 1993 - Journal of the American Ceramic Society - Wiley Online Library." Accessed April 5, 2021. https://ceramics.onlinelibrary.wiley.com/doi/abs/10.1111/j.1151-2916.1993.tb03645.x?casa_token=XyPK4ngFCHgAAAAA:QKRVqtIYxMRal-BfxToZkw-z1GY9mLDcGtKl1OlodUqQ_U8esAMIr3DFHiJPiiAykt3Z1CrRgnB5nA.

[Mizusaki1994a] Mizusaki J., Tagawa H., Saito T., Kamitani K., Yamamura T., Hirano K., Ehara S.,"Preparation of Nickel Pattern Electrodes on YSZ and Their Electrochemical Properties in H2 - H2O Atmospheres." *Journal of The Electrochemical Society* 141, no. 8 (August 1, 1994): 2129. https://doi.org/10.1149/1.2055073.

[Mizusaki1994b] Mizusaki J., Tagawa H., Saito T., Yamamura T., Kamitani K., Hirano K., Ehara S. "Kinetic Studies of the Reaction at the Nickel Pattern Electrode on YSZ in H_2-H_2O Atmospheres." *Solid State Ionics* 70–71 (May 1, 1994): 52–58. https://doi.org/10.1016/0167-2738(94)90286-0.

[Moçoteguy2013] Moçoteguy P. and Brisse A. "A Review and Comprehensive Analysis of Degradation Mechanisms of Solid Oxide Electrolysis Cells." *International Journal of Hydrogen Energy* 38, no. 36 (December 13, 2013): 15887–902. https://doi.org/10.1016/j.ijhydene.2013.09.045.

[Mogensen2017] Mogensen M. B., Hauch A., Sun X., Chen M., Tao Y., Ebbesen S. D., Hansen K. V., Hendriksen P. V. "Relation Between Ni Particle Shape Change and Ni Migration in Ni–YSZ Electrodes – a Hypothesis." *Fuel Cells* 17, no. 4 (2017): 434–41. https://doi.org/10.1002/fuce.201600222.

[Mohsenzadeh2014] Mohsenzadeh A., Bolton K., Richards T. "DFT Study of the Adsorption and Dissociation of Water on Ni(111), Ni(110) and Ni(100) Surfaces." *Surface Science* 627 (September 1, 2014): 1–10. https://doi.org/10.1016/j.susc.2014.04.006.

[Monaco2021] Monaco F., Effori E., Hubert M., Siebert E., Geneste G., Morel B., Djurado E., Montinaro D., Laurencin J. "Electrode Kinetics of Porous Ni-3YSZ Cermet Operated in Fuel Cell and Electrolysis Modes for Solid Oxide Cell Application"." Accepted by Electrochem. Acta (2021).

[Monaco2019] Monaco F., Hubert M., Vulliet J., Ouweltjes J. P., Montinaro D., Cloetens P., Piccardo P., Lefebvre-Joud F., Laurencin J. "Degradation of Ni-YSZ Electrodes in Solid Oxide Cells: Impact of Polarization and Initial Microstructure on the Ni Evolution." *Journal of The Electrochemical Society* 166, no. 15 (2019): F1229–42. https://doi.org/10.1149/2.1261915jes.

[Monaco2018] Monaco F., Tezyk V., Siebert E., Pylypko S., Morel B., Vulliet J., Le Bihan T., Lefebvre-Joud F., Laurencin J. "Experimental Validation of a $La_{0.6}Sr_{0.4}Co_{0.2}Fe_{0.8}O_{3-\delta}$ Electrode Model Operated in Electrolysis Mode: Understanding the Reaction Pathway under Anodic Polarization." *Solid State Ionics* 319 (June 1, 2018): 234–46. https://doi.org/10.1016/j.ssi.2018.02.012.

[Monaco2020] Monaco F. "Analysis of the Degradation in Solid Oxide Cells Operated in Fuel Cell and Electrolysis Modes : Microstructural Evolution and Stability of the Electrodes Materials." Phd thesis, Université Grenoble Alpes, 2020. https://tel.archives-ouvertes.fr/tel-02971294.

[Montella2021] Montella C., Tezyk V., Effori E., Laurencin J., Siebert E. “Linear Sweep and Cyclic Voltammetry of Porous Mixed Conducting Oxygen Electrode: Formal Study of Insertion, Diffusion and Chemical Reaction Model.” *Solid State Ionics* 359 (January 1, 2021): 115485. https://doi.org/10.1016/j.ssi.2020.115485.

[Mortensen2014] Mortensen J. E., Søgaard M., Jacobsen T. “Analytical, 1-Dimensional Impedance Model of a Composite Solid Oxide Fuel Cell Cathode.” *Journal of The Electrochemical Society* 161, no. 3 (2014): F161–75. https://doi.org/10.1149/2.077401jes.

[Mosiałek2018] Mosiałek M., Michna A., Dziubaniuk M., Bielańska E., Kežionis A., Šalkus T., Kazakevičius E. “Composite Cathode Material LSCF-Ag for Solid Oxide Fuel Cells Obtained in One Step Sintering Procedure.” *Electrochimica Acta* 282 (August 20, 2018): 427–36. https://doi.org/10.1016/j.electacta.2018.06.063.

[Moussaoui2018] Moussaoui H., Laurencin J., Gavet Y., Delette G., Hubert M., Cloetens P., Le Bihan T., Debayle J. “Stochastic Geometrical Modeling of Solid Oxide Cells Electrodes Validated on 3D Reconstructions.” *Computational Materials Science* 143 (February 15, 2018): 262–76. https://doi.org/10.1016/j.commatsci.2017.11.015.

[Na2018] Na A., He S., Li N., Zhang Q., Rickard W. D. A., Chen K., Zhang T., Jiang S.P. “Suppressed Sr Segregation and Performance of Directly Assembled $La_{0.6}Sr_{0.4}Co_{0.2}Fe_{0.8}O_{3-\delta}$ Oxygen Electrode on Y_2O_3-ZrO_2 Electrolyte of Solid Oxide Electrolysis Cells.” *Journal of Power Sources* 384 (April 30, 2018): 125–35. https://doi.org/10.1016/j.jpowsour.2018.02.082.

[Nakajo2012] Nakajo A., Mueller F., Brouwer J., Van herle J., Favrat D. “Mechanical Reliability and Durability of SOFC Stacks. Part II: Modelling of Mechanical Failures during Ageing and Cycling.” *International Journal of Hydrogen Energy* 37, no. 11 (June 1, 2012): 9269–86. https://doi.org/10.1016/j.ijhydene.2012.03.023.

[Ni2007] Ni M., Leung M. K. H., Leung D. Y. C. “Parametric Study of Solid Oxide Fuel Cell Performance.” *Energy Conversion and Management* 48, no. 5 (May 1, 2007): 1525–35. https://doi.org/10.1016/j.enconman.2006.11.016.

[Niania2020] Niania M. A., Rossall A. K., Van den Berg J. A., Kilner J. A. “The Effect of Sub-Surface Strontium Depletion on Oxygen Diffusion in $La_{0.6}Sr_{0.4}Co_{0.2}Fe_{0.8}O_{3-\delta}$.” *Journal of Materials Chemistry A* 8, no. 37 (2020): 19414–24. https://doi.org/10.1039/D0TA06058E.

[Niania2018] Niania M., Podor R., Britton T. B., Li C., Cooper S. J., Svetkov N., Skinner S., Kilner J. “In Situ Study of Strontium Segregation in $La_{0.6}Sr_{0.4}Co_{0.2}Fe_{0.8}O_{3-\delta}$ in Ambient Atmospheres Using High-Temperature Environmental Scanning Electron Microscopy.” *Journal of Materials Chemistry A* 6, no. 29 (July 24, 2018): 14120–35. https://doi.org/10.1039/C8TA01341A.

[Nielsen2011] Nielsen J., Jacobsen T., Wandel M. “Impedance of Porous IT-SOFC LSCF:CGO Composite Cathodes.” *Electrochimica Acta*, 56, no. 23 (September 30, 2011): 7963–74. https://doi.org/10.1016/j.electacta.2011.05.042.

[Noh2013] Noh H.-S., Hwang J., Yoon K., Kim B.-K., Lee H.-W., Lee J.-H., Son J.-W. “Optimization of Current Collection to Reduce the Lateral Conduction Loss of Thin-Film-Processed Cathodes.” *Journal of Power Sources* 230 (May 15, 2013): 109–14. https://doi.org/10.1016/j.jpowsour.2012.12.059.

[Nozawa2021] Nozawa K., Orui H., Komatsu T., Chiba R., Arai H. “Development of Highly Efficient Planar Solid Oxide Fuel Cells” 6, no. 2 (2008): 8. https://www.ntt-review.jp/archive/ntttechnical.php?contents=ntr200802sf4.html.

[O'Hayre2016] O'Hayre R., Cha S.-W., Colella W., Prinz F. B. *Fuel Cell Fundamentals*. John Wiley & Sons, 2016.

[Ong2017] Ong K., Hanna J., Ghoniem A. F. "Investigation of a Combined Hydrogen and Oxygen Spillover Mechanism for Syngas Electro-Oxidation on Ni/YSZ." *Journal of The Electrochemical Society* 164, no. 2 (December 6, 2016): F32. https://doi.org/10.1149/2.0161702jes

[Pan2015a] Pan W., Chen K., Ai N., Lü Z., Jiang S. P. "Mechanism and Kinetics of Ni-Y_2O_3-ZrO_2 Hydrogen Electrode for Water Electrolysis Reactions in Solid Oxide Electrolysis Cells." *Journal of The Electrochemical Society* 163, no. 2 (November 25, 2015): F106. https://doi.org/10.1149/2.0801602jes.

[Pan2015b] Pan Z., Liu Q., Zhang L., Zhang X., Chan S. H. "Effect of Sr Surface Segregation of $La_{0.6}Sr_{0.4}Co_{0.2}Fe_{0.8}O_{3-\delta}$ Electrode on Its Electrochemical Performance in SOC." *Journal of The Electrochemical Society* 162, no. 12 (September 1, 2015): F1316. https://doi.org/10.1149/2.0371512jes.

[Pan2018] Pan Z., Liu Q., Lyu R., Li P., Chan S. H. "Effect of $La_{0.6}Sr_{0.4}Co_{0.2}Fe_{0.8}O_{3-\delta}$ Air Electrode–Electrolyte Interface on the Short-Term Stability under High-Current Electrolysis in Solid Oxide Electrolyzer Cells." *Journal of Power Sources* 378 (February 28, 2018): 571–78. https://doi.org/10.1016/j.jpowsour.2018.01.002.

[Pan2016] Pan Z., Liu Q., Zhang L., Zhang X., Chan S. H. "Study of Activation Effect of Anodic Current on $La_{0.6}Sr_{0.4}Co_{0.2}Fe_{0.8}O_{3-\delta}$ Air Electrode in Solid Oxide Electrolyzer Cell." *Electrochimica Acta* 209 (August 10, 2016): 56–64. https://doi.org/10.1016/j.electacta.2016.05.058.

[Panthi2014] Panthi D. and Tsutsumi A. "Micro-Tubular Solid Oxide Fuel Cell Based on a Porous Yttria-Stabilized Zirconia Support." *Scientific Reports* 4, no. 1 (August 29, 2014): 5754. https://doi.org/10.1038/srep05754.

[Patcharavorachot2008] Patcharavorachot Y., Arpornwichanop A., Chuachuensuk A. "Electrochemical Study of a Planar Solid Oxide Fuel Cell: Role of Support Structures." *Journal of Power Sources* 177, no. 2 (March 1, 2008): 254–61. https://doi.org/10.1016/j.jpowsour.2007.11.079.

[Perry Murray2002] Perry Murray E., Sever M. J., Barnett S. A. "Electrochemical Performance of $(La,Sr)(Co,Fe)O_3$–$(Ce,Gd)O_3$ Composite Cathodes." *Solid State Ionics* 148, no. 1 (May 1, 2002): 27–34. https://doi.org/10.1016/S0167-2738(02)00102-9.

[Pihlatie2009] Pihlatie M., Kaiser A., Mogensen M. "Mechanical Properties of NiO/Ni–YSZ Composites Depending on Temperature, Porosity and Redox Cycling." *Journal of the European Ceramic Society* 29, no. 9 (June 1, 2009): 1657–64. https://doi.org/10.1016/j.jeurceramsoc.2008.10.017.

[Prestat2007] Prestat M., Koenig J.-F., Gauckler L. J. "Oxygen Reduction at Thin Dense $La_{0.52}Sr_{0.48}Co_{0.18}Fe_{0.82}O_{3-\delta}$ Electrodes: Part I: Reaction Model and Faradaic Impedance." *Journal of Electroceramics* 18, no. 1–2 (April 19, 2007): 87–101. https://doi.org/10.1007/s10832-007-9012-y.

[Primdahl1997] Primdahl S. and Mogensen M. "Oxidation of Hydrogen on Ni/Yttria-Stabilized Zirconia Cermet Anodes." *Journal of The Electrochemical Society* 144, no. 10 (October 1, 1997): 3409. https://doi.org/10.1149/1.1838026.

[Raz2001] Raz, S., Sasaki K., Maier J., Riess I. "Characterization of Adsorbed Water Layers on Y_2O_3-Doped ZrO_2." *Solid State Ionics* 143, no. 2 (June 2, 2001): 181–204. https://doi.org/10.1016/S0167-2738(01)00826-8.

[Reisert2018] Reisert M., Aphale A., Singh P. "Solid Oxide Electrochemical Systems: Material Degradation Processes and Novel Mitigation Approaches." *Materials* 11, no. 11 (November 2018): 2169. https://doi.org/10.3390/ma11112169.

[Rinaldi2019] Rinaldi G., Nakajo A., Caliandro P., Navratilova L., Van herle J. "Effects of Polarization on the Microstructural Changes at the YSZ/Ni-YSZ Interface." *ECS Transactions* 91, no. 1 (July 10, 2019): 641–52. https://doi.org/10.1149/09101.0641ecst.

[Rinaldi2017] Rinaldi G., Nakajo A., Van Herle J., Burdet P., Oveisi E., Cantoni M. "Strontium Migration at the GDC-YSZ Interface of Solid Oxide Cells in SOFC and SOEC Modes." *ECS Transactions* 78, no. 1 (May 30, 2017): 3297. https://doi.org/10.1149/07801.3297ecst.

[Rolle2012] Rolle A., Thoréton V., Rozier P., Capoen E., Mentré O., Boukamp B., Daviero-Minaud S. "Evidence of the Current Collector Effect: Study of the SOFC Cathode Material $Ca_3Co_4O_{9+\delta}$." *Fuel Cells* 12, no. 2 (2012): 288–301. https://doi.org/10.1002/fuce.201100084.

[Rutman2008] Rutman J. and Riess I. "Placement of Reference Electrode in Solid State Electrolyte Cells." *Solid State Ionics*, Solid State Ionics 16: Proceedings of the 16th International Conference on Solid State Ionics (SSI-16), Part I, 179, no. 21 (September 15, 2008): 913–18. https://doi.org/10.1016/j.ssi.2008.01.071.

[Sanchez Ferreira2017] Sanchez Ferreira D., Grolimund D., Hubert M., Bleuet P., Laurencin J. "A 2D and 3D X-Ray µ-Diffraction and µ-Fluorescence Study of a Mixed Ionic Electronic Conductor." *International Journal of Hydrogen Energy* 42, no. 2 (January 12, 2017): 1203–11. https://doi.org/10.1016/j.ijhydene.2016.11.094.

[Sapountzi2012] Sapountzi F. M., Brosda S., Papazisi K. M., Balomenou S. P., Tsiplakides D. "Electrochemical Performance of $La_{0.75}Sr_{0.25}Cr_{0.9}Mn_{0.1}O_3$ Perovskites as SOFC Anodes in CO/CO_2 Mixtures." *Journal of Applied Electrochemistry* 42, no. 9 (September 2012): 727–35. https://doi.org/10.1007/s10800-012-0459-4.

[Schefold2017] Schefold J., Brisse A., Poepke H. "23,000 h Steam Electrolysis with an Electrolyte Supported Solid Oxide Cell." *International Journal of Hydrogen Energy*, Special Issue on The 21st World Hydrogen Energy Conference (WHEC 2016), 13-16 June 2016, Zaragoza, Spain, 42, no. 19 (May 11, 2017): 13415–26. https://doi.org/10.1016/j.ijhydene.2017.01.072.

[Seenivasan2017] Seenivasan H., Jackson B., Tiwari A. K. "Water Dissociation on Ni(100), Ni(110), and Ni(111) Surfaces: Reaction Path Approach to Mode Selectivity." *The Journal of Chemical Physics* 146, no. 7 (February 17, 2017): 074705. https://doi.org/10.1063/1.4976133.

[Seo2018] Seo K. D., Kim Y. J., Park J.-Y., Lim H.-T. "Investigating the Effect of Current Collecting Conditions on Solid Oxide Fuel Cell (SOFC) Performance with Additional Voltage Probes." *International Journal of Hydrogen Energy* 43, no. 4 (January 25, 2018): 2349–58. https://doi.org/10.1016/j.ijhydene.2017.11.109.

[Shaikh2015] Shaikh S. P. S., Muchtar A., Somalu M. R. "A Review on the Selection of Anode Materials for Solid-Oxide Fuel Cells." *Renewable and Sustainable Energy Reviews* 51 (November 1, 2015): 1–8. https://doi.org/10.1016/j.rser.2015.05.069.

[Shen2020] Shen M. and Zhang P. "Progress and Challenges of Cathode Contact Layer for Solid Oxide Fuel Cell." *International Journal of Hydrogen Energy* 45, no. 58 (November 27, 2020): 33876–94. https://doi.org/10.1016/j.ijhydene.2020.09.147.

[Shin2016] Shin E.-C., Ahn P.-A., Seo H.-H., Lee J.-S. "Application of a General Gas Electrode Model to Ni-YSZ Symmetric Cells: Humidity and Current Collector Effects." *Journal of the Korean Ceramic Society* 53, no. 5 (September 30, 2016): 511–20. https://doi.org/10.4191/kcers.2016.53.5.511.

[Shin2013] Shin S. M., Yoon B. Y., Kim J. H., Bae J. M. "Performance Improvement by Metal Deposition at the Cathode Active Site in Solid Oxide Fuel Cells." *International Journal of*

Hydrogen Energy 38, no. 21 (July 17, 2013): 8954–64. https://doi.org/10.1016/j.ijhydene.2013.04.115.

[Shishkin2010] Shishkin M. and Ziegler T. "Hydrogen Oxidation at the Ni/Yttria-Stabilized Zirconia Interface: A Study Based on Density Functional Theory." *The Journal of Physical. Chemistry C* 114, no. 25 (July 1, 2010): 11209–14. https://doi.org/10.1021/jp1030575.

[Siebert2011] Siebert E., Roux C., Boréave A., Gaillard F., Vernoux P. "Oxido-Reduction Properties of $La_{0.7}Sr_{0.3}Co_{0.8}Fe_{0.2}O_{3-\delta}$ Perovskite Oxide Catalyst." *Solid State Ionics* 183, no. 1 (February 11, 2011): 40–47. https://doi.org/10.1016/j.ssi.2010.11.012.

[Silva2017] da Silva, F. S. and de Souza T. M. "Novel Materials for Solid Oxide Fuel Cell Technologies: A Literature Review." *International Journal of Hydrogen Energy* 42, no. 41 (October 12, 2017): 26020–36. https://doi.org/10.1016/j.ijhydene.2017.08.105.

[Simner2005] Simner S. P., Anderson M. D., Pederson L. R., and Stevenson J. W. "Performance Variability of La(Sr)FeO_3 SOFC Cathode with Pt, Ag, and Au Current Collectors." *Journal of The Electrochemical Society* 152, no. 9 (July 28, 2005): A1851. https://doi.org/10.1149/1.1995687.

[Simrick2012] Simrick N. J., Bieberle-Hütter A., Ryll T. M., Kilner J. A., Atkinson A., Rupp J. L. M. "An Investigation of the Oxygen Reduction Reaction Mechanism of $La_{0.6}Sr_{0.4}Co_{0.2}Fe_{0.8}O_3$ Using Patterned Thin Films." *Solid State Ionics* 206 (January 5, 2012): 7–16. https://doi.org/10.1016/j.ssi.2011.10.029.

[Singhal2000] Singhal, S. C. "Advances in Solid Oxide Fuel Cell Technology." *Solid State Ionics*, Proceedings of the 12th International Conference on Solid State, 135, no. 1 (November 1, 2000): 305–13. https://doi.org/10.1016/S0167-2738(00)00452-5.

[Sonn2008] Sonn, V., Leonide A., Ivers-Tiffée E. "Combined Deconvolution and CNLS Fitting Approach Applied on the Impedance Response of Technical Ni/8YSZ Cermet Electrodes." *Journal of The Electrochemical Society* 155, no. 7 (2008): B675. https://doi.org/10.1149/1.2908860.

[Staffell2019] Staffell I., Scamman D., Velazquez Abad A., Balcombe P., Dodds P. E., Ekins P., Shah N., Ward K. R. "The Role of Hydrogen and Fuel Cells in the Global Energy System." *Energy & Environmental Science* 12, no. 2 (2019): 463–91. https://doi.org/10.1039/C8EE01157E.

[Su2016] Su S., Zhang Q., Gao X., Periasamy V., Kong W. "Effects of Changes in Solid Oxide Fuel Cell Electrode Thickness on Ohmic and Concentration Polarizations." *International Journal of Hydrogen Energy*, Special Issue: 16th China Hydrogen Energy Conference (CHEC 2015), November 2015, Zhenjiang City, Jiangsu Province, China, 41, no. 36 (September 28, 2016): 16181–90. https://doi.org/10.1016/j.ijhydene.2016.04.221.

[Suciu2018] Suciu C., Dorolti E., Hoffmann A. C. "Physico-Chemical Properties of Nanocrystalline YSZ Powders as a Function of Doping Level and Electrical Properties after Sintering." *Materials Science for Energy Technologies* 1, no. 2 (December 1, 2018): 136–45. https://doi.org/10.1016/j.mset.2018.06.007.

[Sun2010] Sun C., Hui R., Roller J. "Cathode Materials for Solid Oxide Fuel Cells: A Review." *Journal of Solid State Electrochemistry* 14, no. 7 (July 1, 2010): 1125–44. https://doi.org/10.1007/s10008-009-0932-0.

[Sun2021] Sun Y., He S., Saunders M., Chen K., Shao Z., Jiang S. P. "A Comparative Study of Surface Segregation and Interface of $La_{0.6}Sr_{0.4}Co_{0.2}Fe_{0.8}O_{3-\delta}$ Electrode on GDC and YSZ Electrolytes of Solid Oxide Fuel Cells." *International Journal of Hydrogen Energy* 46, no. 2 (January 6, 2021): 2606–16. https://doi.org/10.1016/j.ijhydene.2020.10.113.

[Świerczek2009] Świerczek K., Dabrowski B., Suescun L., Kolesnik S. "Crystal Structure and Magnetic Properties of High-Oxygen Pressure Annealed $Sr_{1-x}La_xCo_{0.5}Fe_{0.5}O_{3-\delta}$ ($0 \leqslant x \leqslant 0.5$)." *Journal of Solid State Chemistry* 182, no. 2 (February 1, 2009): 280–88. https://doi.org/10.1016/j.jssc.2008.10.030.

[Tahmasebi2013] Tahmasebi A., Sedaghat A., Kalbasi R., Zand M. M. "Performance Assessment of a Hybrid Fuel Cell and Micro Gas Turbine Power System." *Journal of Energy Equipment and Systems*, January 1, 2013, 59–96.

[Takino2020] Takino K., Tachikawa Y., Mori K., Lyth S. M., Shiratori Y., Taniguchi S., Sasaki K. "Simulation of SOFC Performance Using a Modified Exchange Current Density for Pre-Reformed Methane-Based Fuels." *International Journal of Hydrogen Energy* 45, no. 11 (February 28, 2020): 6912–25. https://doi.org/10.1016/j.ijhydene.2019.12.089.

[Tanaka2012] Tanaka R., Oliveira W. S., Brandão A., Abrantes J. C. C., Frade J. R. "Grain Boundary Conductivity of Heterogeneous Ceria Gadolinia." *Electrochimica Acta* 85 (December 15, 2012): 116–21. https://doi.org/10.1016/j.electacta.2012.08.009.

[Tezyk2019] Tezyk, V., Rossignol C., Sergent N., Djurado E., Laurencin J., Siebert E. "Cyclic Voltammetry and High-Frequency Series Resistance of $La_{0.6}Sr_{0.4}Co_{0.2}Fe_{0.8}O_{3-\delta}$ Electrode Deposited on GDC: Effect of the Electrode Microstructure and the Oxygen Partial Pressure." *Electrochimica Acta* 304 (May 1, 2019): 312–22. https://doi.org/10.1016/j.electacta.2019.02.066.

[The2015] The D., Grieshammer S., Schroeder M., Martin M., Al Daroukh M., Tietz F., Schefold J., Brisse A. "Microstructural Comparison of Solid Oxide Electrolyser Cells Operated for 6100 h and 9000 h." *Journal of Power Sources* 275 (February 1, 2015): 901–11. https://doi.org/10.1016/j.jpowsour.2014.10.188.

[Tietz2006] Tietz, F., Haanappel V. A. C., Mai A., Mertens J., Stöver D. "Performance of LSCF Cathodes in Cell Tests." *Journal of Power Sources*, Selected papers from the 2nd France-Deutschland Fuel Cell Conference, 156, no. 1 (May 19, 2006): 20–22. https://doi.org/10.1016/j.jpowsour.2005.08.015.

[Todd2002] Todd B. and Young J. B. "Thermodynamic and Transport Properties of Gases for Use in Solid Oxide Fuel Cell Modelling." *Journal of Power Sources* 110, no. 1 (July 20, 2002): 186–200. https://doi.org/10.1016/S0378-7753(02)00277-X.

[Trini2021] Trini M., De Angelis S., Jørgensen P. S., Hendriksen P. V., Thornton K., Chen M. "Towards the Validation of a Phase Field Model for Ni Coarsening in Solid Oxide Cells." *Acta Materialia*, April 14, 2021, 116887. https://doi.org/10.1016/j.actamat.2021.116887.

[Trini2020] Trini, M., Hauch A., De Angelis S., Tong X., Vang Hendriksen P., Chen M. "Comparison of Microstructural Evolution of Fuel Electrodes in Solid Oxide Fuel Cells and Electrolysis Cells." *Journal of Power Sources* 450 (February 29, 2020): 227599. https://doi.org/10.1016/j.jpowsour.2019.227599.

[Uhlenbruck2009] Uhlenbruck S., Moskalewicz T., Jordan N., Penkalla H. -J., Buchkremer H. P. "Element Interdiffusion at Electrolyte–Cathode Interfaces in Ceramic High-Temperature Fuel Cells." *Solid State Ionics* 180, no. 4 (April 27, 2009): 418–23. https://doi.org/10.1016/j.ssi.2009.01.014.

[Usseglio-Viretta2014] Usseglio-Viretta, F., Laurencin J., Delette G., Villanova J., Cloetens P., Leguillon D. "Quantitative Microstructure Characterization of a Ni–YSZ Bi-Layer Coupled with Simulated Electrode Polarisation." *Journal of Power Sources* 256 (June 15, 2014): 394–403. https://doi.org/10.1016/j.jpowsour.2014.01.094.

[Villanova2013] Villanova J., Laurencin J., Cloetens P., Bleuet P., Delette G., Suhonen H., Usseglio-Viretta F. "3D Phase Mapping of Solid Oxide Fuel Cell YSZ/Ni Cermet at the

Nanoscale by Holographic X-Ray Nanotomography." *Journal of Power Sources* 243 (December 1, 2013): 841–49. https://doi.org/10.1016/j.jpowsour.2013.06.069.

[Villanova2019] Villanova J., Schlabach S., Brisse A., Léon A. "X-Ray Fluorescence Nano-Imaging of Long-Term Operated Solid Oxide Electrolysis Cells." *Journal of Power Sources* 421 (May 1, 2019): 100–108. https://doi.org/10.1016/j.jpowsour.2019.02.084.

[Virkar2000] Virkar A. V., Chen J., Tanner C. W., Kim J.-W. "The Role of Electrode Microstructure on Activation and Concentration Polarizations in Solid Oxide Fuel Cells." *Solid State Ionics* 131, no. 1 (June 1, 2000): 189–98. https://doi.org/10.1016/S0167-2738(00)00633-0.

[Vivet2011] Vivet, N., Chupin S., Estrade E., Piquero T., Pommier P. L., Rochais D., Bruneton E. "3D Microstructural Characterization of a Solid Oxide Fuel Cell Anode Reconstructed by Focused Ion Beam Tomography." *Journal of Power Sources* 196, no. 18 (September 15, 2011): 7541–49. https://doi.org/10.1016/j.jpowsour.2011.03.060.

[Vogler2009] Vogler M., Bieberle-Hütter A., Gauckler L., Warnatz J., Bessler W. G. "Modelling Study of Surface Reactions, Diffusion, and Spillover at a Ni/YSZ Patterned Anode." *Journal of The Electrochemical Society* 156, no. 5 (March 30, 2009): B663. https://doi.org/10.1149/1.3095477.

[Wang2014a] Wang F., Brito M. E., Yamaji K., Cho D.-H., Nishi M., Kishimoto H., Horita T., Yokokawa H. "Effect of Polarization on Sr and Zr Diffusion Behavior in LSCF/GDC/YSZ System." *Solid State Ionics*, Solid State Ionics 19 Proceedings of the 19th International Conference on Solid State Ionics, 262 (September 1, 2014): 454–59. https://doi.org/10.1016/j.ssi.2014.04.002.

[Wang2014b] Wang G., Wu W., Guan W., Jin L., Wang W. G. "Effect of Conductivity and Adhesive Properties of Cathode Current-Collecting Layer on Cell Performance inside Stack for Planar Solid Oxide Fuel Cells." *Ceramics International* 40, no. 7, Part B (August 1, 2014): 11023–30. https://doi.org/10.1016/j.ceramint.2014.03.117.

[Wang2018] Wang H. and Barnett S. A. "Degradation Mechanisms of Porous $La_{0.6}Sr_{0.4}Co_{0.2}Fe_{0.8}O_{3-\delta}$ Solid Oxide Fuel Cell Cathodes." *Journal of The Electrochemical Society* 165, no. 7 (May 22, 2018): F564. https://doi.org/10.1149/2.1211807jes.

[Wang2016] Wang H., Yakal-Kremski K. J., Yeh T., Rupp G. M., Limbeck A:, Jürgen Fleig, and Scott A. Barnett. "Mechanisms of Performance Degradation of $(La,Sr)(Co,Fe)O_{3-\delta}$ Solid Oxide Fuel Cell Cathodes." *Journal of The Electrochemical Society* 163, no. 6 (2016): F581–85. https://doi.org/10.1149/2.0031607jes.

[Wang2005] Wang W. G. and Mogensen M. "High-Performance Lanthanum-Ferrite-Based Cathode for SOFC." *Solid State Ionics* 176, no. 5 (February 14, 2005): 457–62. https://doi.org/10.1016/j.ssi.2004.09.007.

[Wang2020] Wang Y., Li W., Ma L., Li W., Liu X. "Degradation of Solid Oxide Electrolysis Cells: Phenomena, Mechanisms, and Emerging Mitigation Strategies—A Review." *Journal of Materials Science & Technology*, SI: Energy Conversion & Storage Materials Design, Fabrication and Functionality, 55 (October 15, 2020): 35–55. https://doi.org/10.1016/j.jmst.2019.07.026.

[Wang2013] Wang Z., Peng R., Zhang W., Wu X., Xia C., Lu Y. "Oxygen Reduction and Transport on the $La_{1-x}Sr_xCo_{1-y}Fe_yO_{3-\delta}$ Cathode in Solid Oxide Fuel Cells: A First-Principles Study." *Journal of Materials Chemistry A* 1, no. 41 (October 2, 2013): 12932–40. https://doi.org/10.1039/C3TA11554B.

[Wang2007] Wang Z., Qian J., Cao J., Wang S., Wen T. "A Study of Multilayer Tape Casting Method for Anode-Supported Planar Type Solid Oxide Fuel Cells (SOFCs)." *Journal of*

Alloys and Compounds 437, no. 1 (June 28, 2007): 264–68. https://doi.org/10.1016/j.jallcom.2006.07.110.

[Weber2015] Weber A., Szász J., Dierickx S., Endler-Schuck C., Ivers-Tiffée E. "Accelerated Lifetime Tests for SOFCs." *ECS Transactions* 68, no. 1 (February 6, 2015): 1953–60. https://doi.org/10.1149/06801.1953ecst.

[Yashiro2011] Yashiro K., Nakano I., Kuhn M., Hashimoto S., Sato K., Mizusaki J. "Electrical Conductivity and Oxygen Diffusivity of Perovskite-Type Solid Solution $La_{0.6}Sr_{0.4}Co_{1-y}Fe_yO_{3-\delta}$ (Y=0.2, 0.4, 0.5, 0.6, 0.8)." *ECS Transactions* 35, no. 1 (April 25, 2011): 1899. https://doi.org/10.1149/1.3570179.

[Yurkiv2014] Yurkiv V., Costa R., Ilhan Z., Ansar A., Bessler W. G. "Impedance of the Surface Double Layer of LSCF/CGO Composite Cathodes: An Elementary Kinetic Model." *Journal of The Electrochemical Society* 161, no. 4 (January 1, 2014): F480–92. https://doi.org/10.1149/2.070404jes.

[Zhang2007] Zhang C., Li C.-J., Zhang G., Ning X.-J., Li C.-X., Liao H., Coddet C. "Ionic Conductivity and Its Temperature Dependence of Atmospheric Plasma-Sprayed Yttria Stabilized Zirconia Electrolyte." *Materials Science and Engineering: B* 137, no. 1 (February 25, 2007): 24–30. https://doi.org/10.1016/j.mseb.2006.10.005.

[Zheng2015] Zheng Y., Li Q., Chen T., Wu W., Xu C., Wang W. G. "Comparison of Performance and Degradation of Large-Scale Solid Oxide Electrolysis Cells in Stack with Different Composite Air Electrodes." *International Journal of Hydrogen Energy* 40, no. 6 (February 19, 2015): 2460–72. https://doi.org/10.1016/j.ijhydene.2014.12.101.

[Zhu2017] Zhu J. H. and Ghezel-Ayagh H. "Cathode-Side Electrical Contact and Contact Materials for Solid Oxide Fuel Cell Stacking: A Review." *International Journal of Hydrogen Energy* 42, no. 38 (September 21, 2017): 24278–300. https://doi.org/10.1016/j.ijhydene.2017.08.005.

[Zhu2003] Zhu W. Z. and Deevi S. C. "A Review on the Status of Anode Materials for Solid Oxide Fuel Cells." *Materials Science and Engineering: A*, Papers from the German Priority Programme (Functionally Graded Materials), 362, no. 1 (December 5, 2003): 228–39. https://doi.org/10.1016/S0921-5093(03)00620-8.